UNIVERSITY OF SOUTHAMPTON

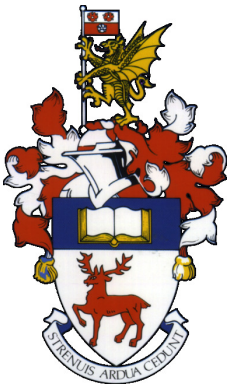

Large eddy simulations of inflow turbulence noise: application to tidal turbines

by

Thomas P. Lloyd

Ph.D. thesis

in the

Faculty of Engineering and the Environment

December 2013

Ph.D. thesis

Thomas Lloyd, December 2013.
T.P.Lloyd@soton.ac.uk
Faculty of Engineering and the Environment,
University of Southampton,
Southampton. SO17 1BJ.
United Kingdom.

Typeset in LaTeX. Page, figure, table and bibliographic references use hypertext. *DOI*s are also hyperlinked.

Abstract

Marine anthropogenic noise is increasing, along with concern about its impact on the environment. Hence minimising noise within engineering design is important, including in applications such as ships, submarines and turbines. The desire to mitigate noise may also be related to reducing the detectability of certain types of marine craft. Noise reduction typically focuses on rotating machinery such as propellers, due to the high velocity of the blades.

A common source of broadband noise in engineering scenarios is often termed *inflow turbulence noise*. Resulting from upstream turbulence impinging onto rotor blades, this source typically dominates the low to mid range of the frequency spectrum. This is due to the high turbulence intensity and large length scales present in the inflow turbulence, which exceed those generating competing noise sources.

This thesis uses a library of numerical tools to simulate broadband inflow turbulence noise. Synthetic turbulence is generated numerically within the simulations. Turbulence is resolved on the grid by solving the filtered Navier-Stokes equations. Based on the assumption of incompressible flow, noise sources may be predicted without resolving acoustic waves on the grid. This decoupling of hydrodynamic and acoustic processes means that radiated noise may be estimated using an *acoustic analogy*.

Validation of two inflow turbulence generators revealed the importance of obtaining the prescribed turbulence statistics, as well as minimising artificial pressure fluctuations. This is used to simulate homogeneous isotropic turbulence impinging onto a foil, allowing acoustic sources to be located. The far-field sound prediction is in good agreement with experimental measurement data for low frequencies. It is then shown that the effect of foil thickness on noise can successfully be predicted using the proposed methodology.

Noise radiation from a tidal turbine is then estimated by fully resolving all turbine blades, both spatially and temporally, in the simulation. A good agreement is seen in comparison to an analytical model, demonstrating that the simulation captures the dominant flow features which affect the acoustic spectrum. These spectral 'humps' are a result of turbulence-rotor interaction, which is implicitly included. Full scale noise estimates made from the simulations are then used to inform environmental impact assessment; the turbine hydrodynamic noise is not expected to be an issue in this regard.

Declaration of Authorship

I, THOMAS LLOYD, declare that the thesis entitled "Large eddy simulations of inflow turbulence noise: application to tidal turbines" and the work presented in the thesis are both my own, and have been generated by me as a result of my own original research. I confirm that:

- this work was done wholly or mainly while in candidature for a research degree at this University;
- where any part of this thesis has previously been submitted for a degree or any other qualification at this University or any other institution, this has been clearly stated;
- where I have consulted the published work of others, this is always clearly attributed;
- where I have quoted the work of others, the source is always given. With the exception of such quotations, this thesis is entirely my own work;
- I have acknowledged all main sources of help;
- where the thesis is based on work done by myself jointly with others, I have made it clear what was done by others and what I have contributed myself.

Signed:.....
Date:.....

Contents

List of Figures

List of Tables

Nomenclature

Symbols are defined in the text at the first point of usage. All symbols used in multiple sections are included in the nomenclature. Where a symbol has dual meaning, this is explicitly stated in the text. In general, bold typeface represents a **vector**. The coordinate system is Cartesian unless otherwise stated, where $x_i = (x_1, x_2, x_3) = (x, y, z)$ represent the streamwise, wall-normal (or vertical) and spanwise directions. Vector notation is generally used, although the Einstein summation convention is used where appropriate i.e. $u_i u_j = \sum_{j=1}^{3} u_i u_j = u_1 u_1 + u_1 u_2 + u_1 u_3$.

Latin symbols

symbol	description	units
A	area	$[m^2]$
C	generic constant	$[-]$
C_S	Smagorinsky constant	$[-]$
c	blade chord	$[m]$
c_0	speed of sound	$[ms^{-1}]$
D	diameter	$[m]$
$\mathbf{e}$	unit vector	$[-]$
$\mathbf{F}, \mathcal{F}$	generalised pressure source	$[kgm^{-3}s^{-2}]$
F	flux	$[m^3s^{-1}]$
f	frequency, function	$[s^{-1}, -]$
G	LES filter kernel function	$[m^{-1}]$
H	height	$[m]$
h	thickness; turbine hub height	$[m]$
I	acoustic intensity	$[kgs^{-3}]$
$\mathcal{I}$	turbulence intensity	$[-]$
k	kinetic energy	$[m^2s^{-2}]$
L	length	$[m]$
$\mathcal{L}$	integral length scale	$[m]$
ℓ	eddy length scale	$[m]$
$\mathcal{M}$	coefficient matrix	$[-]$

N	number of cells; number of samples	$[-;-]$
$\boldsymbol{n}$	unit vector normal to surface	$[-]$
p	pressure	$[kgm^{-1}s^{-2}]$
Q	second invariant of velocity gradient tensor; turbine torque	$[s^{-1}; kgm^2s^{-2}]$
R	radius	$[m]$
$\boldsymbol{r}$	separation vector; receiver distance	$[m; m]$
r	radial distance	$[m]$
$\boldsymbol{S}$	strain rate tensor	$[s^{-1}]$
S	surface	$[m]$
T	total time	$[s^{-1}]$
$\boldsymbol{T}$	Lighthill stress tensor	$[kgm^{-1}s^{-2}]$
$\mathcal{T}$	integral time scale	$[s]$
t	time	$[s]$
U	characteristic velocity scale	$[ms^{-1}]$
U_b	bulk velocity	$[ms^{-1}]$
U_C	convection velocity	$[ms^{-1}]$
$\boldsymbol{u}, \boldsymbol{v}$	velocity vector	$[ms^{-1}]$
u_τ	friction velocity	$[ms^{-1}]$
V	volume	$[m^3]$
v_n	surface normal velocity	$[ms^{-1}]$
$\boldsymbol{x}$	receiver location vector	$[m]$
$\boldsymbol{y}$	source location vector	$[m]$

Greek symbols

α	blade angle of attack	$[deg]$
γ	coherence; blade twist angle	$[-; deg]$
Δ	filter width; grid spacing	$[m; m]$
δ	boundary layer thickness	$[m]$
ε	dissipation rate	$[m^2s^{-3}]$
κ	wavenumber	$[m^{-1}]$
λ	wavelength	$[m]$
μ	dynamic viscosity	$[kgm^{-1}s^{-1}]$
ν	kinematic viscosity	$[m^2s^{-1}]$
ρ	fluid density	$[kgm^{-3}]$
$\boldsymbol{\sigma}$	viscous stress tensor	$[kgm^{-1}s^{-2}]$
$\boldsymbol{\tau}$	stress tensor	$[m^2s^{-2}]$
τ	time scale; time lag	$[s; s]$
Φ	spectrum	$[-]$
ϕ	transport variable; blade pitch angle	$[-; deg]$

ψ	vorton size	$[m]$
$\mathbf{\Omega}$	rotation rate tensor	$[s^{-1}]$
Ω	rotational velocity	$[rads^{-1}]$
$\boldsymbol{\omega}$	vorticity	$[s^{-1}]$
ω	angular frequency	$[rads^{-1}]$

Mathematical operators

$\nabla\times$	curl	$\nabla \times \boldsymbol{u} = \boldsymbol{e}_i \varepsilon_{ijk} \partial_j u_k$
$\nabla\cdot$	divergence	$\nabla \cdot \boldsymbol{u} = \delta_{ij} u_{i,j} = \partial_i u_i$
∇	gradient	$\nabla f = f_{,j} e_j = \partial_i f$
$\nabla^2 = \nabla \cdot \nabla$	Laplacian operator	$\nabla^2 f = f_{,jj} = \partial_{ii} f$
$\otimes$	dyad	$\boldsymbol{u} \otimes \boldsymbol{v} = \boldsymbol{u}\boldsymbol{v}^T$
$\Box^2$	d'Alembert operator	$\Box^2 f = (\partial_{tt} - c_0^2 \nabla^2) f$
$\frac{D}{Dt}$	material derivative	$\frac{D}{Dt} = \frac{\partial}{\partial t} + \boldsymbol{u} \cdot \nabla = \partial_t + u_j \partial_j$
$H(f)$	Heaviside function	$H(f) = \begin{cases} 0, & f < 0 \\ 1, & f \geq 0 \end{cases}$
$\delta(f)$	Dirac delta	$\delta(f) = \begin{cases} \infty, & f = 0 \\ 0, & f \neq 0 \end{cases}$
δ_{ij}	Kronecker delta	$\delta_{ij} = \begin{cases} 1, & i = j \\ 0, & i \neq j \end{cases}$
ε_{ijk}	Levi-Civita symbol	

Subscripts and superscripts

0	reference value
f	(cell) face
sgs	subgrid scale
w	(value at the) wall
$'$	fluctuating quantity
$*$	non-dimensionalised quantity
$\cdot$	time derivative
$+$	normalised wall unit
$\bar{}$	filtered quantity; mean quantity
$\hat{}$	test filtered quantity; normalised wavenumber

Dimensionless groups

$C_{()}$	force coefficient	$2()/\rho A U_0^2$
C_f	skin friction coefficient	$2\tau_w/\rho U_0^2$
C_p	pressure coefficient	$2p/\rho U_0^2$
Co	Courant number	$\lvert U\rvert \Delta t/\Delta x$
He	Helmholtz number	$\omega L/c_0$
J	advance coefficient	U/nD
M	Mach number	U/c_0
Re	Reynolds number	UL/ν
St	Strouhal number	fL/U
U^+	shear normalised velocity	u/u_τ
y^+	normalised wall distance	yu_τ/ν
Λ	tip speed ratio	$\Omega R/U_0$
σ	cavitation number	$2(p-p_v)/\rho_0 U_0^2$

Abbreviations and acronyms

AMI	arbitrary mesh interface
CD	central differencing
CFD	computational fluid dynamics
DES	detached eddy simulation
DMS	dynamic mixed Smagorinsky
DNS	direct numerical simulation
DS	dynamic Smagorinsky
FSM	forward stepwise method
$FW\text{-}H$	Ffowcs Williams-Hawkings
fft	fast Fourier transform
HIT	homogeneous isotropic turbulence
IAT	inhomogeneous anisotropic turbulence
$IT(G)$	inflow turbulence (generator)
$ITTC$	International Towing Tank Conference
LES	large eddy simulation
$LEEs$	linearised Euler equations
$NSEs$	Navier-Stokes equations
$PISO$	pressure implicit splitting of operators
PSD	power spectral density
$RANS(Es)$	Reynolds-averaged Navier-Stokes (Equations)
SAS	scale adaptive simulation
SL	source level

SPL	sound pressure level
SSL	spectral source level
SST	shear stress transport
SVM	synthetic vorton method
TKE	turbulence kinetic energy
TVD	total variation diminishing
UD	upwind scheme
$URANS$	unsteady RANS

Acknowledgements

The last three years have provided everything I envisaged, and certainly more than I expected, a research degree would! And it would certainly not have been possible without the support of numerous people (too many to name) to whom I am very grateful.

Firstly, I wish to acknowledge the experimental data provided by Dr. Mathieu Gruber, which was collected as part of the FLOCON project during his Ph.D. He also dutifully answered my many questions about the experiments. Thanks to Drs. Yusik Kim and Evgeny Shchukin for giving me their inflow turbulence generator codes; the availability of these in OpenFOAM made my task that bit easier. I also wish to mention collectively the numerous OpenFOAM users I have met over the past three years who have shared their insight. We have a growing community of users at Southampton (again too many to mention) who are always willing to help each other. The use of the IRIDIS 3 and 4 high performance computing facilities is also gratefully acknowledged.

Thanks to QinetiQ and dstl for their financial support, and external supervision. To my supervisors, Professors Stephen Turnock and Victor Humphrey, thanks not only for your support, but also for the interesting chats that meetings often involved; the 'bigger picture' was always on my mind as a result. Thanks also to my examiners Dr. Imran Afgan and Professor Phillip Joseph, whose critical input has helped guide the work.

To all those in the Fluid Structure Interactions Research Group, thanks for making it such a sociable place to work. Someone was always free for a coffee or a chat. I particularly wish to acknowledge my co-authors Dr. Joesph Banks, Kutalmis Bercin and Marion James. It was a pleasure to collaborate with you, and a refreshing change from what sometimes felt like Ph.D. isolation! I also appreciate the time taken by Joe to proof-read this document; it is all the better for it.

Finally, thanks to all my friends and family for your support along the way: Prathiban for being a great friend and flatmate, as well as sharing my love of engineering and drum'n'bass; Alek, who was always ready to discuss Ph.D. and LaTeX woes, or distract me with adventures around Europe; to my family, for your love and support, but also a keen interest in my work; lastly, my biggest thanks to Louise, who has been through all I have, and much more. We are always learning from each other, and long may it continue!

Dedicated to my grandparents.

"I'm gonna tell you a little about sound.
Sound is a pressure wave that goes through matter,
And which lies within the frequency range that we can hear.
This is what we usually define as sound.
This is my sound."

Identity by Seba. Secret Operations.

"The heart of man is very much like the sea,
it has its storms, it has its tides,
and in its depths it has its pearls too."

The Letters of Vincent van Gogh by Vincent van Gogh.

1

Introduction

1.1 Motivation

Minimising noise in the design of marine vehicles is important in numerous applications. Military vehicles require low-noise signatures to avoid sonar detection (Andersen *et al.*, 2009). The main sources of noise and induced vibration typically originate from the propeller (Merz *et al.*, 2009). Designers of autonomous underwater vehicles may also wish to reduce noise disturbance when studying marine life in the natural environment (Griffiths *et al.*, 2001). The study of ship propeller noise (both cavitating and non-cavitating) is related to induced hull pressure pulses (van Wijngaarden, 2005) as well as radiated noise (Seol *et al.*, 2004). The issue of anthropogenic noise impact is part of a wider concern regarding human environmental impact in the oceans, and is being addressed via regulation (MEPC, 2007) and research (Erbe, 2013; Erbe *et al.*, 2013; SONIC, 2013). Two examples of marine anthropogenic noise sources are depicted in Figure 1.1.

Less well documented are studies addressing noise modelling and impact of renewable energy devices, despite concern about the potential effect on marine species (Halvorsen *et al.*, 2011). While assessments do exist based on full scale measurements (*e.g.* see Richards *et al.*, 2007), this issue has not been widely addressed using modelling. In contrast to the limited availability of published hydroacoustics studies, a large research field is that of aeroacoustics (see Juvé (2009) for a review). As noise regulation of commercial aircraft, particularly at take-off and landing, has become more stringent, reduction

of turbomachinery and airframe noise has received increased research attention. Noise modelling of wind turbines has also been a research focus (Glegg *et al.*, 1987; Grosveld, 1985; Hubbard, 1991; Oerlemans *et al.*, 2009), due to concerns regarding human perception and annoyance.

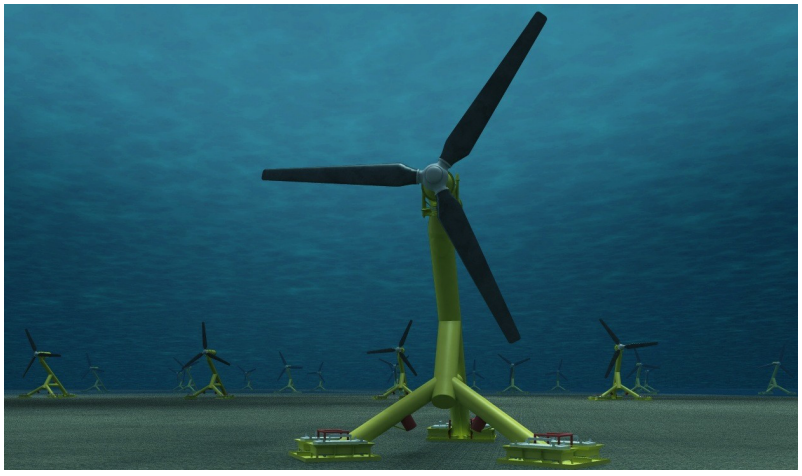

(a) tidal turbine (www.hammerfeststrom.com)

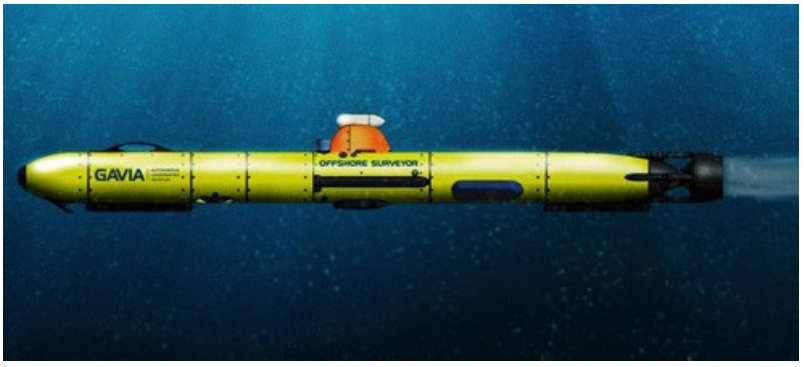

(b) autonomous underwater vehicle (www.gavia.is)

FIGURE 1.1: Examples of marine anthropogenic noise sources.

Computational fluid dynamics (CFD) has the potential for application to these engineering problems. The term CFD is used to describe a numerical method which solves the governing fluid flow equations inside a *domain* (volume) encompassing the flow. The domain is discretised into *grid cells*, allowing small details of the problem geometry and flow features to be captured. Thus many of the simplifications of analytical modelling may be removed.

This approach has several advantages which make it a powerful tool alongside experimentation. Access to high-powered computing facilities and open-source software means a *numerical testing facility* can be created, allowing multiple simultaneous 'tests' to be carried out. Since a large amount of flow field data is available, a detailed insight into the flow can be achieved. In this respect, CFD can be seen as a complimentary tool for experimentation, informing the placement of measurement devices.

In terms of hydroacoustics research, CFD has traditionally seen limited application. When applied to cavitation modelling, unsteady CFD "is not satisfactory to be useful for...noise prediction" (Bensow and Bark, 2010, p.9). Investigations of propeller cavitating and non-cavitating noise have typically utilised *potential flow* methods (*e.g.* see Salvatore and Ianniello, 2003; Seol *et al.*, 2005). When broadband non-cavitating (*i.e.* turbulence) noise is modelled, high fidelity CFD may be applied however, as reported by Pan and Zhang (2010). With computing power continually increasing, numerical simulations of hydroacoustics using large computational grids can become commonplace. Note that such computations are 'routine' within the aeroacoustics field (*e.g.* see Reese *et al.* (2007), Reboul *et al.* (2008), Argüelles Díaz *et al.* (2009) and Greschner and Thiele (2012)).

1.2 Background

Many noise sources can exist in a marine propulsor or turbine. A broad categorisation is presented in Table 1.1. Carlton (2007, chap. 10) provides a discussion of propeller noise. Possible sources for a tidal turbine are similar and thus the same general analysis applies. The relative magnitude of each noise source for tidal turbines has not been studied in detail however. Cavitation has been observed for tidal turbines at shallow immersion depths (Wang *et al.*, 2007). The relatively high design shaft immersion and low tip speed compared to ship propellers means this is not expected to be a dominant noise source in operation (Lloyd *et al.*, 2011*b*).

TABLE 1.1: Categorisation and examples of marine propulsor noise sources.

category	name	type	description
non-cavitating	displacement	tonal	periodic pressure fluctuation resulting from fluid displacement by rotating blade.
	unsteady displacement	narrowband	periodic angle of attack fluctuation due to non-uniform mean inflow velocity.
	turbulence	broadband	range of turbulence length scales interacting with blade.
cavitating	steady sheet	tonal	increased blade thickness (displacement) due to a sheet cavity.
	unsteady sheet	narrowband	size fluctuation of sheet cavity caused by non-uniform inflow velocity.
	tip vortex	broadband	cavitation formation and breakdown inside rotor tip vortex radiate over a broad frequency range.

Figure 1.2 shows that cavitation noise dominates the spectrum across all frequencies. When the risk of cavitation is low, such as for ducted propulsors or submarines (Seol

et al., 2004), reducing turbulence noise becomes more important. Noise due to inflow turbulence is seen to dominate at low frequencies, while trailing edge noise may be more important at high frequencies, or in the absence of inflow turbulence.

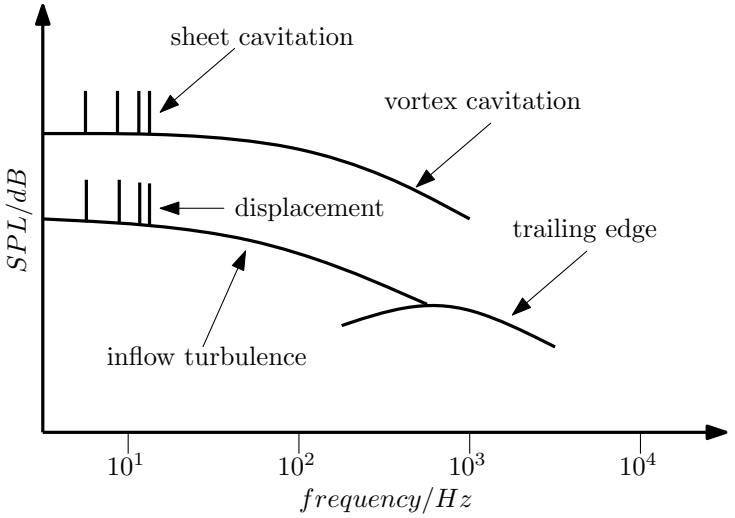

FIGURE 1.2: Representative spectrum of marine propeller noise sources.

Broadband noise in low speed turbomachinery results from randomly fluctuating forces on the blades (Sharland, 1964). This is equivalent to describing the sources as *dipoles* (fluctuating forces) caused by turbulence. The relationship between turbulence and a dipole source can be understood from boundary layer theory. Using order of magnitude arguments, it may be shown that the wall-normal Navier-Stokes equation reduces to a zero pressure gradient[1] (Çengel and Cimbala, 2006*a*, chap. 10). Since the pressure outside the boundary layer is related to fluid velocity by Bernoulli's Equation, it may be deduced that the pressure fluctuations at the wall are caused by velocity (and therefore pressure) fluctuations at some distance away from it (Powell, 1964).

Broadband sources may be divided into the three main categories of (Hubbard, 1991):

- *turbulent boundary layer* (also called *trailing edge*);
- *vortex shedding*;
- *inflow turbulence* (also called *leading edge*).

Turbulent boundary layer noise arises due to scattering of the turbulent boundary layer at the blade trailing edge. The second category includes noise due to trailing edge bluntness and tip vortices, as well as flow separation and blade stall. Inflow turbulence noise relates to the interaction of upstream turbulence with the blade leading edge. An illustration of these sources in terms of physical mechanism and frequency dependence is given in Figure 1.3.

[1] $\partial p/\partial \boldsymbol{n} = 0$, where p is pressure and $\boldsymbol{n}$ is the unit vector normal to the surface.

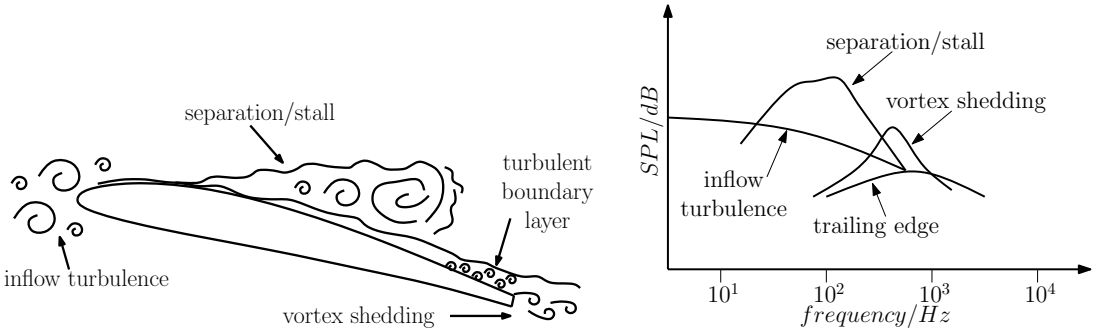

(a) Subsonic turbomachinery broadband noise sources.

(b) Representative noise frequency spectrum (adapted from Grosveld (1985) and Glegg *et al.* (1987), for wind turbines).

FIGURE 1.3: Turbomachinery broadband noise sources.

The relative magnitude of each source will depend on the operating point of the device. For example, reduced flow rate leads to blade stall, increasing stall noise. The far-field pressure is determined not only by the magnitude of the fluctuating forces but also the correlation area of the source (Maruta and Kotake, 1983; Sharland, 1964; Siddon, 1973). Sharland (1964) showed that the sound power

$$W \propto \int_S U_0^4 \overline{C_L'^2} A_C dS, \tag{1.1}$$

based on the argument that the fluctuating surface pressure (dipole source) is equal to the product of the dynamic pressure ($\propto U_0^2$, where U_0 is a reference velocity) and the fluctuating lift coefficient C_L'. Equation 1.1 follows from the fact that $W \propto p^2$.

Noting that the size of the correlation area A_C is related to the turbulence length scale, the relative magnitude of each acoustic source can be deduced. Since the inflow turbulence length scales will typically be larger than those inside the turbulent boundary layer, this source often dominates. This is confirmed by the analytical models of Amiet (1975, 1976). Trailing edge noise may be important at higher frequencies when the inflow turbulence no longer induces large lift fluctuations, or in the absence of any inflow turbulence (see Figure 1.3). Noise due to vortex shedding will be centred at a frequency proportional to the trailing edge bluntness (thickness). Stall noise exhibits a broader spectrum, since a range of scales in the separated flow region increases compared to those shed from a blunt trailing edge.

Inflow turbulence is common in engineering applications. In the case of a ship, the boundary layer formed along the hull will have a thickness of the order of one metre, and be fully turbulent at the propeller plane. Additional vortices may be shed from appendages, adding to the range of turbulence scales flowing into the propeller. For a tidal turbine, operating in a tidal channel means the oncoming flow possesses a large range of length scales. These will be affected by the local channel height and bathymetry. High turbulence intensities may also be expected, particularly close to the sea bed (Stacey

et al., 1999). Therefore inflow turbulence noise is the subject of the modelling presented herein. Although vortex shedding noise may exceed inflow turbulence noise, particularly when operating at 'off-design' conditions, it is assumed this scenario is not typical.

1.3 Aim and objectives

Based on the discussion presented in Sections 1.1 and 1.2, this work is aimed at utilising CFD tools to model broadband noise of marine propulsors and turbines. A significant knowledge gap exists within engineering regarding the application of advanced CFD techniques to the modelling of noise generated by complex geometries such as propellers and turbines. This can be encompassed in the question *"can CFD be used to model hydrodynamic noise sources?"* More specifically, this research is focussed on *"can CFD represent inflow turbulence noise sources in 'realistic' engineering applications?"*

The focus is on investigating the ability of the chosen method to predict noise source strength, which can be used to aid 'low noise' design. To help achieve this, the primary objectives, which are addressed in subsequent chapters, have been identified as:

1. To conduct simulations capable of capturing broadband noise sources and radiated sound. This will include a review of methods capable of resolving a range of turbulence scales and predicting far-field sound.
2. To analyse the impact of numerical schemes, turbulence models and grid resolution on noise source prediction.
3. To utilise a numerical method for generating velocity fluctuations representative of inflow turbulence. This requires evaluation of the method's ability to replicate the desired turbulence statistics.
4. To assess how variations in the prescribed inflow turbulence and rotor blade geometry affect the noise source strengths. In doing so, the ability of the chosen method to capture the effect of these parameters in noise source predictions should be examined.
5. To apply the method to a 'realistic engineering scenario'. A tidal turbine represents a suitable application, with a lack of published studies available.

1.4 Contributions and publications

This monograph represents a research contribution within applied fluid dynamics. In achieving this it contributes to the fields of marine hydrodynamics, hydroacoustics,

aeroacoustics and renewable energy. The key outcomes of the work may be summarised as:

1. Analysis of numerical schemes for finite volume CFD. A systematic evaluation of blended upwind-central convection differencing schemes in terms of their impact on solution fidelity and stability has been made. This builds on existing analyses of such schemes within OpenFOAM (Bensow and Liefvendahl, 2008). The current work extends this to examine a code-specific scheme (*filteredLinear*) which offers improved accuracy and stability for the cases presented herein (see publication 7.).

2. Evaluation (and comparison) of synthetic inflow turbulence generation techniques in terms of induced pressure fluctuations. This contributes to the necessary assessment of such methods within engineering, when dynamic forces and acoustics are important (Kim *et al.*, 2013; Poletto *et al.*, 2013). The effect of inhomogeneity of the inflow turbulence statistics on pressure fluctuations has been investigated (see publication 1.).

3. Application of broadband inflow turbulence to leading edge noise prediction. Encouraging numerical results have been reported, where previous simulations of the same test case were unsuccessful (Deniau *et al.*, 2011). Typically, numerical studies of leading edge noise use Euler equation solvers (Clair *et al.*, 2012; Gill *et al.*, 2013*a*), and do not model broadband turbulence. The work of Christophe (Christophe, 2011; Christophe *et al.*, 2007) constitutes the only other such study discovered in the literature; the present simulations address a higher Reynolds number however, and are therefore more applicable to marine applications (see publications 1,4 and 9).

4. Numerical analyses of the effect of turbulence statistics and geometry on foil noise. Although experiments of 'real' foil geometries are reported in the literature (Devenport *et al.*, 2010; Hutcheson *et al.*, 2012), CFD investigations are less common. The results presented here represent one of only a few such studies (*e.g.* see also Gill *et al.*, 2013*a*) (see publication 4.).

5. Full rotor simulation of a tidal turbine using large eddy simulation. This is the first such study reporting inflow turbulence generation, dynamic forces and hydrodynamic noise of such a device. The only other similar published study (Afgan *et al.*, 2013) did not address noise radiation (see publications 2 and 3). This work also includes comparison to an analytical model, which has itself been used to make environmental impact assessments of tidal turbines, the first such modelling seen in the literature (see publications 5 and 6).

Journal papers

1. Lloyd, T.P., Turnock, S.R., Humphrey, V.F. and Gruber, M. Comparison of two inflow turbulence generators for hydroacoustic simulations (*under revision for Computers & Fluids*).

2. Lloyd, T.P., Turnock, S.R. and Humphrey, V.F. Flow and noise predictions of a horizontal axis tidal turbine using large eddy simulations (*submitted to Renewable Energy*).

Peer-reviewed conference papers

3. Lloyd, T.P., Turnock, S.R. and Humphrey, V.F. (2013) Computation of inflow turbulence noise of a tidal turbine. IN: *Proceedings of the* 10^{th} *European Wave and Tidal Energy Conference*, 2^{nd}-5^{th} September, Aalborg.

4. Lloyd, T.P., Gruber, M. Turnock, S.R. and Humphrey, V.F. (2013) Using an inflow turbulence generator for leading edge noise predictions. IN: A. Talamelli, M. Oberlack. and J. Peinke. (eds.) *Proceedings of the* 5^{th} *Conference on Turbulence*, *vol. 149*, Heidelberg: Springer-Verlag, ISBN 978-3-319-01860-7, pp. 211-216.

5. Lloyd, T.P., Humphrey, V.F. and Turnock, S.R. (2011) Noise modelling of tidal turbine arrays for environmental impact assessment. IN: *Proceedings of the* 9^{th} *European Wave and Tidal Energy Conference*, 5^{th}-9^{th} September, Southampton.

6. Lloyd, T.P., Turnock, S.R. and Humphrey, V.F. (2011) Modelling techniques for underwater noise generated by tidal turbines in shallow waters. IN: *Proceedings of the* 30^{th} *Offshore Mechanics and Arctic Engineering Conference*, 19^{th}-24^{th} June, Rotterdam.

Conference contributions[2]

7. James, M. and Lloyd, T.P. (2013) Large eddy simulations of circular cylinders at a range of Reynolds numbers. IN: *Proceedings of the ITTC Workshop on Wave Run-up and Vortex Shedding*, 17^{th}-18^{th} October, Nantes.

8. Banks, J., Bercin, K., Lloyd, T.P. and Turnock, S.R. (2013) Fluid structure interaction analyses of tidal turbines. IN: *Proceedings of the* 16^{th} *Numerical Towing Tank Symposium*, 2^{nd}-4^{th} September, Mülheim.

9. Lloyd, T.P., Gruber, M., Turnock, S.R. and Humphrey, V.F. (2012) Simulation of inflow turbulence noise. IN: *Proceedings of the* 15^{th} *Numerical Towing Tank Symposium*, 7^{th}-9^{th} October, Cortona

[2]Papers 7. and 8. are collaborative works, involving equal author contribution.

10. Lloyd, T.P., Turnock, S.R. and Humphrey, V.F. (2011) Unsteady CFD of a marine current turbine using OpenFOAM with generalised grid interface. IN: *Proceedings of the* 14^{th} *Numerical Towing Tank Symposium*, 23^{rd}-24^{th} October, Poole.

1.5 Terminology

The work presented herein concerns numerical modelling within the field of acoustics. While the term *acoustics* is generally used to describe the study of phenomena including vibration, sound and ultrasound, only the second of these is addressed here. In addition, note that the term *noise* is used to describe 'unwanted' sound. Defining what exactly is meant by 'unwanted' is difficult and will not be addressed further here. This definition is therefore interpreted loosely throughout *i.e.* "noise" and "sound" are used interchangeably.

A further issue for clarification is the definition of various frequency ranges used as descriptors: *low*, *mid* and *high* frequency. The definition perhaps depends on which field of acoustics is being addressed; for example a 1 m wavelength has a frequency of 1500 Hz in water but only 340 Hz in air. The author found no clear guidance on this, and hence some attempt at clarity is made. Since this work concerns sound generated by turbulence, frequency ranges have been imagined in relation to turbulence time scales; although they have differing length scales, turbulence, and sound radiated by it, will possess the same frequency. Hence the division between low and high frequency is made using the integral time scale, which is assumed to lie at the mid frequency.

It is also pertinent to discuss the presentation of sound amplitude. Sound is typically reported using the *decibel* (dB) scale, since this is how pressure fluctuations are perceived by a receiver. The decibel is a logarithmic unit of a 'power' ratio. The sound power level (SWL) may be written as

$$SWL = 10 \log_{10} \left(\frac{W}{W_0} \right), \tag{1.2}$$

where W and W_0 are two values of acoustic power. Imagined in this way, the dB is a logarithm of pressure squared, since $W \propto p^2$ (as introduced in Section 1.2). The reference power (W_0) or pressure (p_0) are defined for a particular fluid. Values used in the current work are $p_0 = 1\mu Pa$ in water, and $p_0 = 20\mu Pa$ in air. Hence, decibel levels in water and air cannot be compared without appropriate scaling. Spectral amplitudes in this work always denote the reference value used, due to the fact that results concerning both air and water are presented.

The bandwidth of a spectrum (Δf) will also modify the spectral amplitude, since this affects the frequency distribution of the acoustic power. Data are often presented in *third-octave* bandwidths. This is defined such that the upper frequency band-edge is $\sqrt{2}$

higher than the lower frequency band-edge (Raichel, 2006, chap. 3). Throughout this monograph, acoustic spectra are denoted with reference to Hz^{-1}, and accompanied by information regarding the bandwidth used.

1.6 Thesis structure

The structure of the thesis reflects a number of stages of work undertaken towards the development of a reliable simulation-based methodology for predicting inflow turbulence noise. Subsequent chapters report simulation decisions based on both theoretical considerations and test case results. These steps provide important validation of various aspects of the methods employed, culminating in the simulation of a full tidal turbine geometry encountering inflow turbulence.

Chapter 2 introduces relevant physics relating to turbulence and sound generation. The focus is on how hydrodynamic and acoustic processes may be separated to improve the efficiency of hydroacoustic simulations. This leads on to Chapter 3, which presents a review of existing computational work on simulating broadband noise sources, particularly focussing on resolution requirements and turbulence modelling. Chapter 4 provides an outline of the numerical methods that have been utilised. Test case results are used to justify some of the modelling decisions taken, especially relating to the convection schemes used.

In Chapter 5, the suitability of synthetic turbulence generators for hydroacoustic predictions is assessed. Two test cases are presented, in order to evaluate both homogeneous and inhomogeneous turbulence. This not only focusses on the ability to generate prescribed turbulence statistics, but also to minimise artificial pressure fluctuations, which 'pollute' the acoustic sources. Chapter 6 presents results to validate a methodology for simulating homogeneous inflow turbulence noise of stationary foils. The numerical framework is then used to investigate how foil geometry affects noise generation in Chapter 7. The ability to capture such differences is important as part of design development, and offers advantages over certain analytical models. In Chapter 8, the most complex simulations are presented. In this case, the noise of a model scale tidal turbine encountering anisotropic inflow turbulence is predicted, by fully resolving the blade geometry of the turbine. A scaling methodology is also presented, which allows full scale turbine noise predictions and environmental impact assessments to be made.

Finally, a summary is given in Chapter 9. This includes an overview of the research, conclusions and a discussion of the implications of the work, as well as recommendations for further work.

2

Turbulence and Sound

2.1 Introduction

Before any noise predictions of representative tidal turbine geometries can be made, a suitable numerical approach must be developed. An important initial stage in this process is to outline the key physics relating to the flows of interest. This will inform subsequent decisions relating to the design of numerical simulations. Fundamental to this understanding is the fact that hydrodynamic and acoustic processes are governed by the same physical laws. Characterisation of turbulent flows is presented first, followed by its sound radiation.

2.2 Turbulence

2.2.1 Concepts

Pope (2000*a*, p.3) states that "an essential feature of turbulent flows is that the fluid velocity field varies significantly and irregularly in both position and time". In addition, they can be characterised as random, chaotic and three-dimensional. Quantitatively, the flow is turbulent when the Reynolds number is sufficiently high. This is defined as

$$Re = \frac{UL}{\nu}, \tag{2.1}$$

where U and L are characteristic velocity and length scales and ν is the kinematic viscosity. The value of the Reynolds number required for turbulent motion depends on the flow of interest; for example pipe flow is fully turbulent at $Re \approx 4000$ but for a flat plate boundary layer, transition to turbulence does not occur until $Re \approx 10^6$ (Pope, 2000*a*, chap. 1).

Another key concept is the existence of a range of scales of turbulence, described in terms of *eddies* (Hinze, 1975, chap. 1). These can be imagined as coherent swirling regions of the flow, with sizes proportional to the size of the geometry (large scales) down to the *dissipation scales* (smallest scales). Ultimately all turbulent motion is transferred to thermal energy[1]; therefore fluid viscosity plays an important role even at high Reynolds numbers. The range of scales is maintained by the *energy cascade*, the process whereby kinetic energy is transferred from the large scales to the small scales. Thus turbulent flow can be characterised by an *energy spectrum*. Turbulence requires an external source of energy to sustain it, otherwise the motion will decay. This *production* often results from the mean flow kinetic energy.

The behaviour of turbulence at high Reynolds numbers can be described by the theory of Kolmogorov (1991)[2], who presented three hypotheses relating to the energy spectrum. These are as follows:

- The **hypothesis of local isotropy**: the small-scale motions are statistically *isotropic*.
- The **first similarity hypothesis**: the statistics of the small scale motions have a universal form, uniquely determined by ν and ε, the dissipation rate.
- The **second similarity hypothesis**: the statistics of the intermediate scales have a universal form, uniquely determined by ε only.

The term *isotropic* is used to denote turbulence whose statistics possess no directional dependence . When this is not true, the turbulence is described as *anisotropic*. Note there are many statistics which can be used to characterise turbulence. Hence 'anisotropic turbulence' can refer to anisotropy of one statistic or more than one. The spatial character of turbulence is also described using the concept of *homogeneity*. The terms *homogeneous* and *inhomogeneous* refer to turbulence where the statistics either lack, or possess, spatial dependence.

Kolmogorov's hypotheses lead to the definition of three wavenumber ranges of the energy spectrum: the *energy-containing range*; the *inertial subrange*; and the *dissipation range*.

[1] Although the dissipation scales are small, they are much larger than the molecules of the fluid, hence the fluid is treated as a continuum. The term dissipation is used here to describe a transfer of energy by physical processes; this is distinct from *numerical dissipation*, another term used in this work, which is the effect of a numerical discretisation scheme on the amplitude of computed quantity.

[2] The cited paper is an English translation of the original 1941 Russian publication: Doklady Akademiia Nauk SSSR, **30**, pp.301-305.

These are represented schematically in Figure 2.1, where the wavenumber is $\kappa = 2\pi/\ell$. The spectrum assumes an energy-spectrum function of the form $E(\kappa) = C\varepsilon^{2/3}\kappa^{-5/3}$ according to the second similarity hypothesis. Length scales describing each range are:

- L, the *geometric scale* - the largest length scale in the flow;
- $\mathcal{L}$, the *integral scale* - characterises the large scales, $\mathcal{O}(0.1L - L)$;
- ℓ_T, the *Taylor microscale* - corresponds to the inertial subrange, $\ell_T = (\nu\overline{u'^2}/\varepsilon)^{1/2}$;
- ℓ_K, the *Kolmogorov scale* - smallest turbulence scale, $\ell_K \equiv (\nu^3/\varepsilon)^{1/4}$.

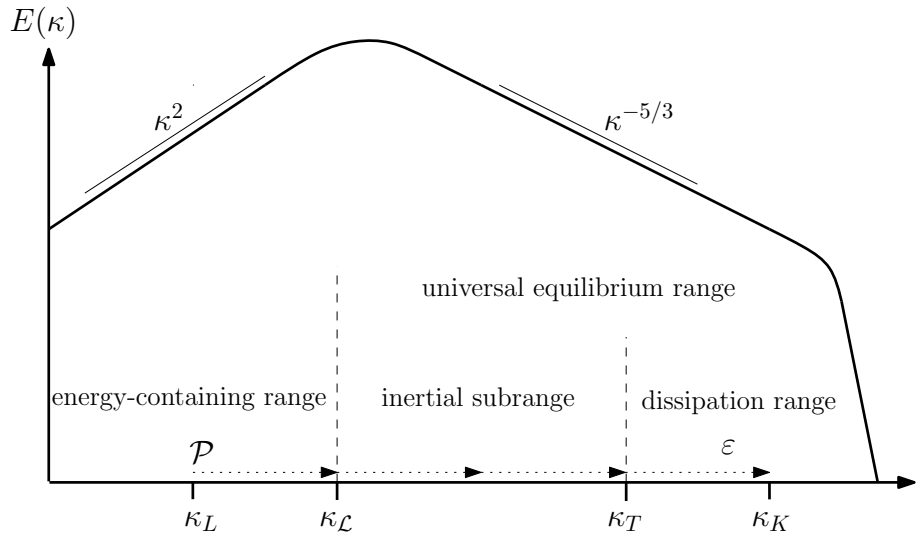

FIGURE 2.1: Wavenumber ranges for high Reynolds number turbulence, and typical energy spectrum (adapted from Pope (2000*b*, chap. 6)). Key length scales indicated by wavenumbers, where the subscript denotes the length scale.

It can be shown that the energy-containing range (80% of the total energy) lies approximately between $6\mathcal{L}$ and $\frac{1}{6}\mathcal{L}$ (Pope, 2000*b*, chap. 6). From Kolmogorov's theory, as the Reynolds number $Re_\mathcal{L} = \mathcal{L}|u'|/\nu$ increases, so does the range of scales, according to

$$\frac{\ell_K}{\mathcal{L}} \sim Re_\mathcal{L}^{-\frac{3}{4}}; \qquad \frac{\ell_T}{\mathcal{L}} \sim Re_\mathcal{L}^{-\frac{1}{2}}. \tag{2.2}$$

This has significant implications for the numerical simulation of turbulence, in terms of the number of grid cells and computational effort required to resolve the flow. One numerical approach, large eddy simulation, takes advantage of the fact that most of the energy is contained in the largest scales, and utilises Kolmogorov's hypotheses to model the small isotropic scales, thereby reducing the computational effort.

It is also important to consider the effect of solid surfaces, since they are included in most engineering problems of interest. A key effect of walls is to introduce anisotropy into the flow. This is caused by damping of the wall-normal fluctuations, due to the *no-slip* condition ($u_w = v_w = w_w = 0$), which transfers energy into the wall-tangential

directions, and leads to smaller scales close to the wall than would otherwise exist. Due to this process, a universal behaviour is often considered to exist in the region of a wall. Called the *law of the wall*, this relies on the division of the flow into distinct zones using normalisation of velocity and wall-normal distance by the friction velocity as

$$y^+ = \frac{u_\tau y}{\nu}; \quad U^+ = \frac{u}{u_\tau} \tag{2.3}$$

where $u_\tau = \sqrt{(\tau_w/\rho)}$ is the friction velocity, $\tau_w = \mu\frac{du}{dy}$ the wall-shear stress and ρ the fluid density. The dynamic viscosity μ is related to the kinematic viscosity by $\mu = \rho\nu$. A summary of the boundary layer regions is given in Table 2.1, in terms of both y^+ and δ, the boundary layer thickness.

TABLE 2.1: Definition of boundary layer regions (adapted from Pope (2000*c*, chap. 7)).

region	location	property
inner layer	$y/\delta < 0.1$	Mean velocity determined by u_τ and y^+, independent of U_0 and δ.
viscous wall region	$y^+ < 50$	Viscous contribution to shear stress is significant.
viscous sublayer	$y^+ < 5.0$	Reynolds shear stress negligible compared to viscous contribution ($U^+ = y^+$).
outer layer	$y^+ > 50$	Effect of viscosity on the mean velocity negligible.
overlap region	$y^+ > 50, y/\delta < 0.1$	Overlap between inner and outer layers
log-law region	$y^+ > 30, y/\delta < 0.3$	Mean velocity profile follows the *log-law* $U^+ = \frac{1}{\kappa}\ln y^+ + B$.
buffer layer	$5 < y^+ < 30$	Region between viscous sublayer and log-law.

2.2.2 Statistical definitions

Consider a fluctuating variable, $u(t)$. It is assumed that the signal is statistically *stationary*, that is, invariant under time shift. For a detailed discussion of random variables and processes see Pope (2000*d*, chap. 3). The mean and variance are

$$\overline{u} = \lim_{T\to\infty}\frac{1}{T}\int_0^T u dt \tag{2.4a}$$

and

$$\sigma^2 = \overline{u'^2} = \lim_{T\to\infty}\frac{1}{T}\int_0^T [u-\overline{u}]^2 dt. \tag{2.4b}$$

and indicate the average value and spread of the signal. Note that σ is the standard deviation, also referred to as the *root mean square* (*rms*). Assuming that the variable u

corresponds to a velocity component, the turbulence intensity[3] can be defined as

$$\mathcal{I}_x = \frac{\sigma_x}{\overline{u}} \tag{2.5}$$

The variance σ is an example of a more general definition, the *covariance*. This is a measure of how two random variables change together. The autocovariance and autocorrelation coefficient take the form

$$r(\tau) \equiv \overline{u'(t)u'(t-\tau)} \tag{2.6a}$$

and

$$\mathcal{R}(\tau) \equiv \frac{\overline{u'(t)u'(t-\tau)}}{\overline{u'(t)^2}}, \tag{2.6b}$$

where τ is a time lag. The correlation coefficient may take values $0 \leq \mathcal{R} \leq 1$ where $\mathcal{R} \to 0$ indicates uncorrelated variables, and $\mathcal{R} \to 1$ perfectly correlated variables. These definitions are used to recover the turbulence integral time and length scales. The integral time scale may be obtained from an autocorrelation coefficient in time as

$$\mathcal{T} \equiv \int_0^\infty \mathcal{R}(\tau) d\tau. \tag{2.7}$$

Since it is generally more convenient to sample data in time rather than space, Taylor's frozen turbulence hypothesis (Taylor, 1938) may be used to estimate the integral length scale. This requires that $u' << \overline{u}$, which is true for homogeneous isotropic turbulence but may not be valid in shear flows (Pope, 2000*b*, chap. 6). Assuming that Taylor's hypothesis holds, the integral length scale is

$$\mathcal{L} = \overline{u}\mathcal{T}. \tag{2.8}$$

A further method for analysing turbulence is the use of spectra. Here the power spectral density (PSD) is used, which reveals how the 'power' of a signal is distributed over frequency. The power is taken as the square of the signal, *i.e.* $u(t)^2$. The PSD may then be defined as the expected value of the square magnitude of the Fourier transform of $u(t)$, or

$$\Phi_{uu}(\omega) = \lim_{T\to\infty} \boldsymbol{E}\left[|u_T(\omega)|^2\right]. \tag{2.9}$$

where $u_T(\omega)$ is the Fourier transform of $u(t)$. The most convenient form of the PSD consists of the Fourier transform of the autocovariance $r(\tau)$, thus

$$\Phi_{uu}(\omega) = \int_{-\infty}^{\infty} r(\tau) e^{-i\omega\tau} d\tau. \tag{2.10}$$

In this work, the algorithm proposed by Welch (1967), which is a *fast Fourier transform (fft)*. Specifically the *pwelch* function available in *matlab*® is used.

[3]It should be noted that the most common definition for the turbulence intensity is based on all velocity components *i.e.* $\mathcal{I} = \sqrt{|\boldsymbol{\sigma}|/3}/|\overline{\boldsymbol{u}}|$ where $\overline{\boldsymbol{u}}$ is the mean velocity vector.

2.2.3 Governing equations

Here the most general set of governing flow equations is considered, with other forms presented later as appropriate. The compressible Navier-Stokes equations may be written as

$$\underbrace{D_t(\rho \boldsymbol{u})}_{\substack{\text{momentum}\\ \text{acceleration}}} = \underbrace{\nabla \cdot \boldsymbol{\sigma}}_{\substack{\text{diffusion of}\\ \text{momentum}}} + \underbrace{\boldsymbol{f}}_{\substack{\text{momentum}\\ \text{source}}} \tag{2.11}$$

where $\boldsymbol{\sigma}$ is the Cauchy stress tensor, which can be written as

$$\boldsymbol{\sigma} = -p\boldsymbol{I} + \boldsymbol{D}. \tag{2.12}$$

Equation 2.11 can be described as Newton's 'second law' applied to a fluid volume. The tensor $\boldsymbol{D}$ denotes the deviatoric stress tensor. This is written as

$$\boldsymbol{D} = 2\mu(\boldsymbol{S} - \frac{1}{3}(\nabla \cdot \boldsymbol{u})\boldsymbol{I}) \tag{2.13}$$

where

$$\boldsymbol{S} = \frac{1}{2}(\nabla \boldsymbol{u} + (\nabla \boldsymbol{u})^T) \tag{2.14}$$

is the strain rate tensor. Combining Equations 2.11 - 2.14 , the compressible Navier-Stokes equations are

$$\underbrace{\partial_t(\rho \boldsymbol{u})}_{\substack{\text{unsteady}\\ \text{acceleration}}} + \underbrace{\nabla \cdot (\rho \boldsymbol{u} \otimes \boldsymbol{u})}_{\substack{\text{convective}\\ \text{acceleration}}} = \underbrace{-\nabla p}_{\substack{\text{pressure}\\ \text{gradient}}} + \underbrace{\left[\mu(-\nabla(\frac{2}{3}\nabla \cdot \boldsymbol{u}) + \nabla \cdot \left(\nabla \boldsymbol{u} + (\nabla \boldsymbol{u})^T\right)\right]}_{\substack{\text{viscous}\\ \text{stresses}}} + \boldsymbol{f}. \tag{2.15}$$

Convection can be imagined as the collective movement of fluid particles within the flow. Diffusion is a process resulting in mixing and mass transport. Both the pressure gradient and viscous stress terms in Equation 2.15 contribute to diffusion. The term $\boldsymbol{f}$, also called a *body force*, includes the gravitational force $\rho \boldsymbol{g}$, but also accounts for other momentum sources in the flow. Considering conservation of mass results in the continuity equation

$$\partial_t \rho + \nabla \cdot (\rho \boldsymbol{u}) = 0. \tag{2.16}$$

Equations 2.15 and 2.16 represent the key governing equations used in this work. Two further equations are required to complete the system; an equation of state and equation for conservation of energy. Since these are not used here, their formulations are omitted. Full derivations of the complete set of equations can be found in, for example, Versteeg and Malalasekera (1995*a*, chap. 2) or Hirsch (2007*a*, chap. 1).

2.3 Sound radiated by turbulence

2.3.1 Governing equations

Aerodynamic (and hydrodynamic) sound in an unbounded fluid is that generated by vorticity (Howe, 1998*a*, chap. 2). It is therefore clear that, in the context of high-Reynolds number engineering flows, turbulent eddies will radiate sound. Furthermore, the effect of solid boundaries on the sound generation and radiation will generally be important (*e.g.* see Curle, 1955; Lighthill, 1954; Wang *et al.*, 2006), and any theory used should account for this appropriately.

Acoustics concerns small amplitude oscillations of a compressible fluid relative to a state of rest (Crighton, 1975). To examine this, the equations for conservation of momentum and mass are considered again. These may be written as (Howe, 1998*b*, chap. 1)

$$\partial_t(\rho \boldsymbol{u}) + \nabla \cdot (\rho \boldsymbol{u} \otimes \boldsymbol{u}) = -\nabla p + \mathcal{F}(\boldsymbol{y}, t) \tag{2.17a}$$

and

$$\partial_t \rho + \nabla \cdot (\rho \boldsymbol{u}) = 0. \tag{2.17b}$$

Note that Equation 2.17b is the same as Equation 2.16. The generalised source $\mathcal{F}$ is located in the sound generation region $\boldsymbol{y}$ and defined to be zero in the acoustic far-field $\boldsymbol{x}$. Equation 2.17a can be re-written in linearised form as

$$\partial_t(\rho \boldsymbol{u}) + c_0^2 \nabla \rho = \mathcal{F}(\boldsymbol{y}, t) \tag{2.18}$$

using the relationship $p = c_0^2 \rho$, where c_0 is the speed of sound. Acoustic variables ρ' and p' are defined relative to mean values ρ_0 and p_0 as $\rho' = \rho - \rho_0$ and $p' = p - p_0$. Taking the spatial derivative of Equation 2.18 and the time derivative of Equation 2.17b, the difference between the resulting equations yields

$$\left(\partial_{tt} - c_0^2 \nabla^2\right) \rho' = \Box^2 \rho' = \mathcal{F}(\boldsymbol{y}, t). \tag{2.19}$$

Here $\Box^2$ is termed the D'Alembert operator, and governs wave propagation, with source description accounted for on the *rhs* of the equation. Equation 2.19 is an inhomogeneous wave equation describing the pressure field due to $\mathcal{F}$, which includes any sound generation mechanism.

Alternatively, a more exact formulation for the sound source may be obtained by considering the difference between the compressible Navier-Stokes equations (Equation 2.15) and the linearised momentum equations (Equation 2.18) as first proposed by Lighthill (1952). This approach, termed an *acoustic analogy*, fully characterises the acoustic source, unlike Equation 2.19. This means that Equations 2.18 and 2.19 can be written

as

$$\partial_t(\rho \boldsymbol{u}) + c_0^2 \nabla \rho = -\nabla \cdot \boldsymbol{T} \tag{2.20a}$$

and

$$\Box^2 \, \rho' = \nabla^2 \boldsymbol{T}. \tag{2.20b}$$

The tensor $\boldsymbol{T}$ is defined as $\rho \boldsymbol{u} \otimes \boldsymbol{u} - \boldsymbol{\sigma} - c_0^2(\rho - \rho_0)\boldsymbol{I}$, and termed the *Lighthill stress tensor*. It characterises the sound generated by a volume distribution of turbulent stresses. Lighthill also justified the approximation

$$\boldsymbol{T} \approx \rho_0 \boldsymbol{u} \otimes \boldsymbol{u} \tag{2.21}$$

for low Mach numbers. The Mach number is defined as $M = u/c_0$, with the error in this approximation proportional to M^2.

Recognising that sound is radiated by vortical motion, the theory can be extended to describe the source in terms of vorticity (Powell, 1964). The manipulation is based on the vector identity

$$\nabla^2 \boldsymbol{T} = \nabla^2 \left(\frac{\boldsymbol{u}^2}{2} \right) + \nabla \cdot (\boldsymbol{\omega} \times \boldsymbol{u}) \tag{2.22}$$

where the vorticity is defined as $\boldsymbol{\omega} = \nabla \times \boldsymbol{u}$ and $\boldsymbol{\omega}, \boldsymbol{u} \to 0$ as $|\boldsymbol{x}| \to \infty$. Written in this way, the relationship between sound and vorticity is revealed more directly.

Next, account is made for stationary and moving solid boundaries. Curle (1955) developed Lighthill's work to account for the effect of solid boundaries on the acoustic field. This was achieved by writing an inhomogeneous wave equation (Equation 2.20b) involving both volume and surface integrals of Lighthill's stress tensor. The effect of an impermeable surface is to modify $\boldsymbol{T}$, such that the Reynolds stress term becomes zero due to the zero normal velocity condition, $u_n = \boldsymbol{u} \cdot \boldsymbol{n} = 0$, where $\boldsymbol{n}$ is the surface normal vector. Thus Equation 2.20b becomes

$$\Box^2 \, \rho' = \nabla^2 \boldsymbol{T} + \nabla (p \cdot \boldsymbol{n}). \tag{2.23}$$

Ffowcs Williams and Hawkings (1969) derived a generalised formulation for the noise generated by a moving surface. For a closed volume of fluid V, the rate of change of mass is written as

$$\int_V (\partial_t \rho + \nabla \cdot (\rho \boldsymbol{u})) dV = \int_S [\rho(\boldsymbol{u} - \boldsymbol{v})] \boldsymbol{n} dS, \tag{2.24}$$

where $\boldsymbol{u}$ and $\boldsymbol{v}$ are the velocities of the fluid and the surface S respectively, and the square brackets mean the difference between two regions separated by S. A function $f = 0$ is defined such that $f < 0$ inside S and $f > 0$ outside S, as shown in Figure 2.2(a).

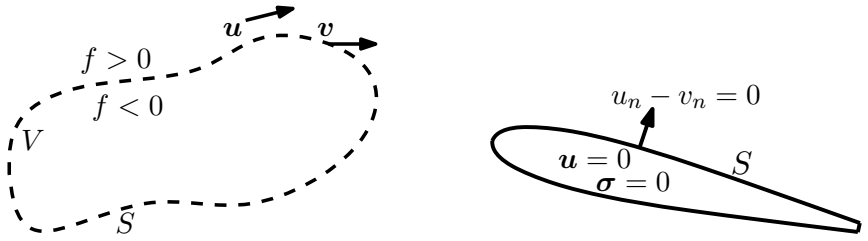

(a) Permeable surface (b) Impermeable surface

FIGURE 2.2: Illustrations of the permeable and impermeable surface definitions used to derive the Ffowcs Williams-Hawking equation.

By applying Gauss' theorem, the surface integral in Equation 2.24 can be written as a volume integral, resulting in

$$\partial_t \rho + \nabla \cdot (\rho \boldsymbol{u}) = [\rho(\boldsymbol{u} - \boldsymbol{v})]\delta(f)\nabla f. \tag{2.25}$$

Similarly, the momentum equation can be written as

$$\partial_t(\rho \boldsymbol{u}) + \nabla \cdot (\rho \boldsymbol{u} \otimes \boldsymbol{u}) + \nabla p = [\rho \boldsymbol{u} \otimes (\boldsymbol{u} - \boldsymbol{v})]\delta(f)\nabla f. \tag{2.26}$$

Assuming that S is an impermeable rigid surface, it follows that: inside S, $\boldsymbol{u} = 0$, $\boldsymbol{\sigma} = 0$ and $\rho = \rho_0$; outside S, $u_n - v_n = 0$. Applying these conditions, and utilising the same manipulations used to derive Equation 2.20b, the result is a generalised inhomogeneous wave equation of the form

$$\Box^2 \rho' H(f) = \nabla^2 \boldsymbol{T} H(f) - \nabla \cdot (\boldsymbol{\sigma} \cdot \boldsymbol{n})\delta(f)\nabla f + \partial_t \rho_0 \boldsymbol{v} \delta(f) \nabla f, \tag{2.27}$$

where $H(f)$ is the Heaviside function. Using Equation 2.27 the sound radiated by different types of sources can be predicted. The physical origin and relative importance of relevant sources is discussed in the next section.

2.3.2 Dimensional analysis

The order of $\mathcal{F}$ is defined in terms of the *multipole sources* which describe it. $\mathcal{F}$ is then written as

$$\mathcal{F} = \frac{\partial^n F_{ijk}}{\partial x_i \partial x_j \partial x_k} ... \tag{2.28}$$

describing a multipole of order 2^n where $n = 0, 1, 2$. Here F is a function of the variables which characterise the particular source *e.g.* velocity or vorticity. The far-field pressure fluctuation due to a multipole source is defined as, following Howe (1998*b*, chap. 1),

$$p'(\boldsymbol{x}, t) = \frac{\partial^n}{\partial x_i \partial x_j \partial x_k ...} \int_{-\infty}^{\infty} \frac{F_{ijk...}(\boldsymbol{y}, t - |\boldsymbol{x} - \boldsymbol{y}|/c_0)}{4\pi |\boldsymbol{x} - \boldsymbol{y}|} d^3\boldsymbol{y}, \tag{2.29}$$

assuming propagation in free space. Inspection of Equation 2.27 reveals three multipole sources of order 2,1 and 0. Next it is convenient to invoke some simplifying assumptions by referring to Figure 2.3.

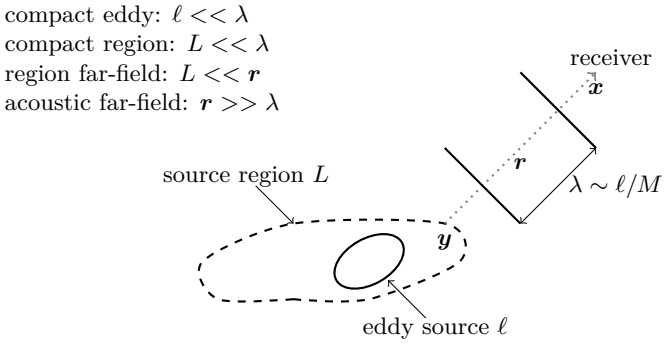

FIGURE 2.3: Hydrodynamic and acoustic length scales (adapted from Wang *et al.* (2006)).

Using the definition of the acoustic far-field, $|\boldsymbol{r}| >> \ell/M$, spatial derivatives become temporal derivatives (Crighton, 1975) as

$$\frac{\partial}{\partial x_i} = -\frac{1}{c_0}\frac{\partial}{\partial t}. \tag{2.30}$$

In addition, if the source region is *compact*, i.e. $L << \lambda$. This may also be written in terms of the Helmholtz number $He = \omega L/c_0$, where $He << 1$ for compactness. In this case, retarded time differences across it may be neglected, such that $t - |\boldsymbol{x} - \boldsymbol{y}|/c_0$ becomes $t - |\boldsymbol{r}|/c_0$, where it is assumed that $\boldsymbol{y}$ now lies at the global coordinate origin, and $|\boldsymbol{r}| = |\boldsymbol{x}|$. These assumptions provide significant advantages in the evaluation of the far-field sound. Hence Equation 2.29 may be written as

$$p'(\boldsymbol{x}, t) \approx \frac{(-1)^n x_i x_j x_k}{4\pi c_0^n |\boldsymbol{r}|^{n+1}} \frac{\partial^n}{\partial t^n} \int_{-\infty}^{\infty} F_{ijk...}(\boldsymbol{y}, t - |\boldsymbol{x}|/c_0) d^3\boldsymbol{y}. \tag{2.31}$$

Dimensional analysis of multipoles follows from Equation 2.31 assuming representative velocity and length scales u and ℓ, from which the time scale $\tau = u/\ell$ is defined. It follows that the contribution to the far-field density fluctuation from the n^{th} multipole is

$$p'(\boldsymbol{x}, t) \propto \frac{1}{c_0^n |\boldsymbol{r}|} \frac{u^n}{\ell^n} \cdot \mathcal{O}(F_{ijk...}). \tag{2.32}$$

Order of magnitude estimates can be made for $F_{ijk...}$ based on the terms on the *rhs* of Equation 2.27, where for:

- a *monopole* ($n = 0$), $\int_S (\rho_0 \boldsymbol{v}) dS \propto \rho_0 \ell^2 u$. This represents the rate of change of mass inside the fluid volume. An example is displacement noise.
- a *dipole* ($n = 1$), $\int_S (\boldsymbol{\sigma} \cdot \boldsymbol{n}) dS \propto \rho_0 \ell^2 u^2$, which is the force exerted on the fluid by a solid surface. This is generally termed 'loading' noise.

- a *quadrupole* ($n = 2$), $\int_V (\rho_0 \boldsymbol{u} \otimes \boldsymbol{u}) dV \propto \rho_0 \ell^3 u^2$. This is a distribution of turbulent stresses in the fluid volume. An example is the noise from a turbulent jet.

It follows that, by substituting these estimates into Equation 2.32,

$$p'_{monopole}(\boldsymbol{x}, t) \propto \frac{\rho_0}{|\boldsymbol{r}|} \ell u^2, \tag{2.33a}$$

$$p'_{dipole}(\boldsymbol{x}, t) \propto \frac{\rho_0}{|\boldsymbol{r}|} \ell u^2 M \tag{2.33b}$$

and

$$p'_{quadrupole}(\boldsymbol{x}, t) \propto \frac{\rho_0}{|\boldsymbol{r}|} \ell u^2 M^2. \tag{2.33c}$$

Based on this analysis each multipole scales as M^n. For low Mach number flows, it is therefore common to ignore quadrupole radiation. Exactly how low the Mach number needs to be for this assumption to be valid is a point of debate however. Compressibility effects can be shown to be negligible below $M = 0.3$; however, a high frequency quadrupole contribution to radiated sound has been reported for $M = 0.21$ (Greschner *et al.*, 2008). In the context of hydroacoustics, the Mach number is rarely higher than 0.01 (Howe, 1998*b*, chap. 1), and therefore no quadrupole sources are included in this work. This assumption implies that Powell's sound source term (Equation 2.22), which consists of both quadrupole and dipole terms, reduces to $\mathcal{F} = \nabla \cdot (\boldsymbol{\omega} \times \boldsymbol{u})$ (Howe, 1998*c*, chap. 3).

Howe (1998*b*, chap. 1) also estimated the radiation efficiency of each multipole based the ratio of the source and far-field pressures squared. This is equivalent to the ratio of the sound intensities at $\boldsymbol{y}$ and $\boldsymbol{x}$, since this quantity can be defined as

$$I = \frac{\overline{p'^2}}{\rho_0 c_0}. \tag{2.34}$$

The sound intensity is a measure of acoustic energy flux. The result of this analysis is

$$\frac{I(\boldsymbol{x})}{I(\boldsymbol{y})} \propto \left(\frac{\ell}{|\boldsymbol{r}|}\right)^2 \left(\frac{\ell}{\lambda}\right)^{2n}. \tag{2.35}$$

Hence the sound intensity ratio is dependent on two length scale ratios: the ratio of the source length scale to far-field distance, which is independent of the order of the multipole; and the ratio of source length scale to acoustic length scale. Considering a typical underwater scenario, the following values are assumed: $\ell = 0.12\ m$; $f = 1\ kHz$; and $|\boldsymbol{r}| = 1000\ m$. Intensity ratios for monopoles, dipoles and quadrupoles are then 1×10^{-8}, 1×10^{-10} and 1×10^{-12}. This highlights both the difference in magnitude between each of the poles, and the inefficiency of acoustic radiation.

2.4 Summary

As a first step towards the numerical simulation of tidal turbine noise, background theory regarding sound radiation from turbulence has been outlined. Key theories have been presented which suit application to the computation of low Mach number sound from rotating blades. Although hydrodynamics and hydroacoustics may be represented by the same governing equations, there is a large disparity between the characteristic turbulence and acoustic wavelengths. In addition, the ratio of acoustic energy to total energy in the flow is very small; therefore it is appropriate to separate the modelling of these two processes.

This is commonly achieved using acoustic analogies, which separate sound generation and propagation. Brentner and Farassat (2003, p.93) state that, for reasons outlined in Section 2.3.2, "the acoustic analogy approach is an ideal partner to [computational fluid dynamics]". The following chapter discusses how computational fluid dynamics may be used to predict acoustic sources in low Mach number flows.

3

Numerical Approaches for Acoustics

3.1 Introduction

Having established that the physical processes involved in hydroacoustics may be separated into sound generation and propagation, it is important to select a suitable numerical method for addressing the problem of tidal turbine noise due to inflow turbulence. A broad discussion of computational aspects involved in the prediction of low Mach number turbomachinery noise relevant to tidal turbines is now presented. In particular, numerical methods for simulating the scenarios outlined in Chapters 1 and 2 are reviewed. An initial overview of the requirements of a numerical method are discussed first, followed by a more detailed examination of various methods. The most appropriate method is then discussed in more detail, using both the literature and a canonical test case to justify the decisions made.

3.2 Overview of computational methods for acoustics

Strategies for computational aero- and hydro-acoustics are outlined in Figure 3.1. The choice of an appropriate method is based on a number of considerations: the source type (broadband or narrowband); the fluid (sound speed and viscosity); and the flow speed. The source type dictates whether random or periodic signals must be resolved, and how important viscous effects are. Sound speed determines whether or not a source

is compact, and where the acoustic far-field begins (see Figure 2.3). Flow speed determines the Mach number, which is an indicator of compressibility. The Reynolds number determines the range of turbulence scales (see Section 2.2).

Figure 3.2 relates some of these considerations to typical noise simulation scenarios. The hydrodynamic domain illustrated in Figure 3.2(a) is the flow region where pressure fluctuations result from both hydrodynamic and acoustic waves. The hydrodynamic fluctuations may result from inflow turbulence (Figure 3.2(a)), or the wake of an upstream body (Figure 3.2(b)). A suitable numerical method should propagate the acoustic source to a receiver in the far-field, where pressure fluctuations result solely from acoustic waves.

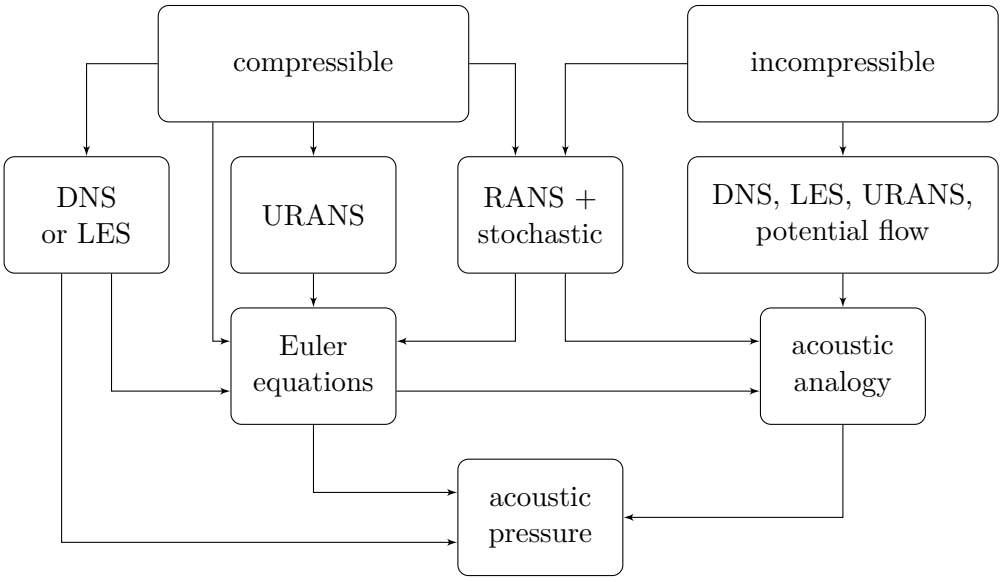

FIGURE 3.1: Computational acoustics approaches to far-field sound prediction: DNS=direct numerical simulation; LES=large eddy simulation; RANS=Reynolds-averaged Navier-Stokes; URANS=unsteady RANS.

Disparity between λ and ℓ is especially large in the case of high Reynolds number flows, since $\lambda/\ell_K = Re^{3/4}/M$ (Colonius and Lele, 2004). As elucidated in Section 2.3.2, the ratio of acoustic energy to hydrodynamic energy is also very small. Generally speaking, acoustic simulations require resolving low energy, large wavelength phenomena, whilst the converse is typically true in hydrodynamics. This makes solving for hydrodynamics and acoustics simultaneously a challenge when using the same numerical method and grid. It is therefore common to use a *scale separation*, in which the two problems are treated separately (Wang *et al.*, 2006). This is achieved by deriving an equation in the form of Equation 2.19, whereby the *lhs* governs sound propagation, with the *rhs* providing acoustic source description.

The full range of turbulence scales can be resolved using a direct numerical simulation (DNS), since no turbulence model is used. Precise broadband noise source descriptions could be achieved using this method. The main drawback of DNS is the large number of grid cells required to resolve the entire turbulence spectrum. Pope (2000*e*, chap. 9)

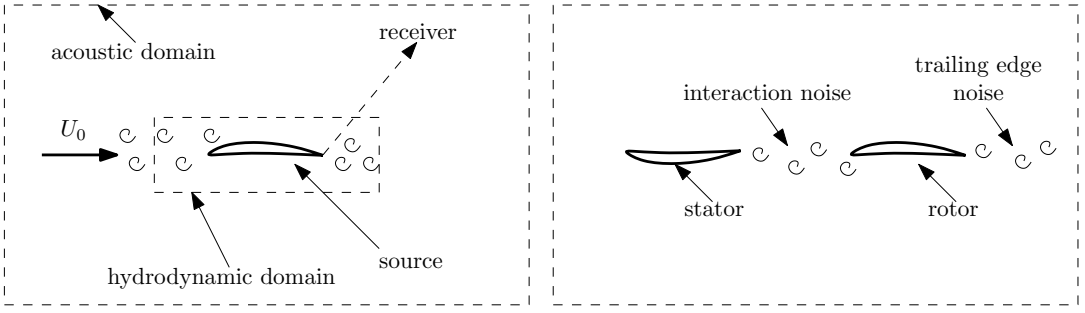

(a) Hydrodynamic and acoustic domains (b) Viscous and vortical interactions

FIGURE 3.2: Illustrations of scenarios suited to hybrid computational acoustics.

estimates the total number of cells required to scale as $N \propto Re^{9/4}$, meaning DNS will be limited to moderate Reynolds number flows for the foreseeable future (Spalart, 2000).

Large eddy simulation (LES) presents the opportunity to reduce the computational cost somewhat. By applying a filter to the velocity field, only the larger energy-containing scales are resolved, with a turbulence model used for the small scales. Despite the required number of cells decreasing ($N \propto Re^{1.8}$), Piomelli and Balaras (2002) note that at $Re \approx 10^6$, 99% of the cells inside the boundary layer are used to resolve the inner layer ($\approx 10\%$ of the boundary layer thickness). Streamwise and spanwise grid spacings, defined in the same way as Δy^+, of $\Delta x^+ \approx 100$ and $\Delta z^+ \approx 20$ mean that, whilst LES can be applied at high Reynolds numbers, often only limited geometries can be simulated, or additional modelling must be introduced. One 'hybrid RANS-LES' method is detached-eddy simulation (DES), where the near-wall region is modelled using RANS (Spalart *et al.*, 1997). This approach is commonly applied to broadband noise problems such as rod-aerofoil (Greschner *et al.*, 2008) and rotor-stator (Greschner and Thiele, 2012) interaction noise. In the case of free flows, such as jets, the need to resolve boundary layers is removed. However, the modelling approach may still affect the sound source resolution, as reported by Bogey and Bailly (2006). These authors found that the *subgrid* turbulence model had a large effect on the resolution of the quadrupole noise source in a jet.

Table 3.1 provides a summary of computational work related to leading edge noise for low Mach number flows. The cited studies are divided into *interaction* noise, where the flow features contributing to noise are included in the simulation *e.g.* a stator wake impinging onto a rotor (as in Figure 3.2(b)); and *inflow turbulence* noise, which concern numerical representations of the inflow turbulence (Figure 3.2(a)). It is evident that LES and Euler methods are most commonly used, alongside the Ffowcs Williams-Hawkings (FW-H) equation.

On the other hand, Reynolds-averaged Navier-Stokes (RANS) simulations are mature in their application at high Reynolds numbers, since the turbulence is treated entirely by a model and the required number of grid cells is often significantly lower. However

TABLE 3.1: Summary of computational aeroacoustics studies of low Mach number leading edge noise sources. Horizontal lines separate the cited works into *interaction* (1) and *inflow turbulence* (2) noise studies; dash indicates information not available. $Re : \times 10^{-6}$; $N : \times 10^{-6}$; $\Delta t : \times 10^{6}$.

	study	type	Re	M	CFD	subgrid	acoustics	N	Δt	Δy_w^+
1	Boudet *et al.* (2005)	rod-aerofoil	0.48	0.20	LES	S	FW-H	2.4	-	1.3
1	Greschner *et al.* (2008)	rod-aerofoil	0.48	0.2	DES	EASM	FW-H	2.3	1	1.5
1	Reboul *et al.* (2008)	fan	2.2	0.22	LES	-	FW-H/Kirch.	12	0.13	-
1	Argüelles Díaz *et al.* (2009)	fan	1	0.33	LES	S+WF	FW-H	2	50	60
1	Weinmann *et al.* (2010)	tandem cylinders	0.166	0.13	DES/FSM/SAS	SST	Curle	2.0	-	0.7
1	Spalart *et al.* (2011)	landing gear	0.166	0.12	DES	S-A	Curle/FWH	18	50	-
1	Giret *et al.* (2012)	rod-aerofoil	0.48	0.2	LES	DS	FW-H	8.5	0.25	-
1	Greschner and Thiele (2012)	rotor-stator	0.2	0.22	LES	S-A	FW-H	14.5	1	0.5
1	de Laborderie *et al.* (2013)	rotor-stator	0.6	0.33	LES	S	Goldstein	14	0.004	1
2	Christophe *et al.* (2007)	aerofoil	0.036	0.04	LES	DS	Curle/Amiet	3.0	10	2.0
1/2	Reese and Carolus (2008)	fan	0.018	0.14	DES/LES/SAS	DS+WF	FW-H	4.9	10	-
2	Olausson and Eriksson (2009)	fan	-	-	LES-URANS	S	FW-H	15	-	-
2	Deniau *et al.* (2011)	aerofoil	0.65	0.175	LES	-	FW-H	20	0.13	0.8
2	Deniau *et al.* (2011)	aerofoil	0.65	0.175	Euler (2D)	N/A	FW-H	1.2	-	-
2	Clair *et al.* (2013)	aerofoil	0.65	0.175	Euler (3D)	N/A	FW-H	8.5	-	-
2	Gill *et al.* (2013*a*)	aerofoil	4.5-13.5	0.2-0.6	Euler (2D)	N/A	FW-H	-	-	2

the unsteadiness inherent in the acoustic sources being simulated does not exist, and they must be reconstructed. The quality of the predictions is affected by the level of empiricism invoked by the chosen turbulence model. Approaches such as stochastic noise generation and radiation (*e.g.* see Bailly and Juvé, 1999; Billson *et al.*, 2004; Dieste and Gabard, 2010; Ewert, 2008) are attractive when limited time and computational power is available, or propagation effects are more important than source description. The unsteady RANS (URANS) equations allow only large scale unsteadiness to be resolved and hence are not suitable for broadband noise prediction (Reese and Carolus, 2008).

When near-field acoustic propagation effects are important it is common to solve the compressible Euler equations. This allows a dedicated acoustic grid to be used, removing the need to resolve hydrodynamics and acoustics simultaneously. The acoustic sources in the Euler equations may be provided either from unsteady simulations such as LES (Terracol *et al.*, 2005) or a stochastic method (Dieste and Gabard, 2010). When near-field effects are no longer important, a 'surface-based' (*i.e.* impermeable surface) acoustic analogy may be used to estimate the far-field pressure.

One final approach considered here is that of potential flow, a method commonly used in the field of hydrodynamics. The velocity field is assumed to be irrotational[1], and represented as the derivative of a scalar function, termed the *potential* (Lamb, 1945, chap. 3). Computations are time-efficient compared to viscous Navier-Stokes solvers since no volume grid is used, yet turbulence is not treated. Thus its application to hydroacoustics is limited to narrowband noise, as discussed in Section 3.3.

3.3 Potential flow

The modelling of marine propeller noise, for both cavitating and non-cavitating cases, has commonly been approached using boundary element (potential flow) methods coupled with acoustic analogies. This is because blade rate (thickness) noise has traditionally been of primary interest due to the hull vibrations it can induce (van Wijngaarden, 2005). If the FW-H formulation is to be used, then the solution for the acoustic pressure may be written as (following Farassat, 1975)

$$p'(\boldsymbol{x},t) = \frac{1}{4\pi}\frac{\partial}{\partial t}\int_{f=0}\left[\frac{\rho_0 \boldsymbol{v}_n}{r|1-M_r|} + \frac{p\cos\theta}{c_0 r|1-M_r|}\right]_\tau dS + \frac{1}{4\pi}\int_{f=0}\left[\frac{p\cos\theta}{r^2|1-M_r|}\right]_\tau dS, \quad (3.1)$$

where the quadrupole term has been neglected, assuming $M << 1$. Here M_r is the Mach number projected in the source-receiver direction, and $\cos\theta = \boldsymbol{e}_n \cdot \boldsymbol{e}_r$, where $\boldsymbol{e}_n$ and $\boldsymbol{e}_r$ are the unit vectors in the normal and receiver directions respectively.

Salvatore and Ianniello (2003) and Testa *et al.* (2008) compared the use of the 'Farassat 1A' formulation (where the time derivatives appear inside the integrals of the FW-H

[1]Mathematically this requires $\nabla \times \boldsymbol{u} = 0$ and hence the vorticity is zero.

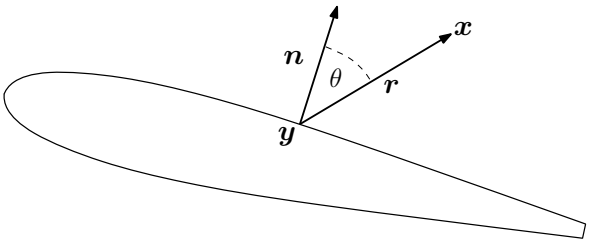

FIGURE 3.3: Coordinate system notation for Ffowcs Williams-Hawkings acoustic analogy.

equation) with Bernoulli's equation, for predicting the thickness (monopole) and loading (dipole) noise of a ship propeller. Cavitation is accounted for using a transient sheet cavity model whilst a non-uniform inflow velocity is prescribed to include the effect of the hull wake. The authors term this approach 'pseudo-acoustic', since no acoustic waves are resolved numerically. The cavitation noise, which is monopole in nature, is seen to dominate the non-cavitation noise, hence justifying the focus of research on cavitation noise in marine applications. "Satisfactory agreement" (Salvatore and Ianniello, 2003, p.299) is exhibited between the FW-H and Bernoulli methods although Testa *et al.* (2008) recommend using the Farassat 1A model, since it is more "robust"[p.60].

Seol *et al.* (2005) investigated both cavitating and non-cavitating noise, with a non-uniform inflow velocity profile also used. The loading noise is seen to dominate over the thickness noise in the non-cavitating case. This is attributed to the unsteady blade surface pressures caused by the non-uniform inflow. In the cavitating case, the loading noise reduces, since surface pressure fluctuations are suppressed by the presence of the cavity. Cavitation dominates the thickness noise component however; the blade thickness is effectively increased by the sheet cavity. Whilst the use of a non-uniform inflow velocity allows unsteady loading to be included in the computational model, this only accounts for narrowband sound, since the angle of attack changes experienced by the blades are periodic. In order to model broadband unsteady loading, a turbulent inflow velocity must be specified. However, the hydroacoustic methodology used by these authors *is* appropriate for this study.

3.4 Euler equations

The Euler equations are the governing equations of inviscid flow. The momentum equation is the same as Equation 2.15 without the viscous stress term. Compressible Euler equations solvers are used in acoustics simulations, particularly to model near-field sound propagation. For example, Terracol *et al.* (2005) used a coupled LES-Euler equation-Kirchoff surface[2] method to predict airframe noise. The advantage is that a dedicated acoustic grid can be used for the near-field sound propagation (see Figure 3.2). This alleviates the issue of disparate turbulence and acoustic length scales discussed in Section

[2]The Kirchoff surface method is an alternative to the FW-H method for modelling acoustic propagation (see, for example, Brentner and Farassat (1998) for a full description and evaluation).

3.1. When near-field effects are no longer important, *i.e.* in homogeneous mean flow, an acoustic analogy method is used for far-field propagation. This reduces the size of the acoustic grid required.

Bogey *et al.* (2002) compared linearised Euler equation (LEE) results to DNS/LES for simple cases such as co-rotating vortices, with the LEE source terms provided from the Navier-Stokes equations. An excellent agreement is observed between the two methods. When an expensive hydrodynamic simulation is to be avoided, the Euler equations may be combined with a stochastic source representation. This approach is discussed in Section 3.5.

Euler equations solvers may also be used to model acoustic sources where viscous effects are not important. This is the case for inflow turbulence noise (see Figure 3.2). Clair *et al.* (2013) used an Euler equations solver to predict inflow turbulence noise from an aerofoil. The inlet gusts were modelled using Fourier modes. The agreement in terms of surface and far-field pressure when compared to the analytical model of Amiet (1975) is good. This approach shows significantly better results than an LES of the same test case, where the acoustic sources are polluted by viscous effects due to the turbulent boundary layer (Deniau *et al.*, 2011).

Gill *et al.* (2013*a*) used the LEEs to examine the effect of aerofoil geometry on radiated noise, in a similar approach to Clair *et al.* (2013). However, the analysis is limited to two-dimensional flow, and thus spanwise variations in the inflow are omitted. This makes the method less suitable for 'engineering' flows. Lau *et al.* (2013) conducted three-dimensional simulations in order to investigate the effect of a wavy leading edge profile on noise reduction. The use of single-frequency gusts however makes the approach less appropriate for broadband noise simulation, unless numerous frequencies are superimposed.

3.5 Stochastic noise generation and radiation

As alluded to in the previous section, computationally expensive hydrodynamic simulations are not always desirable, particularly when an additional acoustic propagation simulation must be carried out. This has led to the development of methods which are generally categorised as *stochastic noise generation and radiation*. The approach is to approximate the source terms in the acoustic propagation equations using a time-efficient method. The acoustic equations may be, for example, the LEEs or the acoustic perturbation equations (APEs) derived by Ewert and Schröder (2003).

In order to describe the acoustic sources, a mathematical representation is required, as well as a means of deriving the necessary input parameters. For example, Bailly and Juvé (1999) used values of mean velocity, turbulence kinetic energy and dissipation rate

from a RANS simulation of a jet to describe source terms in the LEEs. The required velocity spectra and correlations are based on Fourier modes and an assumed form of the energy spectrum, although it is noted that these could come directly from a LES. Billson *et al.* (2004) extended this approach to model anisotropic turbulence, since it affects the noise directivity of the jet.

Ewert (2008) combined the APEs with a *random-particle mesh* method to predict airframe noise. The RANS equations are again used to characterise the two- or three-dimensional flow. The source reconstruction method relies on deriving a velocity correlation function from filtered white noise. Using homogeneous isotropic turbulence, a good agreement with an empirical model is observed for slat trailing edge noise (Ewert, 2008). The predictions are seen to be sensitive to the underlying RANS model however. When the method is extended to include anisotropic velocity correlations (Ewert *et al.*, 2011), improvements in slat interaction noise are seen.

A similar approach was adopted by Dieste and Gabard (2010). In this case, the method of Ewert (2008) was adapted into a *Lagrangian* formulation. The vortex particles are 'injected' into a two-dimensional LEE solver to study broadband interaction noise. An accurate prediction of far-field noise is achieved compared to the model of Amiet (1975). Although little difference is observed for Gaussian, Von Kármán and Liepmann representations of the turbulence spectra, the Von Kármán model is preferred when the method is compared to measurement data (Dieste, 2011). Although it is possible to extend the method to anisotropic turbulence, this is not presented.

3.6 Large eddy simulation

Large eddy simulation is used widely for simulating broadband acoustics, and is particularly good for gaining insight into underlying source mechanisms (Colonius and Lele, 2004). Large eddy simulation consists of solving the filtered Navier-Stokes equations, resolving the large scale turbulence, and modelling the small scales. Let the velocity field be decomposed as $\boldsymbol{u} = \overline{\boldsymbol{u}} + \boldsymbol{u}'$ with a similar expression for pressure. If large scales of turbulence are to be resolved (*e.g.* by LES), the operation is defined as a filter (see Section 4.2.1), whereas if all scales are modelled (RANS), the operation is an ensemble (time) average. Assuming the applied operation and differentiation commute *i.e.* $\overline{\nabla \cdot \boldsymbol{u}} = \nabla \cdot \overline{\boldsymbol{u}}$, the resulting incompressible equations are

$$\nabla \cdot \overline{\boldsymbol{u}} = 0 \tag{3.2a}$$

and

$$\partial_t(\overline{\boldsymbol{u}}) + \nabla \cdot (\overline{\boldsymbol{u} \otimes \boldsymbol{u}}) = -\frac{1}{\rho}\nabla p + \nu \nabla^2 \overline{\boldsymbol{u}}. \tag{3.2b}$$

The non-linear term cannot be calculated directly from the flow field and must be modelled. It can be written as

$$\overline{\boldsymbol{u}\otimes\boldsymbol{u}} = \underbrace{\overline{\overline{\boldsymbol{u}}\otimes\overline{\boldsymbol{u}}}}_{\mathscr{L}} + \underbrace{\overline{\overline{\boldsymbol{u}}\otimes\boldsymbol{u}'} + \overline{\boldsymbol{u}'\otimes\overline{\boldsymbol{u}}}}_{\mathscr{C}} + \underbrace{\overline{\boldsymbol{u}'\otimes\boldsymbol{u}'}}_{\mathscr{R}}. \tag{3.3}$$

The grouped terms in Equation 3.3 represent the interactions between the: large scales ($\mathscr{L}$); the large and small scales ($\mathscr{C}$); and the small scales ($\mathscr{R}$) respectively. Requiring that all terms be evaluated from the single-filtered field, Leonard (1974) re-wrote Equation 3.3 to include the double filtered velocity term in the modelled part of the equation, thus

$$\boldsymbol{\tau} = \overline{\overline{\boldsymbol{u}}\otimes\overline{\boldsymbol{u}}} - \overline{\boldsymbol{u}}\otimes\overline{\boldsymbol{u}} + \overline{\overline{\boldsymbol{u}}\otimes\boldsymbol{u}'} + \overline{\boldsymbol{u}'\otimes\overline{\boldsymbol{u}}} + \overline{\boldsymbol{u}'\otimes\boldsymbol{u}'}, \tag{3.4}$$

meaning the momentum equation can be written as

$$\partial_t(\overline{\boldsymbol{u}}) + \nabla\cdot(\overline{\boldsymbol{u}}\otimes\overline{\boldsymbol{u}}) = -\frac{1}{\rho}\nabla p + \nu\nabla^2\overline{\boldsymbol{u}} + \nabla\cdot\boldsymbol{\tau}. \tag{3.5}$$

The new term $\boldsymbol{\tau}$ is the subgrid stress tensor. A large proportion of studies using LES have concentrated on trailing edge noise, since it is able to accurately model turbulent boundary layers and the associated surface pressure sources. This is not the focus here, but is discussed in detail in reviews of LES for acoustics; see, for example, Colonius and Lele (2004), Wang *et al.* (2006) and Wagner *et al.* (2007, chap. 1). Large eddy simulation is the most widely used method for low Mach number broadband noise simulation (see Table 3.1). For acoustic propagation, the FW-H method is generally preferred. A suitable formulation for loading noise, based on Equation 3.1, is

$$p'(\boldsymbol{x},t) \approx \frac{1}{4\pi}\frac{\partial}{\partial t}\int_{f=0}\left[\frac{p\cos\theta}{c_0 r|1-M_r|}\right]_\tau dS. \tag{3.6}$$

This is the equation used by Reese and Carolus (2008) and Argüelles Díaz *et al.* (2009) when investigating fan noise. All acoustic predictions made in the present work use Equation 3.6, implemented into the fluid solver as a run-time post-processing library. The implementation of this code is described in Appendix A.

3.6.1 Resolution requirements

A vast range of grid sizes and time steps are seen across the studies cited in Table 3.1. In general, fine grids and small time steps are required to 'wall resolve' turbulent boundary layers, which is important for wake-leading edge interaction studies. Georgiadis *et al.* (2010) recommend for LES that

$$\Delta x^+ \leq 150, \tag{3.7a}$$

$$\Delta y_w^+ \leq 1, \tag{3.7b}$$

$$\Delta z^+ \leq 40 \tag{3.7c}$$

and

$$\Delta t^+ \leq 1, \tag{3.7d}$$

where $\Delta t^+ = u_\tau^2 \Delta t/\nu$. Whilst this level of resolution is much less than that for DNS, it still represents potentially prohibitive requirements for large engineering problems. Small time steps may mean that a compromise must be made in terms of total simulation time. Since the focus of inflow turbulence noise is not on resolving turbulent boundary layers, *wall functions*, which approximate the inner part of the boundary layer using a model, may be used. These are described further in terms of the current work in Section 4.5. This approach allows a reduction in total grid size as well as generally resulting in an increase in the time step (*e.g.* see Argüelles Díaz *et al.*, 2009; Olausson and Eriksson, 2009; Reese and Carolus, 2008).

Spatial resolution

Wang (1999) presented one of the first studies to investigate the effect of using wall functions on far-field noise prediction, based on a requirement to compute high Reynolds number flows for naval applications. The wall model allows the first grid point to be located in the logarithmic region, with the velocity related to the wall shear stress using the log-law relationship. A 90% reduction in CPU time is seen but the approach sacrifices fidelity in that the viscous sublayer is not resolved. The main effect on the noise spectrum is a reduction in the highest frequency that can be predicted; an over-prediction of the wall pressure spectra at lower frequencies is also seen. Wang (1999) suggests this may be attributed to inaccuracies in the streamwise turbulence intensity inside the boundary layer.

Hybrid RANS-LES has become more common, with several studies comparing different modelling techniques as well as turbulence models (see Table 3.1). Reese and Carolus (2008) presented comparisons of LES, DES and scale adaptive simulation (SAS) for the simulation of an axial fan subject to turbulent inflow (Menter and Egorov (2010) introduced SAS as an alternative to DES, eliminating the influence of the grid on the 'switch' between LES and RANS). All methods are seen to provide an acceptable agreement with experimental data at the blade leading edge. Since DES and SAS are primarily designed to resolve separated unsteady flow features, the small scale structures radiating high frequency sound are under predicted above 1 kHz. This may not be an issue if low frequency inflow turbulence is of primary interest however. The LES provides a more accurate source strength up to 5 kHz. However, the poor resolution of the blade boundary layer in the LES case leads to over prediction of the trailing edge wall pressure spectra. Hence the hybrid RANS-LES methods or wall function approach are preferable when a high-quality wall resolved LES grid is not achievable.

Ask and Davidson (2006) present results comparing DES and LES for a generic vehicle side mirror, and see a similar effect on the wall pressure spectra due to the modelling

introduced by DES. They estimate the grid cut-off frequency as

$$f_{max} = \frac{u'_{rms}}{2\Delta x} \tag{3.8}$$

where u'_{rms} and Δx are the *rms* resolved fluctuating velocity and the local grid spacing in the wall-parallel direction. It is observed that, when using the original 'DES97' formulation (Spalart *et al.*, 1997), the grid cut-off frequency is approximately half that of the LES, due to the RANS modelling introduced inside the boundary layer. Thus a method which allows more unsteady resolution inside the boundary layer is desirable.

One consideration for turbomachinery applications is that the convection velocity of the resolved eddies will increase as they pass through the rotor. Hence the maximum resolvable frequency of the noise source will increase by the ratio of the blade and inflow convection velocities (Carolus *et al.*, 2007). Reese and Carolus (2008) found that LES resolves pressure fluctuations due to inflow turbulence up to frequencies at least three times higher than DES or SAS. Despite the use of a wall function, the LES approach shows very good agreement with experimental sound power level data.

It is assumed that an LES is sufficiently well resolved when less than 20% of the turbulence kinetic energy is modelled (Pope, 2000*f*, chap. 13). Although it cannot be guaranteed that this condition is satisfied *a priori*, it is pertinent to estimate resolution requirements as part of the grid design. While such estimates are typically based on simplified analyses, such as homogeneous isotropic turbulence, there is considerable variation in suggested minimum grid cell size ($\overline{\Delta}$). For example, Feymark *et al.* (2012) suggest an LES should resolve down to the Taylor microscale (ℓ_T). Contrastingly, Pope (2000*f*, chap. 13) requires that $\overline{\Delta} \approx \ell_I$, where ℓ_I is a length scale characterising the boundary between the energy containing and inertial subranges. These length scales are identified in Figure 3.4, where the Kolmogorov spectrum is presented.

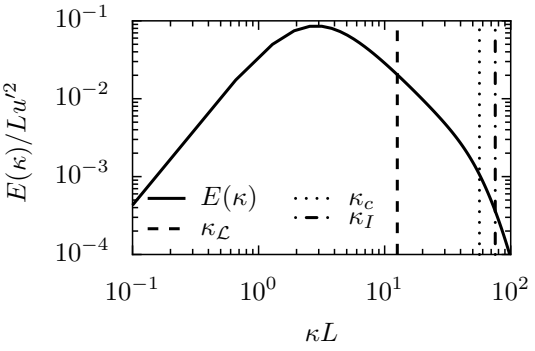

FIGURE 3.4: Example Kolmogorov spectrum, normalised by L and u', where $\mathcal{L} = 0.009\ m$, $L = 2\mathcal{L}$, $u' = 0.25\ ms^{-1}$ and $U_0 = 20\ ms^{-1}$, in air. Integral length, inertial subrange and grid cutoff wavenumbers shown as vertical lines. The cutoff wavenumber is $\kappa_c = \pi/\overline{\Delta}$. Note that $\kappa_T L \approx 160$ and therefore is not shown.

A further approximation can be made based on the subgrid turbulence kinetic energy (TKE) resulting from an assumed filter size and shape. Pope (2000*f*, chap. 13) estimates for the Gaussian filter that $k_{sgs}/k \approx 0.9 C_{Kol}(\overline{\Delta}/L)^{2/3}$, where $C_{Kol} = 1.5$. Assuming 80% of the energy is to be resolved, the cutoff wavenumber can be approximated as $\kappa_c L \approx 54$. Using the values presented in Figure 3.4, the required grid cell size is $\overline{\Delta} \approx 1 \times 10^{-3}\ m$.

Resolving ℓ_T in this case would require $\approx 3^3$ times as many grid cells as for ℓ_I, which would typically be unrealistic in terms of computational requirement. Colonius and Lele (2004) presented a similar analysis, based on a modified Kraichnan-Von Kármán spectrum, in terms of the maximum resolvable frequency. This can be approximated as $\kappa_c/\kappa_{\mathcal{L}} \approx 0.5\left(\overline{\Delta}/\mathcal{L}\right)^{-2/3}$. Based on the values assumed in Figure 3.4, $\kappa_c/\kappa_{\mathcal{L}} \approx 2.2$ or $\kappa_c L \approx 50$.

Even when acoustic waves are not captured in a simulation, the grid size requirements relating to sound source prediction are important. Michel *et al.* (2009) recommend using 4 grid points per convection length scale L_C, where $L_C = U_C/f$ for a convective velocity U_C. This leads to the definition of a local grid Strouhal number

$$St_\Delta = \frac{f\Delta x}{U_C}, \tag{3.9}$$

which should be limited to $St_\Delta < 0.25$. Making sure this condition is satisfied *a priori* may not be straightforward however, as the local convection velocity will not be known accurately.

Spanwise domain width should also be considered. In the case of a compressible near-field solution, the radiated noise will be two-dimensional when $\lambda > L_z$ (Greschner and Thiele, 2012). Although this does not occur for an incompressible simulation, the spanwise domain width affects the coherence of the broadband source, limiting the size of the largest spanwise length scale which can be simulated. In reality, it is often unreasonable to simulate the full spanwise domain at sufficient resolution. Hence corrections to numerical results can be used to allow comparison to experimental data. Boudet *et al.* (2005) and Giret *et al.* (2012) outline corrections based on the work of Kato *et al.* (1993), involving the coherence length $L_\gamma(f)$. Kato *et al.* (1993) assume a boxcar function shape for the coherence function γ^2, resulting in

$$SPL_\gamma(f) = \begin{cases} SPL_{sim}(f) + 10\log_{10}\dfrac{L_{exp}}{L_{sim}}, & L_\gamma(f) < L_{sim} \quad (3.10a) \\ SPL_{sim}(f) + 20\log_{10}\dfrac{L_\gamma}{L_{sim}} + 10\log_{10}\dfrac{L_{exp}}{L_\gamma}, & L_{sim} < L_\gamma(f) < L_{exp} \quad (3.10b) \\ SPL_{sim}(f) + 20\log_{10}\dfrac{L_{exp}}{L_{sim}}, & L_{exp} < L_\gamma(f) \quad (3.10c) \end{cases}$$

where *exp* and *sim* refer to the experimental and simulation spanwise domain widths. These corrections account for source coherence. Equations 3.10a and 3.10c represent geometric corrections between simulated and true source area. Since coherent and incoherent sources scale as $\propto L^2$ and $\propto L$ respectively, the magnitude of these corrections differ by a factor of two. For the intermediate case $L_{sim} < L_\gamma < L_{exp}$ (Equation 3.10b), contributions from the coherent and incoherent parts of the source are accounted for.

More elaborate corrections are possible by using a different approximation for the coherence function, such as a Gaussian form *e.g.* see Peth *et al.* (2006) or Seo and Moon (2007). Estimates of the correction applied based on exemplar values are presented in Figure 3.5. The coherence length has been estimated using the Von Kármán model, which is

$$L_\gamma(f) \approx \ell_z(f) = \frac{8\mathcal{L}}{3}\left[\frac{\Gamma(1/3)}{\Gamma(5/6)}\right]^2 \frac{\hat{\kappa}_x^2}{(3+8\hat{\kappa}_x^2)\sqrt{1+\hat{\kappa}_x^2}} \tag{3.11}$$

where the carets denote normalised wavenumbers $\hat{\kappa}_x = \kappa_x/\kappa_e$, $\kappa_x = \omega/U_0$, $\kappa_e = \sqrt{\pi}\Gamma(5/6)/\mathcal{L}\Gamma(1/3)$ and $\Gamma(n) = (n-1)!$ is the gamma function. The model values given in Figure 3.5 have been chosen to illustrate the frequency dependence of ΔSPL_γ. Since desirably $L_{sim} > \mathcal{L}$ for broadband noise sources, it is typical to only use Equation 3.10a unless very low frequencies are to be resolved. In this case it is preferable to increase L_z to be larger than the maximum L_γ in order to avoid spurious coherence from the numerical boundary conditions. This may only reasonably be achieved by reducing the highest resolved frequency, in order to maintain the same total grid size.

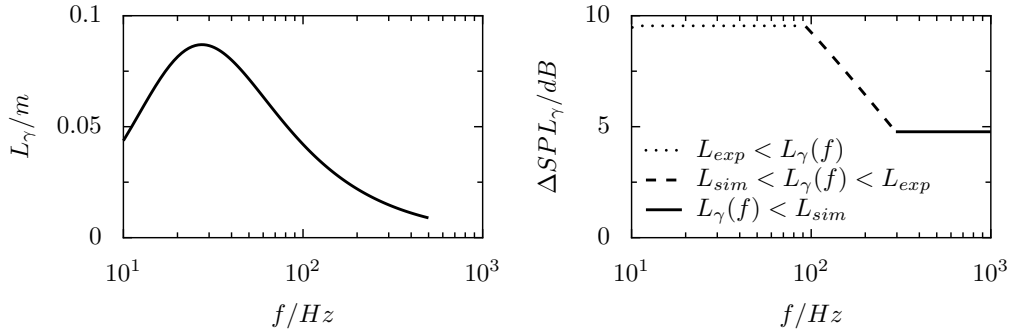

(a) coherence function and length

(b) decibel correction

FIGURE 3.5: Spectrum decibel correction based on coherence length (Equations 3.10a-3.10c). Coherence length estimated using Von Kármán model: $U_0 = 20\ ms^{-1}$, $\mathcal{L} = 0.09\ m$, $L_{sim} = 0.015\ m$ and $L_{exp} = 0.045\ m$.

Temporal resolution

Temporal resolution concerns both time step, and total sampling time. The former influences the resolution of the smallest scales of turbulence, while the latter affects the lowest resolved frequency as well as the amplitude of the resulting spectra, calculated from simulation time traces. Argüelles Díaz *et al.* (2009) considered the time step, Δt, required to resolve a particular eddy time scale. They estimated that

$$\Delta t \approx \frac{1}{15}t', \tag{3.12}$$

where $t' = \ell/u'_{rms}$ is the eddy turnover time. Numerical stability requirements also dictate time step limits however. This can be defined in terms of the Courant number

$$Co = \frac{|u|\Delta t}{\Delta x}. \tag{3.13}$$

where $|u|$ is the magnitude of the grid cell velocity. For example, the pressure implicit splitting of operators (PISO) algorithm (Issa, 1986) requires that $Co < 1$ in order to guarantee stability (convergence). In terms of an LES this ensures that an eddy of a particular convection speed does not move more than one grid cell in one time step; without this limit, numerical *dispersion*, or phase error, could effectively 'kill' the eddy. This requirement is similar to $\Delta t^+ < 1$ (Georgiadis *et al.*, 2010). Hence if a maximum Courant number of less than unity is maintained, the temporal resolution estimated by Equation 3.12 will be satisfied.

Total sampling time has been addressed by Michel *et al.* (2009). For a simulation duration T, and spectra computed at frequency bandwidths of Δf, the statistical error is $\approx (T\Delta f)^{-0.5}$. Hence smaller bandwidths require a long simulation duration to avoid increasing the statistical error. Michel *et al.* (2009) recommend that $T\Delta f = 25$ is achieved, although they note this is not always possible due to the long simulation times this may entail. In addition, the initial part of the time series equal to L_x/U_C should be discarded, where L_x is the streamwise domain length. This avoids including transient flow effects in the acoustic sources, and is equivalent to one flow-through of the domain.

3.6.2 Subgrid modelling

Another important consideration is the choice of subgrid model to use in order to close the LES equations. Since only the resolved turbulence spectrum will contribute to the noise prediction, a model should be chosen which does not affect the smallest resolved scales. One of the simplest and most commonly used subgrid closures is the 'Smagorinsky' model (Smagorinsky, 1963). It utilises the 'Boussinesq' hypothesis (Boussinesq, 1877), in a similar way to many RANS models. This allows the subgrid stress tensor to be modelled as proportional to the resolved velocity field using an artificial viscosity. This can be written as

$$\boldsymbol{\tau} - \frac{1}{3}\boldsymbol{\tau} \cdot \boldsymbol{I} = -\nu_{sgs}\boldsymbol{S} \tag{3.14}$$

where $\nu_{sgs} = \left(C_S\overline{\Delta}\right)^2|\boldsymbol{S}|$, with $|\boldsymbol{S}| = (2\boldsymbol{S}\cdot\boldsymbol{S})^{1/2}$. The Smagorinsky constant C_S takes a value of *0.1 - 0.2*, depending on the flow type. For example, Moin and Kim (2006) recommend using 0.13. Using a fixed value for C_S however is a considerable simplification when simulating complex flows, or using complex grids. This is because the subgrid stress cannot fully adapt to the local flow in this case.

An alternative approach is based on the *scale similarity* hypothesis. This states that the largest subgrid scales are analogous to the smallest resolved scales, thus better

representing the structure of the subgrid stress tensor (Sagaut, 2006*a*, chap. 7). Colonius and Lele (2004) suggest the application of this type of model for LES of aeroacoustic problems. This class of models better accounts for the effect of the subgrid scales on the resolved field. The subgrid tensor for the 'Bardina' model (Bardina *et al.*, 1980) is obtained by applying the double filtering operation:

$$\boldsymbol{\tau} = \overline{\boldsymbol{u} \otimes \boldsymbol{u}} - \overline{\boldsymbol{u}} \otimes \overline{\boldsymbol{u}} \approx \overline{\overline{\boldsymbol{u}} \otimes \overline{\boldsymbol{u}}} - \overline{\overline{\boldsymbol{u}}} \otimes \overline{\overline{\boldsymbol{u}}}. \tag{3.15}$$

Since the coefficient C_S is dependent on the grid resolution as well as the flow type, improvements to the subgrid model can be made be dynamically evaluating C_S, both spatially and temporally. Germano *et al.* (1991) used a *test filter* (denoted by a *caret*) to define the *resolved stress tensor* $\boldsymbol{L} = \widehat{\overline{\boldsymbol{u}} \otimes \overline{\boldsymbol{u}}} - \hat{\overline{\boldsymbol{u}}} \otimes \hat{\overline{\boldsymbol{u}}}$. The resolved stress tensor represents scales between the test and grid filter cutoff. The test filter is defined in the same way as the grid filter (Equation 4.1), but uses a different filter width (typically $\hat{\Delta} = 2\overline{\Delta}$). By comparing $\boldsymbol{L}$ to the test and grid-filtered forms of Equation 3.14, the result can be written as

$$\boldsymbol{L} - \frac{1}{3}\boldsymbol{L} \cdot \boldsymbol{I} = C_S \boldsymbol{M}, \tag{3.16}$$

with $\boldsymbol{M} = 2(\overline{\Delta}/\hat{\Delta})^2 |\hat{\overline{\boldsymbol{S}}}| \hat{\overline{\boldsymbol{S}}} - \hat{\Delta}^2 \widehat{|\overline{\boldsymbol{S}}| \overline{\boldsymbol{S}}}$. Lilly (1992) showed that by minimising the least square error of Equation 3.16, the modified constant can be written as

$$C_S^2 = \left(\frac{\boldsymbol{L} \cdot \boldsymbol{M}}{\boldsymbol{M} \cdot \boldsymbol{M}} \right). \tag{3.17}$$

To overcome the disadvantages of both 'structural' (scale similarity type) and 'functional' (Smagorinsky type) models, *mixed* models have been proposed. These aim to combine the superior energy transfer and vorticity production of functional models with the subgrid stress tensor structure of the structural models. The dynamic mixed Smagorinsky model (Zang *et al.*, 1993) can be written in the form

$$\boldsymbol{\tau}^S - \frac{1}{3}\boldsymbol{\tau}^S \cdot \boldsymbol{I} = \frac{1}{2}(-2\nu_{sgs}\overline{\boldsymbol{S}} + \boldsymbol{\tau}^B - \frac{1}{3}\boldsymbol{\tau}^B \boldsymbol{I}), \tag{3.18}$$

where the superscript B denotes the contribution from the Bardina model. The dynamic Smagorinsky constant is now

$$C_S^2 = \frac{1}{2}\left(\frac{(\boldsymbol{L} - \boldsymbol{B}) \cdot \boldsymbol{M}}{\boldsymbol{M} \cdot \boldsymbol{M}} \right) \tag{3.19}$$

where $\boldsymbol{B} = \widehat{\overline{\overline{\boldsymbol{u}}} \otimes \overline{\overline{\boldsymbol{u}}}} - \hat{\overline{\overline{\boldsymbol{u}}}} \otimes \hat{\overline{\overline{\boldsymbol{u}}}}$. The dynamic Smagorinsky model has been shown to provide significantly improved results provided statistical homogeneity prevails (Meneveau and Katz, 2000). For more complex flows, a dynamic Lagrangian procedure is preferred (Meneveau *et al.*, 1996). A 'memory length' function (temporal stencil) is used to estimate the numerator and denominator of Equation 3.17 along fluid particle trajectories.

This requires solving transport equations involving a time scale which determines the length of temporal averaging. The Smagorinsky coefficient is written as

$$C_S^2(\boldsymbol{y},t) = \frac{\mathscr{I}_{LM}}{\mathscr{I}_{MM}}. \tag{3.20}$$

Equations for $\mathscr{I}_{LM}$ and $\mathscr{I}_{MM}$ take the form

$$\mathscr{I}_{LM} = \int_{-\infty}^{t} \boldsymbol{L}\cdot\boldsymbol{M}(\boldsymbol{y}'(t'),t')\mathscr{W}(t-t')dt', \tag{3.21}$$

where $\boldsymbol{y}'$ and t' denote the old position and time of the fluid particle in the Lagrangian frame and $\mathscr{W}$ is a weighting function in time. A similar equation is provided for $\mathscr{I}_{MM}$ (Meneveau *et al.*, 1996). The transport equation for $\mathscr{I}_{LM}$ is given by

$$D_t(\mathscr{I}_{LM}) = \frac{1}{\mathscr{T}}(\boldsymbol{L}\cdot\boldsymbol{M} - \mathscr{I}_{LM}) \tag{3.22}$$

with $\mathscr{T}$ the memory length time scale. The exact form of $\mathscr{T}$ is not fixed; Meneveau *et al.* (1996) propose multiple formulations, preferring those proportional to $\overline{\Delta}\mathscr{I}^{-1/4}$.

The disadvantage of the more complex LES subgrid models, particularly when transport equations must be solved, is the increased computational time required. A comparison of the models discussed here is now presented in terms of velocity and Reynolds stress profiles in turbulent channel flow, as well as the difference in computational requirements. The models tested are the: Smagorinsky (S) model; dynamic Smagorinsky (DS) model; mixed Smagorinsky (MS) model; dynamic mixed Smagorinsky (DMS) model; and Lagrangian dynamic mixed (LDM) model. A full description of the simulations is given in Section 5.5. One important aspect of the simulation setup concerns the near-wall modelling. Since C_S does not reduce to zero at the wall for the Smagorinsky model, a damping function is introduced. This takes the form

$$C_S(y) = \left[C_S(1-\exp(-y^+/A^+)^3)\right]^{1/2} \tag{3.23}$$

where $A^+ = 26$, following van Driest (1956). When a dynamic model is used however, C_S is adjusted appropriately close to the wall; therefore the damping function is not used. Figure 3.6(a) shows normalised computational times; the values presented are the proportional change in time compared to the 'baseline' Smagorinsky model. Figures 4.3(a)-4.3(e) show the predicted mean velocity and Reynolds stress profiles compared to the DNS data of Moser *et al.* (1999).

In this case, the superior models are seen to be the dynamic Smagorinsky (DS) model and the Lagrangian dynamic mixed (LDM) model. Figure 3.6(a) reveals however that the LDM requires the highest computational time; this is due to the need to solve three additional transport equations. The time penalty of the dynamic Smagorinsky models (DS and DMS) is relatively small considering the improvements in the results compared

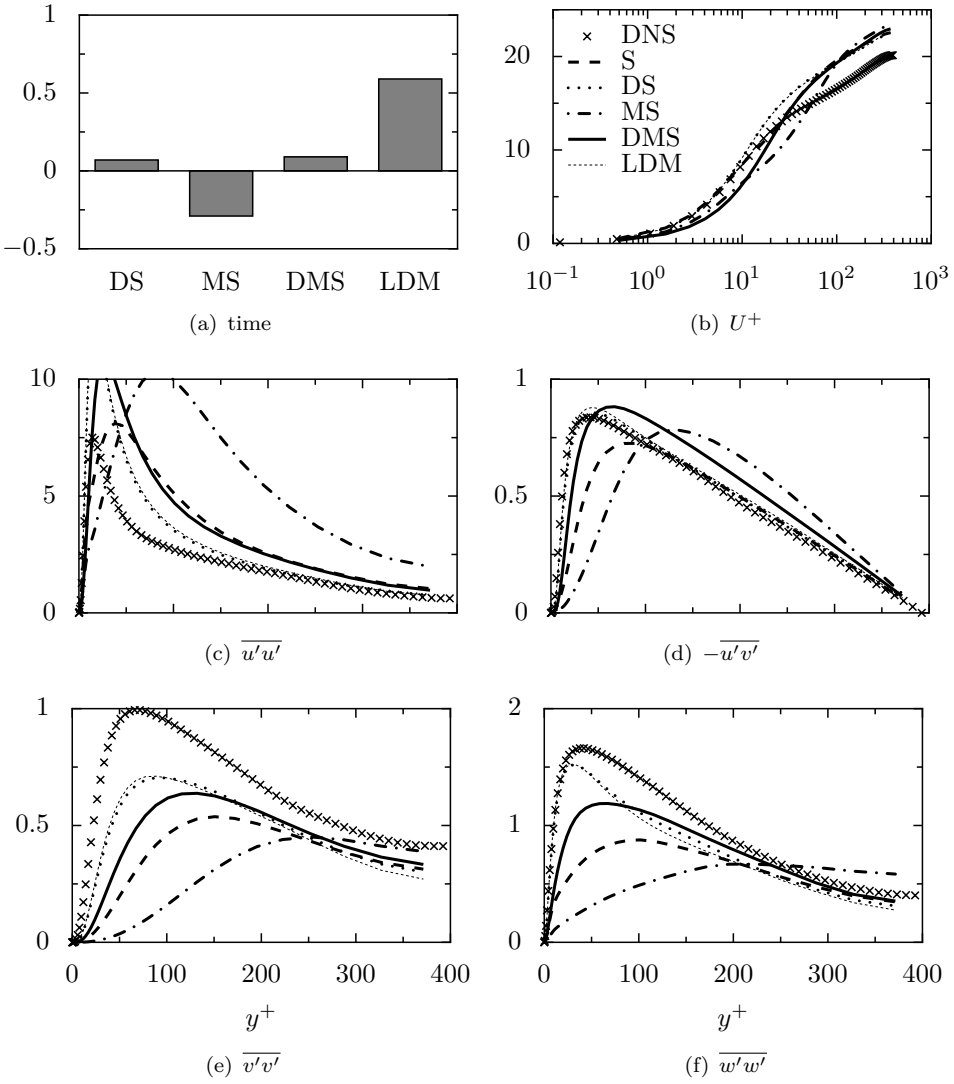

FIGURE 3.6: Comparison of OpenFOAM LES subgrid models: total computation time; and normalised mean velocity and Reynolds stress profiles for cyclic channel flow at $Re_\tau = 395$. S=Smagorinsky; DS=dynamic Smagorinsky; MS=mixed Smagorinsky; DMS=dynamic mixed Smagorinsky; LDM=Lagrangian dynamic mixed.

to the Smagorinsky model. It is noted that the DS model has also been used in the inflow turbulence studies of Christophe *et al.* (2007) and Reese and Carolus (2008). The reason for the reduction in computational time for the MS model remains unclear.

As previously mentioned, the mixed models can provide improved results for complex flows, despite this not being evident for the channel flow case. Further investigation of Smagorinsky-type subgrid models was made in James and Lloyd (2013), for the flow around a smooth circular cylinder at $Re \approx 10^5$. This may be considered a complex case due to the strong Reynolds number dependency of the dominant flow features, which include laminar separation, strong shear layers, transition and wake turbulence. In this case, the DMS model was found to be the most suitable subgrid model. The DS model failed to capture the dominant flow features correctly on the relatively coarse

grid, causing mean drag to be under-predicted ($\overline{C}_D = 0.40$ compared to an experimental value of 1.10).

An alternative is to omit any form of subgrid model, and account for these scales using a numerical scheme, in an approach termed *implicit* LES (*e.g.* see Grinstein *et al.*, 2007). Fureby (2007) computed the flow around a generic automobile side mirror using this method, but found the sound pressure level to be over-predicted compared to a 'traditional' *explicit* LES. Svennberg and Fureby (2010) compared ILES, LES and DES for trailing-edge vortex shedding noise. They found little difference between the methods across the entire frequency range. Explicit LES performs better in predicting the correct vortex-shedding peak frequency however. Further evaluation of implicit LES is presented in Section 4.3.2, where numerical convection schemes are investigated.

The missing part of the noise spectrum may be estimated using a subgrid scale or empirical noise model. Christophe *et al.* (2007) applied this technique to the simulation of inflow turbulence noise on an aerofoil. It is found that the model of Amiet (1975) provides satisfactory prediction of the high frequency part of the spectrum, while the LES is more appropriate at lower frequencies. This approach may be useful when a grid cannot be created to resolve the entire frequency range of interest.

3.7 Summary

Large eddy simulation has been identified as an appropriate methodology for the current work. This is primarily because a range of turbulence scales can be resolved allowing broadband acoustic source prediction. When combined with a simplified acoustic analogy, far-field sound may be estimated for low Mach number compact sources with reasonable accuracy. It has been shown that this approach has commonly been used in the literature. Since only the resolved turbulence will contribute to the acoustic source spectrum, computational grids must capture an appropriate range of scales relevant to a specific problem. It was demonstrated that a grid cutoff of approximately $\mathcal{L}/12$ should resolve 80% of the turbulence kinetic energy. The subgrid turbulence model was shown to have an effect on the resolved turbulence, and therefore selection of an appropriate model is important. For complex flows, geometries and grids, simple models will not provide satisfactory results. Hence 'dynamic' models are preferred in the current work.

Chapter 4 outlines some of the code-specific details used in this work, including domain discretisation, equation solution and boundary conditions. It is important to highlight some of the features of the numerical methods used, and justify the choices of numerical schemes, since these will influence simulation fidelity. An investigation of convection schemes is also presented, confirming that this numerical setting can have a large effect on flow resolution. This is shown using the two test cases referred to in this chapter: turbulent channel flow; and steady flow around a smooth cylinder.

4

Computational Methods

4.1 Introduction

Before investigating the complex case of tidal turbine noise, preferred numerical methods are chosen using simpler test cases. These are the 'channel flow' case and vortex shedding from a smooth circular cylinder already presented in Section 3.6.2. Since detailed validation data exist for the selected test cases, confidence in the numerical methods may be established. In addition to the test case results presented, other relevant numerical details are provided. Key features of the code used to solve the flow problems addressed in this work are outlined. A description of how the governing equations presented in Section 3.6 are discretised, constrained and solved is also provided.

The finite volume method is used throughout, since it offers a compromise between accuracy and flexibility (in terms of the high complexity of the grids which can be used). See Versteeg and Malalasekera (1995*b*) for a detailed description of the finite volume method. For information on a number of different approaches for solving the governing equations, including *finite difference* and *finite element* methods, see Hirsch (2007*b*).

4.2 Fluid code

The code used is *OpenFOAM*[1]. It is an open-source, finite volume code for the solution of general continuum mechanics problems, particularly fluid mechanics (Jasak *et al.*, 2007). The code is based on a set of dynamically-linked object-oriented C libraries, and executed through *applications*, which consist of *solvers* and pre- and post-processing *utilities*. Top-level code syntax is designed to closely resemble the equations to be solved (Weller *et al.*, 1998). The code is fully open-source, which allows significant user modification and massive parallelisation, which is achieved using the *OpenMPI* message passing interface. Here grids are decomposed using the *hierarchical* method.

4.2.1 Filtering

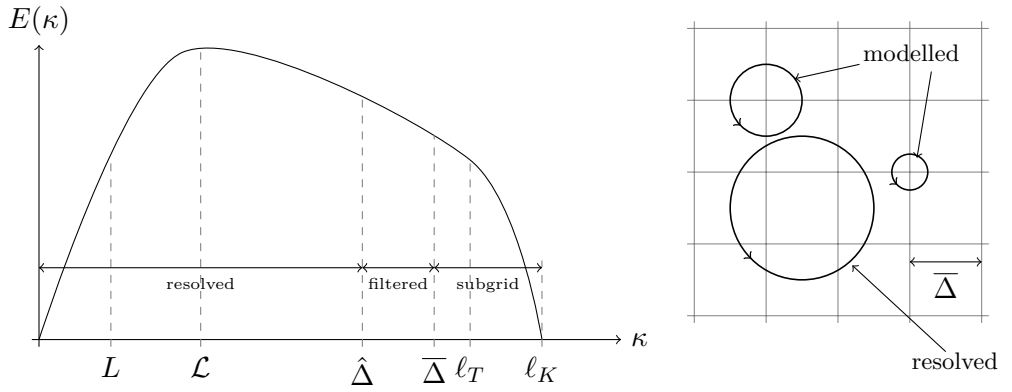

(a) Key length scales in turbulence spectrum.

(b) resolved and modelled scales

FIGURE 4.1: Representations of resolved and modelled scales in large eddy simulation.

Central to the concept of large eddy simulation is the definition of a *filter*. When performed on the governing equations, this operation separates the resolved and subgrid (modelled) scales. The filtering operation required by LES is defined (following Sagaut, 2006*b*, chap. 2) as

$$\overline{\boldsymbol{u}}(\boldsymbol{y},t) = \int_{-\infty}^{\infty} G(\overline{\Delta}, \boldsymbol{y}-\boldsymbol{y}')\boldsymbol{u}(\boldsymbol{y}',t)d^3\boldsymbol{y}' \tag{4.1}$$

where $\boldsymbol{y}'$ is the separation vector. The filter G can assume a number of *explicit* forms such as Gaussian and *sharp cutoff* (for more details see, for example, Pope (2000*f*, chap. 13) or Sagaut (2006*b*, chap 2)). The filter generally removes turbulence scales smaller than the grid size *i.e.* $\boldsymbol{y}-\boldsymbol{y}' < \mathcal{O}(\overline{\Delta})$. Alternatively, an *implicit* filter may be used. In this case, the grid itself acts as the filter kernel. This results in a tophat filter, defined as

[1] `http://www.openfoam.org/`

$$G(\overline{\Delta}, \boldsymbol{y}') = \begin{cases} 1/\overline{\Delta} & if \ \ |\boldsymbol{y}'| \leq \overline{\Delta}/2 \\ 0 & otherwise \end{cases} \tag{4.2}$$

and has been adopted by OpenFOAM. A further decision is how to choose the filter width $\overline{\Delta}$. Typically the maximum dimension of the grid cell, or the cube root of its volume, are used. These definitions are sufficient provided the grid is isotropic, since subgrid models are commonly formulated based on the assumption of isotropy of the modelled scales. If the grid is strongly anisotropic, the maximum cell dimension would be a more rigorous choice.

4.3 Discretisation

4.3.1 Finite volume method

The key feature of the finite volume method (FVM) is the discretisation of the governing equations in integral form, thereby enforcing conservation of basic variables such as mass. Defining a control volume V, Equations. 3.2a and 3.2b must be integrated in space, with Equation 3.2b also integrated in time in the case of a transient solution. This can be written as

$$\int_V \nabla \cdot \overline{\boldsymbol{u}} dV = 0 \tag{4.3}$$

and

$$\int_t^{t+\Delta t} \left[\partial_t \int_V \overline{\boldsymbol{u}} dV + \int_V \nabla \cdot (\overline{\boldsymbol{u}} \otimes \overline{\boldsymbol{u}}) dV - \int_V \nu_{eff} \nabla^2 \overline{\boldsymbol{u}} dV \right] dt = - \int_t^{t+\Delta t} \left[\frac{\nabla \overline{p}}{\rho} dV \right] dt, \tag{4.4}$$

where $\nu_{eff} = \nu + \nu_{sgs}$ is the effective viscosity. The discretisation of Equation 4.4 must now be carried out, both spatially and temporally. This procedure relies on the use of the *divergence* (Gauss') theorem, in the following forms:

$$\int_V (\nabla \cdot \phi) dV = \oiint_S (\phi \cdot \boldsymbol{n}) dS \tag{4.5a}$$

and

$$\int_V \nabla \phi dV = \oiint_S \phi \boldsymbol{n} dS \tag{4.5b}$$

where ϕ is a generic transport variable and dS is an infinitesimal area of the control volume surface S.

Figure 4.2 defines two cells labelled 'P ' and 'N ' connected by a face f of area $\boldsymbol{A}_f$, which is used to explain the discretisation approach. Equation 4.4 represents a second-order equation, due to the diffusion term. Since an accurate solution requires equal or higher discretisation order, second-order discretisation is preferable. This requires the

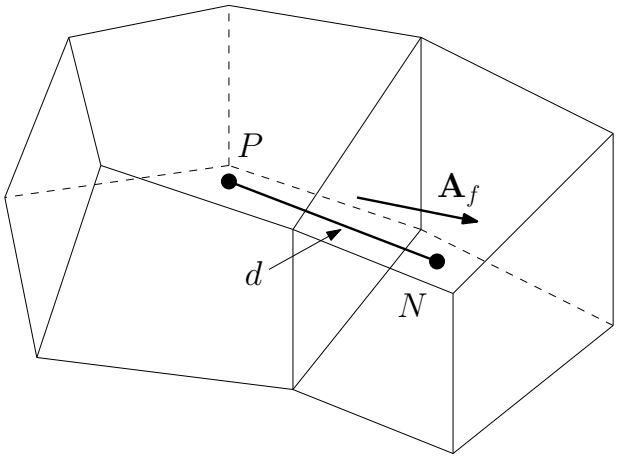

FIGURE 4.2: Finite volume discretisation schematic (adapted from The OpenFOAM Foundation (2011, p.30)).

assumption that a variable behaves linearly in both space and time *i.e.* interpolations follow

$$\phi(\boldsymbol{y}) = \phi_P + (\boldsymbol{y} - \boldsymbol{y}_P) \cdot (\nabla\phi)_P \tag{4.6}$$

and

$$\phi(t + \Delta t) = \phi^t + \Delta t \left(\frac{\partial\phi}{\partial t}\right)^t. \tag{4.7}$$

The cell face area is defined as $\boldsymbol{A}_f = \int_f \boldsymbol{n} dS$ whilst the location of P satisfies $\int_{V_P}(\boldsymbol{y} - \boldsymbol{y}_P)dV = 0$. The resulting semi-discretised Navier-Stokes equations (NSEs) assume the form

$$\int_t^{t+\Delta t}\left[\partial_t(\overline{\boldsymbol{u}})_P V_P + \sum_f \left(F \cdot \overline{\boldsymbol{u}}_f - (\nu_{eff}(\nabla\overline{\boldsymbol{u}})_f)\right)\right]dt = \int_t^{t+\Delta t}\left[-\frac{1}{\rho}(\nabla\overline{p})_P V_P\right]dt \tag{4.8}$$

where $F_f = \boldsymbol{A}_f \cdot \overline{\boldsymbol{u}}_f$ is the face flux. Note that a linearisation of the convection term $\int_V \nabla \cdot (\overline{\boldsymbol{u}} \otimes \overline{\boldsymbol{u}})dV$ is introduced by using the face value from the previous time step, $F_f^{n-1} = \boldsymbol{A}_f \cdot (\overline{\boldsymbol{u}})_f^{n-1}$. Following Feymark *et al.* (2012), the fully discretised NSEs can be written as

$$\sum_{i=0}^{m}\left(\alpha_i(\overline{\boldsymbol{u}})_P^{n-i}V_P + \beta_i\Delta t\sum_f\left[F_f \cdot \overline{\boldsymbol{u}}_f - (\nu_{eff}(\nabla\overline{\boldsymbol{u}})_f)\right]^{n-i}\right) = \Delta t\sum_{i=0}^{m}\beta_i\left[-\frac{1}{\rho}(\nabla\overline{p})_P^{n-i}V_P\right] \tag{4.9}$$

where α_i and β_i are coefficients of the time stepping scheme. A backward scheme is used here, which is second-order and *semi-implicit*. Semi-implicit means the scheme uses data at the current time $t + \Delta t$ as well as the old time t to solve at $t + \Delta t$. Defining $\phi^{n-2} = \phi^{t-\Delta t}$, $\phi^{n-1} = \phi^t$ and $\phi^n = \phi^{t+\Delta t}$, the coefficients in Equation 4.9 are $m = 2$,

$\alpha_0 = 1.5$, $\alpha_1 = -2$, $\alpha_2 = 0.5$, $\beta_0 = 1$ and $\beta_1 = \beta_2 = 0$. The continuity equation is then discretised as

$$\left(\int_V \nabla \cdot \overline{\boldsymbol{u}} dV\right)^n = \sum_f \left(\int_f d\boldsymbol{A}_f \cdot \overline{\boldsymbol{u}}_f\right)^n = \sum_f F_f^n = 0. \tag{4.10}$$

4.3.2 Upwind and hybrid differencing

The previous section described second-order spatial discretisation (Equation 4.6). Central differencing (CD) is the preferred scheme for LES due to it's second-order accuracy. A CD scheme (referred to as a *linear* scheme in OpenFOAM) may be written as

$$\phi_f = f_y \phi_P + (1 - f_y)\phi_N, \tag{4.11}$$

where $f_y = \overline{fN}/\overline{PN}$ *i.e.* the ratio of the distances from the cell centre of 'P' to the face shared with 'N' and the cell centre of 'N'. This is used to estimate the cell face values of a variable based on *both* the adjacent cell centre values. In certain circumstances, a central differencing scheme may provide unphysical flow solutions, caused by high values of the Péclet number. This is discussed in Appendix B. An alternative differencing scheme is *upwind*, which provides boundedness (stability) by introducing numerical stability at the expense of accuracy (Jasak, 1996). A first-order upwind scheme is defined as

$$\phi_f = \begin{cases} \phi_P & \text{if } F \geq 0 \\ \phi_N & \text{if } F \leq 0. \end{cases} \tag{4.12}$$

This simple formulation assigns the current cell centre value to the face if flow is moving out of the cell, and uses the neighbour cell centre value for flow moving into the cell; hence the name 'upwind'. Using a first-order scheme for LES would result in a significant reduction in solution accuracy and is therefore not desirable. However, introducing a small amount of upwinding may be important in order to provide stability. This is particularly important on unstructured or coarse grids, where the cell shapes and orientations may not provide good linear interpolation.

Blended upwind-central schemes are referred to as *hybrid* differencing schemes. As detailed by Jasak (1996), such schemes satisfy boundedness, and are therefore called *total variation diminshing* (TVD) schemes (Sweby, 1984). The total variation (TV) is written as

$$TV(\phi^n) = \sum_f |\phi_N^n - \phi_P^n|, \tag{4.13}$$

which must satisfy the condition $TV(\phi^n) \leq TV(\phi^{n-1})$. Next, a description is provided of two TVD schemes available in OpenFOAM. These are by no means the only examples of such schemes; Jasak (1996) provides details of numerous TVD schemes. The *limitedLinear* scheme represents a simple hybrid scheme. Here a *Sweby limiter* (Sweby, 1984)

is used to add a fixed amount of upwinding to the central scheme, so that

$$\phi_f = \phi_f^u + \Psi \left(\phi_f^c - \phi_f^u \right). \tag{4.14}$$

Here ϕ_f^u is the value calculated using the upwind scheme, ϕ_f^c is the value calculated using central differencing and Ψ is the Sweby limiter, which takes a value from zero to one. Written in this way, $\Psi = 0$ corresponds to fully upwind, and $\Psi = 1$ to fully central.

An alternative hybrid scheme in OpenFOAM is the *filteredLinear* scheme, which uses an active control on the limiter Ψ to only apply upwinding where it is needed. In this case, the Sweby limiter is defined as

$$\Psi = (1 + \Pi) - \Upsilon \left[\frac{min\left(|\Delta F - (\nabla F)_P|, |\Delta F - (\nabla F)_N|\right)}{max\left(|(\nabla F)_P|, |(\nabla F)_N|\right)} \right] \tag{4.15}$$

where Π and Υ are the overshoot and gradient scaling coefficients, which may take a value between zero and one. If the relative increase in the flux difference between the two neighbouring cells, ΔF, is large compared to the gradient ∇F, more upwinding is introduced for the interpolation at the face(s) shared by P and N. Appendix B provides more details of the *filteredLinear* scheme.

Evaluation using channel flow case

The effect of these two schemes was investigated using the same channel flow simulation presented in Section 3.6.2. Cases are presented using 5% upwinding (denoted as 0.05), both with and without subgrid turbulence modelling. Omitting the subgrid model corresponds to implicit LES (ILES; see Section 3.6.2), where the additional numerical dissipation introduced accounts for the small scales. The results are presented in Figure 4.3.

A key observation from Figure 4.3 is the difference between cases with and without the subgrid model. The ILES cases not only underpredict the magnitudes of the normal (Figure 4.3(d)) and spanwise (Figure 4.3(e)) Reynolds stresses, but the peak value shifts away from the wall. This suggests that, compared to explicit subgrid modelling, ILES does not account correctly for the near-wall turbulence behaviour. A similar effect is observed for the streamwise Reynolds stress (Figure 4.3(b)), although the peak magnitude is closer to the DNS. Overall however, this analysis suggests that the dynamic subgrid model is more appropriate for channel flow. A possible caveat is the fact that the grid used is structured and provides a high level of resolution (see Section 5.5 for a full description of the channel case and grid used); hence the subgrid model functions appropriately.

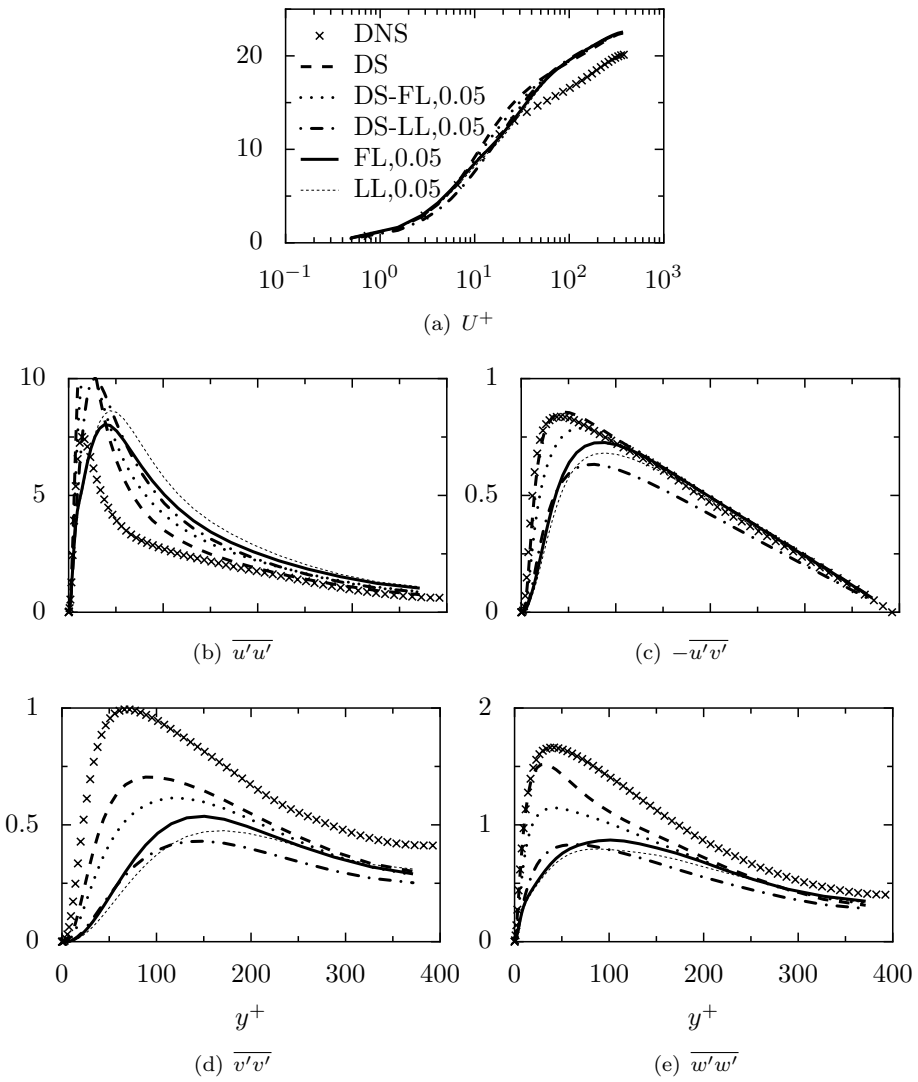

FIGURE 4.3: Comparison of divergence schemes: Normalised mean velocity and Reynolds stress profiles for cyclic channel flow, $Re_\tau = 395$. DS=dynamic Smagorinsky; FL=*filteredLinear*; LL=*limitedLinear*.

This does not mean that ILES is not always suitable however. Engineering simulations often use coarse and/or unstructured grids, thus violating some of the assumptions inherent in eddy-viscosity subgrid models. Bensow and Liefvendahl (2008) compared different explicit and implicit LES settings when considering a marine propeller with a unstructured tetrahedral grid. In terms of mean performance values, ILES using the *vanLeer* scheme with 5% upwinding gives the closest results to experimental values. Since hybrid differencing schemes in OpenFOAM can be applied to each velocity component individually, they can effectively be made to act as anisotropic subgrid models. This is a potential explanation for the improved predictions when using anisotropic grids.

Evaluation using circular cylinder case

Further investigation of convection schemes has been carried out using another test case: smooth flow around a smooth circular cylinder at high Reynolds number. The study was carried out as part of a benchmark study for the International Towing Tank Conference (ITTC) Ocean Engineering committee, and is reported in James and Lloyd (2013). The paper includes a grid convergence study, as well as assessment of different subgrid turbulence models; results presented here are used to provide assessment of OpenFOAM convection schemes. A short description of the test case is now provided; the reader is referred to the original paper for a full description.

The test case was designed to replicate the experiments of de Wilde *et al.* (2006), with a cylinder diameter (D) of 0.2 m. Although a span of 3.4 m was tested, simulations are limited to $S = 0.34$ m. The domain is represented in Figure 4.4, showing the coordinate system, domain size and boundary designations. The z direction is along the cylinder span. The domain size and boundary conditions are similar to those from other CFD investigations of cylinders *e.g.* Rosetti *et al.* (2012). A fixed value Dirichlet velocity inlet is used, with Neumann pressure. The outlet uses a convective condition, which allows vortical waves to exit the domain without reflection. A no-slip condition is applied to the cylinder. All other boundaries are treated as symmetry planes. The flow was allowed to develop for 20 shedding cycles. After this statistics were recorded for a further 20 cycles, based on a Strouhal number $St = fD/U_0 = 0.19$.

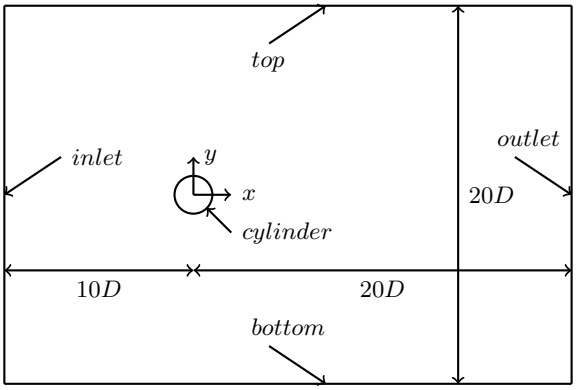

FIGURE 4.4: Schematic of circular cylinder test case domain.

For this flow, the convection scheme is expected to be important, due to the complex vortex shedding behaviour exhibited, which includes both laminar and turbulent boundary layer separation, as well as transition. This is compounded by the difficulty in designing *a priori* a grid which adequately resolves enough turbulence kinetic energy for LES. All the results presented here concern a Reynolds number $Re = U_0 D/\nu = 1.26 \times 10^5$, although a range of Reynolds numbers were investigated in the paper.

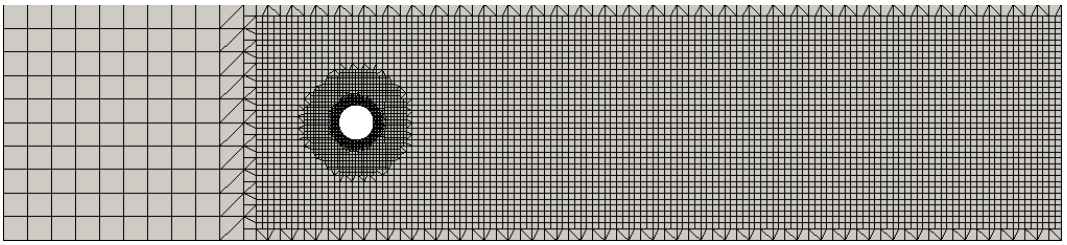

(a) grid

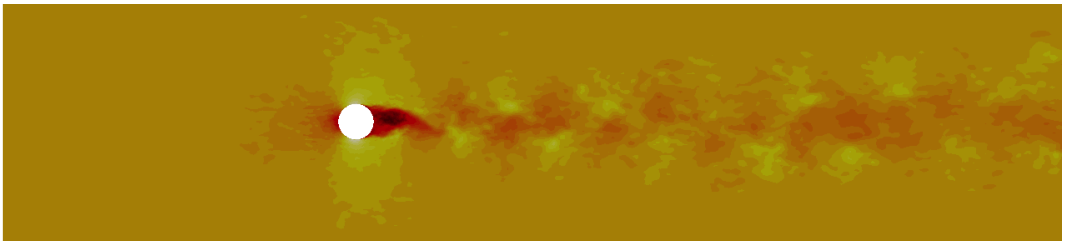

(b) *linear*

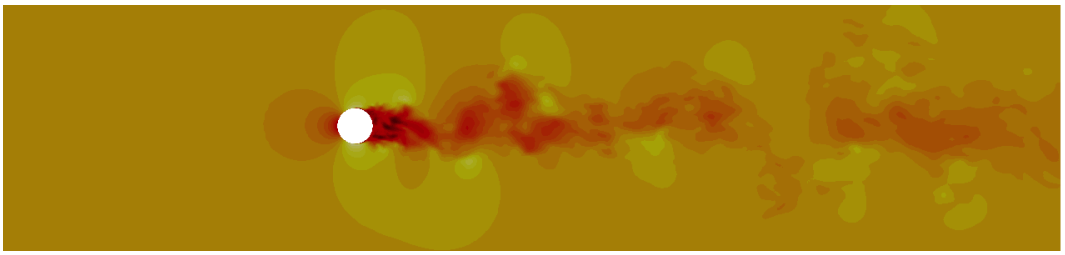

(c) *limitedLinear*, 10% upwind (LL01).

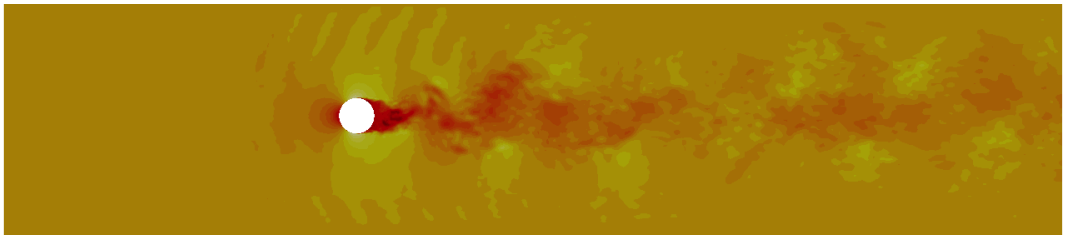

(d) *filteredLinear*, up to 10% upwind (FL01).

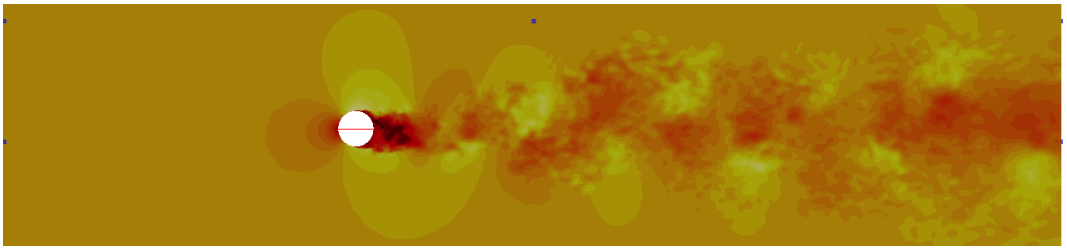

(e) *filteredLinear*, up to 100% upwind (FL1).

FIGURE 4.5: Comparison of convection schemes for steady flow around a smooth circular cylinder at $Re = 1.26 \times 10^5$: contours of normalised axial velocity u^* on $x - y$ plane slices at domain centreline. Colour scale from -1.15 to $+1.85$ in increments of 0.1.

case	$\overline{C}_D$	$\overline{C_L'^2}$	St
comp.	1.10	0.52	0.200
linear	0.43	0.07	0.331
FL01	0.58	0.10	0.260
LL01	0.79	0.16	0.189
FL1	1.10	0.34	0.205

TABLE 4.1: Summary of cylinder forces and vortex shedding prediction using various convection schemes, at $Re = 1.26 \times 10^5$. Comparison data: drag and Strouhal number taken from experiments of de Wilde and Huijsmans (2001); *rms* lift from empirical estimates proposed by Norberg (2003).

The effect of four schemes is visualised in Figure 4.5, alongside a two-dimensional slice of the grid used, which was common to all cases. Figures 4.5(b) and 4.5(d) show the cases with the least upwinding. Using fully linear interpolation (Figure 4.5(b)), small patches of high velocity are observed in front of, as well as above and below the cylinder. These are related to grid coarsening, and are unphysical. Adding up to 10% upwinding reduced this phenomenon, but induces artificial 'wiggles' in the solution above and below the cylinder (Figure 4.5(d)). The data presented in Table 4.1 for these cases shows that the chosen schemes have a large effect on force prediction; the mean drag and fluctuating lift are much lower than the comparison values, while the Strouhal number has increased. These are indications that the Reynolds number has been artificially increased, forcing the boundary layer to become fully turbulent and remain attached (Norberg, 2003; Williamson, 1996).

Figure 4.5(c) shows the case with a fixed amount of upwinding. This scheme serves to remove the unphysical velocity fluctuations observed for the previous two cases, causing the prediction of mean forces to improve somewhat. However, since the upwinding is applied everywhere, the scheme becomes too dissipative; this can be seen from the lack of fine scale turbulence in the wake region. The final case is shown in Figure 4.5(e), where *up to* 100% upwinding is permitted, but only added dynamically based on Equation 4.15. The advantages of this scheme are notable based on Table 4.1. It shows the best agreement with the comparison data across all the coefficients. Figure 4.5(e) shows that upwinding is only added where required for stability. Hence the accurate spatial resolution of turbulence in the wake region, essential for drag prediction, is maintained. All other numerical schemes used are *linear* (second-order), with upwinding applied to the subgrid turbulence kinetic energy if necessary for stability, via the *limitedLinear* scheme.

In order to confirm that the *filteredLinear* scheme is functioning as intended, it is useful to visualise the amount of upwinding introduced. Figure 4.6 shows cell-averaged values of Ψ on a domain centreline slice; white corresponds to fully central differencing, while black shows 50% upwinding. This plot reveals that scheme operates as required; linear differencing is maintained in the important flow regions (predominantly the cylinder boundary layer and wake). The most upwinding occurs far away from the cylinder, as well as at the boundaries of the grid refinement regions. Hence the appropriateness of the scheme on 'hanging-node' type unstructured grids is elucidated.

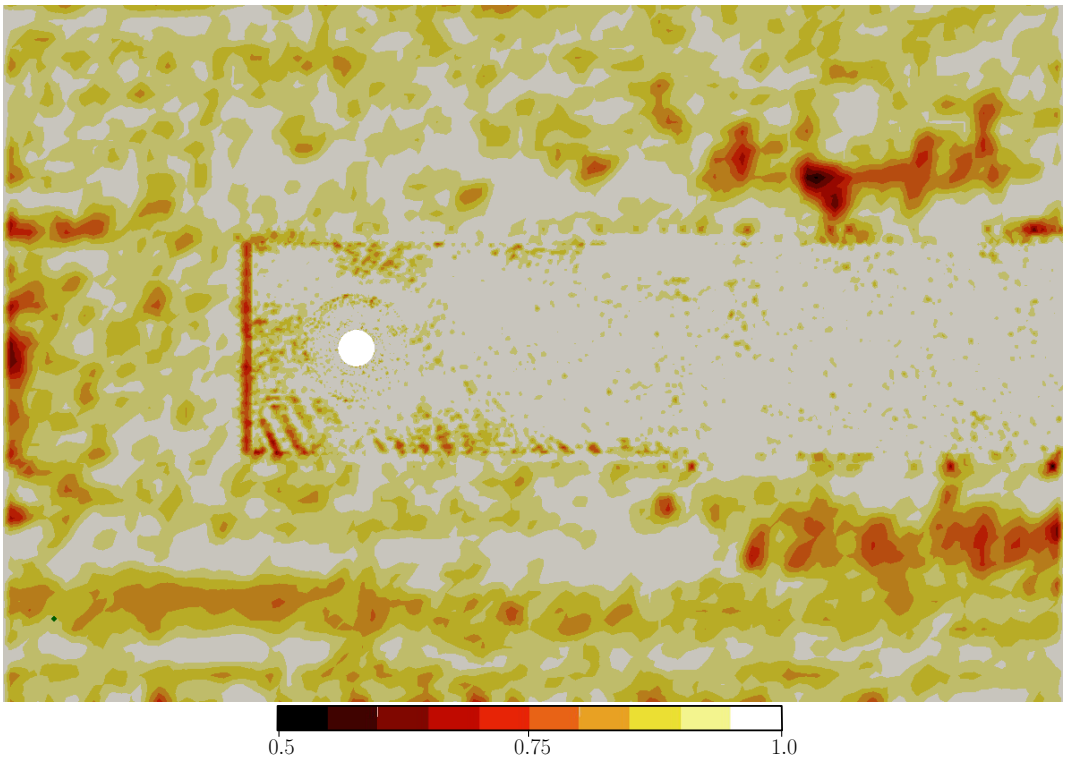

FIGURE 4.6: Instantaneous cell-averaged value of the Sweby limiter on a centreline slice of the cylinder domain. Colour scale from 0.5 (black) to 1 (white) in increments of 0.05.

4.4 Solution algorithms

4.4.1 Pressure-velocity coupling

The pressure-implicit splitting of operators (PISO) algorithm is used for solving the governing equations (Issa, 1986). This technique is known to be efficient, and provide good temporal accuracy. Stability requirements however mean that the Courant number should not exceed unity. Since OpenFOAM uses a *colocated* grid arrangement to store pressure and velocity values, a procedure similar to that suggested by Rhie and Chow (1983) is implemented in order to avoid unphysical oscillations in the solution. Full details are provided by Kärrholm (2008). Writing the discretised momentum equation (Equation 4.9) in the form $\mathcal{M}[\overline{\boldsymbol{u}}] = -\nabla[p]$, $\mathcal{M}$ is split into the discretisation operators $\mathcal{A}$ and $\mathcal{H}$ so that

$$\mathcal{A}[\overline{\boldsymbol{u}}] = \mathcal{H} - \nabla[\overline{p}] \tag{4.16a}$$

$$\implies [\overline{\boldsymbol{u}}] = \frac{\mathcal{H}}{\mathcal{A}} - \frac{1}{\mathcal{A}}\nabla[\overline{p}]. \tag{4.16b}$$

Taking the divergence of Eqn 4.16b and applying Eqn 4.3, it follows that

$$\nabla \cdot \left(\frac{1}{\mathcal{A}}\nabla[\overline{p}]\right) = \nabla \cdot \left(\frac{\mathcal{H}}{\mathcal{A}}\right). \tag{4.17}$$

The velocity flux on the faces is then computed as

$$F_f = \boldsymbol{A}_f \cdot \overline{\boldsymbol{u}}_f^n = \boldsymbol{A}_f \cdot [(\mathcal{H}/\mathcal{A})_f - (1/\mathcal{A})_f(\nabla[p])_f] \tag{4.18}$$

where $\overline{\boldsymbol{u}}^n$ is the velocity held constant when Equation 4.17 is solved. The solution procedure is outlined in Figure 4.7, which represents a general algorithm, but includes all the PISO features. Kim *et al.* (2013) also presented details of the OpenFOAM PISO algorithm. In Figure 4.7, the algorithm steps 'make fluxes absolute' and 'make fluxes relative' refer to the fact that one grid region is moving relative to the other; the variables inside the rotating region must be relative during the PISO loop within each time step. Thus the grid is rotated (and effect of the grid velocity then removed) before entering the PISO loop (see Wan *et al.* (2013) for further discussion of this procedure in OpenFOAM).

OpenFOAM has the option to use the *pimpleFoam* algorithm, which is a combination of the PISO and SIMPLE (Patankar, 1980, chap. 6) algorithms. This allows partial convergence inside the PISO loop, permitting Courant numbers greater than unity without the solution diverging. In combination with dynamic gridding (moving grids), the solver is referred to as the *pimpleDyMFoam* solver. The custom algorithm used in this work, *XCDyMFoam*[2], combines *pimpleDyMFoam* with the turbulence generator of Kim *et al.* (2013), which is included as a source term during the first inner corrector loop. A description of turbulence generators is provided later in Section 5.3.

4.4.2 Linearised equation solution

Linear solvers are algorithms used to solve systems of linear equations, such as the discretised NSEs. In general the procedure required is to solve a set of equations

$$A\boldsymbol{x} = \boldsymbol{b}. \tag{4.19}$$

Here A is a matrix of coefficients, which will involve physical (*e.g.* viscosity) as well as grid (*e.g.* cell spacing) parameters, $\boldsymbol{x}$ are the unknown values on the domain interior and $\boldsymbol{b}$ are known values, such as boundary conditions.

Typically sparse matrices (containing few non-zero elements) result from discretising the equations. In solving the resulting matrices, iterative methods are commonly used. Saad (2003) provides a detailed background to iterative methods. The various methods used within OpenFOAM can be classed as:

- *solvers*, which are algorithms to solve the matrix equation. Those used are:

[2]This name reflects the original developers of the inflow turbulence generator (Xie and Castro, 2008), although the algorithm itself was created by the author.

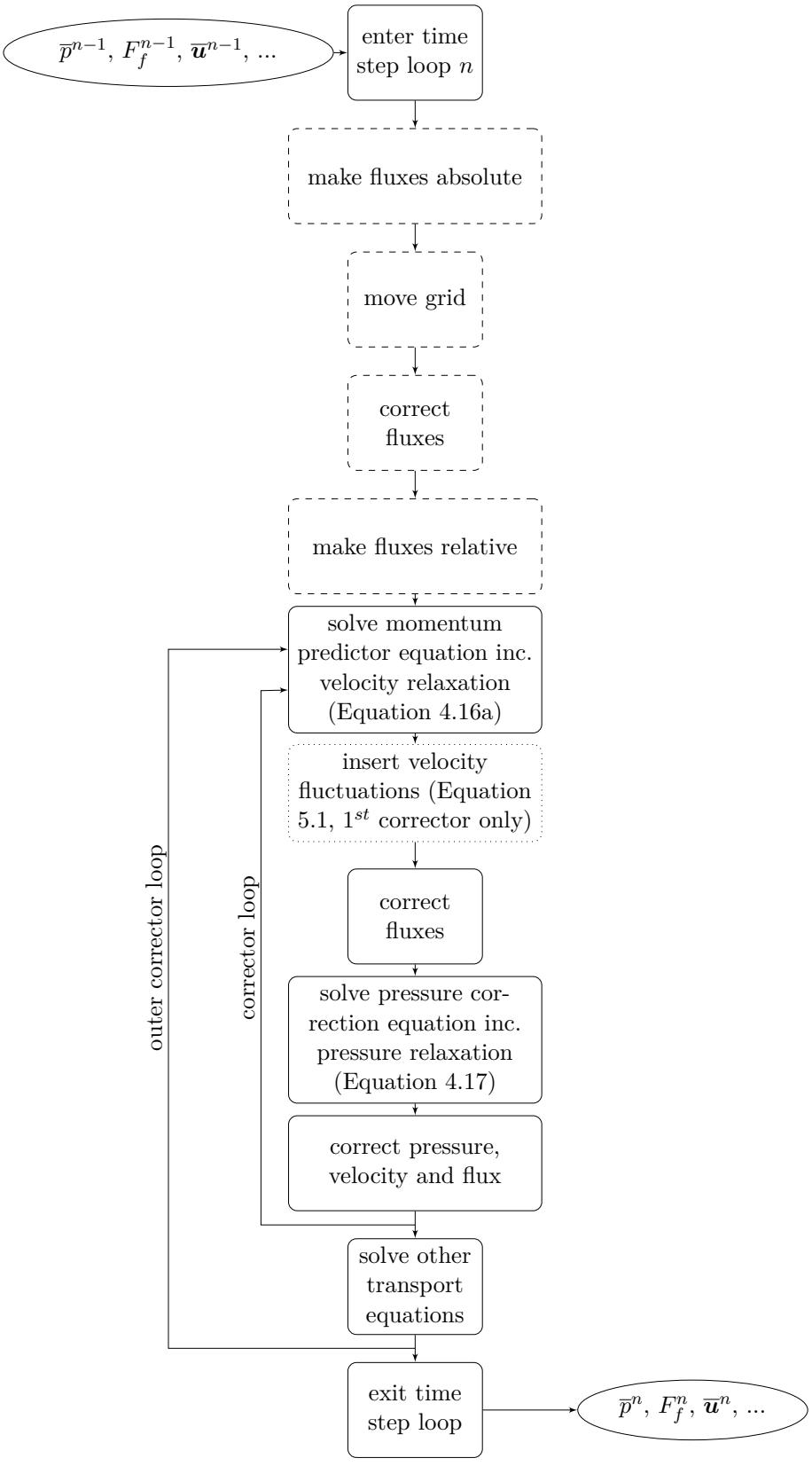

FIGURE 4.7: Flowchart for the modifed solution algorithm *XCDyMFoam*. The *pimpleFoam* algorithm is shown in solid boxes; features of *pimpleDyMFoam* are shown in dashed boxes; further modifications by *XCDyMFoam* are denoted by dotted boxes.

  - The *preconditioned conjugate gradient* (PCG) method, a solver for positive definite ($\boldsymbol{x}^T A\boldsymbol{x} > 0$), symmetric ($A^T = A$) matrices.
  - The *preconditioned bi-conjugate gradient* (PBiCG) method, a conjugate gradient solver for asymmetric matrices.
  - The *generalised algrbraic multi-grid* (GAMG) solver: which provides faster convergence using coarsening of the solution. The coarse 'grid' is constructed from the matrices (algebraically), rather than the geometric grid.
  - The *smooth solver*, which improves solution stability.

- *preconditioners*. These are algorithms to accelerate solver convergence, generally involving modifying the matrix equations to make them easier to solve. The two methods used are:

  - The *diagonal incomplete Cholesky* (DIC), a factorisation method using lower triangular matrix.
  - The *diaginal incomplete lower upper* (DILU), a factorisation method using lower and upper triangular matrices based on Gaussian elimination.

  The GAMG solver may also be used as a preconditioner for the PCG solver when solving the pressure equation.

- *smoothers*. These algorithms smooth convergence, and are used by the smooth solver. Typically they use curve-fitting to remove oscillations in the solution. The smoothing method used here is based on:

  - *GaussSeidel* elimination, which uses matrix decomposition into lower and upper triangular matrices.

The settings used throughout this work are summarised in Table 4.2. There are two noteworthy modifications to the 'standard' OpenFOAM solver settings. Firstly, the subgrid kinetic energy k is solved using a smooth solver. This was adopted to improve simulation stability. Secondly, the choice of pressure solver depends on the grid type. The GAMG solver is preferred for unstructured grids. The PCG solver was found to give faster convergence on structured grids however, using GAMG preconditioning.

4.5 Boundary conditions

Boundary conditions may generally be described as either fixed value (*Dirichlet*), fixed gradient (*Neumann*), or mixed (*e.g. convective*). Table 4.3 summarises the boundary conditions used in this work. The OpenFOAM nomenclature is also included for clarity. Typically, one of velocity or pressure is prescribed as Dirichlet. Hirsch (2007*c*, chap. 3) and Versteeg and Malalasekera (1995*c*, chap. 9) provide detailed information on

TABLE 4.2: Linear solver settings for primitive variables. Acronyms use the OpenFOAM nomenclature. Relative tolerance values outside parentheses refer to partial convegence limits within the *pimpleFOAM* outer corrector loop.

variable	$\boldsymbol{u}(Final)$	$k(Final)$	$p(Final)$	
			structured	unstructured
solver	$PBiCG$	$smooth$	PCG	$GAMG$
preconditioner	$DILU$	-	$GAMG$	-
smoother	-	$GaussSeidel$	-	$GaussSeidel$
tolerance	10^{-9}	10^{-9}	10^{-6}	10^{-6}
relative tolerance	0.1(0)	0.1(0)	0.1(0)	0.1(0)

TABLE 4.3: Summary of boundary conditions used in simulations, in terms of velocity and pressure. U_C is convection velocity; $\boldsymbol{u}_g$ is grid velocity.

boundary	OpenFOAM	description	definition
inlet	*fixedValue*	velocity - fixed value (FV); pressure - zero gradient (ZG)	$\boldsymbol{u} = \boldsymbol{U}_0$; $\frac{\partial p}{\partial n} = 0$
outlet	*convectiveOutlet*	convective velocity; pressure - FV	$\frac{\partial \boldsymbol{u}}{\partial t} + U_C\,(\nabla \cdot \boldsymbol{u}) = 0^a$; $p = 0$
wall	*fixedValue*	no-slip condition: velocity - FV0; pressure - ZG	$u = v = w = 0$; $\frac{\partial p}{\partial n} = 0$
slip wall	*slip*	frictionless wall; parallel flow only	$u = w \neq 0$, $v = 0$; $\frac{\partial p}{\partial n} = 0$
moving wall	*movingWall*	no-slip condition for a moving wall	$\boldsymbol{u} - \boldsymbol{u}_g = 0$; $\frac{\partial p}{\partial n} = 0$
symmetry	*symmetryPlane*	no flow across boundary	
cyclic (periodic)	*cyclic*	variables passed between conformal linked faces	
grid interface	*cyclicAMI*	interpolation between non-conformal linked faces	

[a] used to prevent hydrodynamic reflections

CFD boundary conditions. Specific comments on, and details of, some of the boundary conditions used are now provided.

A *convective outlet* condition is important for LES, since resolved vortices should leave the domain without hydrodynamic reflections. This becomes more important when the outlet is placed closer to the body than recommended, or the grid is not coarsened towards the outlet. Such outlet conditions are commonly used in LES, particularly when studying acoustics (*e.g.* see Fleig *et al.*, 2004; Kim *et al.*, 2006; **?**).

The grid interface provides interpolation between *non-conformal* patches. The term non-conformal is used to denote adjacent cells which do not share the same face(s). In the context of this work, the non-conformal patches are the boundaries of two grid regions, one of which rotates inside the other. The grid regions do not necessarily have to move relative to each other however. Several approaches to the interpolation are possible. Referring to Figure 4.8, the task of the procedure is to estimate the face value, ϕ_f, using values from the two grid regions: *donor* ($\mathcal{D}$) and *target* ($\mathcal{T}$).

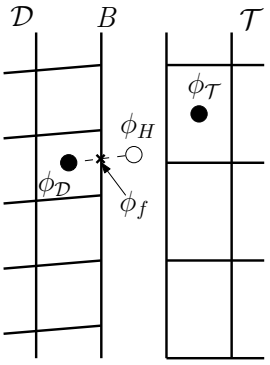

FIGURE 4.8: Schematic of sliding interface. The face value of the variable, ϕ_f, must be calculated on the boundary B. Donor and target grid cells are denoted by $\mathcal{D}$ and $\mathcal{T}$. The 'halo' value uses the subscript H.

McNaughton *et al.* (2013*a*) report a 'simple' procedure, based on the concept of a 'halo' point. The location of the halo point is estimated by linear extrapolation based on $x_{\mathcal{D}}$ and x_f (see Figure 4.8). The value of ϕ at the halo point is then interpolated from the target grid, and ϕ_f calculated using linear interpolation. This is equivalent to treating the interface B as a Dirichlet boundary condition, but does not guarantee conservativeness (Farrell and Maddison, 2011). The approach has been applied to unsteady simulations of tidal turbines (Afgan *et al.*, 2013; McNaughton *et al.*, 2013*b*).

The OpenFOAM implementation, termed *arbitrary mesh interface* (AMI), is based on Galerkin projection. Conservativeness is ensured by minimising the L_2 norm of the interpolation error (Farrell and Maddison, 2011). This may be written as $\int_S \phi_{\mathcal{D}} dS = \int_S \phi_{\mathcal{T}} dS$, while the L_2 norm is defined as $|\phi|^2 \equiv \phi \cdot \phi \equiv \phi(x)^2$. Minimising this quantity requires that $\int |\phi(x)^2| dx = 0$. The result is a matrix equation of the form

$$\mathcal{M}_{\mathcal{T}} \phi_{\mathcal{T}} = \mathcal{M}_{\mathcal{T}\mathcal{D}} \phi_{\mathcal{D}}, \tag{4.20}$$

where $\mathcal{M}$ are mass matrices consisting of basis functions, satisfying the conservativeness criterion. The matrix $\mathcal{M}_{\mathcal{T}\mathcal{D}}$ is a mixed matrix between the two grids. Farrell and

Maddison (2011) report linear scalability of the algorithm for both two and three dimensional grids. It has been applied to unsteady simulations of wind turbines (Wang *et al.*, 2012), as well as LES of marine propellers (Bensow, 2013). The AMI has also been shown to scale well with increasingly parallelised simulations (Bensow, 2013). Further investigation of the grid interface is required in the current work, based on the numerical dissipation issues experienced by Reese and Carolus (2008), using the *CFX* code. It is important that resolved turbulence convects through the AMI so that it can interact with the rotor. This is addressed further Section 8.4.

Next, wall modelling is discussed. Generally, a 'wall resolved' grid requires $y_1^+ = 1$, with a further four grid points inside the viscous sublayer ($y^+ < 5$). In typical marine applications, which involve high Reynolds numbers, the grid resolution requirements for LES cannot be satisfied without infeasible grid sizes (see Section 3.6.1). If these conditions are not satisfied, an approximation for the inner layer should be introduced. This is typically referred to as a *wall function*. As discussed in Section 3.1, most of the cells inside the boundary layer are required to resolve the inner layer (Piomelli and Balaras, 2002); hence using such an approximation considerably reduces the total number of cells required for a computation. Discussions of wall functions within LES are provided by Cabot and Moin (2000) and Piomelli and Balaras (2002).

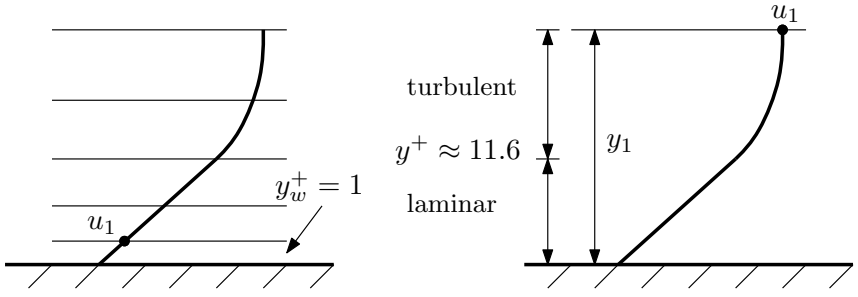

(a) wall resolved approach (b) wall modelled approach

FIGURE 4.9: Schematic of near-wall grid resolution and modelling.

A wall function provides a continuous velocity profile to the wall without the need to resolve the inner layer[3]. In the wall region, the subgrid model viscosity is modified to include an additional contribution from the wall, ν_w. Based on the definition of the wall shear stress, $\tau_w = \rho_0 u_\tau^2$, the 'wall viscosity' is found as

$$\nu_w = \frac{u_\tau^2}{(\partial u/\partial y)_1} - \nu. \tag{4.21}$$

The subscript '1' denotes values at the first grid point away from the wall, as defined in Figure 4.9. Some wall functions use different equations for U^+ depending on the value of y^+. This value is typically taken as $y^+ = 11.6$, which is the intersection of the linear

[3]The inner layer is approximately located at $y^+ < 50$ (see Table 2.1 in Section 2.2 for boundary layer definitions).

and log-law profiles (Versteeg and Malalasekera, 1995*c*, chap. 9). In this case, the flow is assumed to be laminar for $y^+ < 11.6$, in which case u_1 can be obtained from $U^+ = y^+$. This type of wall function is available in OpenFOAM[4], and has been used for LES of marine propellers (Bensow and Liefvendahl, 2008). However, $y^+ = 11.6$ lies inside the buffer layer, a region where the relationship between the velocity and the wall is not fully understood. Since this is not preferable, an alternative is to use an estimate for U^+ which integrates all the way to the wall. This is known as Spalding's *law of the wall*[5] (Spalding, 1961) where

$$y^+ = u^+ + \frac{1}{E}\left[\exp\left(\kappa u^+\right) - 1 - \kappa u^+ - \frac{1}{2}(\kappa u^+)^2 - \frac{1}{6}(\kappa u^+)^3\right], \tag{4.22}$$

with $y^+ = y_1 u_\tau/\nu$, $E = 9.8$, $\kappa = 0.41$ and $u^+ = u_1/u_\tau$. The total effective viscosity is then $\nu_{eff} = \nu + \nu_{sgs} + \nu_w$.

4.6 Summary

A key feature of the numerical approach adopted is the use of the OpenFOAM convection scheme *filteredLinear*, which was been shown to be suitable for the challenging test case of vortex shedding from a smooth circular cylinder. The scheme provides dynamic upwinding, *i.e.* stability, when the localised flow is convection-dominated. This means that complex flow features may be resolved without significant numerical dissipation, whilst avoiding unphysical solutions which may result from purely central schemes.

The finite volume method is used since to allows complex geometries to be simulated using arbitrary cell shapes. A custom solution algorithm has been developed for the simulation of tidal turbines. This combines the moving grid functionality of the *pimpleDyMFoam* solver with a numerical inflow turbulence generator. A detailed description and evaluation of the inflow turbulence generators used in provided in the next chapter. The arbitrary mesh interface boundary condition is also key. This allows interpolation of variables between grid regions undergoing independent motion. In the context of a tidal turbine, this allows the turbine to rotate inside a cylindrical domain. Evaluation of the arbitrary mesh interface is presented in Chapter 8.

[4]termed *nutUWallFunction* in OpenFOAM
[5]termed *nutUSpaldingWallFunction* in OpenFOAM

5

Evaluation of Inflow Turbulence Generators

5.1 Introduction

To establish a suitable numerical framework for simulating tidal turbine broadband noise, turbulence modelling and numerical methods have been reviewed and evaluated. It has been shown that large eddy simulation using a dynamic subgrid turbulence model is appropriate for simulating the acoustic sources, while an acoustic analogy may be used to estimate far-field sound. A dynamic hybrid convection scheme was also shown to be the best choice for complex flows on unstructured grids. The final part of the numerical approach to be presented is a method for generating inflow turbulence. This is essential in order to simulate the unsteady forces experienced by a tidal turbine, which lead to noise generation.

Firstly a review of inflow turbulence generation methods is made, comparing two main classes of approach: *precursor* and *synthetic*. Following this, the chosen methods are outlined and evaluated using two test cases: a planar jet and channel flow. These test cases have been chosen since they allow analysis of both homogeneous isotropic turbulence (HIT) and inhomogeneous anisotropic turbulence (IAT).

5.2 Review of inflow turbulence methods

Including some form of inlet turbulence is necessary for the correct spatial evolution of turbulence in LES. This is also essential when studying unsteady forces and acoustic sources due to inflow turbulence. Tabor and Baba-Ahmadi (2010) outlined requirements for a method designed to achieve this. The inlet field should be turbulence-like and stochastically varying, representing turbulence scales down to the grid filter size. In addition, it should be compatible with the Navier-Stokes equations, such that the fluctuations satisfy continuity and are not damped by the solver. This is particularly important for hydroacoustics, where a divergence-free field is required in order to avoid spurious pressure fluctuations. The technique would ideally allow easy specification of properties characterising the field, such as turbulence intensities and length scales. Since most engineering applications involve wall-bounded flows, an additional requirement is to include the effects of anisotropy and inhomogeneity. Thus, specifying Reynolds shear stress profiles would also seem to be particularly important.

A review of various methods for generating appropriate inlet conditions for LES and its derivatives is provided by Tabor and Baba-Ahmadi (2010). The authors divide these into two categories, precursor and synthetic, each containing several methods. One further method, although less commonly reported, is to include the physical grid in the simulation domain (Blackmore *et al.*, 2013; Carolus *et al.*, 2007). In this case however, the inlet turbulence is restricted to be homogeneous and isotropic, while the domain must be re-gridded in order to vary the turbulence statistics.

5.2.1 Precursor methods

The first family of approaches is termed *precursor* since it involves generating turbulence using a Navier-Stokes simulation, with realisations of the statistical profiles introduced at the inlet of the main simulation. These are separated into: preprepared library; concurrent library; and internal mapping. Figure 5.1 illustrates each concept, with (a) and (b) representing library techniques, which can be used for generating prepared or concurrent libraries, and (c) internal mapping.

Precursor methods are noted for their accuracy compared with synthetic methods, since the instantaneous realisations which constitute the library are extracted from a turbulence simulation, rather than a mathematical representation. For a simple case such as a channel flow, cyclic streamwise boundary conditions may be used to obtain fully developed turbulent flow. A library of field data is saved and fed directly into the main simulation, provided the inlet cross-section is consistent with the auxiliary simulation. Lund *et al.* (1998) proposed a more complex approach, whereby the auxiliary simulation consists of a spatially evolving boundary layer. A 'recycle' plane is placed downstream of the inlet, and the field fed back to the inlet using a rescaling procedure. This is

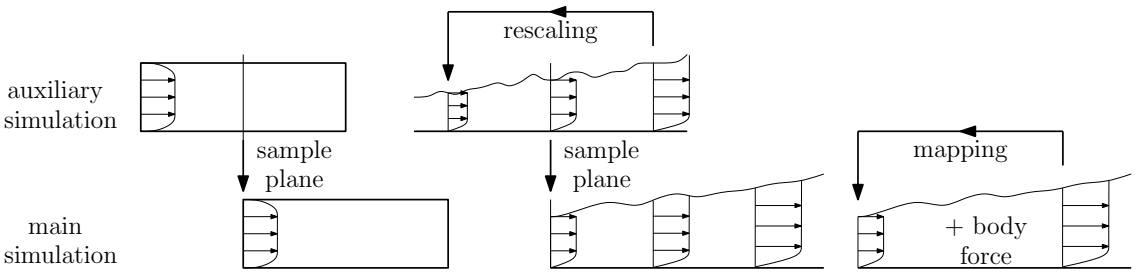

(a) cyclic method (b) rescaling method (c) internal mapping

FIGURE 5.1: Summary of precursor methods for generating inlet turbulence.

described as a *concurrent library* method, since the inlet condition supplied to the main simulation is extracted 'on-the-fly' from the auxiliary simulation. A key advantage of this method is in the drastically reduced data storage requirements.

A simpler method, encompassing the advantages of the concurrent library technique, is to recycle the data inside the inlet section of the main simulation, thus avoiding the need for an auxiliary calculation. Baba-Ahmadi and Tabor (2009) adopted this technique for the simulation of turbulent channel flow and swirling pipe flow. In order to control the flow in the mapping region, they applied a body force and velocity correction, in order to drive the flow towards specified three-dimensional velocity distributions. This approach shows very good predictions of mean velocity and Reynolds stress components compared to the fully cyclic case. A downside is that the inlet turbulence may exhibit a periodicity depending on the length of the recycling region, which is undesirable in certain cases (Tabor *et al.*, 2004). This issue may be overcome using a method such as that of Spille-Kohoff and Kaltenbacher (2001), who combined random inlet fluctuations with a body force technique, designed to correct the Reynolds shear stress profile in a turbulent boundary layer.

While providing precise flow field data, precursor methods have generally been limited in their application to canonical flows. The need to generate turbulence at the inlet for engineering flows has led to the development of a number of synthetic methods, described next. These are motivated by the need to simulate complex geometries where recycling close to the inlet may not be possible as well as the fact that detailed length scale or stress component information is generally not available and may have to be estimated or assumed.

5.2.2 Synthetic methods

Synthetic methods, based on mathematical representations of turbulence, consist of: *Fourier series* techniques; *proper orthogonal decomposition* methods; *digital filtering*; and *vortex/synthetic eddy* methods. It is widely accepted that using random fluctuations

based on 'white noise' is not sufficient to generate realistic turbulence, and such non-physical perturbations will be damped by the solver (Tabor and Baba-Ahmadi, 2010). An effective synthetic method should provide some ability to represent the desired energy spectra, as well as velocity correlations and anisotropy.

Fourier series techniques utilise a Fourier summation representation of the fluctuating velocity components. Energy spectra and temporal correlations can be prescribed using the amplitude and phase coefficients of the Fourier series. Coefficients are generated using a random process, with the turbulence properties controlled by specifying mean and variance. Tabor *et al.* (2004) used an Ornstein-Uhlenbeck process to achieve this, but do not see close agreement with the cyclic case in terms of correlations. This is explained by the method producing an infinite correlation length across the channel. This suggests that the Fourier representations of inflow gusts discussed in Section 3.4 (Clair *et al.*, 2013; Gill *et al.*, 2013*a*; Lau *et al.*, 2013), may not be suitable for modelling broadband inflow conditions.

Smirnov *et al.* (2001) presented a more advanced technique. Having generated an isotropic field based on a modelled energy spectrum, the authors performed a scaling transformation based on the Reynolds stress tensor to produce an anisotropic field. The required input data (length and time scales, as well as Reynolds stress tensor) may be obtained from a RANS calculation or experiments. The technique is divergence free for homogeneous turbulence, and almost divergence free in the inhomogeneous case. An improvement of this method, made by Huang *et al.* (2010), shows better prediction of force spectra on an idealised building. This is due to the specification of anisotropic spatial correlations at the inlet.

Proper orthogonal decomposition (POD) can be used to represent turbulence data as a set of spatial and temporal modes or *eigenvectors*. Usually only a small number of basis functions are required to model the data. This method provides excellent representation of both one-point and two-point statistics, as shown by Perret *et al.* (2006). One disadvantage of the POD method is the requirement for detailed spatial and temporal data in order to reproduce the turbulence accurately. In some cases, the insufficient temporal resolution of particle image velocimetry data means that a random component may have to be added to represent the high frequency part of the velocity signal (Perret *et al.*, 2008). This adds considerable complexity to the method.

Digital filter-based methods (di Mare *et al.*, 2006; Klein *et al.*, 2003; Veloudis *et al.*, 2007; Xie and Castro, 2008) differ from Fourier methods in that the velocity components are generated using random numbers, and filtered to achieve the desired turbulence statistics. The required filter coefficients are derived from a relationship involving the desired first and second-order statistics. A simple approach, based on prescribing a single length scale and Reynolds stresses, has been shown to be suitable for free flows or turbulent

jets (di Mare *et al.*, 2006). This is based on the assumption that the specified parameters should be derived from a RANS calculation or from heuristic estimates. For wall-bounded flows it is observed that a more sophisticated method, involving specification of the full Reynolds-stress tensor, as well as spatial and temporal correlations, is more appropriate. This is deemed to be due to the simpler method not providing the right amount of energy to the smaller near-wall structures, and the Reynolds shear stresses not developing correctly.

Xie and Castro (2008) implemented a similar method, specifying two-dimensional profiles of Reynolds stresses and integral length scales. They observe a satisfactory prediction for the turbulence intensities compared to a cyclic inlet-outlet for the flow over a staggered cube arrangement. It is concluded that a three-dimensional profile (spanwise variation) of the inlet data is preferable, but not always achievable. Kim *et al.* (2013) improved the method of Xie and Castro (2008) to ensure divergence-free turbulence. It was found that this feature delays the streamwise development of the correct wall shear stress. This method has been used to simulate dynamic loads on a model building by Daniels *et al.* (2013), who found the peak load to be sensitive to turbulence intensity but not length scale.

The final technique is the vortex (or synthetic eddy) method. In this approach, the lateral velocity components are generated using an equation for the vorticity, which involves the vortex circulation and a shape function. Jarrin *et al.* (2006) estimate the vortex circulation using the turbulent kinetic energy (TKE) obtained from a RANS simulation, and generate the streamwise velocity component using a stochastic differential equation. Whilst this method provides good prediction of the Reynolds normal stresses, the shear stress component is not well represented.

A newer version of the method (Jarrin *et al.*, 2009), including a transformation based on the Reynolds stress tensor improves this issue. It is noted that the synthetic eddy method requires a shorter development length than a Fourier technique, by comparing the spatial evolution of the skin friction for a channel flow. Pamiés *et al.* (2009) also showed that accounting for anisotropy at the inlet is essential for the correct development of wall-bounded turbulence using this method. Christophe *et al.* (2007) used the original version of the method to generate a round jet flow for studying inflow turbulence noise. One issue observed was the over prediction of the turbulence intensity in the jet compared to experimental data.

Kornev and Hassel (2007) take a similar approach, but term the fluctuations 'vortons'. This method relates the shape function of the generated fluctuations to the specified spatial correlation, allowing a solution for the shape function using polynomial representations. A simplified version of the method is proposed, based on specifying length scales as opposed to spatial correlations, suitable for engineering problems. An implementation of the vorton method has been used to simulate unsteady flow at a ship's

stern (Kornev *et al.*, 2009), where a single length scale is prescribed based on a RANS calculation. Excellent agreement in terms of boundary layer thickness and TKE wall-normal distribution is seen compared to a LES. However, higher-order statistics are not presented.

5.2.3 Overall comparison

While library methods generate the most realistic turbulence at the inlet, they are limited in terms of either high data storage requirements or in their application to engineering problems. Conversely, synthetic methods allow inlet turbulence statistics to be 'tuned' and are more easily applied to complex inlet geometries. However, the turbulence generated may not always possess truly physical characteristics. From an engineering point of view, specifying simplified parameters at the inlet is preferable. Anisotropy and inhomogeneity are important for wall-bounded flows, as is divergence-free turbulence where surface pressure fluctuations must be predicted.

Next, numerical details of the two inflow turbulence generators (ITGs) used in this work are given. They are the synthetic vorton method (Kornev and Hassel, 2007; Kornev *et al.*, 2009), and the forward stepwise method (Kim *et al.*, 2013; Xie and Castro, 2008). Both codes have been provided by the developers for use with OpenFOAM.

5.3 Description of inflow turbulence models used

The synthetic turbulence generation methods used exhibit some common traits. These are outlined first before a description of each method is given. The generated velocity fluctuations are superimposed onto the mean inlet velocity field such that

$$u_i = \bar{u}_i + a_{ij}\tilde{u}'_j \tag{5.1}$$

where a_{ij} is a transformation tensor and $\tilde{u}'$ is the unscaled velocity fluctuation, which possesses zero mean ($\overline{\tilde{u}'} = 0$) and unit variance ($\overline{\tilde{u}'\tilde{u}'} = 1$), as well as spatial and temporal correlations. The transformation tensor, first proposed by Lund *et al.* (1998), is a Cholesky decomposition of the Reynolds stress tensor. It accounts for scaling of the generated fluctuations including the effect of anisotropy, *i.e.* cross-correlations. The tensor is defined as

$$a_{ij} = \begin{bmatrix} \sqrt{r_{11}} & 0 & 0 \\ r_{21}/a_{11} & \sqrt{r_{22} - a_{21}^2} & 0 \\ r_{31}/a_{11} & (r_{32} - a_{21}a_{31})/a_{22} & \sqrt{r_{33} - a_{31}^2 - a_{32}^2} \end{bmatrix}. \tag{5.2}$$

where τ_{ij} is the Reynolds stress tensor.

The velocity $\tilde{u}'$ is generated on a two-dimensional slice, and convected into the domain with the required temporal correlations. In the synthetic vorton method (SVM) of Kornev and Hassel (2007), the data are introduced directly into the simulation domain using the physical inlet grid. Hence the method constitutes an inlet boundary condition. Conversely, the forward stepwise method (FSM) of Kim *et al.* (2013) generates fluctuations on a virtual grid placed slightly downstream of the simulation inlet. This means Equation 5.1 is applied inside the PISO algorithm, with a steady mean velocity specified at the inlet boundary.

5.3.1 Synthetic vorton method

The method described here is that developed by Kornev and Hassel (2007) and implemented into OpenFOAM for ship hydrodynamics problems (Kornev *et al.*, 2009). The method is based around the concept of 'random spots' generated using prescribed autocorrelations and summed over the inlet boundary to obtain the velocity field at each time step. The key theoretical background is presented here, with reference to Kornev and Hassel (2007), who provide a full description.

Random spots are sections of the inlet plane with length $2\psi_{kl}(y_l)$, where $\mathcal{R}(y_l, 2\psi_{kl}(y_l)) = 0$. Here ψ_{kl} is the distance from the k^{th} spot centre $\boldsymbol{y}_k$ to its edge, y_l is the location of the face centres on the inlet plane and $l = 1, 2, 3$. For each time step $n = 1, N$, there are K spots on the inlet, each with an inner velocity distribution $f_l(\boldsymbol{y}_k^{(n)}, y_l, \psi_{kl})$ about the spot centre $\boldsymbol{y}_k^{(n)}$. The spot velocity is zero outside of the spot. The velocity fluctuation is then generated by conditioning sets of random numbers ran using the inner velocity distributions as

$$\tilde{v}'^{(n)}(\boldsymbol{y}) = \sum_{k=1}^{K} \prod_{l=1}^{3} f_l(\boldsymbol{y}_k, y_l, \psi_{kl})\ sign(\ ran_k^{(n)} - 0.5). \tag{5.3}$$

The procedure is illustrated schematically in Figure 5.2.

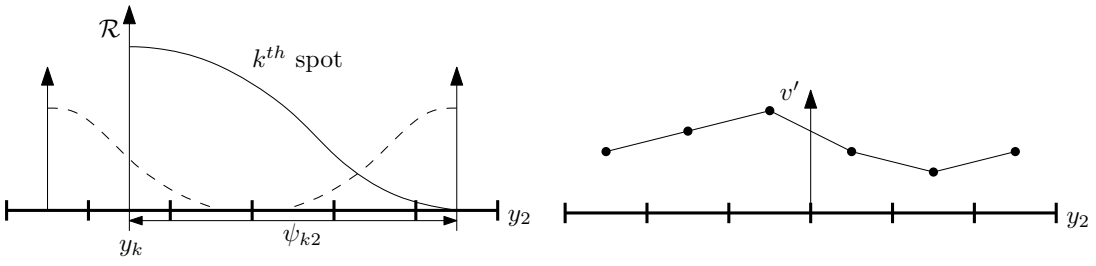

(a) spot length based on autocorrelation (b) velocity field generated as summation of spots

FIGURE 5.2: Schematic of vorton method, using one-dimensional example.

An equation for the temporal autocorrelation can be obtained by replacing $\boldsymbol{y}$ with t. Physically this consists of a correlation in terms of the upstream distance at which each fluctuation is generated, $x_k^{(n)} = -2\psi_{k1}(1 + ran)$. The spot length can be estimated from

the autocorrelation, or integral length scale, by solving an equation involving f and $\mathcal{L}$. For this a 'predictor-corrector' method is used. This generates fluctuations based on an assumed spot length, which are then corrected using the ratio of the assumed and actual integral lengths. Whilst the spot lengths can be based on autocorrelations $\mathcal{R}_{ii}$, the authors prefer to use integral length scales, as they are a more heuristic measure appropriate for engineering applications. The version implemented into OpenFOAM uses only a single length scale at each inlet face *i.e.* the length scale is isotropic. The technique for generating the velocity fluctuations requires:

1. calculation of spot velocity distribution functions $f_l(\boldsymbol{y}_k, y_l, \psi_{kl})$ at each point of the inlet plane using autocorrelations or integral length scales;
2. generation of velocity fluctuations using Equation 5.3;
3. conditioning of fluctuations to give $\tilde{u}'_j$ unit variance, and zero covariance with each component of the velocity;
4. transformation of the velocity field to account for one-point cross-correlations using a_{ij} (Equation 5.2);
5. writing the velocity field $u_i^{(n)} = \bar{u}_i + a_{ij}\tilde{u}_j'^{(n)}$.

This procedure is carried out at each time step, thus providing low data storage requirements. The method implemented into OpenFOAM allows specification of inhomogeneous integral length scales and Reynolds stresses, but only provides "generation of divergence free [fluctuations for] homogeneous anisotropic vortex fields" (Kornev *et al.*, 2009, p.10). Any divergence in the inhomogeneous case is caused by the insertion of the fluctuations as a boundary condition, which occurs after the pressure corrector in the PISO algorithm. Hence divergence is corrected for during the following time step, which introduces spurious pressure fluctuations.

5.3.2 Forward stepwise method

Now the forward stepwise method of Kim *et al.* (2013) is presented. It can be considered as a divergence-free extension of the digital filtering method of Xie and Castro (2008). The notation from Section 5.3.1 has been utilised where possible. An intermediate velocity $\tilde{v}'$ is generated at each time step on a two-dimensional plane as

$$\tilde{v}'^{(n)}(\boldsymbol{y}) = \sum_{m=-M}^{M} b_{km} ran_k^{(n)}, \tag{5.4}$$

where $M = 2\mathcal{I}/\Delta y$ with Δy is the grid spacing. The coefficent b_{km} is the filter coefficient at the k^{th} face. The velocity $\tilde{v}'$ possesses zero mean, unit variance and spatial correlation

through the form of b, which is

$$b_m = \tilde{b}_m / \left(\sum_{m=-M}^{M} \tilde{b}_m \right)^{1/2} \tag{5.5}$$

where $\tilde{b}_m = \exp(-\pi|\psi|\Delta y/2\mathcal{I})$. The distance from the face centre ψ can be considered equivalent to the spot length in Section 5.3.1. The two-dimensional instantaneous velocity is then correlated in time using

$$\tilde{u}'_j(t+\Delta t) = \tilde{u}'_j(t) \exp\left(-\frac{\pi \Delta t}{4\mathcal{T}}\right) + \tilde{v}'_j(t) \left[1 - \exp\left(-\frac{\pi \Delta t}{2\mathcal{T}}\right)\right]^{1/2}. \tag{5.6}$$

The Lagrangian time scale $\mathcal{T}$ is estimated based on Taylor's hypothesis as $\mathcal{T} = \mathcal{I}_x/\overline{U}_C$, using the mean convective velocity. In all, nine length scales may be specified in the FSM *i.e.* the length scales are fully anisotropic. The streamwise length scales are inhomogeneous in that they are proportional to the mean velocity profile. The other length scales assume homogeneous values, although a 'near-wall' scale may be specified in the region $y/\delta < 0.1$.

The method follows a similar procedure to that of Kornev and Hassel (2007), apart from the way the temporal correlations are included. Divergence-free fluctuations are ensured by inserting $\tilde{u}'_j$ as a source term in the Navier-Stokes equations during the first corrector step of the PISO algorithm. During the second corrector step, the fluctuations are modified slightly to satisfy continuity, before being inserted into the domain. Kim *et al.* (2013) showed that only two corrector steps are necessary in the PISO algorithm, and the modifications to the velocity field to remove divergence are small.

The results presented in the remainder of this chapter constitute a quantitative analysis of the two methods' abilities to generate realistic turbulence, building on the discussion presented in Section 5.2. In particular, comparisons are made in terms of the streamwise development of the: Reynolds stress profiles; integral length scales; skin friction coefficient; and unsteady pressure field induced at the inlet.

5.4 Homogeneous isotropic turbulence: planar jet

5.4.1 Test case description

This section concerns homogeneous isotropic turbulence. Since no shear (and more specifically wall) effects are present, the specification of the inflow parameters is somewhat simplified. Although the case considered is artificial, the inflow is designed to replicate the turbulence measured by Gruber (2012) in the *DARP* facility at the University of Southampton. The purpose is to examine the ability of the models described in

Section 5.3 to replicate experimental measurements of grid-generated turbulence. Since the SVM is divergence-free for the homogeneous case, comparisons focus on first and second moments of the velocity field, as well as spectra.

Gruber (2012) measured the mean velocity and streamwise turbulence intensity generated by two grids of square wooden bars mounted in the contraction of an open jet wind tunnel. Measurements were made 145 mm downstream of the jet nozzle exit, which has a height (H) of 0.15 m and width of 0.45 m. Here, simulations are designed to replicate a grid of spacing $d_G = 22$ mm. A schematic showing the grid layout is given in Figure 5.3. The bar width was $w_G = 8.5$ mm.

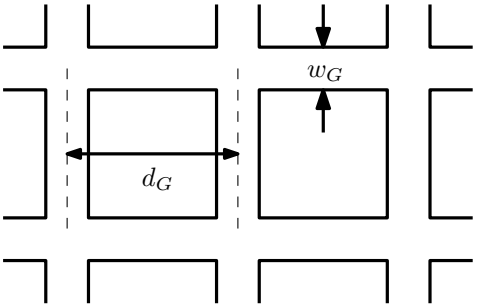

FIGURE 5.3: Schematic of grid geometry used to generate homogeneous isotropic turbulence. Bar width w_G relates to blockage ratio, and therefore modifies the turbulence intensity, while the bar spacing d_G affects the size of the integral length scale.

Since the fluctuating velocities decay as they convect downstream, estimations of the parameters at the inflow generation plane are necessary. The relationship proposed by Comte-Bellot and Corrsin (1966) is

$$\frac{\overline{u'^2}}{U_0^2} \propto \frac{1}{A_1}\left(\frac{x - x_0}{d_G}\right)^{-n}, \tag{5.7}$$

where x is the streamwise distance from the grid, x_0 is a reference distance and A_1 and n are calibration constants. The dataset provided by Comte-Bellot and Corrsin (1966) was used to estimate the constants. This results in $A_1 \approx 17$ and $n = 1.27$. Significant simplification of the geometry of the jet used in the experiments was made, with the flow inside the nozzle treated as a planar channel with slip walls. Figure 5.4 shows these simplifications schematically. Note also the difference between the location of the grid in the experiment and the inflow generator plane. In order to account for this, the location of the grid ($x/H \approx -5.7$) was used to calibrate Equation 5.7 via the constant x_0.

Gruber (2012) estimated $\mathcal{I}$ by fitting a Von Kármán spectrum to measured hot wire probe data. The spectrum is given by

$$\Phi_{uu}(\omega) = \frac{\mathcal{L}\overline{u'^2}}{\pi U_0}\frac{1}{(1 + \hat{\kappa}_x^2)^{5/6}}. \tag{5.8}$$

The spectrum captures the $-5/3$ fall off of homogeneous isotropic turbulence, and depends simply on three parameters: integral length scale; turbulence intensity; and mean velocity. Here, a further estimate is made using Taylor's hypothesis to predict the integral length scale (Equation 2.8). Figure 5.5(a) shows the effect of changing $\mathcal{I}$ and $\mathcal{L}$ on

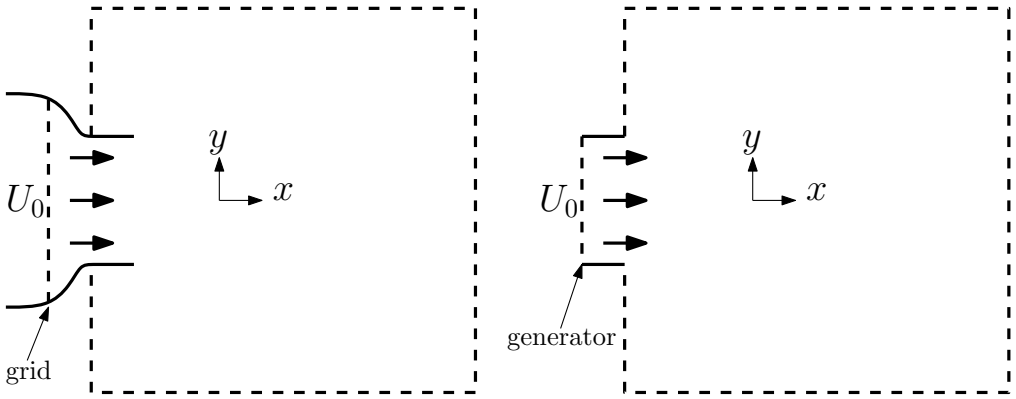

(a) Experiment rig geometry. (b) Simplified geometry.

FIGURE 5.4: Schematic representations of open jet nozzle.

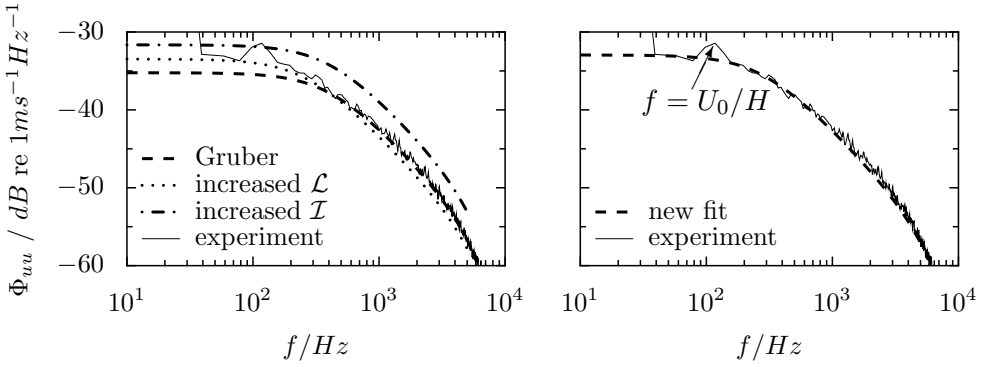

(a) Effect of changing $\mathcal{I}$ and $\mathcal{L}$ (b) New fit: $\mathcal{I} = 2.7\%$ and $\mathcal{L} = 0.0087\ m$

FIGURE 5.5: Von Kármán spectra used to fit to experimental data of streamwise velocity in jet. Probe located at $x/H = -1$ on domain centreline ($yH = 0; z/H = 0$).

the analytical spectra. Higher turbulence intensity increases the spectrum amplitude for all frequencies; increasing integral length scale shifts energy to lower frequencies. The fit proposed by Gruber (2012) matches the high frequencies well, but shows a discrepancy below $\approx 500\ Hz$. A new fit has been made based on the re-assessment of the integral length scale, and is shown in Figure 5.5(b). Note the slight low frequency hump in the experimental spectrum is associated with an eddy frequency $f = U_0/H$, where H is the height of the jet. This is associated with a turbulence structure resulting from the turbulence grid located inside the jet nozzle.

This re-assessment of the jet turbulence statistics is inline with Dieste and Gabard (2010), who estimated $\mathcal{L} = 0.01\ m$ using a Von Kármán spectrum. Using the known values of d_G and $\mathcal{I}$, the turbulence intensity required at the inflow generator location may be estimated. A summary of the relevant values, which are used in all simulations, is given in Table 5.1.

TABLE 5.1: Homogeneous isotropic turbulence statistics used in jet simulations: $x/H = -1$ corresponds to measurement location; $x/H = -1.97$ to inflow generation plane, with $\mathcal{I}$ estimated using Equation 5.7.

x/H	U_0/ms^{-1}	$\mathcal{I}_x/\%$	$\mathcal{L}/m$
-1.00	20	2.70	0.0087
-1.97	20	3.00	0.0087

5.4.2 Numerical setup

The domain consists of a two-dimensional cross-section of dimensions $L_x = 7H$ and $L_y = 6H$, similar to that shown in Figure 5.4, with a spanwise width of $L_z/H = 0.1$. This width has been chosen to ensure that $\mathcal{L}_z/L_z < 1$, implying the turbulence will be incoherent across the domain width. The global origin is the same as that used in the experiments, such that the exit of the jet nozzle is at $x/H = -1.97$. It is noted that the domain width, although larger than $\mathcal{L}$, is only $\approx 0.68d_G$. Hence an approach based on including the grid geometry in the simulation (*e.g.* see Carolus *et al.*, 2007) would fail for this domain width. Blackmore *et al.* (2013) investigated this approach for generating homogeneous isotropic turbulence, and recommend that a domain width of at least $3d_G$ is used to allow for the correct development of turbulence. Hence in the present study, the domain would need to be more than four times wider than is used. This observation highlights an advantage of using a synthetic inflow turbulence generator.

A grid was created using the OpenFOAM utilities *blockMesh* and *snappyHexMesh*. All cells are hexahedral and isotropic, with a total grid size of 1.8×10^6 cells. Refinement was focussed in the jet region, with a target cell size of 7.5×10^{-4} m; this value was chosen to achieve a cutoff frequency equivalent to $\mathcal{L}/12$. Approximately ten cells were placed inside the nozzle region of the domain. The inflow plane for the FSM was located in the middle of this region ($x/H \approx -2$), ensuring that there were five cells between the domain inlet and the inflow plane. Turbulence in the SVM case was generated on the inlet.

The turbulence statistics presented in Table 5.1 were prescribed at the inlet. The intensities $\mathcal{I}_y$ and $\mathcal{I}_z$ were scaled to 90% of $\mathcal{I}_x$, based on the slight anisotropy of grid generated turbulence (Comte-Bellot and Corrsin, 1966). This effect was included to try to recreate as closely as possible the experimental conditions; no hot-wire probe data are available for the v and w velocity components however. All turbulence statistics are homogeneous across the inlet plane.

Both SVM and FSM cases were simulated using the *pimpleFoam* solver, initialised from a converged RANS solution. The time step was limited to give a maximum Courant number of unity. The flow was allowed to develop for a duration of $T^* = TU_0/H = 6.4$ (one flow-through of the domain), before statistics were recorded at 10 kHz for a further $T^* = 122$.

5.4.3 Results and discussion

Firstly, flow visualisations are presented in terms of the vertical (upwash) velocity. Figures 5.6-5.8 reveal some clear qualitative differences between the two methods. Figure 5.7 consists of the same time snapshot as Figure 5.6, but shows the velocity only within the jet height. The colour scale has also been adjusted in order to reveal the flow features more clearly, since in Figure 5.6 the shear layers dominate over the jet turbulence.

The SVM produces what appear to be isotropic velocity fluctuations. Figure 5.6 reveals the eddies are relatively large scale when injected into the domain, but become finer and stretched in the streamwise direction as they convect downstream. The structures added to the solver using the FSM look quite different. The upwash velocity appears to have a larger vertical correlation, while the vorticity shows streamwise-elongated eddies convecting from the inflow plane. The magnitude of the vorticity inside the jet is also diminished compared to the SVM.

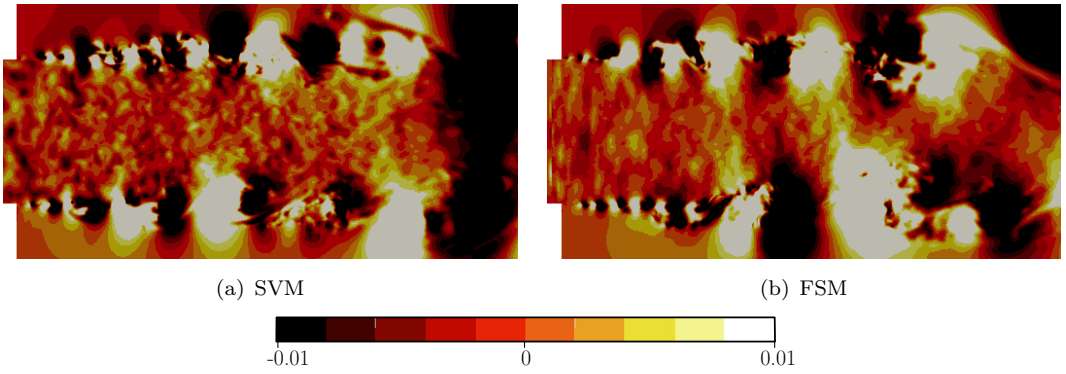

FIGURE 5.6: Flow visualisation of jet simulations: x-y slices of vertical velocity $v^* = v/U_0$.

Quantitative comparison is now made in terms of turbulence statistics. Figure 5.9 shows the streamwise mean velocity and turbulence intensity sampled over the jet height. The SVM shows excellent prediction of the mean velocity profile compared to the experiment. The FSM slightly over-predicts $\overline{u}^* = \overline{u}/U_0$ at the domain centreline ($y/H = 0$), but still gives an approximately homogeneous velocity distribution. In terms of turbulence intensity, the SVM shows the best prediction close to the jet shear layers; at the domain centreline, $\mathcal{I}_x$ is higher than the experimental data, but close to the value used to fit the Von Kármán spectrum previously (2.7%). The profile shows a lack of homogeneity across the jet height however. By contrast, the FSM data is closer to the experiment at the centreline, but displays a distinctly inhomogeneous profile. Difficulties in accurately predicting jet turbulence intensity using ITGs were also experienced by Christophe *et al.* (2007); the authors presented discrepancies between numerical and experimental turbulence intensity of up to 50%. Hence the differences seen here ($\approx 10\%$) are not considered too critical.

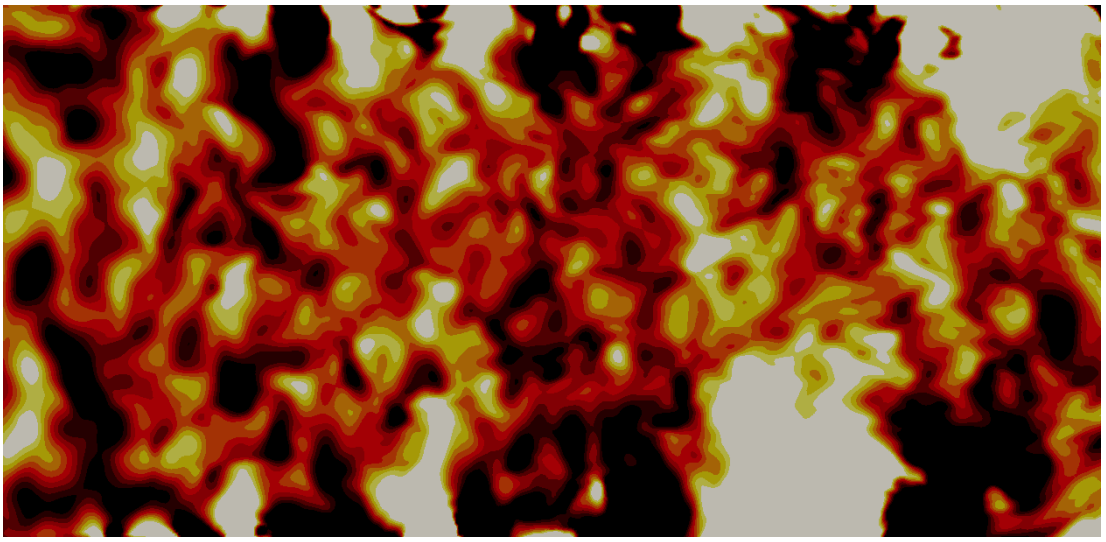

(a) SVM

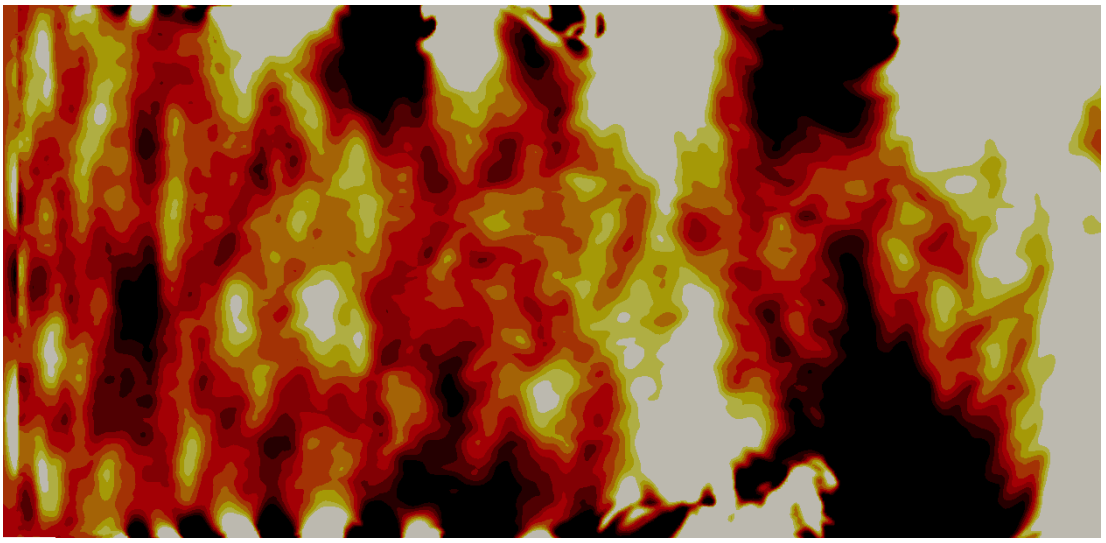

(b) FSM

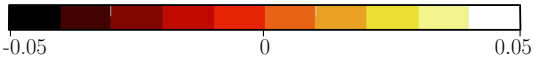

FIGURE 5.7: Flow visualisation of jet simulations: x-y slices of vertical velocity $v^* = v/U_0$ inside the jet.

A summary of the key turbulence statistics at the experimental measurement location is provided in Table 5.2. The key difference is in the integral length scale, which is close to the desired value for the SVM, but almost 90% over-predicted by the FSM. This is linked to the observed structure of the turbulence in Figure 5.8, where streamwise vortices were generated by the FSM.

Since the two ITGs have shown qualitative discrepancies in terms of the structure of the turbulence generated, the streamwise development of the turbulence intensities is now considered. Figure 5.10 shows each of the turbulence intensity components sampled along the domain centreline. In purely grid-generated turbulence, one would expect the

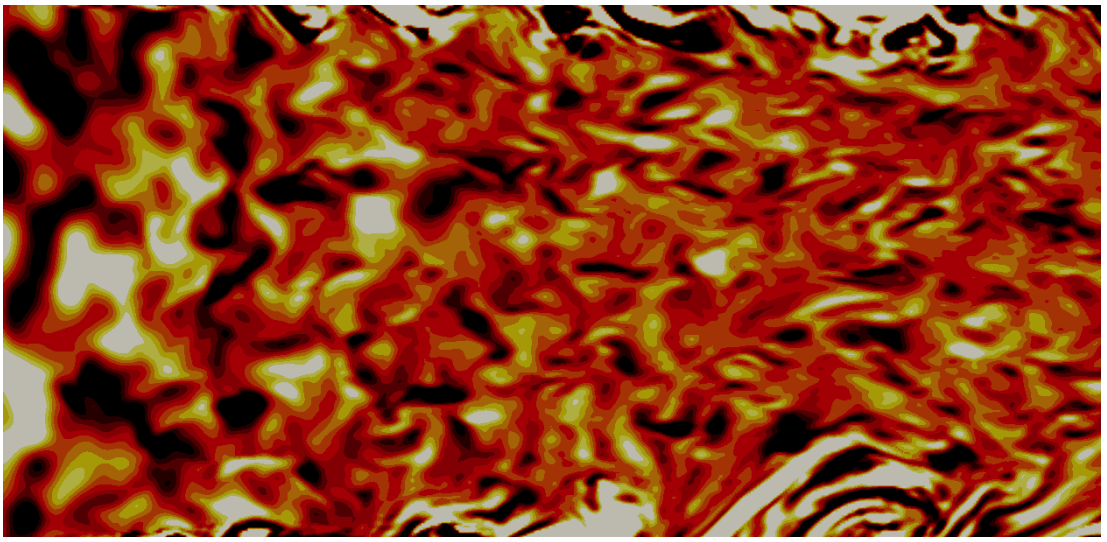

(a) SVM

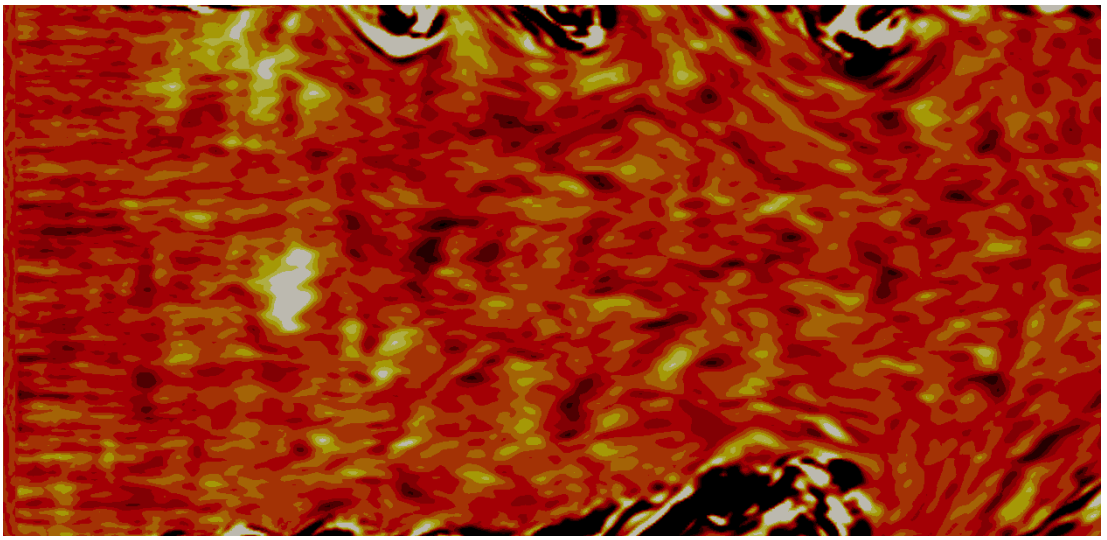

(b) FSM

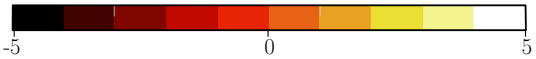

FIGURE 5.8: Flow visualisation of jet simulations: x-y slices of vorticity $\omega_x^* = \omega_x H/U_0$.

TABLE 5.2: Turbulence statistics extracted from jet simulations at $(x/H, y/H, z/H) = (-0.15, 0, 0.05)$, corresponding to experiment hot-wire probe location.

	$\overline{u}/U_0$	$\mathcal{I}_x/\%$	$\mathcal{L}_x/m$
exp.	0.97	2.3	0.0087
SVM	0.97	2.8	0.0089
FSM	1.00	2.3	0.0164

$\mathcal{I}^2$ to decay according to Equation 5.7; the influence of the jet in the present scenario should increase $\mathcal{I}$ downstream however, as the shear layers spread and turbulence mixing increases.

Streamwise decay is observed in both numerical cases. However $\mathcal{I}_x$ begins to increase

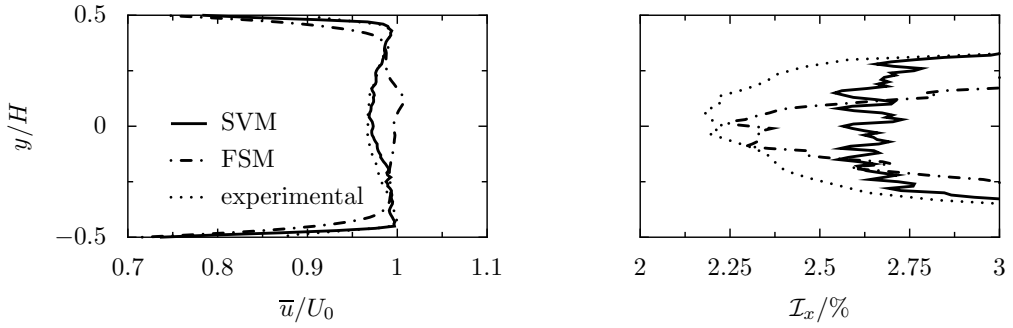

(a) Streamwise mean velocity.

(b) Streamwise turbulence intensity.

FIGURE 5.9: Velocity profiles in the jet, sampled across the height of the jet centreline, at $x = -0.15m$.

further upstream in the SVM case than for the FSM. This explains the over-prediction of turbulence intensity at the measurement location seen in Figure 5.10(a). The SVM case produces y and z components $\approx 10\%$ lower than x at the measurement location (vertical dashed line), although $\mathcal{I}_y$ is initially slightly higher than $\mathcal{I}_x$. This agrees with the inlet statistics specified. The x and y profiles in the FSM case (Figure 5.10(b)) show some clear differences to the SVM. The streamwise turbulence intensity is much lower than the prescribed value close to the inlet; the profile then increases towards the desired value at the measurement location, but does not exceed $\mathcal{I}_z$ until after this point. $\mathcal{I}_y$ decays rapidly close to the inflow plane, and remains at only $\approx 66\%$ of the desired value upstream of the measurement location.

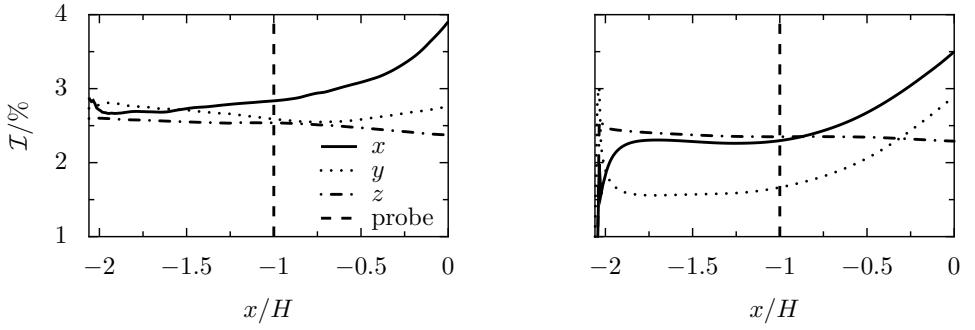

(a) SVM

(b) FSM

FIGURE 5.10: Development of turbulence intensity along the jet centreline. Data sampled at $(y/H, z/H) = (0, 0.05)$. Each turbulence intensity component normalised by U_0. Location of hot-wire probe (experimental measurement point) denoted by vertical dashed line.

The streamwise velocity spectra estimated from both cases are now compared to the experimental and analytical data previously presented in Figure 5.5. Figure 5.11(a) reveals a dissimilar spectral shape between the two numerical cases, particularly at higher frequencies. The SVM case agrees well with the experimental data up to the cutoff frequency of the Fourier transform. The FSM spectrum falls off faster than expected, from approximately 500 Hz. This suggests a spectrum of higher integral length, as

observed previously (Table 5.2). Figure 5.11(b) shows both the original Von Kármán spectrum, and a new fit based on the data in Table 5.2. This new fit (VK2) agrees with the numerical result up to $\approx 1500\ Hz$. However the FSM spectrum still falls off more quickly; this is likely to have been caused by the anisotropy of the turbulence intensities, meaning the velocity field cannot be modelled using the Von Kármán spectrum. It is suggested therefore that the fluctuations generated by the FSM are weakly correlated, leading to incorrect streamwise evolution of the Reynolds stresses. The accurate results obtained from the SVM are partially attributed to the explicit use of a velocity spectrum in the code, which does not exist for the FSM.

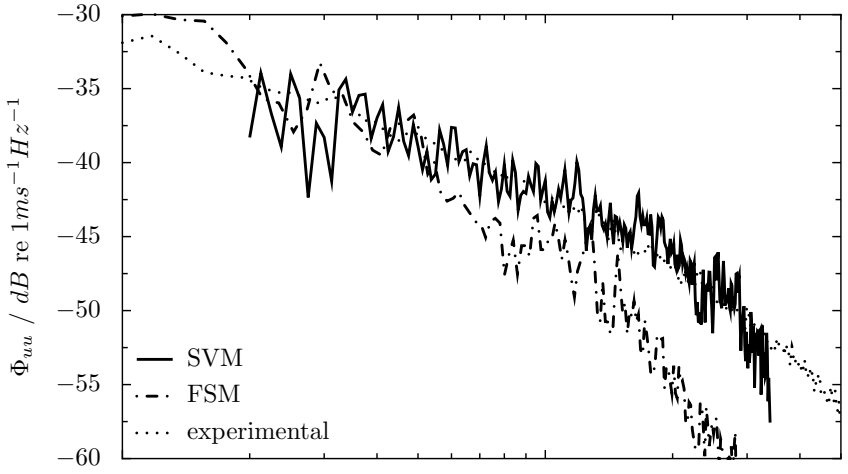

(a) Comparison between numerical and experimental data.

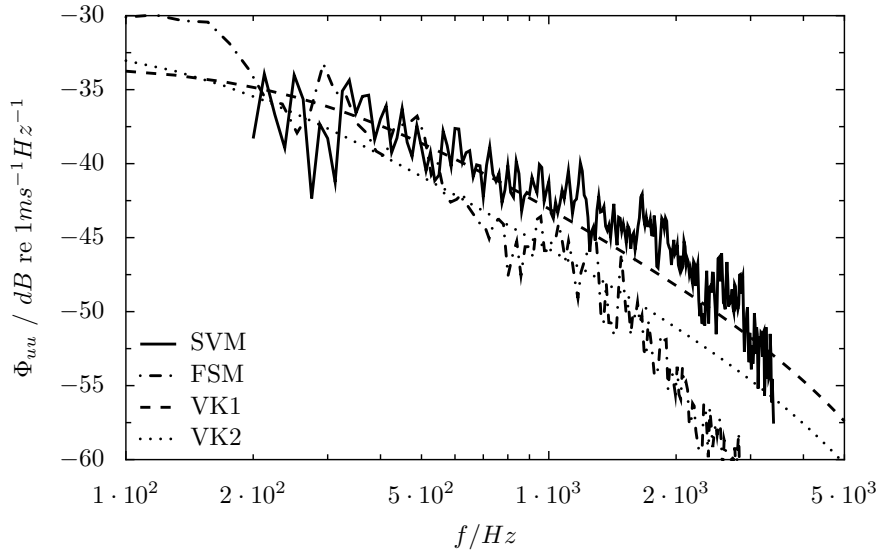

(b) Von Kármán spectra fits: VK1 - as in Figure 5.5(b); VK2 - $\mathcal{L} = 0.0164m$, $\mathcal{I} = 2.3\%$.

FIGURE 5.11: Streamwise velocity spectra in the jet using inflow turbulence generators. Bandwidth Δf is 12.5 Hz.

It may be concluded from this analysis that the SVM is superior in terms of producing the correct turbulence statistics and spectra. This makes it the preferred method for

predicting homogeneous isotropic turbulence. The deficiencies of the FSM are not grid-related; the virtual and physical grids were configured to have the same number of faces, and hence the interpolation from virtual to physical grid should not affect the turbulence generated.

It is expected that some additional error was introduced due to the estimation procedure used to specify the turbulence intensity at the inflow plane. This was due to the location of the grid in the experiments being estimated. The measured turbulence may also have been slightly more isotropic than that modelled, since the grid has placed inside the contraction of the nozzle; this cannot be confirmed due to the lack of measurement data.

The following section compares the two methods' abilities to replicate inhomogeneous anisotropic turbulence. Validation of the FSM has previously been presented by the developers of the method in Kim *et al.* (2013).

5.5 Inhomogeneous anisotropic turbulence: channel flow

The channel flow case provides a canonical flow with a large amount of published data to compare against. It has already been used to evaluate subgrid models (Section 3.6.2) and numerical schemes (Section 4.3.2). The case used here is that of Moser *et al.* (1999), at $Re_\tau = u_\tau \delta / \nu = 395$, who provide a DNS database of velocity and stress profiles. Results are also compared to a cyclic channel case, which was used to extract the stress profiles used in the inflow generators.

5.5.1 Numerical setup

Simulations consist of two walls, separated by $H = L_y = 2\ m$, with cyclic sides. The channel length and width are 64 m and 3.2 m respectively. Streamwise, wall-normal and spanwise grid spacings are $\Delta x^+ \approx 47$, $\Delta y_w^+ \approx 0.5$ and $\Delta z^+ \approx 23$, constituting a well-resolved LES. Mid-way between the walls, the wall-normal spacing is approximately equal to the spanwise spacing. This results in a total of 1.8×10^6 grid cells.

In the cyclic channel case, the *channelFoam* solver is used. This imposes a body force during each time step, to correct the streamwise pressure gradient based on the required Re_τ. The strength of the body force is determined using

$$\frac{dp}{dx} = \frac{\tau_w}{H}. \tag{5.9}$$

A non-dimensional time step of $u_\tau \Delta t / H \approx 1 \times 10^{-3}$ is used, which corresponds to a Courant number of approximately 0.6. In all cases, the flow is allowed to develop for

$u_\tau \Delta t/H \approx 10$, or 5 flow-throughs of the domain, after which statistical quantities are recorded over a further $u_\tau \Delta t/H \approx 30$. These data are then collapsed across the spanwise direction to produce velocity and Reynolds stress profiles. As well as the inflow data, the cyclic case provides an instantaneous flow field from which to initialise the inflow generator cases. Table 5.3 summarises the cases using the inflow turbulence generators. A further case (SVM1) was also simulated, but is not reported; SVM1 used homogeneous turbulence statistics at the inlet, and therefore realistic turbulence did not develop. In all cases the mean velocity profile is also specified.

TABLE 5.3: Summary of channel flow simulations: specified inflow turbulence profiles.

case	integral length scales		Reynolds stresses	
FSM	homogeneous	anisotropic	inhomogeneous	anisotropic
SVM2	homogeneous	isotropic	inhomogeneous	anisotropic
SVM3	inhomogeneous	isotropic	inhomogeneous	anisotropic

A major consideration in the choice of cases simulated is an assessment of the divergence of the generated velocity field, and the effect this has on pressure fluctuations at the inlet. As noted by Xie and Castro (2008), this analysis is not widely presented in the literature, and it remains an important issue for computational acoustics. It is known that inhomogeneity of prescribed turbulence statistics will increase divergence for the SVM (Kornev and Hassel, 2007). By contrast the FSM has been formulated to avoid this problem. Since velocity fluctuations are added during the first inner loop of the solver, they are conditioned to satisfy continuity prior to being added to the solution (see Sections 4.4.1 and 5.3.2). Kim *et al.* (2013) showed that this procedure does not have a large effect on the generated velocities, but minimises induce pressure fluctuations within the domain. Hence varying degrees of inhomogeneity have been introduced for the SVM. However, the integral length scale remains isotropic, in contrast to the FSM method. When integral length scales are required by the SVM, they are estimated from the mean velocity profile of the cyclic channel simulation. Since Kim *et al.* (2013) recommend $\mathcal{L}_x = 1\ m$ at the channel centreline, the derived profile has been adjusted to fit this stipulation, as depicted in Figure 5.12.

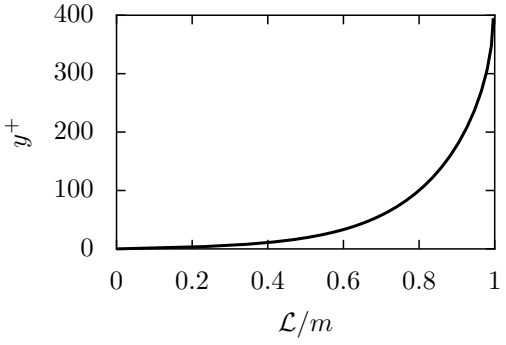

FIGURE 5.12: Integral length scale distribution derived from RANS simulation of cyclic channel flow at $Re_\tau = 395$. Note that $y^+ = 395$ corresponds to δ or $H/2$.

For the inhomogeneous case (SVM3), the length scale profile used is depicted in Figure 5.12. The other SVM cases used $\mathcal{L} = 1.0\ m$. A full distribution of stresses extracted

from the cyclic channel flow simulation with dynamic Smagorinsky subgrid model is also used (see Figure 3.6).

5.5.2 Results and discussion

The following discussion concerns results obtained from the four cases described in Table 5.3. Figures 5.13 and 5.14 show wall-normal slices of the streamwise vorticity ω_x at $y^+ = 395$ (the mid-plane) and $y^+ = 15$ (the approximate location of the peak turbulence production). The visualisations have been truncated to the front half of the channel in order to focus on the initial stages of turbulence development within the channel.

The snapshots appear quite similar at $y^+ = 395$, where large scale unsteadiness dominates. For the FSM, long streamwise structures are observed, as was the case in Section 5.4. In the SVM2 case, turbulence production added by the inhomogeneous Reynolds stress profiles increases the shear velocities and encourages transition. Case SVM3 shows the finest turbulence structure close to the inlet, and the fastest development length. These observations will be corroborated later by examining Reynolds stress profiles, but Figure 5.13 suggests that the length scale profile is important for the turbulence development. This intuitively makes sense, since the length scales represent spatial velocity correlations *i.e.* the prescribed inlet turbulence contains more realistic second-order statistics.

Similar conclusions may be made from the slices at $y^+ = 15$ shown in Figure 5.14. The Reynolds stress profiles are seen to be key to near-wall turbulence development, since they add the high levels of production needed inside the inner layer (SVM2). The homogeneous length scale profile used in SVM2 generates large structures close to the wall; these are non-physical, and are not sustained on the grid. Transition occurs close to the inlet in this case, but turbulence is not fully developed until $x/L_x \approx 0.25$. Turbulence develops fastest for SVM3; despite the inhomogeneous length scale profile used for FSM, turbulence develops much later. At $x/L_x = 0.5$, FSM, SVM2 and SVM3 are qualitatively comparable in the sense that turbulence appears fully developed.

Figure 5.16 shows that the FSM is the most accurate in terms of streamwise Reynolds stress at $x/L_x = 0.05$. SVM3 is the best of the two SVM cases. The large near-wall length scales added in SVM2 cause $\overline{u'u'}$ to be over-predicted throughout the boundary layer. This effect persists until $x/L_x = 0.75$, at which point all the profiles agree well with the DNS data.

Figure 5.17 shows the $\overline{u'v'}$ distribution. The FSM shows the best profile shape compared to the DNS data, although the magnitude is significantly under-predicted. This explains the late development of turbulence seen in Figure 5.14. Turbulence production may be written as

$$\mathcal{P}_{TKE} = -\overline{u'v'}\frac{\partial u}{\partial y}, \tag{5.10}$$

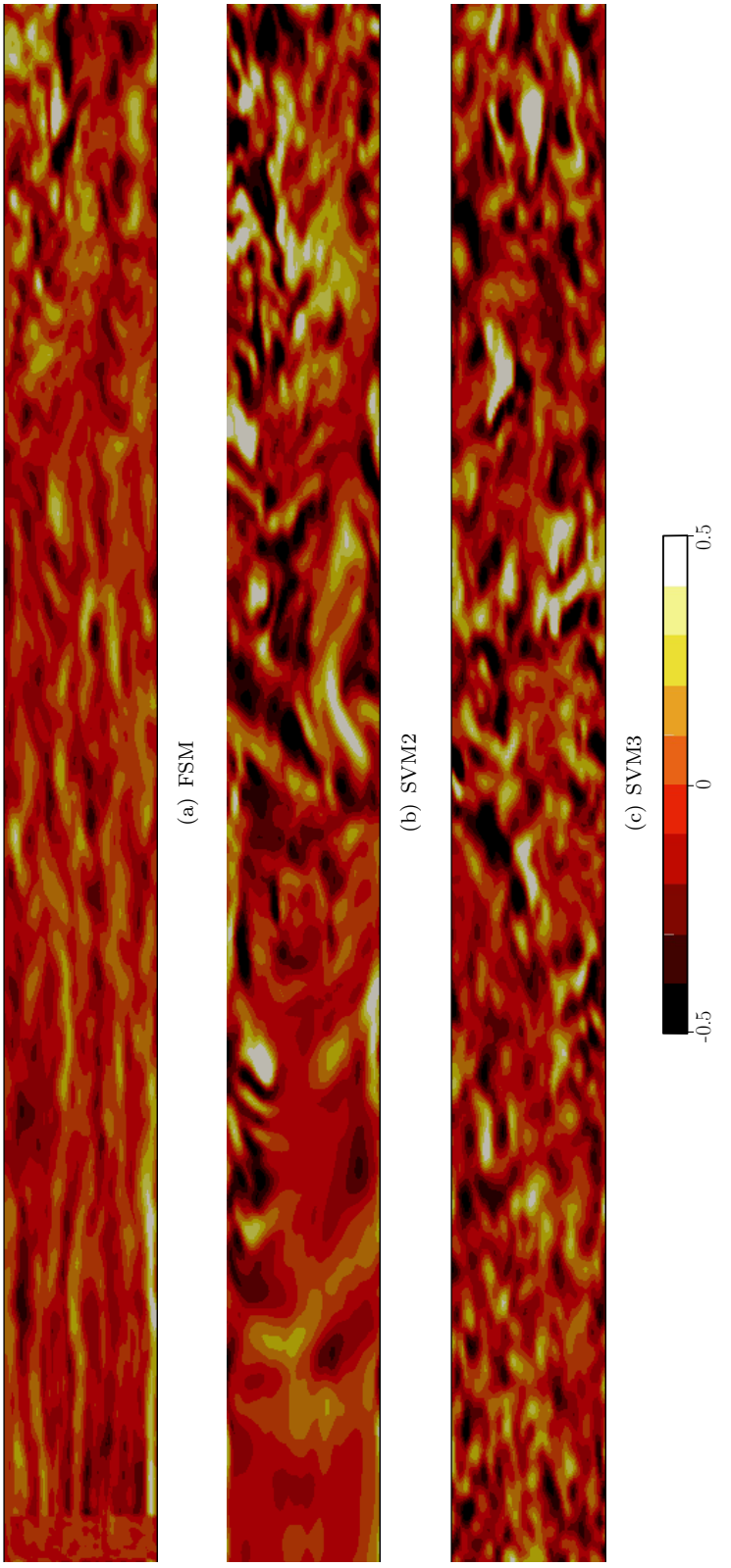

FIGURE 5.13: Wall-parallel ($x-z$ plane) non-dimensionalised streamwise vorticity $\omega_x^* = \omega_x \delta / U_b$ at $y^+ = 395$ in front half of channel. Inlet on left at $x/L_x = 0$.

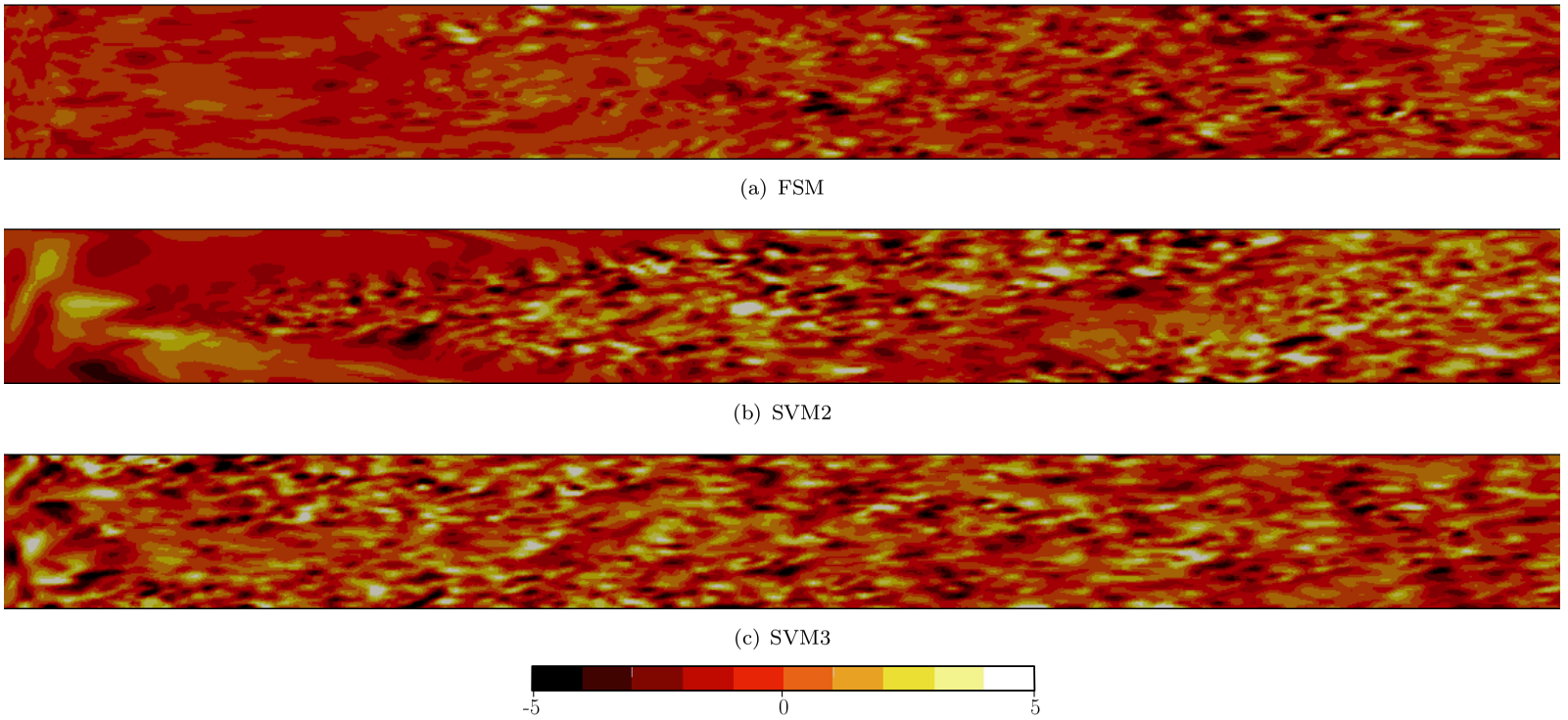

FIGURE 5.14: Wall-parallel ($x - z$ plane) non-dimensionalised streamwise vorticity $\omega_x^* = \omega_x \delta / U_b$ at $y^+ = 15$ in front half of channel domain. Inlet on left at $x/L_x = 0$.

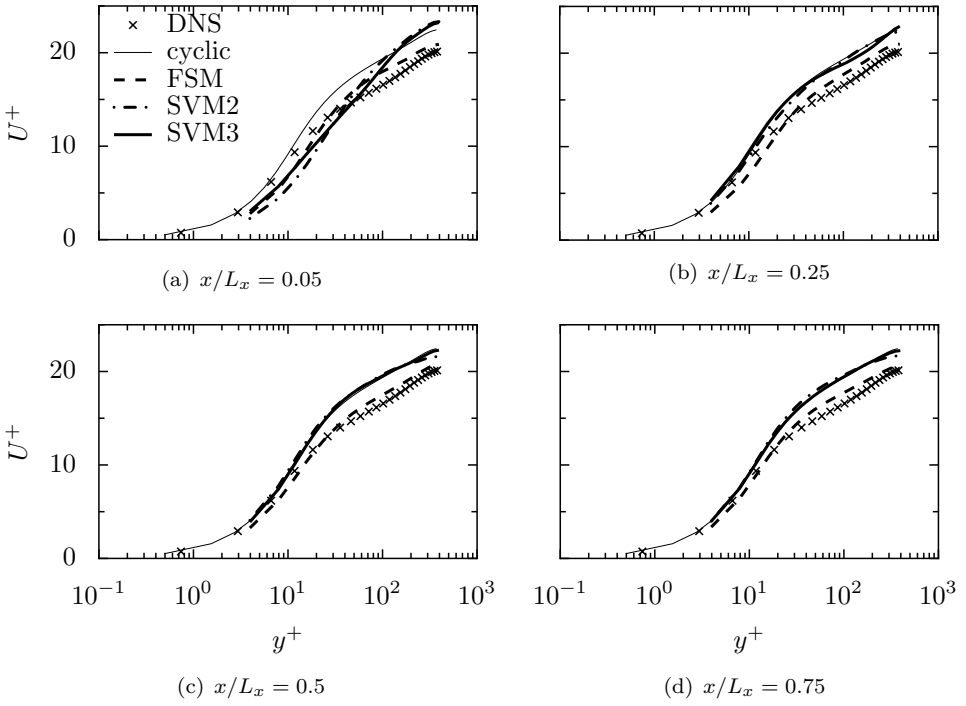

FIGURE 5.15: Normalised mean velocity profiles for channel flow using inflow generators.

meaning that correctly predicting shear stress is important for turbulence to develop. When the magnitude of $\overline{u'v'}$ is higher, transition occurs further upstream in the channel, as seen for SVM2 and SVM3. This is due to the faster development of $\overline{v'v'}$, as seen in Figure 5.18. Since

$$\mathcal{P}_{uv} = \overline{v'v'}\frac{\partial u}{\partial y}, \tag{5.11}$$

an under-prediction of wall-normal Reynolds stress will lead to reduced shear production and slower transition. Both $\overline{u'v'}$ and $\overline{w'w'}$ are initially over-predicted by SVM2 and SVM3; this promotes turbulence production but does not accelerate the development of the correct stress profiles. The FSM again provides very small $\overline{v'v'}$ at $x/L_x = 0.05$; the profile shape is however much improved at $x/L_x = 0.25$ and shows excellent agreement with DNS at $x/L_x = 0.5$. The results for $\overline{w'w'}$ are similar. Figure 5.19 shows that the FSM gives the closest agreement to, and fastest attainment of, the correct spanwise stress distribution.

The development of the streamwise integral length scale is also used as a measure of the ITGs' ability to replicate the prescribed inflow conditions. Table 5.4 shows values of $\mathcal{L}_x$ evaluated at the same streamwise locations used in Figures 5.15-5.19. The desired value at the channel centreline is 1.0 m. In relation to the desired value, SVM3 gives the closest prediction of $\mathcal{L}_x$. The value is slightly over-predicted, but to a lesser extent than for FSM. In the case where no length scale profile is specified (SVM2), the value is

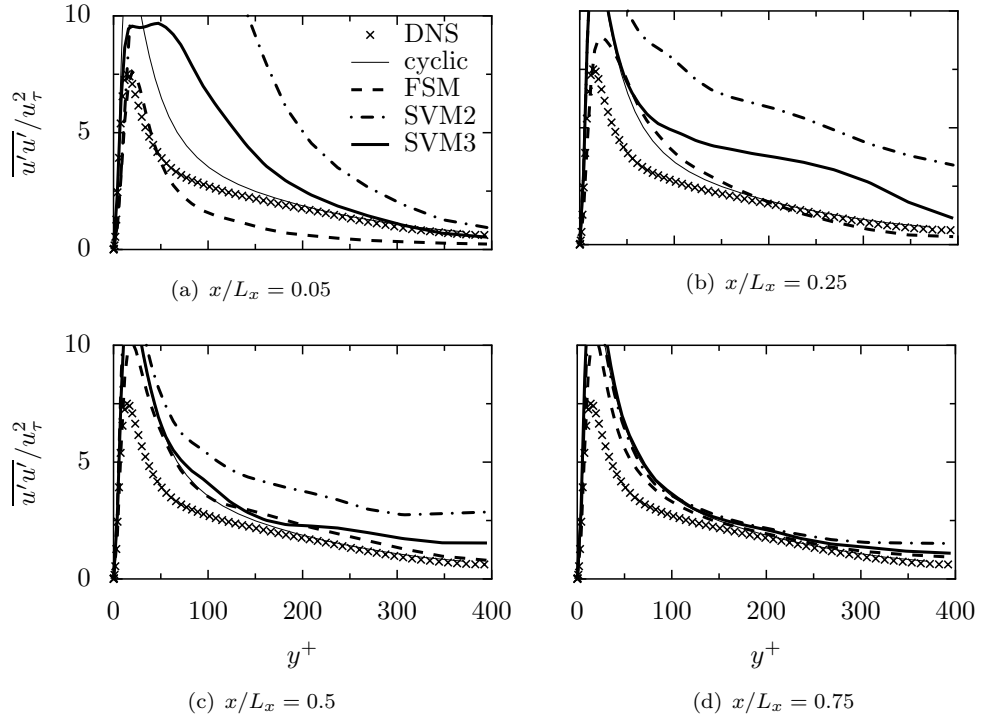

(a) $x/L_x = 0.05$ (b) $x/L_x = 0.25$

(c) $x/L_x = 0.5$ (d) $x/L_x = 0.75$

FIGURE 5.16: Normalised $\overline{u'u'}$ Reynolds stress profiles for channel flow, using inflow generators.

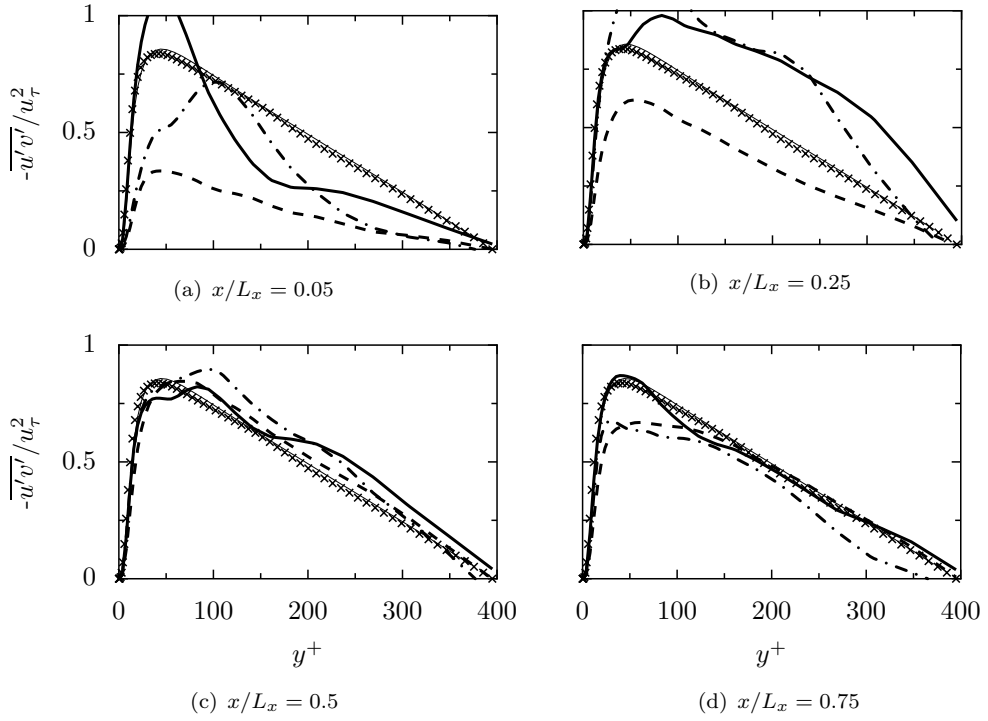

(a) $x/L_x = 0.05$ (b) $x/L_x = 0.25$

(c) $x/L_x = 0.5$ (d) $x/L_x = 0.75$

FIGURE 5.17: Normalised $\overline{u'v'}$ Reynolds stress profiles for channel flow using inflow generators. Legend as in Figure 5.16.

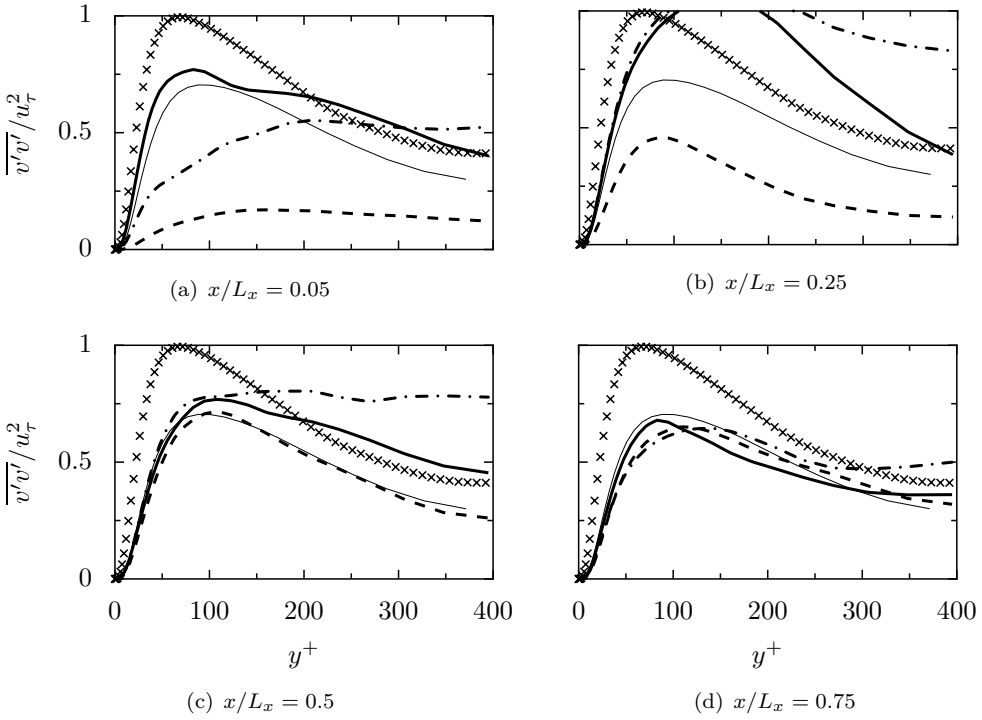

(a) $x/L_x = 0.05$ (b) $x/L_x = 0.25$

(c) $x/L_x = 0.5$ (d) $x/L_x = 0.75$

FIGURE 5.18: Normalised $\overline{v'v'}$ Reynolds stress profiles for channel flow, using inflow generators. Legend as in Figure 5.19.

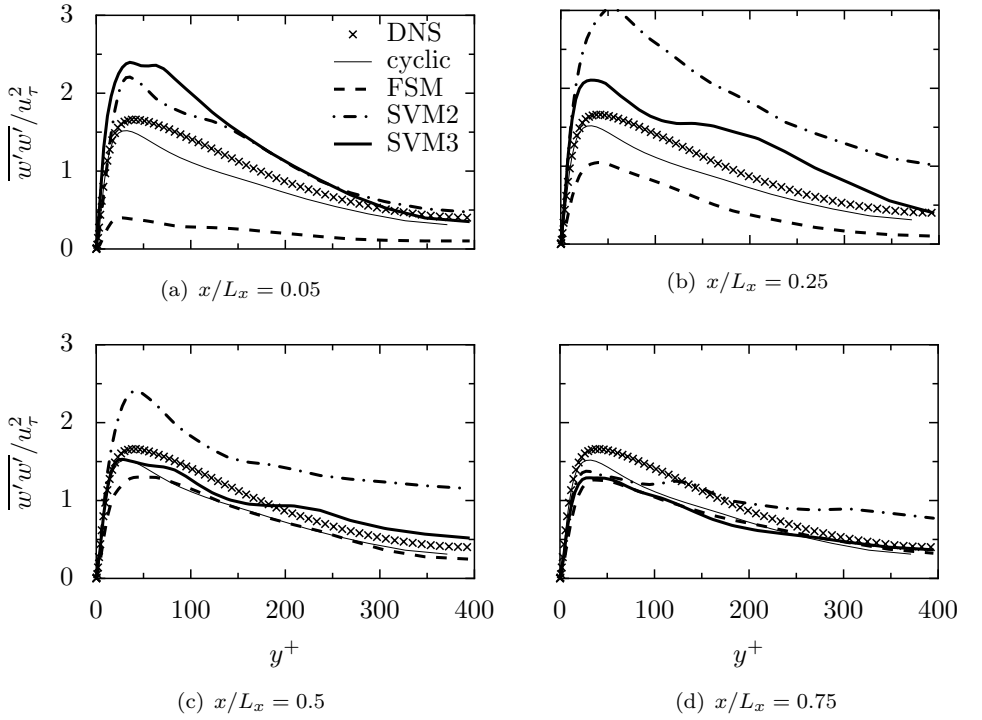

(a) $x/L_x = 0.05$ (b) $x/L_x = 0.25$

(c) $x/L_x = 0.5$ (d) $x/L_x = 0.75$

FIGURE 5.19: Normalised $\overline{w'w'}$ Reynolds stress profiles for channel flow, using inflow generators.

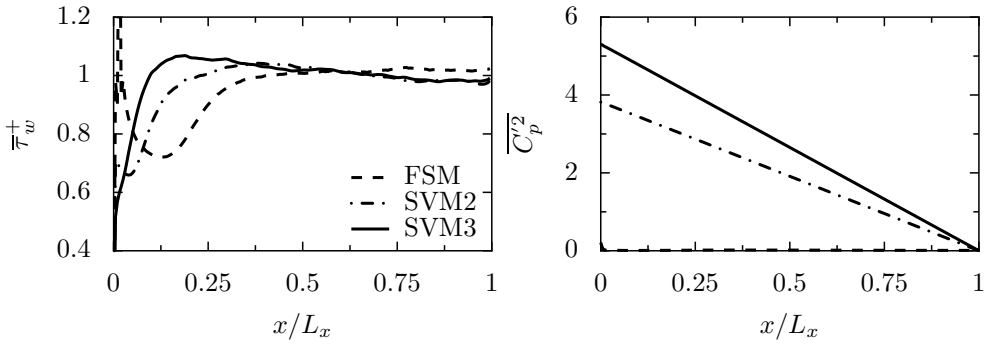

(a) Normalised wall shear stress

(b) *rms* pressure fluctuation

FIGURE 5.20: Streamwise development of channel wall shear stress and pressure fluctuations.

initially over-predicted, and decays in the streamwise direction; the length scale eventually undershoots the desired value. This again highlights the importance of specifying a length scale profile in order to promote turbulence development.

TABLE 5.4: Integral length scales at four streamwise probe locations on channel centreline, estimated using Taylor's hypothesis.

x/L_x	FSM	SVM2	SVM3
0.05	0.84	2.61	0.89
0.25	0.96	1.51	1.05
0.5	1.27	1.00	1.06
0.75	1.31	0.71	1.11

A further measure of correct turbulence development is the wall shear stress, since it is determined from the velocity gradient, and hence indicates how well near-wall turbulence has developed. Case SVM3 overshoots the desired value at $x/L_x = 0.1$, but does slowly recover to give a good prediction at the outlet; SVM2 attains a similar value with less overshoot. The FSM case takes longer to reach the correct value, but never overshoots; this is due to the later development of the correct stress profiles, as seen in Figure 5.14. This delay has been highlighted as an effect of the divergence-free implementation of the method, as mentioned in Section 5.2, and by Kim *et al.* (2013).

Figure 5.20(b) shows the centreline decay of the *rms* pressure induced at the domain inlet. This is a key consideration in assessing the effect of divergence on the flow solution. As expected, the FSM produces minimal pressure fluctuations. The SVM cases show a trend of increasing pressure unsteadiness as inhomogeneity is added. The inclusion of Reynolds stress profiles is seen to have the largest effect. This has significant implications for the use of the SVM when surface pressures and forces on bodies must be calculated.

Finally, velocity and pressure spectra at two of the streamwise probe locations are compared in Figure 5.21. In terms of velocity spectra, similar results are seen to those

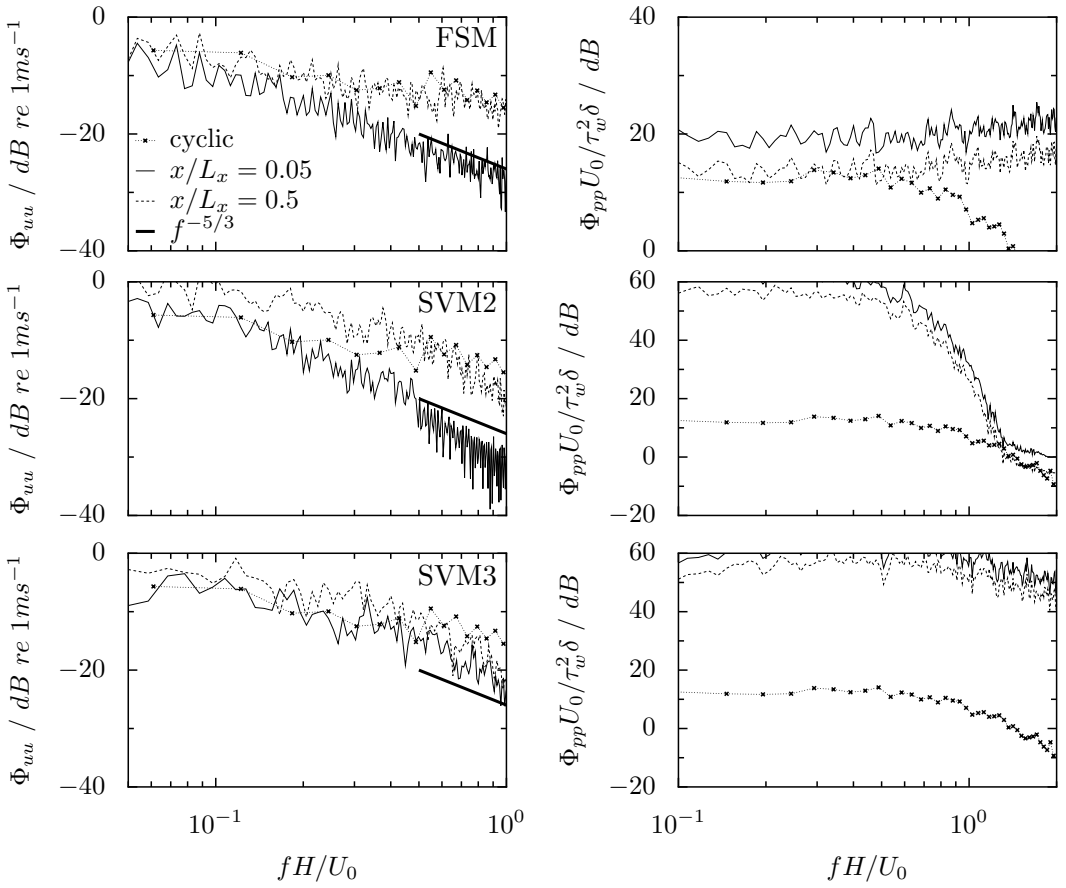

(a) velocity (b) pressure

FIGURE 5.21: Scaled spectra at two streamwise probe locations on channel centreline: (a) velocity; (b) pressure. Dissipation range power-law decay indicated with thick solid line.

discussed in Section 5.4. The SVM gives a better characteristic spectrum shape than the FSM; in this case, the FSM results do not show a clear inertial subrange fall-off at $x/L_x = 0.05$. A close agreement with the cyclic case is seen at $x/L_x = 0.5$ however. Both SVM cases however show the expected decay slope, most clearly seen for SVM2 and SVM3. The main difference between the SVM cases is the change in spectral level between the two probe locations for SVM2. This is due to the large reduction in $\mathcal{L}_x$ between the two locations (see Table 5.4), which shifts energy to higher frequencies. SVM3 shows the best agreement with the cyclic channel at $x/L_x = 0.05$. This is further evidence that the FSM requires a longer development distance than the SVM.

The pressure spectra also reveal some interesting differences between the cases. The FSM appears to provide no noticeable spectral shape. The spectral level is however noted to be typically 40 dB lower than the SVM cases. This is due to the elimination of pressure fluctuations induced at the inlet, as described previously. For the SVM cases, the addition of inhomogeneous inflow profiles increases the spectral level. Again, the large length scales of SVM2 appear to shift the spectrum to lower frequencies, resulting

in a sharper fall-off than SVM3. The highest pressure amplitude is seen for SVM3, which follows from Figure 5.20(b). The level also does not fall-off by more than 10 dB across the entire spectrum. Figures 5.20(b) and 5.21 also reveal that the SVM is not fully divergence-free for homogeneous isotropic turbulence. The effect of this will be discussed further in the next chapter.

5.6 Summary

Investigations have been presented, using two test cases, of the performance of two inflow turbulence generators. The synthetic vorton method is based on using 'engineering' estimates of the inflow quantities. This method has been shown to provide better turbulence statistics than the forward stepwise method, when simulating homogeneous isotropic turbulence.

However, one of the key attractions of such techniques is being able to generate boundary layer inflows, which are both anisotropic and inhomogeneous. This was evaluated using turbulent channel flow. It was found that the prescribed inflow statistics have a significant effect on the streamwise development distance of realistic turbulence. In general, the FSM performed best in this case, matching DNS data well within $\approx 30\delta$. This still constitutes a large development length however compared to the recycle methods outlined in Section 5.2. Inhomogeneous profiles included in the SVM cases did accelerate turbulence development (although stress profiles were largely over-predicted in these cases), but at the expense of divergence-free fluctuations. These induce large pressure fluctuations at the domain inlet, increasing the pressure spectra amplitude by up to 40 dB. This makes the SVM unsuitable for simulations where unsteady forces and acoustic sources must be predicted.

In subsequent results chapters, both the SVM and FSM will be used. In Chapters 6 and 7, both methods are again compared when simulating the noise generated from a stationary foil in a turbulent jet; the same case as used in Section 5.4. In Chapter 8, the FSM is used to model a tidal turbine located in a turbulent tidal channel.

6

Simulation of Homogeneous Inflow Turbulence Noise

6.1 Introduction

The numerical methods outlined in the previous three chapters are now applied to an aeroacoustics test case. This allows assessment of the performance of the inflow turbulence generators in terms of predicting acoustic sources and far-field sound. Before simulating a full tidal turbine geometry, a simplified case is considered: a stationary foil in a turbulent jet. This has been chosen since detailed experimental measurement data is available for validation. In addition, some of the complexity of simulating a tidal turbine, such as rotation and spanwise blade shape variation, is omitted. Although the chosen test case consists of measurements made in air, the Mach number is low ($M \approx 0.06$) meaning the conclusions should be applicable in hydroacoustics applications.

Evaluations of both the synthetic vorton method (SVM) and forward stepwise method (FSM) are presented; this was conducted since both methods were shown to exhibit deficiencies in Chapter 5. The FSM did not replicate the homogeneous isotropic turbulence (HIT) statistics as well as the SVM, tending to over-estimate the streamwise integral length scale. On the other hand, the SVM, which was expected to be divergence-free for homogeneous isotropic turbulence, was found to induce pressure fluctuations at the inlet (observed for SVM1 case; not reported). Although not as severe as those seen for inhomogeneous turbulence, these will affect the prediction of acoustic sources.

6.2 Amiet's inflow turbulence model

In this, and the subsequent chapter, comparisons are made to an analytical model for inflow turbulence noise. Amiet's model (Amiet, 1975) is arguably the most widely used of such models, and has been compared to the experimental data referred to here by Gruber (2012). The model is derived based on thin aerofoil theory, and has inputs consisting of geometric parameters, turbulence spectrum and an aerofoil loading function. Amiet (1975) assumed that a frequency component of the pressure jump on an infinite span aerofoil (tip effects ignored) is produced by a gust of chordwise wavenumber K_x, and showed that the infinite span assumption is valid for $K_x s > 5$, where s is the aerofoil span. It may also be shown that, for a receiver located at midspan ($z = 0$), skewed gusts (gusts possessing a non-zero spanwise wavenumber) do not contribute to the far-field sound, that is $\kappa_z = \kappa z/|\boldsymbol{r}| = 0$. This assumption is used here, meaning the far-field noise spectrum predicted by the model may be written as

$$\Phi_{pp}(\boldsymbol{x},\omega) \approx \left(\frac{\rho_0 \omega y c}{2c_0|\boldsymbol{r}|}\right)^2 \pi U_0 \frac{s}{2} \Phi_{vv}(K_x,0)|\mathscr{L}(x,K_x,0)|^2, \tag{6.1}$$

where Φ_{vv} is a turbulence spectrum for the upwash velocity, $\mathscr{L}$ is an aerofoil loading function and $K_x = -\omega/U_0$. In order to account for the spanwise correlation of the inflow turbulence, Equation 6.1 can be modified to include the spanwise correlation length, previously defined in Equation 3.11, such that

$$\Phi_{pp}(x,y,0,\omega) \approx \left(\frac{\rho_0 \omega y c M}{2|\boldsymbol{r}|}\right)^2 \frac{s}{2} \mathscr{S}_{vv}(\omega) \ell_z(\omega) |\mathscr{L}(x,K_x,0)|^2, \tag{6.2}$$

where $\mathscr{S}_{vv}(\omega)$ and $l_z(\omega)$ are the modified turbulence spectrum of the upwash velocity and the spanwise correlation length scale respectively. Here, the von Kármán model is used for the upwash spectrum, resulting in

$$\mathscr{S}_{vv}(\omega) = \frac{\mathcal{L}\overline{u'^2}}{6\pi U_0} \frac{3 + 8\hat{\kappa}_x^2}{(1+\hat{\kappa}_x^2)^{11/6}} \tag{6.3}$$

where the *carets* denote normalised wavenumbers (as in Section 3.6.1). Hence, the noise due to inflow turbulence is expected to scale with $\mathcal{L}$ and $\overline{u'^2}$ based on Equation 6.3. A complete formulation of the model used in this work is provided by Roger and Moreau (2010), including representations of $\mathscr{L}$.

One of the shortcomings of Amiet's model is the lack of explicit thickness correction, that is, foil geometry effects are not taken into account. The importance of including a thickness correction has been highlighted by numerous authors (Mish and Devenport, 2006*a*,*b*; Moreau *et al.*, 2005; Roger and Moreau, 2010). Both Moreau *et al.* (2005) and Mish and Devenport (2006*b*) proposed modifications to the theory which are seen to be necessary for moderately thick foils (these authors used NACA 0012 and 0015 profiles). These are based on rapid distortion theory (Batchelor and Proudman, 1954;

Hunt, 1973), which can be used to account for the effect of mean flow distortion on the inflow turbulence, due to the foil leading edge. It is this phenomenon that reduces the isotropy of grid-generated inflow turbulence. An advantage of the numerical approach is expected to be implicit inclusion of all mean flow distortion (and other foil geometry) effects on the flow solution and surface pressure prediction.

6.3 Simulation details

6.3.1 Test case description

In order to validate the numerical approach, a test case was chosen involving homogeneous isotropic turbulence impinging onto a stationary rigid aerofoil. This experiment is documented by Gruber (2012) and Clair *et al.* (2013), and has been used as validation for several numerical studies (Clair *et al.*, 2013; Deniau *et al.*, 2011; Dieste, 2011). The same case was used in Section 5.4 to evaluate the inflow turbulence generators (ITGs). Experiments were carried out by Gruber (2012) in the *DARP* facility at the University of Southampton. As well as the measurements described in Section 5.4, noise measurements made using a microphone array mounted at $|\boldsymbol{r}| = 1\ m$ from the aerofoil trailing edge. A schematic of the coordinate system is presented in Figure 6.1. The trailing edge noise is lower than the inflow turbulence noise up to 10 kHz.

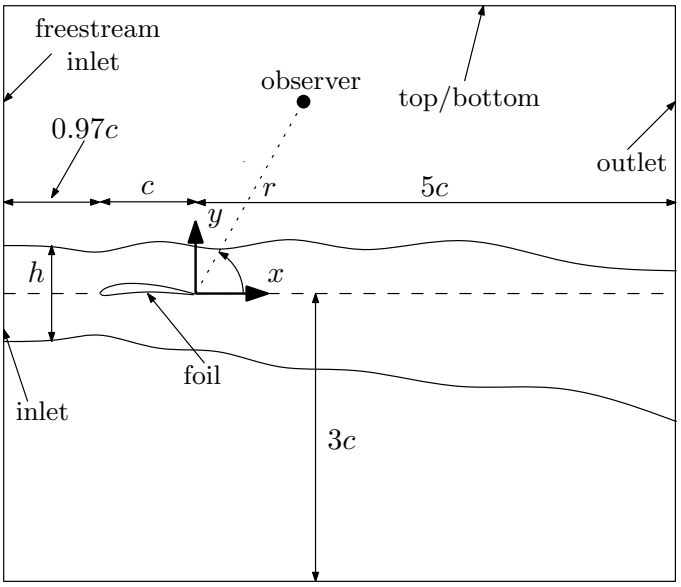

FIGURE 6.1: Foil noise coordinate system and simulation domain layout. Summary of boundary conditions: inlet - FV/ITG; freestream inlet - FV; outlet - mixed ZG/FV; foil - slip; top/bottom - symmetry; sides - cyclic.

Measurements were made of a NACA 65_1210 foil of chord 0.15 m and span 0.45 m, mounted on end plates in the exit stream of the jet. This '6 series' NACA section has minimum pressure at 50% chord (notation in tenths; second digit), a favourable

pressure gradient $+/-0.1$ (denoted by subscript) of the design lift coefficient of 0.2 (notation in tenths; third digit), and a maximum thickness of ten percent (fourth and fifth digits) (Abbott and von Doenhoff, 1959, chap. 6). The foil section profile, along with geometrical definitions, is given in Figure 6.2.

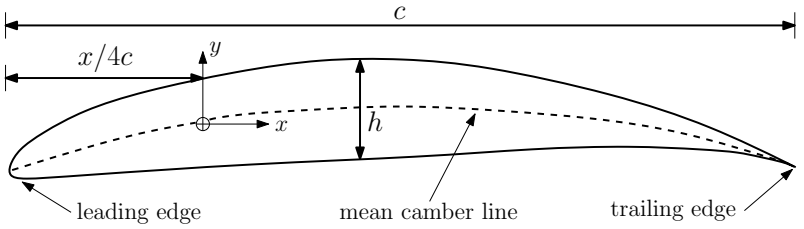

FIGURE 6.2: Definitions relating to foil geometry: c and h and chord and thickness respectively. The section origin is located at the nominal *aerodynamic center*, which is assumed to be a quarter chord behind the leading edge.

Difficulties were experienced when simulating the turbulent boundary layer of the NACA 65_1210 cambered profile (Lloyd *et al.*, 2012, 2013*a*). This was due to a leading edge recirculation bubble on the foil pressure side at zero degrees angle of attack, and the inability to trip the boundary layer to match the experiments. These issues, which caused non-physical trailing edge noise sources, were also experienced by Deniau *et al.* (2011), and remain unresolved. In the case of Deniau *et al.* (2011), an Euler equation solver was used to remove the problem. In this case, the issues are negated by neglecting the effects of viscosity *i.e.* no boundary layer develops. Since a viscous solver is used in the current work, an alternative approach was adopted. Recalling that inflow turbulence noise is independent of the boundary layer flow on the aerofoil, the wall may be treated using a slip boundary condition. This allows non-zero velocity parallel to the wall, and hence the boundary layer is again neglected in the simulations.

6.3.2 Numerical setup

In order to inform the grid design and simulation setup, a survey of parameters from previously cited literature was made. This is presented in Table 6.1. Evidently the grid requirements of the two cited studies are quite different. This is largely due to an order of magnitude difference in the Reynolds number. Both studies satisfy grid resolution criteria for typical LES (see Section 3.6.1), yet Deniau *et al.* (2011) require over six times as many grid cells to achieve this.

Another key difference is in the temporal resolution of the simulations. Christophe (2011) used much larger time step than Deniau *et al.* (2011), again due to the lower Reynolds number. However, Christophe (2011) found that a key parameter affecting the accuracy of the turbulence intensity spatial distribution, as well as spectral amplitudes of the jet turbulence and SPL, was T^*. A case using $T^* = 25$ showed worse agreement with measurement data, especially at high frequencies. In the case of Deniau *et al.* (2011),

the small value of t^* limited the total sampling time, and hence may have influenced the quality of the statistics derived from that simulation. The present simulations benefit in this regard by neglecting to resolve the turbulent boundary layer on the foil.

TABLE 6.1: Summary of inflow turbulence noise studies using large eddy simulation. Non-dimensional time $T^* = TU_0/c$. *Re*: $\times 10^{-5}$; N: $\times 10^{-6}$; t^*: $\times 10^4$.

study	Christophe (2011)	Deniau *et al.* (2011)	present
Re	0.36	6.5	2.2
M	0.04	0.18	0.06
N	2.8	20	1.7
L_z/c	8.8	0.4	0.1
N_z	79	100	64
Δx_w^+	10	-	24
Δy_w^+	< 2	< 2.6	24
Δz_w^+	10	< 40	24
T^*	70	21	67
t^*	8.8	0.53	6.6
t^*_{sample}	0.016	0.011	0.013
Co	0.6	-	1.0

The aerofoil coordinates were generated using the open source tool *javafoil*[1], and checked against coordinate data provided by Abbott and von Doenhoff (1959, chap. 6). A stereolithography file was used to create an unstructured grid using *snappyHexMesh*. An unstructured grid was preferred since it allows grid refinement to be focussed more easily without a large penalty in terms of total grid size (James and Lloyd, 2013).

In order to reduce the total number of cells in the grid, a spanwise strip of $L_z/c = 0.1$ was used. This is the same width as was used in Section 5.4, ensuring that turbulence is incoherent across the domain, based on the arguments made in Section 3.6.1. Deniau *et al.* (2011) used a wider domain width of $L_z/c = 0.4$, but only placed $N_z = 100$ cells across this width. Hence the spanwise grid resolution in the present study is higher than Deniau *et al.* (2011), despite the much smaller total grid size. Views of the grid are provided in Figure 6.3.

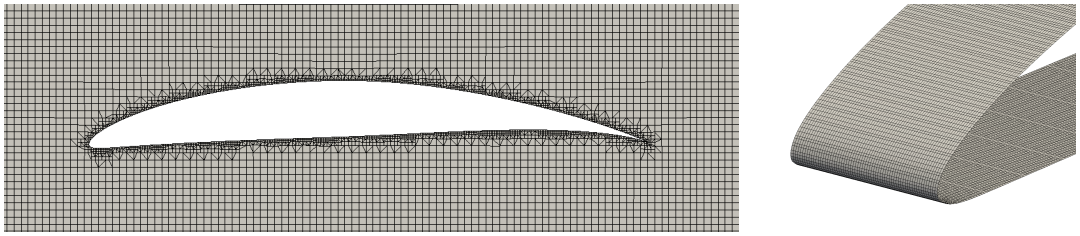

(a) x-y plane slice (b) leading edge

FIGURE 6.3: Views of the NACA65 foil grid.

[1] http://www.mh-aerotools.de/airfoils/javafoil.htm

6.4 Results and discussion

6.4.1 Is modelling the jet necessary?

Removing the jet (as was simulated in Section 5.4.3) provides several simplifications in terms of gridding and solution. These include:

- removing the need to resolve the jet shear layers;
- removing the requirement to initialise the simulation from a RANS solution. The potential flow solver *potentialFoam* was instead found to be suitable for this purpose, reducing overall computational cost.
- avoiding simulation stability issues caused by the jet passing through the domain outlet[2].

Omitting the jet does potentially affect the comparison between measurement and simulation data however. This is due to the fact that the jet is deflected by the presence of the aerofoil (either due to camber or angle of attack), meaning the angle of attack is modified compared to free flow (Brooks *et al.*, 1986, 1989). Hence the *effective* angle of attack, α_e, will be lower than the *geometric* angle of attack, α_g, affecting the mean lift and drag. Brooks *et al.* (1986) provide a method for correcting α_g based on two-dimensional thin aerofoil theory. Although no correction is applied to a symmetric foil at $\alpha_g = 0°$, this is not the case for a cambered foil. Based on this theory, Gruber (2012) estimated α_e for the NACA 65_1210 at $\alpha_g = 0°$. Measured mean lift coefficient compared well to the thin aerofoil theory equation

$$C_L = 2\pi\alpha + C_{L_0}, \tag{6.4}$$

where $\alpha = \alpha_e$ and $C_{L_0} = 0.1$ for the NACA 65_1210. This results in $\alpha_e \approx -1.4°$, meaning a simulation without the jet should account for this angle of attack difference in order to predict the correct lift coefficient. In the case of inflow turbulence however, it has been shown that the resulting noise is independent of angle of attack when $\mathcal{L}/c << 1$ (Hutcheson *et al.*, 2012; Moreau *et al.*, 2005). Thus it is assumed justifiable to simulate the case without the presence of the jet.

In order to remove the effect of the jet, the inlet velocity outside of the jet height is adjusted from $0.1U_0$ to U_0. This is illustrated in Figure 6.4. Hence the same grid may be used for both simulations.

[2]The *convectiveOutlet* condition proved unstable when a large shear velocity profile was present at the outlet. This was due to the requirement to specify a single convection speed U_C across the entire outlet boundary.

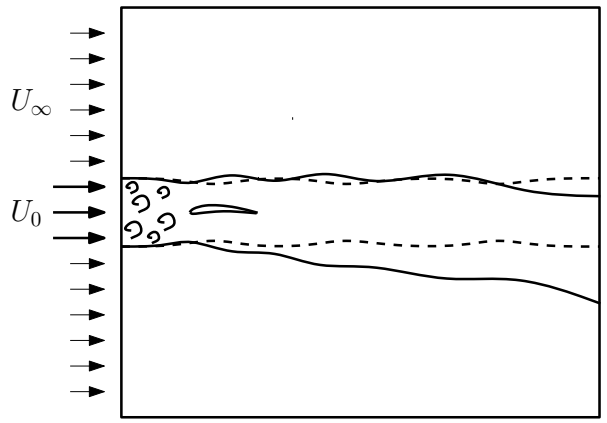

FIGURE 6.4: Schematic illustration of cases with and without jet. The jet velocity $U_0 = 20\ ms^{-1}$ in both cases. The freestream velocity U_∞ is set to $0.1U_0$ when the jet is included (solid line), and U_0 when it is omitted (dashed line).

Figures 6.5 and 6.6 illustrate the differences between the cases with and without the jet, in terms of the normalised upwash velocity fluctuation $v^* = (v - \overline{v})/U_0$, and the associated dynamic pressure coefficient $C_p = (v - \overline{v})^2/U_0^2$. Inflow turbulence has been generated using the synthetic vorton method. The figures show the large velocity and pressure fluctuations present in the jet shear layer. These do in fact interact with the foil. This leads to an increase in sound pressure level (SPL) for reducing frequency in the experimental data presented later in Figure 6.12. Therefore, based on the reasoning already presented, the only effect of omitting the jet would be to reduce the low frequency noise, which is in itself an artifact of the experimental setup and would not manifest in a 'real' scenario.

6.4.2 Comparison of inflow turbulence generators

The flow is further visualised in Figures 6.7 and 6.8. These quantities provide qualitative indications of the unsteady flow field around the foil induced by both ITGs. The qualitative difference between the methods, first highlighted in Section 5.4.3, is again evident. Note that the colur scales of Figures 6.7 and 6.8 have been modified compared to Figures 6.5 and 6.6 in order to highlight the magnitude of the fluctuations generated by the FSM. The main effect observed is the leading edge interaction between the turbulence and foil, as well as the mean flow distortion of the turbulence.

Next, the unsteady lift on the foil is examined, since this generates the acoustic source. Figure 6.9 shows time traces, and derived frequency spectra, for the FSM and SVM cases. A clear difference is observed, with the values of C_L for the FSM (Figure 6.9(a)) scaled by a factor of ten in order to provide easier visualisation. The amplitude of the lift spectrum Φ_{LL} for the FSM case is also small compared to the SVM case. This 'flat' spectrum is similar to that seen for the channel flow pressure spectra in Figure 5.21. The low magnitude of the pressure fluctuations in the inflow turbulence has resulted in similarly small lift fluctuations. This effect also manifests in the surface pressure coefficients, and severely affects the far-field sound prediction. On the other hand, the

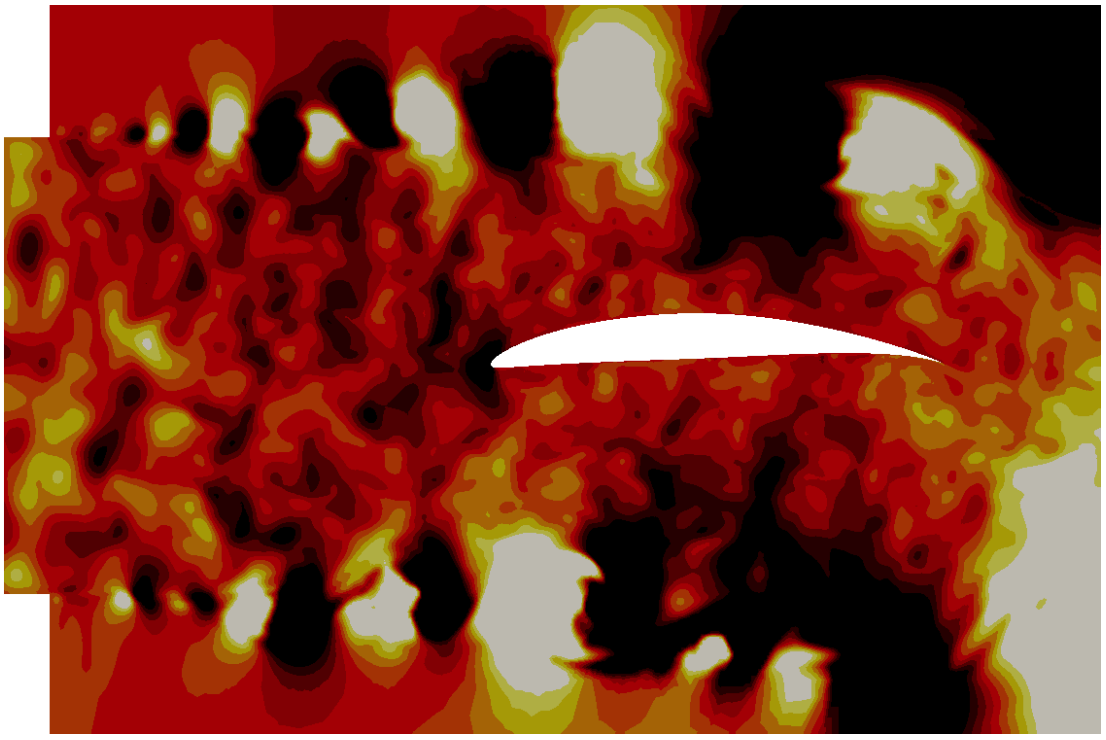

(a) with jet

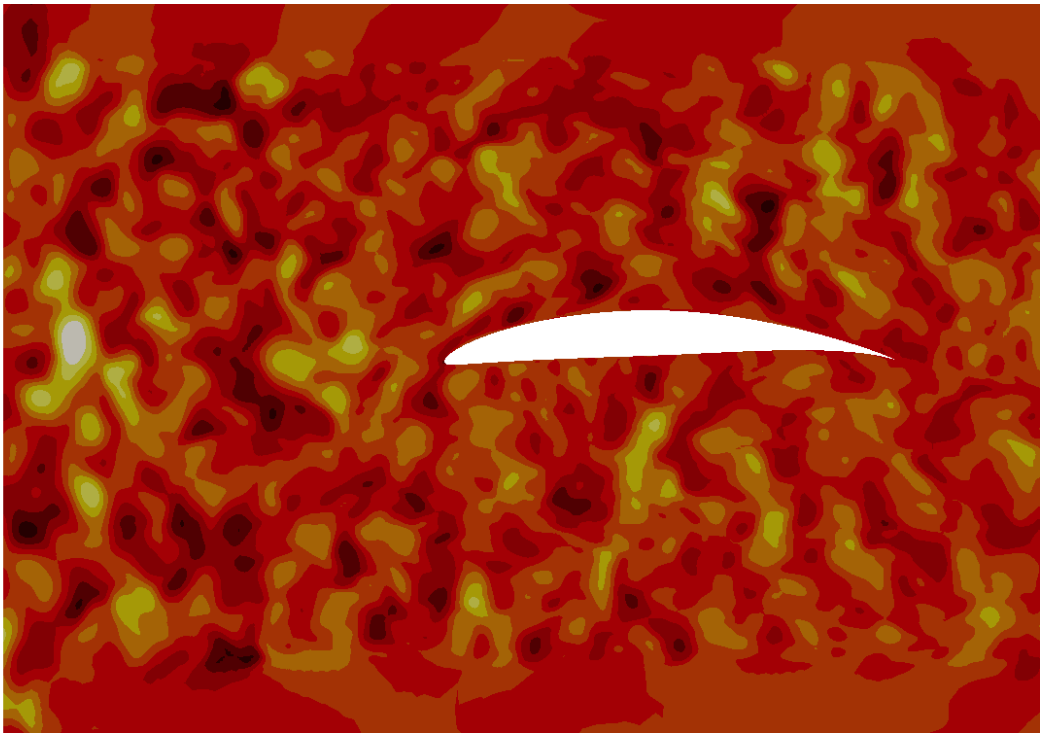

(b) without jet

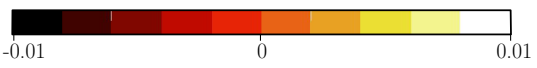

FIGURE 6.5: x-y plane slices of instantaneous upwash velocity around NACA65 foil for cases with and without jet. Inflow turbulence generated by SVM.

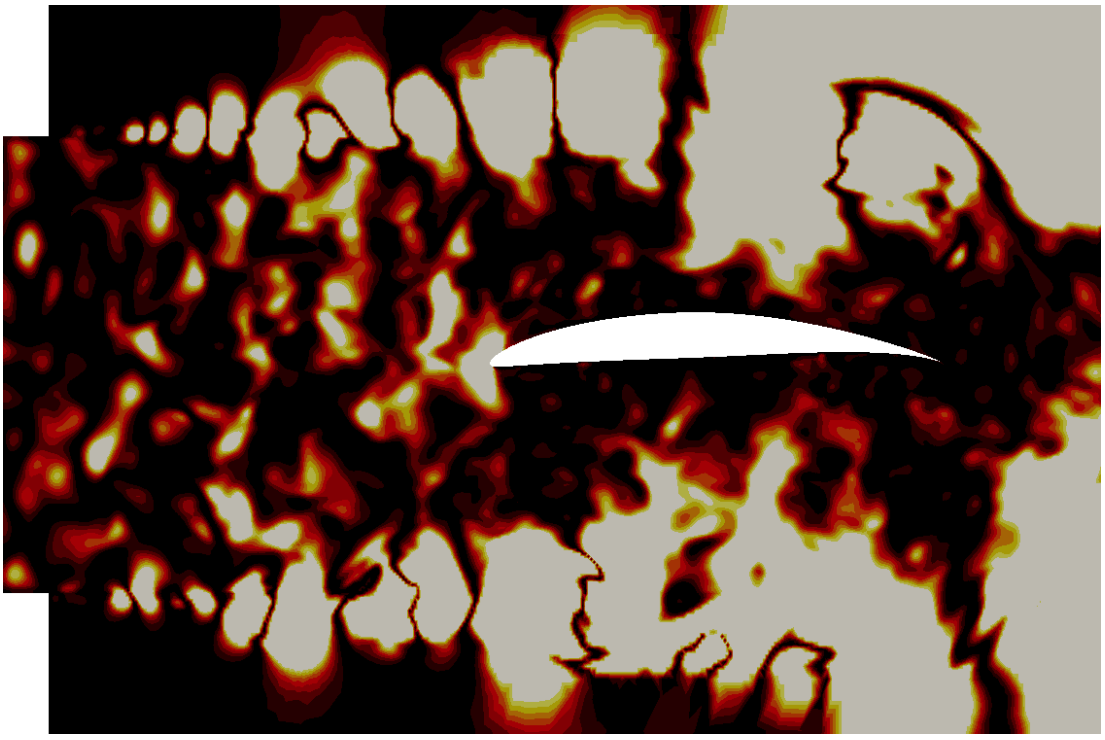

(a) with jet

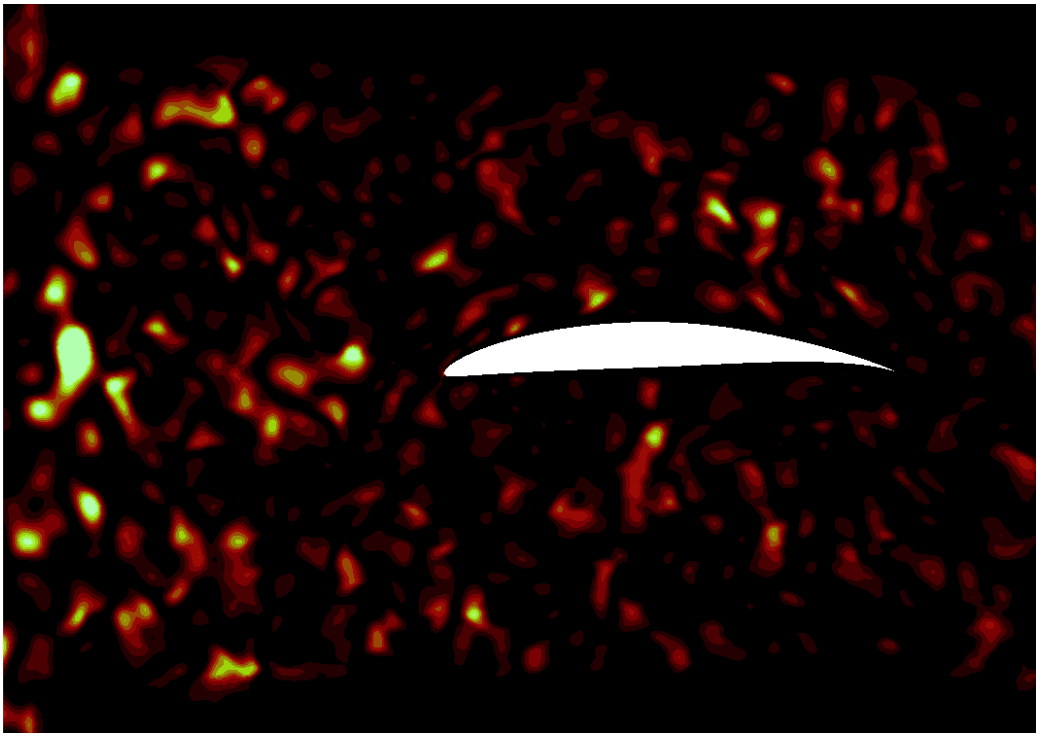

(b) without jet

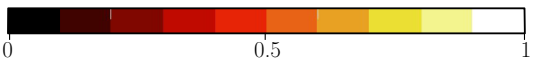

FIGURE 6.6: x-y plane slices of instantaneous dynamic pressure around NACA65 foil for cases with and without jet. Inflow turbulence generated by SVM.

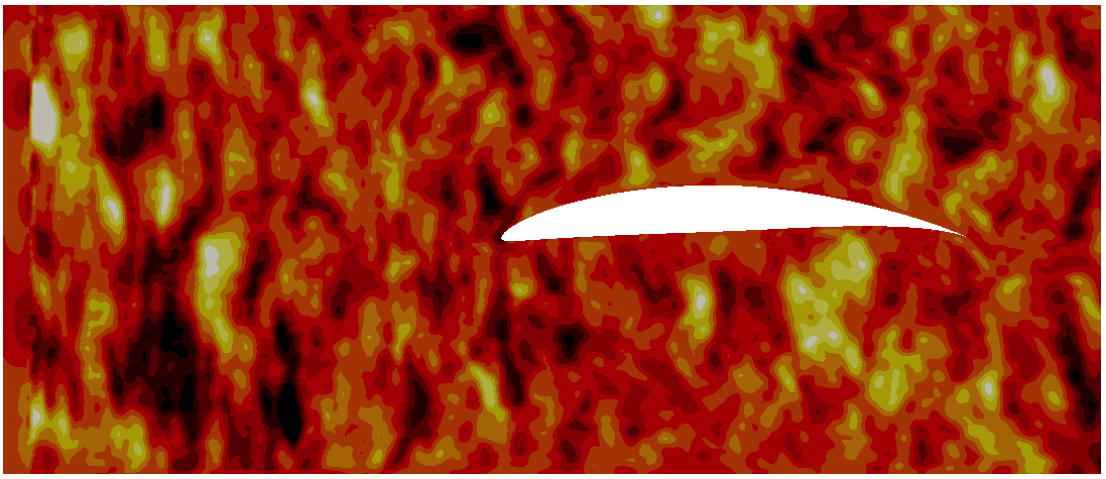

(a) FSM

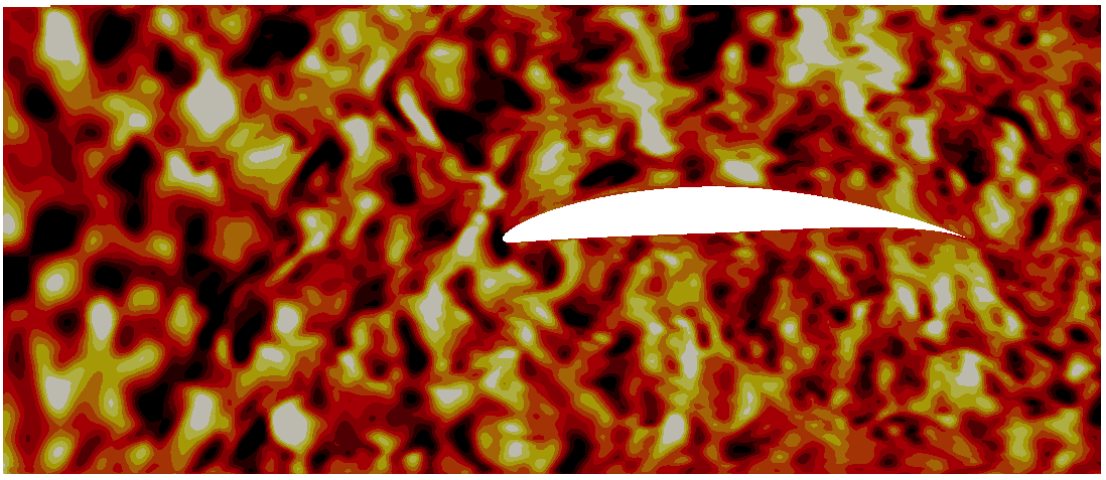

(b) SVM

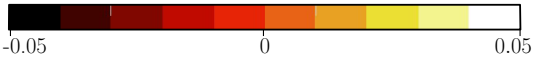

FIGURE 6.7: x-y plane slices of instantaneous upwash velocity around NACA65 foil. Inflow turbulence generated by FSM and SVM.

SVM data exhibits a clear broadband spectrum. The spectral amplitude however is affected by the pressure fluctuations induced at the simulation inlet.

The mean and *rms* pressure coefficients are defined as

$$\overline{C}_p = \frac{2(\overline{p} - p_0)}{\rho_0 U_0^2} \tag{6.5a}$$

and

$$\overline{C'}_{p,rms} = \frac{2\overline{p'}_{rms}}{\rho_0 U_0^2}. \tag{6.5b}$$

These quantities are plotted in Figure 6.10 as chordwise distributions. The chordwise coordinate origin is taken as the nominal aerodynamic center *i.e.* 25% from the leading edge; note this is not the same as the origin used for the acoustic predictions, which follow

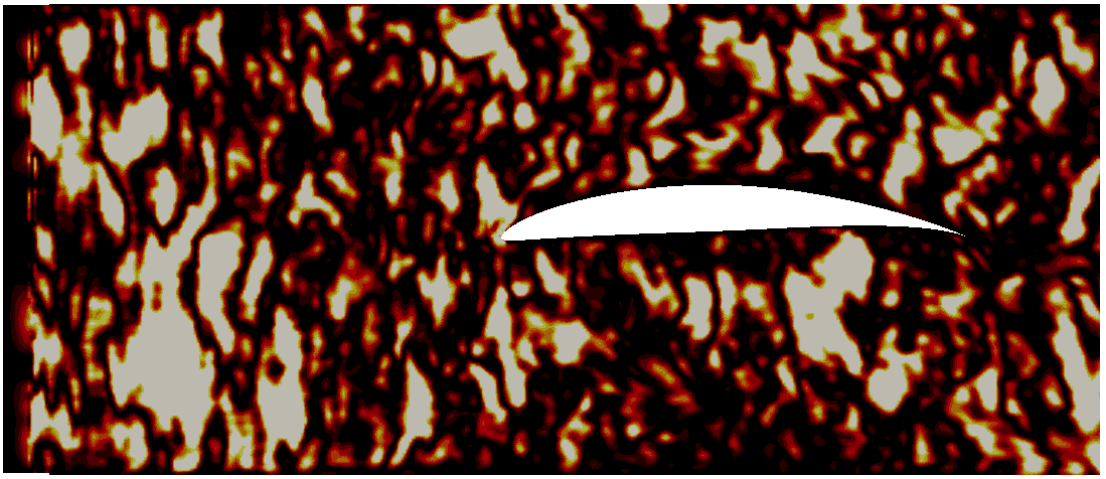

(a) FSM

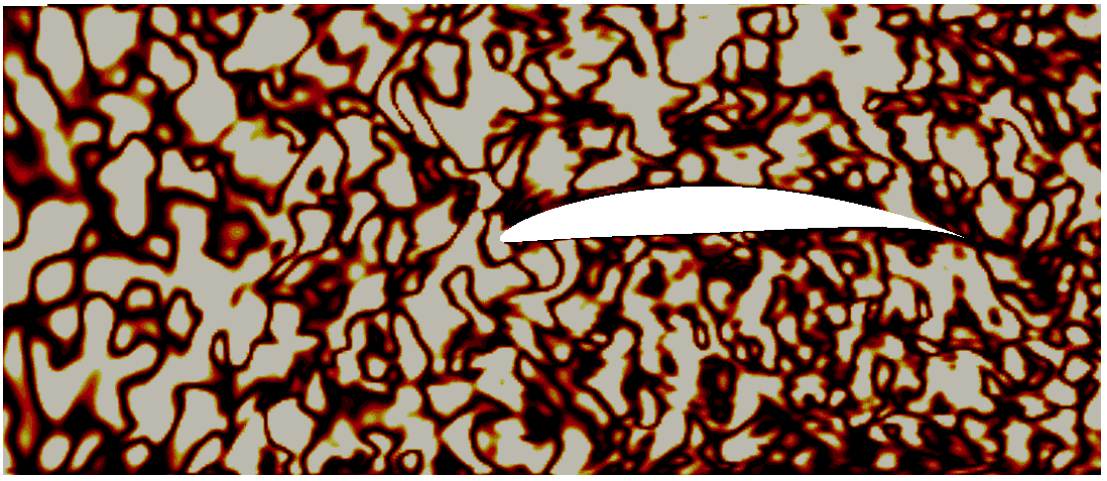

(b) SVM

FIGURE 6.8: x-y plane slices of instantaneous dynamic pressure around NACA65 foil. Inflow turbulence generated by FSM and SVM.

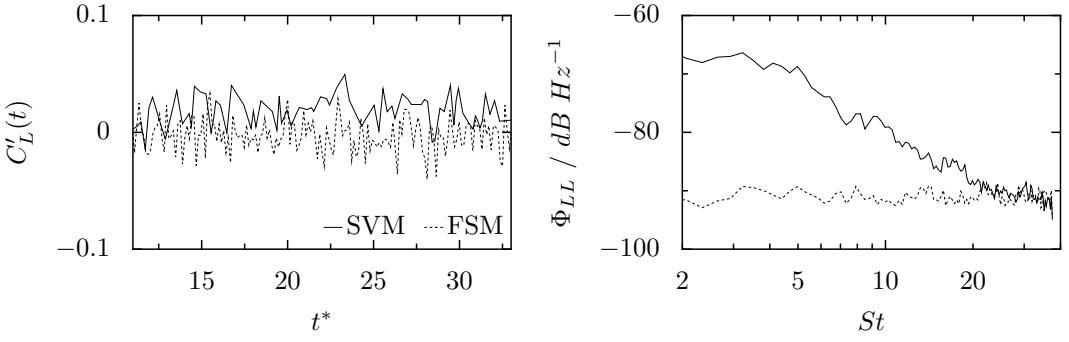

(a) time trace (FSM data scaled up by ten)

(b) lift spectrum

FIGURE 6.9: Lift fluctuations on NACA 65 foil due to inflow turbulence: comparison of FSM and SVM.

that used in the experiment, centred on the foil trailing edge. The SVM data shows a discrepancy close to the leading edge on the pressure side. This has been attributed to the fact that the boundary layer is tripped in the experiments by Deniau *et al.* (2011); Gruber (2012). The mean pressure predicted by the FSM shows a poor agreement with the experimental data; the suction side data is highly oscillatory, the cause of which has not been deduced.

The peak in *rms* pressure at the leading edge is clear in both cases, and occurs on the pressure side of the foil. This is shown in Figure 6.10(b), where the values have been normalised by the maximum chordwise value of $\overline{C'}_{p,rms}$. The chordwise decay of pressure peak is however quite different between the two grids. For the FSM, $\overline{C'}_{p,rms}$ diminishes to approximately one quarter of its maximum value within 5% of the leading edge; this was expected from existing experimental (Lorenzoni *et al.*, 2012) and numerical (Clair *et al.*, 2013; Gill *et al.*, 2013*a*) results. For the SVM, the initial *rms* pressure peak only reduces by approximately 10% within the region plotted. This is again attributed to the inlet pressure fluctuations, and is confirmed by the value of $\overline{C'}_{p,rms}$ at the foil trailing edge, which is still $\approx 68\%$ of the leading edge value.

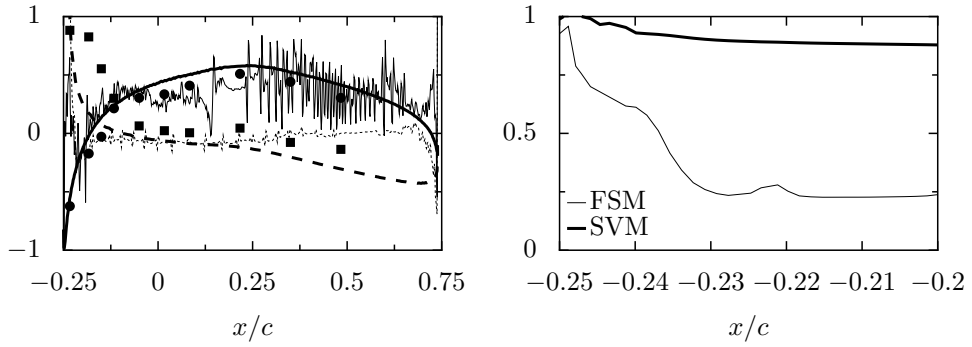

(a) mean surface pressure (FSM data scaled up by 100)

(b) *rms* surface pressure

FIGURE 6.10: NACA 65 foil surface pressure: comparison of experimental and numerical results. Experimental results shown as symbols; SVM as thick lines and FSM as thin lines. Solid and dashed lines denote suction and pressure side data respectively.

These analyses have divulged deficiencies in both the inflow turbulence methods examined. These are attributed wholly to the inflow turbulence generators, since no other simulation settings were changed. Despite the induced pressure fluctuations of the SVM, it is able to predict mean surface pressure and lift spectra; subsequent results for far-field sound are presented from this method, since the FSM did not produce meaningful noise predictions. Conversely, the FSM predicts the chordwise distribution of *rms* surface pressure well, and as such provides better visualisation of the acoustic sources. These are visualised in terms of the sound pressure level on the wall (SPL_w), following Maruta and Kotake (1983). This quantity is defined as

$$SPL_w = 10 \log_{10}\left(\frac{\overline{p_w'^2}}{p_0^2}\right) \tag{6.6}$$

where $p_0 = 20\mu Pa$. This is shown in Figure 6.11, as a colour map on the foil pressure side.

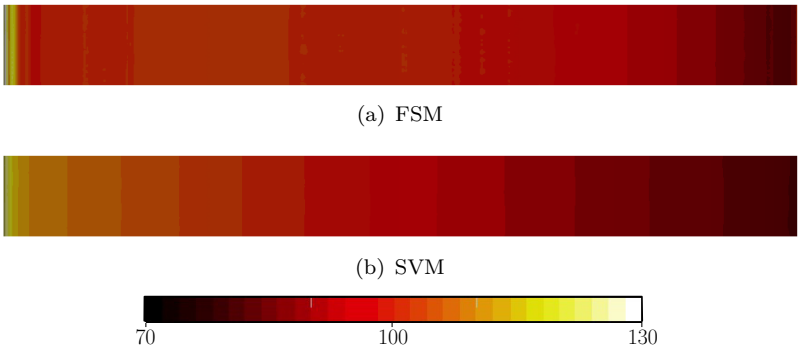

FIGURE 6.11: Acoustic source on NACA 65 using different inflow turbulence generators, visualised as surface sound pressure level; view from below foil (pressure side). Leading edge on left ($x/c = -0.25$). Colour scale in dB.

Examining Figures 6.11(a) and 6.11(b), a clear difference between the distribution of SPL_w is seen. This is directly related to the chordwise distribution of $\overline{C'}_{p,rms}$ shown in Figure 6.10(b). The FSM case shows a concentrated source close to the leading edge; the SVM exhibits a slower chordwise decay of SPL_w, in agreement with Figure 6.10(b).

Finally, a prediction of far-field sound is presented. Figure 6.12 compares the numerical result obtained using the SVM to both experimental and analytical results. The difference at low frequency between the experimental and numerical results is related to omitting the jet from the numerical simulations. This is reinforced by the SPL predicted by Amiet's model at low frequencies, which begins to fall off below approximately 400 Hz. The numerical spectrum shows a good agreement with the experiment (within 4 dB) up to a frequency of 1 kHz. Over-prediction of SPL at higher frequencies is a result of the additional pressure fluctuations generated by the SVM, which contribute to the foil loading and far-field sound. The issues relating to the poor acoustic predictions made using the FSM are certainly specific to this case, and therefore require further investigation. This conclusion is justified by other test cases which have used the FSM to successfully predict unsteady loading and far-field noise (see for example Daniels *et al.* (2013) or Chapter 8 of this monograph).

6.5 Summary

The results presented in Section 5.4.3 for a turbulent jet have been extended to analyse flow and noise of a stationary foil geometry encountering inflow turbulence. This chapter provided further evaluation of the two inflow turbulence generators used in this work:

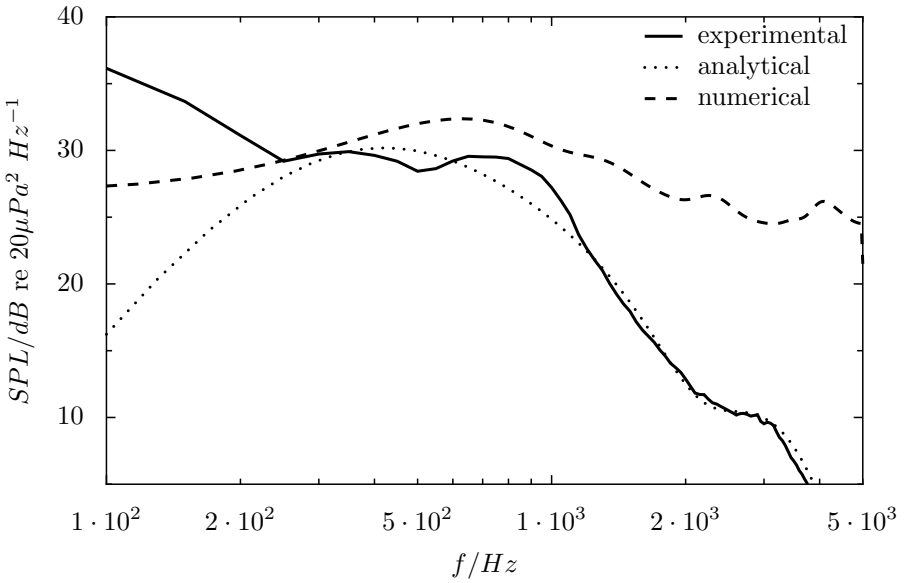

FIGURE 6.12: Sound pressure level for NACA 65: comparison of numerical, experimental and analytical results. Receiver located at $\theta = 90°$ and $|\boldsymbol{r}| = 1\ m$. Bandwidth $\Delta f = 10\ Hz$.

the synthetic vorton method; and the forward stepwise method. It was found that the synthetic vorton method is not fully divergence-free for homogeneous turbulence, as claimed by the method's developers. Although smaller than for the inhomogeneous case, the induced pressure fluctuations pollute the prediction of acoustic sources and far-field sound. This method was found to provide a better prediction of mean pressure distribution however, as well as far-field sound, compared to the forward stepwise method. The main failing of the forward stepwise method was the prediction of lift fluctuations; a 'flat' spectrum was reported, suggesting than the impinging turbulence does not induce the correct acoustic source on the foil surface. Although the magnitude of the surface pressure fluctuations is small in this case, the acoustic sources exhibit a chordwise distribution similar to that expected from the literature.

While the aim of analysing both inflow turbulence generators was to choose one for further use, this has been complicated by the issues described previously. Hence, in the next chapter, both methods are used to investigate the effect of foil thickness on acoustic source distribution and radiated sound. The synthetic vorton method will be used to present lift and sound pressure level spectra, while the forward stepwise method provides visualisation of the acoustic sources.

7

Effect of Foil Geometry on Noise

7.1 Introduction

Having validated a methodology for predicting foil noise due to inflow turbulence, this chapter uses the same approach to analyse the effect of changes in foil geometry on acoustic behaviour. Such investigations also act as further validation of the numerical simulations utilised in the present study, which provide the final test case before simulating a full tidal turbine geometry. The deficiencies of both inflow turbulence generators were examined in Chapter 6; it was therefore decided to include results in this chapter using both methods, since they can provide 'complimentary' results in terms of acoustic sources and far-field sound. It is again emphasised that the issues associated with the forward stepwise method (FSM) are related to the test case, since validated acoustic predictions using this method are successfully made later in Chapter 8.

In terms of foil geometry, two key factors affecting noise are thickness (or thickness/length scale ratio) and chord (Hutcheson *et al.*, 2012). Other effects such as camber and angle of attack have been shown to be small (Devenport *et al.*, 2010; Moreau *et al.*, 2005). Hutcheson *et al.* (2012) found that larger chord increases SPL at low frequencies. The effect of thickness has received the most research attention (Devenport *et al.*, 2010; Gill *et al.*, 2013*a*; Hutcheson *et al.*, 2012; Moreau *et al.*, 2005; Roger and Moreau, 2010). In general, thinner foil shapes are seen to increase noise. The increase is larger or higher frequencies (Gill *et al.*, 2013*a*). Moreau *et al.* (2005) plotted the reduction in dB level for varying thickness, frequency and flow speed. For the case addressed here ($U_0 = 20$

ms^{-1}, $t/c = 0.1$), a reduction of 8-9 dB could be expected at 1 kHz, relative to an infinitely thin flat plate. These investigations have led to a proposed scaling relationship for the reduction in thickness noise Roger and Moreau (2010), which may be written as

$$\Delta SPL = f\left(\frac{(t/c)_B}{(t/c)_A}, \frac{f}{U_0}, \frac{(\mathcal{L}/t)_A}{(\mathcal{L}/t)_B}\right), \tag{7.1}$$

where the subscripts 'A' and 'B' denote two different foil profiles. Evidently, the ratio $\mathcal{L}/t$ is an important parameter for noise reduction. This has implications for foil section design when taking into account inflow turbulence noise.

7.2 Simulation details

Thickness distributions for the foil profiles used in this chapter are shown in Figure 7.1. The $NACA\ 65_1210$ is the same as used previously, while the $C4$ has been chosen as a representative profile for a marine propulsor. Details of this section may be found in Howell (1945). The notation used denotes a ten percent thickness, camber line based on a 30 degree arc between the leading and trailing edges. A thickness of $h/c = 0.01$ was chosen for the flat plate, making it one tenth of the maximum foil thickness. In addition, an elliptical leading edge shape of major axis $h/c = 0.01$ was specified (see Figure 7.1 insert). The trailing edge has a square shape.

In order to examine the effect of foil profile, the C4 shown in Figure 7.1 was used. The chosen section has the same chord and maximum thickness as the NACA 65, but a different leading edge shape and thickness distribution. A circular trailing edge shape was used since the profile is not closed at this location' the circle diameter was $h/c = 0.01$. The C4 has a thicker leading edge, and hence the flow and noise source should be somewhat modified compared to the NACA 65. This variation in thickness distribution is plotted in Figure 7.2. The thicker leading edge results in a larger leading edge radius, which has also been shown to reduce noise at mid to high frequencies (Gill *et al.*, 2013*a*).

It is emphasised that grid design, simulation setup and total time remain the same as for Chapter 6. The only difference is the change of foil geometry. The results presented for the NACA 65 are the same as those given in Chapter 6. For reasons explained in Sections 6.5 and 7.1, both inflow turbulence generators are used in this investigation.

7.3 Results and discussion

7.3.1 Lift and surface pressure fluctuations

Lift fluctuations and associated spectra are shown in Figure 7.3, when using the SVM. The magnitude of lift fluctuations for the NACA 65 and C4 profiles is similar across

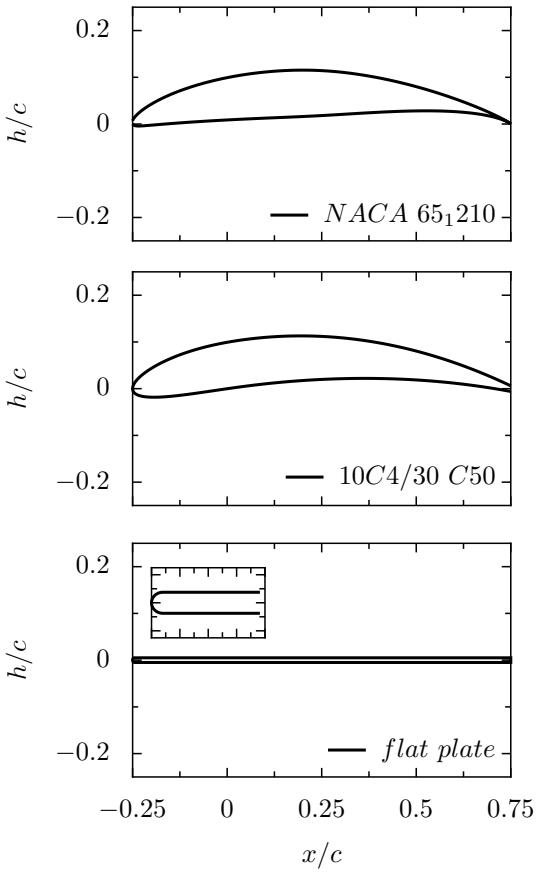

FIGURE 7.1: Views of foils used in thickness and profile investigations. Insert on bottom right figure shows flat plate leading edge shape.

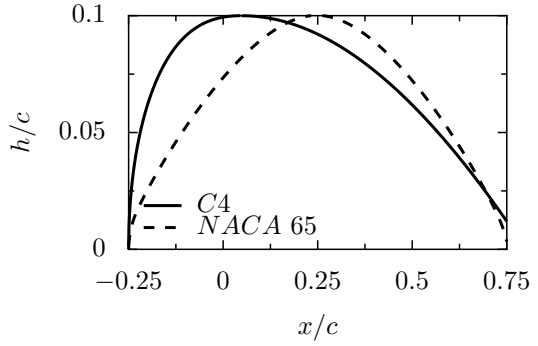

FIGURE 7.2: Thickness distribution comparison for NACA 65 and C4 foil sections.

all frequencies; the flat plate shows a slightly higher broadband level however. This was anticipated based on the literature (Hutcheson *et al.*, 2012; Moreau *et al.*, 2005), although it was expected that there would be a clear difference in spectral level between the thick and thin sections at higher frequencies.

Figure 7.4 shows the leading edge surface pressure fluctuations in terms of $\overline{C'}_{p,rms}$. A difference in both magnitude and distribution is seen for the different profile thicknesses. The fluctuations on the flat plate are approximately three times larger than for the $h/c = 0.1$ foils; a similar difference was observed by Gill *et al.* (2013*b*) between NACA

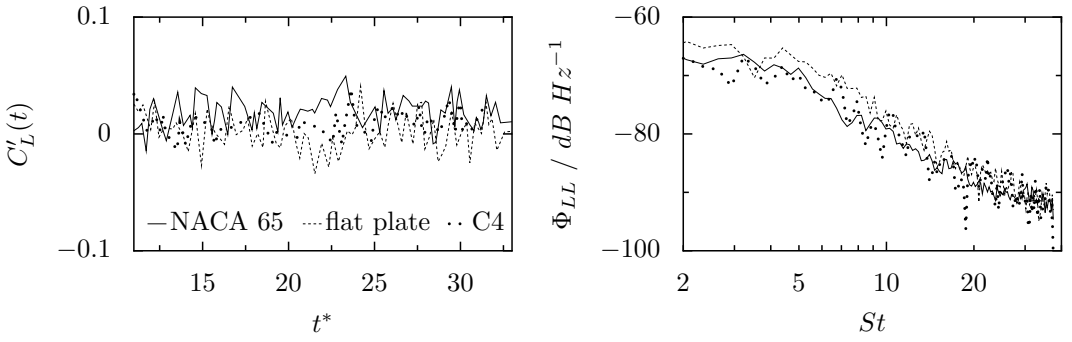

(a) time trace (b) lift spectrum ($\Delta f = 10\ Hz$)

FIGURE 7.3: Lift fluctuations on NACA 65, flat plate and C4 due to inflow turbulence, using SVM.

0002 and 0012. It is also noted that the minimum value of $\overline{C'}_{p,rms}$ for the flat plate is ≈ 0.007, which is larger than the maximum value for the thicker foils. This shows that a larger part of the flat plate chord interacts with the inflow turbulence compared to the NACA 65 and C4.

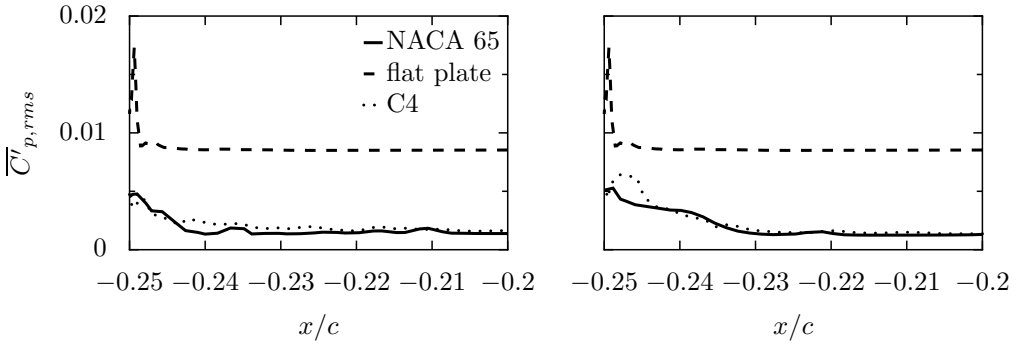

(a) suction side (b) pressure side

FIGURE 7.4: Root mean square surface pressure coefficient for NACA 65, flat plate and C4, using SVM. Only front 5% of chord shown.

No large difference in magnitude is observed for the NACA 65 and C4 profiles. A small change in $\overline{C'}_{p,rms}$ is observed on the pressure side in Figure 7.4(b), which is likely to be related to the difference in leading edge shape (see Figure 7.1). The small humps in the data for both foils are the result of leading edge separation, which is not fully suppressed by the slip wall boundary condition; simulating the cases with a small angle of attack may have removed this issue.

7.3.2 Acoustic sources and radiated sound

The indicator defined in Equation 6.6 is now used to examine the distribution of the acoustic sources on the three foil profiles. The results presented are derived from simulations using the FSM. Figure 7.5 shows the surface sound pressure level SPL_w, scaled to

include the maximum and minimum values from all three cases; this means the source distribution on the flat plate is not well defined, although this is corrected later in Figure 7.7.

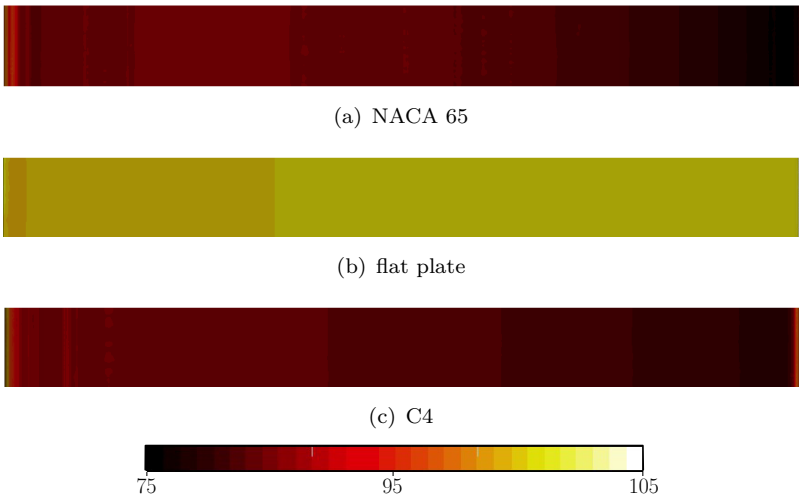

FIGURE 7.5: Acoustic source on all three foils, visualised as surface sound pressure level; view from below foil (pressure side). Leading edge on left ($x/c = -0.25$). Colour scale in dB.

The concentration of the sources is seen at the leading edge, a direct result of the pressure distributions shown in Figure 7.4. Similarly, the magnitude of the flat plate source, when scaled in this way, is seen the exceed that of the other profiles across the entire chord. An increase in SPL_w is seen at the trailing edges of the flat plate and C4, due to vortex shedding. This is caused by the shear layer induced at the trailing edge as a result of the blunt profiles simulated, and is not evident of the NACA 65, where a sharp trailing edge was used.

Next, the far-field SPL prediction for the three cases is presented in Figure 7.6. As expected, there is little difference between the NACA 65 and C4; the flat plate does show an increase in radiated sound however. The spectra are similar to those for the lift fluctuation, plotted in Figure 7.3(b). This is not surprising given that the source is an acoustic dipole due to fluctuating lift. Based on the scaling presented by Moreau *et al.* (2005), a $\approx 7\ dB$ increase in SPL would be expected at 1 kHz, when thickness reduces from $h/c = 0.1$ to 0.01. The present study predicts a $\approx 4\ dB$ difference at this frequency. If the spectra for the NACA 65 were in better agreement with the experimental and analytical results, this difference may be more in line with the estimates of Moreau *et al.* (2005).

7.3.3 Flow field analysis

Despite the poor agreement between numerical and experimental SPL, the simulations may still be used to study the sound generation process in more detail. Figure 7.7 shows

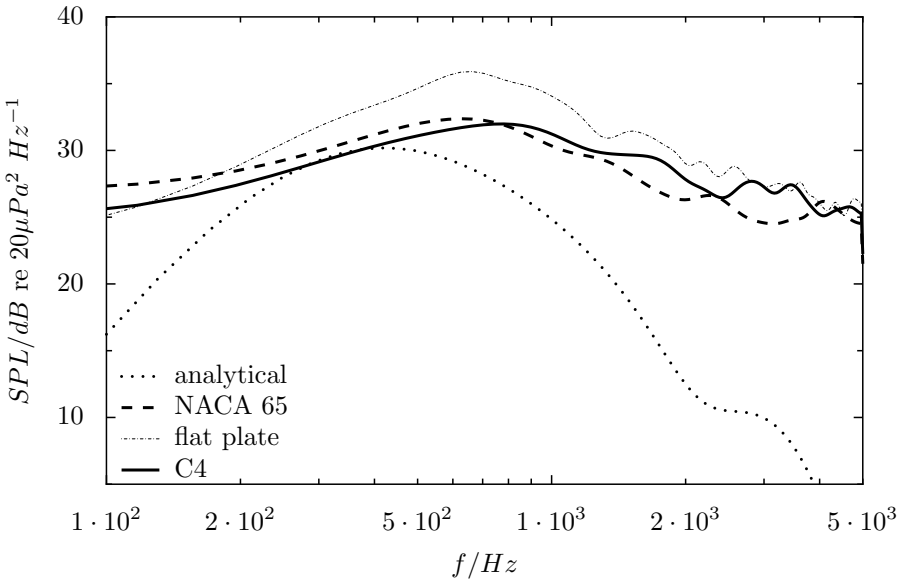

FIGURE 7.6: Sound pressure level prediction for all three foils, using SVM. Receiver located at $\theta = 90°$ and $|\boldsymbol{r}| = 1\ m$.

the flow field close to, and surface pressure fluctuations on, the leading edges of the three foils, using results obtained by the FSM. Figure 7.7(a) shows velocity streamlines as well as an x-y plane slice of mean upwash velocity. This reveals the mean flow distortion effect due to foil thickness. A similar effect was also predicted by Gill *et al.* (2013*b*), who attributed the reduction in upwash velocity to the increased size of the stagnation region in the case of thicker foil profiles. For the present study, the flat plate not only shows less mean flow distortion, but that the upwash velocity is more concentrated at the leading edge than for the thicker foils. This effect translates into a more localised acoustic source, as show in Figure 7.7(b). The flat plate source is located either side of the stagnation region, on the elliptical leading edge. Sources on the NACA 65 and C4 are seen to be more distributed, as well as lower in magnitude. This analysis shows that the present methodology is suited to analysing the effect of foil geometry on leading edge noise sources. The next section discusses how recommendations for reducing broadband noise must be weighed against conflicting design and noise considerations.

7.4 Design considerations for noise reduction

Being able to predict differences in radiated noise due to foil section profile means that simulations of the type presented here can be incorporated into a design process where noise mitigation is a key issue. Targets for reducing broadband noise however must be weighed up against other noise sources and design drivers, including blade strength and mass, as well as propulsor thrust and torque. Increasing thickness, particularly towards the leading edge (resulting in higher leading edge radii) has been shown to reduce the SPL across a broad range of frequencies. This decision however comes at the expense

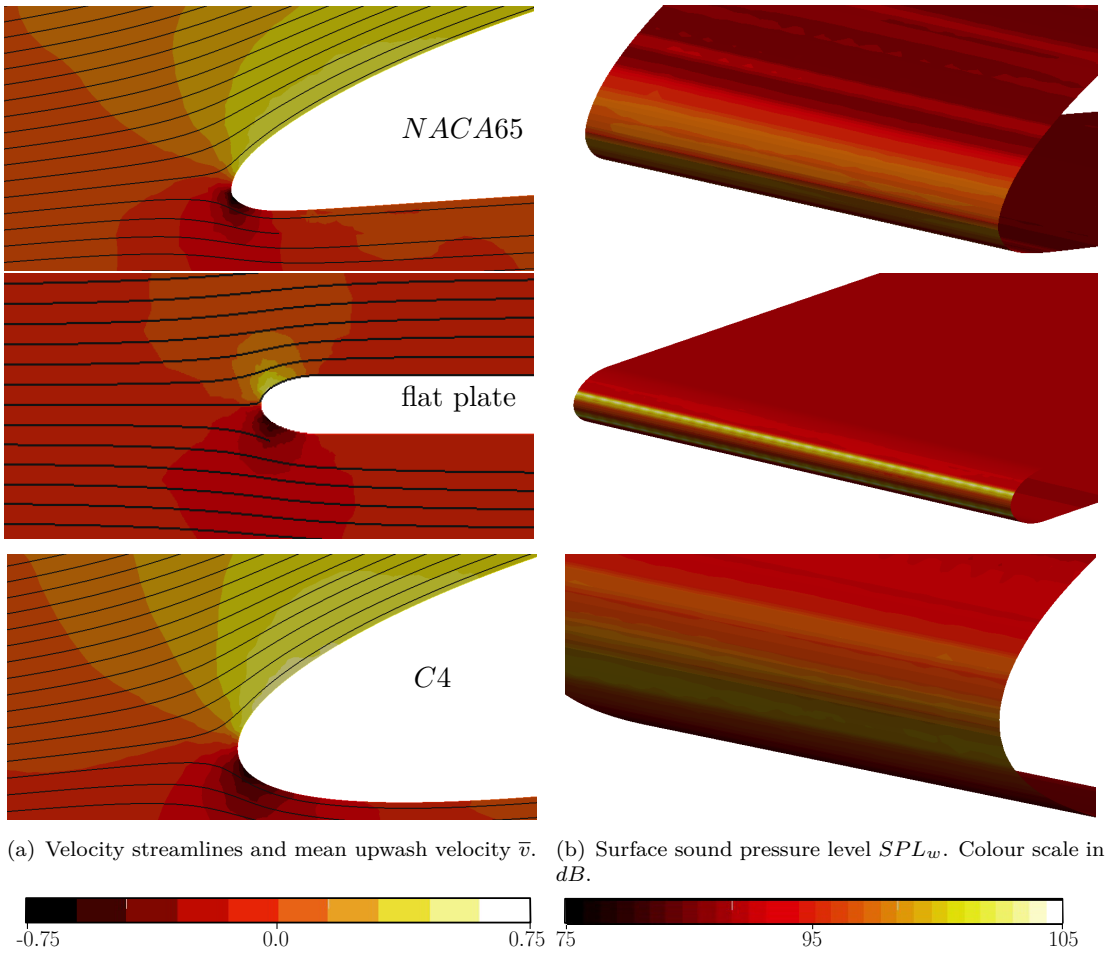

(a) Velocity streamlines and mean upwash velocity $\overline{v}$. (b) Surface sound pressure level SPL_w. Colour scale in dB.

FIGURE 7.7: Leading edge flow and surface pressure fluctuations for NACA 65 (top); flat plate (middle); and C4 (bottom), using FSM.

of increased displacement thickness noise. Hence, if tonal noise is to be reduced, a compromise must be met.

A further consideration is hydrodynamic performance on the blade section, which typically focusses on maintaining on optimum lift/drag ratio in order to achieve the desired thrust and torque characteristics. Thicker sections will experience higher pressure drag, and therefore possibly also higher total drag (Çengel and Cimbala, 2006*b*, chap. 11). In order to maintain lift/drag ratio, a low peak suction pressure (high value of $-C_p$) may be required. This however increases the likelihood of cavitation inception (which occurs when $\sigma < -C_p$, where σ is the cavitation number), and therefore cavitation noise (Molland *et al.*, 2011, chap. 12). This is illustrated in Figure 7.8(a). Molland *et al.* (2011, chap. 12) also present cavitation limit formulae for sheet and bubble cavitation,

$$\sigma = 0.06\frac{(C_L - C_{L_0})^2}{(r_{LE}/c)} \tag{7.2a}$$

and

$$\sigma = \frac{2}{3}C_L + \frac{5}{2}\left(\frac{t}{c}\right) \tag{7.2b}$$

where C_{L_0} and r_{LE} are the ideal lift coefficient and leading edge radius. Hence smaller leading edge radii reduce sheet cavitation, while thicker foils are required to mitigate bubble cavitation. Observations of cavitation inception have shown that sheet cavitation is likely for high values of C_L (tonal source), while bubble cavitation (broadband source) may occur at lower C_L if σ reduces sufficiently.

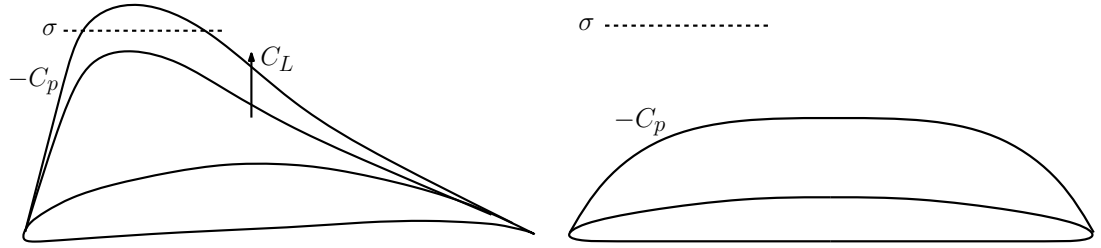

(a) typical foil section (b) roundback section

FIGURE 7.8: Effect of foil shape on chordwise pressure distribution and cavitation inception.

Since cavitation is more likely to occur at a highly loaded chordwise position (typically close to the leading edge), marine propulsors may use *roundback* type sections (see Figure 7.8(b)). Since this type of foil re-distributes the loading towards the trailing edge, cavitation is reduced. It is noted however that such foil profiles have smaller leading edge radii than typical aerofoils. Thus there may be an increase in broadband noise due to inflow turbulence if roundback sections are adopted.

7.5 Summary

The effects of foil thickness on radiated noise can be captured using CFD. This provides significant advantage over analytical models assuming thin aerofoil theory. Simulations were shown to be able to predict the difference between noise source and radiation for thin (one percent thickness) and thick (ten percent thickness) foils. The acoustic source on the flat plate was seen to be more localised at the leading edge, and of higher magnitude along the entire chord when compared to NACA 65 and C4 profiles.

Differences in the radiated noise between foil profiles of the same thickness were not evident however, motivating further studies to improve the results obtained using the forward stepwise method. As noted by Gill *et al.* (2013*b*), leading edge radius is often related to foil thickness, and hence predicting differences in noise due to thickness changes may be in some cases a primary objective compared to leading edge shape. When simulating a tidal turbine in the next chapter, the blades possess spanwise variation of chord and thickness; hence these effects must be captured in the simulations. However, the ratio of integral length scale to blade chord is much higher than that for the test case in this chapter, and therefore it is expected that leading edge shape will play a less important role in noise radiation.

8

Anisotropic Turbulence: Tidal Turbine Noise

8.1 Introduction

Previous chapters have focussed on developing and evaluating a numerical method for studying inflow turbulence noise. This process allowed simulation design to be validated in terms of, for example, choice of turbulence model and convection scheme, and spatial and temporal resolution requirements. Until now, only stationary foils have been considered; the analysis is now extended to a tidal turbine. Two key features of the results presented in this chapter are: modelling of multiple blades rotating in a time-resolved manner, such that rotor-turbulence interaction effects are explicitly included; and representation of inhomogeneous anisotropic inflow turbulence, with the aim of simulating a 'realistic' engineering scenario. In this work, a tidal turbine has been chosen, since noise radiation of such devices has become an important issue with regards to environmental impact assessment (Lloyd *et al.*, 2011*a*), and therefore design approval.

This chapter presents acoustic results in terms of both sound pressure level (SPL) and source level (SL). An acoustic source level is used to characterise a source, and is based on correcting far field SPL back to a distance of $|\boldsymbol{r}| = 1\ m$. While SLs are typically quoted as integrated values *i.e.* overall source levels, in the present study they are reported at particular frequencies. Hence, these are termed *spectral source levels* (SSLs). Spectral source levels are therefore referred to using $1\mu Pa^2\ Hz^{-1}$ at $1\ m$.

8.2 Problem review

Key literature relating to tidal turbine hydrodynamic noise are now reviewed. This is addressed in three parts: discussion of full and model scale turbine noise levels, including a review of wind turbine noise literature; review of inflow turbulence simulations for tidal turbines; and an assessment of turbomachinery response to inflow turbulence.

8.2.1 Turbine noise

The noise emitted by tidal turbines has become one of the key concerns as part of environmental impact assessment studies (Halvorsen *et al.*, 2011; Richards *et al.*, 2007). Both these studies concluded that the dominant noise sources will be low frequency ($< 100\ Hz$); this includes the hydrodynamic noise. Hence the noise is expected to primarily affect fish, motivating studies into their response to noise (Halvorsen *et al.*, 2011). These authors used sound pressure levels of $155 - 163\ dB\ re\ 1\mu Pa^2$, in the frequency range 100-400 Hz to investigate noise impact. Richards *et al.* (2007) used full scale measurements of a dual-rotor 1 MW device (Parvin *et al.*, 2005) to make environmental impact assessments. They used a third-octave SSL of 158.5 $dB\ re\ 1\mu Pa^2\ Hz^{-1}$ at 1 m for $f = 10\ Hz$.

Model scale noise measurements and predictions of tidal turbines have been made experimentally (Wang *et al.*, 2007) and numerically (Li and Çalişal, 2010). Wang *et al.* (2007) reported full scale source levels made using a scaling procedure designed for ship propeller cavitation noise (see ITTC, 1987). They reported SLs up to 150 $dB\ re\ 1\mu Pa^2\ Hz^{-1}$ at 1 m in the frequency range 10-15 Hz. The authors note a strong dependence of the source level on the turbine immersion depth, since this affects tip vortex cavitation significantly. Li and Çalişal (2010) made predictions for a vertical axis turbine based on the acoustic intensity. They find the peak noise level to be at 4 Hz, and despite the frequency sensitivity of various fish species being presented, no direct assessment of noise impact is made.

Studies concerning wind turbine noise are also relevant to tidal turbines, and are more commonly reported. Grosveld (1985), Glegg *et al.* (1987) and Hubbard (1991) addressed the relative magnitudes of different wind turbine broadband noise sources. Grosveld (1985) reported inflow turbulence as being the dominant noise source across most of the frequencies considered (63-4000 Hz); trailing edge vortex shedding exceeds inflow turbulence noise in the mid-frequency range however (1-2 kHz). Glegg *et al.* (1987) predicted that trailing edge noise would exceed inflow turbulence noise at $\approx 1\ kHz$. Similar results were presented by Moriarty *et al.* (2005) and Migliore and Oerlemans (2004) using semi-empirical modelling and experimental measurements respectively. Oerlemans *et al.* (2007) claims that vortex shedding noise is not important; this conclusion depends on the specific blade trailing edge shape however.

Oerlemans *et al.* (2007, 2009) presented measurements and estimates of full scale wind turbine turbulent boundary layer trailing edge noise. They noted that the highest SPL occurs as the blade moves towards a receiver located on the ground. This is termed '*swishing*' noise, and attributed to the directivity of trailing edge noise, which the authors note is more complex than for inflow turbulence noise. Hubbard (1991) showed that the highest SPL (including inflow turbulence) occurs in the upstream and downstream (rotor axis) directions, although pure dipole directivity is not exhibited; the SPL in the rotor plane is 5-10 dB lower than in the rotor axis.

A further point of note is the location of the dominant acoustic sources along the blade span. This was discussed by Oerlemans *et al.* (2007), in terms of trailing edge noise. The maximum SPL is observed in the outer region of the blade, but not at the tip. The source is centred at $r/R \approx 0.85 - 0.93$, with the higher frequency noise further towards the tip. In addition, when the blade boundary layer was tripped, the SPL increased and the source centre moved further towards the blade tip. Boundary layer tripping would not affect inflow turbulence noise however (Migliore and Oerlemans, 2004; Oerlemans *et al.*, 2007).

No studies identifying the spanwise distribution of the inflow turbulence noise source have been reported. Although Migliore and Oerlemans (2004) measured the inflow turbulence noise of typical wind turbine blade sections, a full rotor geometry was not investigated. This issue may therefore be elucidated in the present study. The conclusion that tip noise is less important than trailing edge noise is supported by measurements of stationary foils by Brooks and Marcolini (1986), although these authors state that this may not be the case for rotors. They noted that highly loaded tips will result in increase tip vortex noise. Tip shape *has* been shown to be important for noise generation in certain cases however. Fleig *et al.* (2004) used large eddy simulations to investigate wind turbine tip noise reduction using modified tip shapes.

8.2.2 Simulation of tidal turbines encountering inflow turbulence

Although no numerical noise predictions for horizontal axis tidal turbines exist, computational fluid dynamics studies of turbine performance are widely reported. Three different approaches have been considered when simulating turbines in inflow turbulence. Gant and Stallard (2008) combined an inflow turbulence generator (ITG) with a simple porous disk (to model turbine thrust and wake development), within an unsteady Reynolds-averaged Navier-Stokes equations (URANS) simulation. This approach has the advantage of reducing the computational cost in terms of resolving the turbine, and allows the influence of inflow turbulence on wake recovery to be examined. However, this simplification, in combination with the URANS, is not appropriate for resolving acoustic sources, which requires the spatial and temporal characteristics of the blade

surface pressure to be captured. The authors provide recommendations for prescribing inflow turbulence statistics, based on guidelines from the wind energy industry.

The work of Churchfield *et al.* (2013) can be considered as a development of that presented by Gant and Stallard (2008). Large eddy simulations were used to analyse an array of turbines in a tidal channel. Turbines were modelled using an *actuator line* model, which adds time-dependent momentum sources to the flow solver in order to represent the blades. This means the effects of array spacing on turbine performance can be examined, although this method is not suited to acoustic simulations for the same reasons as previously mentioned. Another key part of the methodology used is to develop inflow turbulence profiles based on a precursor simulation of a tidal channel. These are added to the turbine simulation from a stored library, removing the issue of streamwise development experienced by inflow turbulence generators (as reported in Chapter 5).

Comparisons are commonly made to the experimental data of Bahaj *et al.* (2007). The only reported large eddy simulation of this turbine is by Afgan *et al.* (2013), who resolved the turbine geometry, including hub and mast, within the computational grid. This study represents the most suitable approach for turbine noise simulation. Inflow turbulence was generated using the divergence-free synthetic eddy method of Poletto *et al.* (2013). They showed that LES is more accurate at predicting mean thrust and power than RANS. In addition, three inflow turbulence intensities (1, 10 and 20%) were used. The *rms* power is seen to increase with turbulence intensity; however the *rms* thrust is of similar magnitude for all cases.

8.2.3 Rotor response to turbulence

Unsteady propeller forces are of interest because they can cause increased noise levels, as well as leading to large blade root bending moments, and in the maritime context, unsteady cavitation behaviour. The arguments of Sharland (1964) presented in Section 1.2 may be developed to consider the dependency of the inflow turbulence noise on the rotor thrust. Blake (1984, chap. 10) writes

$$\overline{p'^2}(f, \Delta f) \approx B q_T^2 \left(\frac{D}{r}\right)^2 M_T^2 \frac{c_T \Delta f}{U_T} f(\alpha), \tag{8.1}$$

where q_T, M_T, c_T and U_T are the dynamic pressure, Mach number, chord and velocity at the blade tip, B is number of blades, D rotor diameter and $f(\alpha)$ is a function depending on the angle of attack α. The unsteady thrust is then

$$T' \propto \frac{1}{2} \rho_0 U_T^2 A C_L' \alpha'. \tag{8.2}$$

Assuming that all angle of attack and lift fluctuations are accounted for in T', for a value of the dimensionless frequency $c_T \Delta f / U_T$ equal to unity, the mean square pressure scales as

$$\frac{\overline{p'^2} r^2}{U_T^6 A} \propto \frac{B \rho_0^2}{c_0^2} C_T'^2. \tag{8.3}$$

Similar arguments are presented by Catlett *et al.* (2012). The loading noise depends directly on the unsteady thrust, and this must be included in any prediction method. Rotor tip velocity is also an important parameter. Despite the low rotational velocity of tidal turbines compared to, for example, the rotors investigated by Catlett *et al.* (2012), Morton *et al.* (2012) and Alexander *et al.* (2013), the large rotor diameter means that the tip velocity is not as proportionally low. Due to the high aspect ratio blades typically used, the acoustic sources could be expected to be strongest towards the blade tips.

Since turbulent inflows are common in engineering scenarios, the analysis of unsteady rotor loading has received significant research attention. In the context of ship propellers, Kornev *et al.* (2011) used an analytical model for propeller loading to estimate thrust spectra. The input to the model comes from velocity spectra extracted from a LES of the flow around a ship hull; hence, fully inhomogeneous anisotropic turbulence is considered. Since the propeller itself is not included in the simulation however, the induced velocities are not accounted for in the model. Mean flow distortion has been found to have a large effect on rotor noise spectra (e.g. see Glegg *et al.*, 2013), thus including the interaction between inflow and rotor is important for any numerical or analytical investigation.

Experimental studies have typically focussed on scenarios involving grid-generated turbulence (Scharpf and Mueller, 1995; Wojno *et al.*, 2002*a*,*b*). In this case, the inflow turbulence is homogeneous, and nominally isotropic. Scharpf and Mueller (1995) presented a study of a model-scale marine propeller at low speed (the advance coefficient $J = U_0/nD$ was 0.8). Tones are attributed to distortion of the mean inflow velocity. The authors report a broadband level increase of approximately 2 dB for every 1% increase in turbulence intensity. Similar conclusions are made by Wojno *et al.* (2002*a*,*b*), who considered both four- and ten-bladed rotors in grid-generated turbulence. In this case, tones are seen for the four-bladed rotor, since the number of blades corresponds to the dominant harmonic of the mean circumferential velocity. This effect is not observed for the ten-bladed rotor.

To model rotor-turbulence interaction, models considering homogeneous anisotropic turbulence have been derived *e.g.* see Blake (1984, chap. 10) and Jiang *et al.* (1994). In this case, the spectral shape is determined by the ratio of the streamwise integral length scale ($\mathcal{L}_x$) to the blade passing pitch (P/B). For $\mathcal{L}_x >> P/B$, spectral 'humps' will exist at multiples of the BPF, caused by cutting of the turbulence by multiple blades. This is referred to as *haystacking*. Analytically, this behaviour is captured by the blade-to-blade correlation function (Blake, 1984, chap. 10). Jiang *et al.* (1994) investigated the effect of various parameters on rotor broadband forces. They found that for:

- increasing integral length scale, the broadband level decreases;
- increasing advance coefficient, the broadband level increases, while the haystacks decrease in peak-to-trough amplitude;
- increasing geometric pitch skews the hump centre frequency ahead of the BPF;
- increasing rotor rotational speed at constant advance coefficient, the broadband level increases, with the spectral peak shifting to higher frequency.

More recently, generalised theories which can account for inhomogeneous turbulence have been developed (Glegg *et al.*, 2012, 2013). Validation is often provided through experiments (Alexander *et al.*, 2013; Catlett *et al.*, 2012; Morton *et al.*, 2012). Such studies are of interest when modelling a rotor operating inside a boundary layer such as a tidal turbine.

Glegg *et al.* (2012) presented a model for thrust loading noise based on considering inhomogeneous anisotropic turbulence. The effect of haystacking is included. Exemplar results may be obtained by assuming the form of the velocity correlations which constitute the inputs to the model. These parameters may however be obtained more accurately from experiments, as carried out by Morton *et al.* (2012). In this study, a rotor mounted inside a wind tunnel boundary layer is considered. They noticed that the noise directivity is affected by the advance coefficient. As J decreases, the noise field exhibits monopole directivity, suggesting the increased loading causes the dominant source to radiate from the blade tips. Catlett *et al.* (2012) also presented comparisons between analytical and experimental predictions of rotor noise. They noted that modelling an inhomogeneous anisotropic (IAT) spectrum improves the analytical prediction of the haystacking phenomenon.

Glegg's theory has been developed to include the effects of mean flow distortion (Glegg *et al.*, 2013). Modelled using rapid distortion theory, this modification is seen to significantly affect the noise spectrum; haystacks are seen to be narrower, while the peak-to-trough amplitude increased. Noise measurements were used to evaluate the revised theory in Alexander *et al.* (2013). In agreement with Morton *et al.* (2012), true dipole directivity is not seen. However, a 20 dB reduction in SPL is seen between receiver angles of 0° and 90° to the rotor axis. The broadband spectrum dependency on advance coefficient, predicted by Jiang *et al.* (1994), is captured in the experiments. A key observation is the model's failure to predict the skewed centre frequencies of the spectral humps (observed by Jiang *et al.* (1994)), which are captured in the experiments. This is not a result of the input data; rather the model must explicitly include correlations between streamwise and tangential velocity components. Both measurements and modelling predict that the peak-to-trough amplitude of the haystacks increases as J reduces.

8.3 Simulation details

8.3.1 Test case description

A model scale turbine geometry was chosen for the simulations. This was primarily due to the availability of detailed blade geometry information, as well as experimental performance data, which are not readily divulged by turbine manufacturers. The turbine design is detailed in Bahaj *et al.* (2007), with performance data from both towing tank and cavitation tunnel tests presented. A blockage correction has been applied to the experimental data to represent a 'free-field' operating condition. The corrected scenario has been used in the simulations, and hence the walls of the experimental facility are not included. A summary of the key parameters is given in Table 8.1. This operating point was chosen since it represents a high thrust loading condition, but avoids large amounts of blade stall. This justifies some of the modelling assumptions made in the next section.

TABLE 8.1: Summary of key tidal turbine test case parameters. Tip speed ratio $\Lambda = \Omega R/U_0$.

symbol	meaning	value	unit
R	rotor radius	0.4	m
B	number of blades	3	-
U_0	mean freestream velocity	1.4	ms^{-1}
n	rotational velocity	3.29	s^{-1}
Λ	tip speed ratio	5.96	-
γ	hub twist angle	15	deg

The turbine blades were designed using NACA 63 series cambered foil profiles (see Bahaj *et al.* (2007) for a full description of chord, thickness and twist distribution). For the chosen case, example blade sections are shown in Figure 8.1.

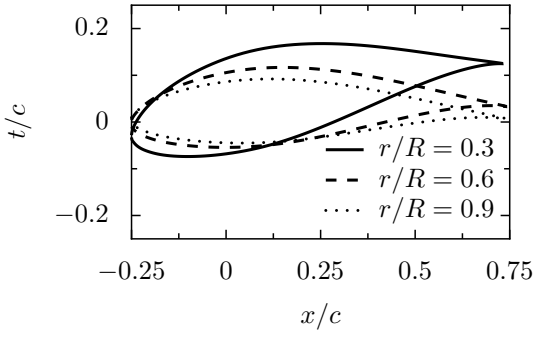

FIGURE 8.1: Turbine blade section profiles at three radial locations, showing thickness and twist distribution: root ($r/R = 0.3$); mid-span (0.6) and tip (0.9). Non-dimensionalisation by local chord. x denotes chordwise, not streamwise, coordinate. Zero twist angle (at the tip) corresponds to alignment with the abscissa, which is turbine rotation plane.

Nomenclature specific to the turbine is depicted in Figure 8.2(a). Definitions of the local velocity components, pitch angles and force vectors are provided in Figure 8.2(b). This figure may also be used to derive blade element momentum theory (BEMT). For brevity, this is not included here; Molland *et al.* (2011, chap. 15) describe BEMT in

detail. BEMT is an efficient method for analysing turbine performance, and may be adapted to suit engineering analyses, such as fluid structure interaction (Bercin *et al.*, 2013). In this work, mean performance coefficients derived from BEMT are compared to those obtained by LES.

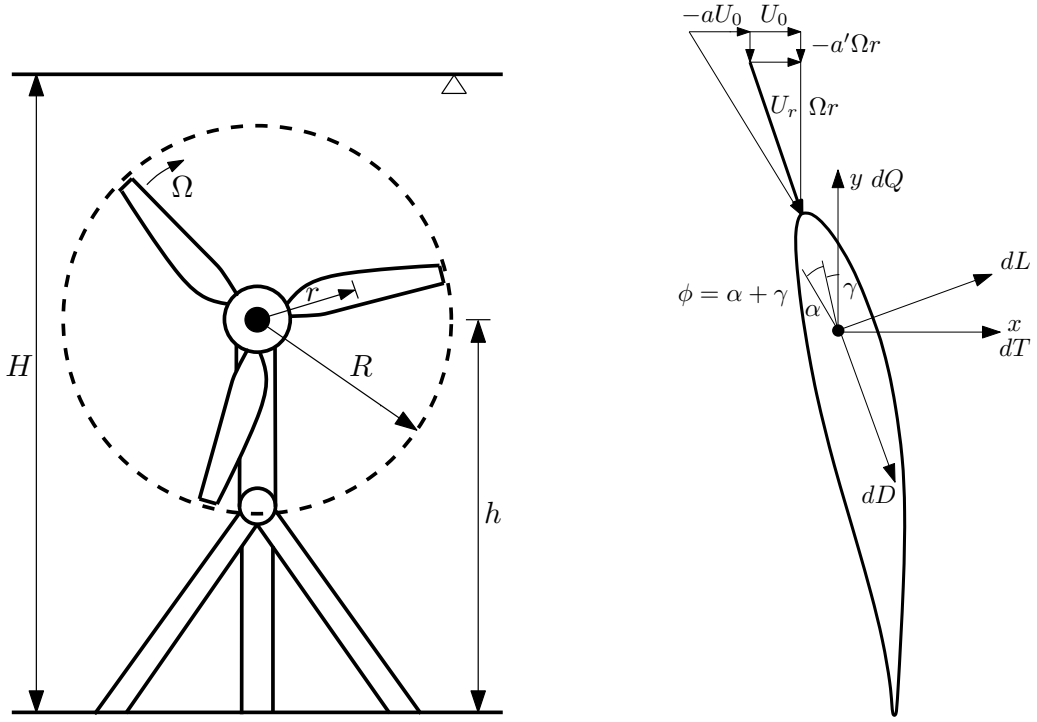

(a) Turbine situated in a channel

(b) Blade element diagram

FIGURE 8.2: Turbine specific nomenclature. The blade element diagram refers to a blade section located at r. The streamwise and tangential inflow factors a and a' serve to modify the local flow velocities (U_r is resultant velocity), and therefore the angle of attack, α, and blade forces. Thrust (dT) and torque (dQ) contributions at the section result from resolving the lift (dL) and drag (dD) forces into the streamwise and tangential directions. The hydrodynamic pitch ϕ is simply a combination of the geometric pitch (twist) and angle of attack.

In order to simulate stochastic loading on the turbine, inflow turbulence statistics must be prescribed. Since no inflow turbulence was considered in the experiments, homogeneous statistics are specified following Gant and Stallard (2008). These authors based their choice of inflow turbulence statistics on wind engineering guidelines, as well as a shallow water boundary layer model (Stansby, 2003). This results in:

- a turbulence intensity ($\mathcal{I}$) of 10%;
- horizontal length scales ($\mathcal{L}_x$ and $\mathcal{L}_z$) of $1.4R$ (based on $\mathcal{L} = 0.7h$);
- and a vertical length scale of $\mathcal{L}_y \approx 0.23R$.

A uniform mean velocity was also used. Since the anisotropy of the length scales serves to characterise the spectral shape, this phenomena has been focussed upon, rather than

modelling the full inhomogeneity of a tidal channel. The present study has several differences compared to the stationary foil cases presented in Chapters 6 and 7 however. These may be summarised as:

- *Thickness*: variation of thickness along the blade span, a parameter that been shown to affect radiated noise in certain cases (Devenport *et al.*, 2010; Hutcheson *et al.*, 2012; Moreau *et al.*, 2005). A more specific discussion was presented in Chapter 7, and it not repeated here. The length scale/thickness ratio varies as $\mathcal{L}_y/h \approx 7.5 - 35$ from blade root to tip.
- *Chord*: Hutcheson *et al.* (2012) reported that inflow turbulence noise scales as c^2; hence chord variation along the blade span is expected to affect the location of the peak source level. Another important parameter is the length scale/chord ratio, which varies from $\mathcal{L}_y/c \approx 1.8 - 4.5$ from root to tip. It has been shown that angle of attack affects noise when $\mathcal{L}/c > 1$ (Hutcheson *et al.*, 2012), which may therefore apply in the present study.
- *Velocity*: variation of inflow velocity along the blade span. This will affect the location of the peak source level on the blade, due to the u^6 dependency of the sound pressure (see Section 8.2.3).

These factors highlight the additional complexity of the tidal turbine simulation compared to a stationary foil. It is also noted that the ratios $\mathcal{L}_y/h$ and $\mathcal{L}_y/h$ lie above the values typically tested in wind tunnels for stationary foils, and hence the findings of the cited studies may not directly apply.

8.3.2 Numerical setup

Grids consist of two regions, the *rotor* and *stator*, connected using the arbitrary mesh interface. Cell faces on the interface patches must be high quality, in order to ensure stable interpolation of variables. This was achieved using cylindrical stereolithography files. Views of the grid are shown in Figure 8.3. Note the uniform cell size on the arbitrary mesh interface (AMI; Figure 8.5) and the refinement at the blade leading edge (Figure 8.3(d)).

The cell dimension in the stator region and on the AMI patch was chosen as $\Delta y = \mathcal{L}_y/6$, resulting in a square cell size of 0.015 m. As a result, the energy spectrum should be very well resolved in the streamwise direction. A comparable study of the same tidal turbine using LES (Afgan *et al.*, 2013) used 24×10^6 grid cells as part of a grid dependency study, thus resolving scales smaller than the Taylor microscale. This was verified by showing that the contribution from the subgrid model represents 5% of the total energy spectrum. The present study would require a similar total grid size if this were to

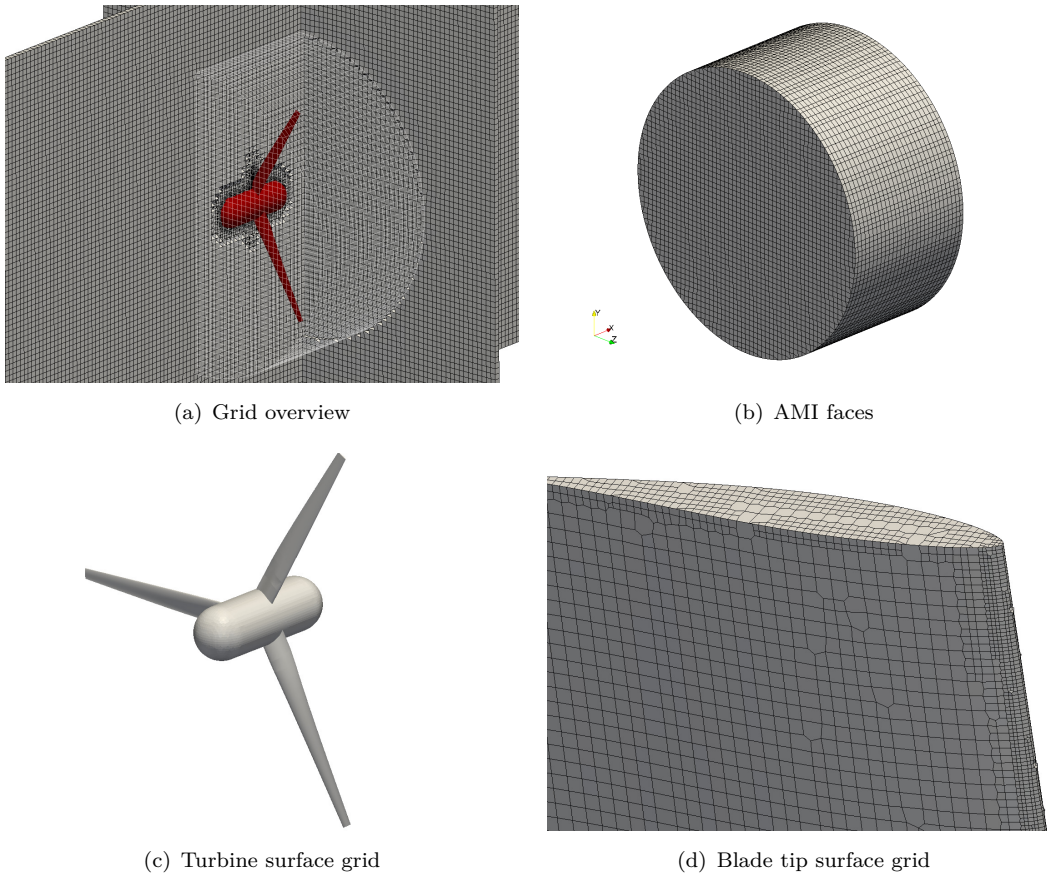

(a) Grid overview

(b) AMI faces

(c) Turbine surface grid

(d) Blade tip surface grid

FIGURE 8.3: Views of turbine grid.

be achieved; however the grid used meets the requirement to resolve 80% of the total turbulent kinetic energy (used throughout the current work).

Using the freestream velocity, an estimate of the highest resolvable frequency of the inflow turbulence is $f_{max} = U_0/2\overline{\Delta} \approx 47\ Hz$. Following Carolus *et al.* (2007), the cutoff frequency of the noise spectra are expected to be higher than the inflow turbulence by a factor $\approx U_r/U_0$. For a blade section at $r/R = 0.7$, $U_r \approx 6\ ms^{-1}$; therefore noise spectra should be resolved up to a frequency of $\approx 200\ Hz$. The total grid size is approximately 4.6×10^6 cells, with 1.6×10^6 in the rotor region. This is larger than the total grid size reported in Lloyd *et al.* (2013*b*) for the same case, where the stator grid region contained fewer cells (total grid size of 3.3×10^6 cells). The additional cells added in the present study are located in the turbine wake region.

A summary of the boundary conditions is given in Table 8.2. The subgrid viscosity was set to zero gradient everywhere except the blades, where a wall function was used. This was chosen since the grid was not fine enough in the boundary layer region. A mean resolution of $\Delta y_w^+ \approx 40$ was achieved, but no boundary layer grid was used, in order to avoid restrictively small time steps. This implies that viscous phenomena such as flow separation will not be accurately captured. Note that due to the grid refinement

algorithm used by *snappyHexMesh*, and the initially square hexahedral domain used as the starting point for the grid, the chordwise and spanwise wall resolution of the grid is the same as in the wall-normal direction. This spatial resolution is similar to that used in Chapters 6 and 7. The location of the inflow turbulence generator plane was chosen as $x/D = -2$, ensuring there were 15 cells between the inlet and inflow plane. The same distance between inflow plane and turbine rotor was used by Gant and Stallard (2008).

TABLE 8.2: Tidal turbine boundary conditions. Patch locations relative to global origin centred on turbine rotor plane FV=fixed value; FV0=fixed value zero; ZG=zero gradient.

patch	location	velocity	pressure
inlet	$-3D$	FV	ZG
outlet	$7D$	convective	FV0
sides	$3D$	symmetry	symmetry
top	$3D$	symmetry	symmetry
bottom	$3D$	symmetry	symmetry
blades		moving wall	ZG
hub		slip	ZG

Simulations utilised the *XCDyMFoam* solver described in Figure 4.7, which includes inflow turbulence generation via the forward stepwise method (FSM). Rotational speed was prescribed as a fixed value. The *pimpleFoam* solver allowed the maximum Courant number limit to be set to four, considerably reducing total simulation time. A maximum time step of $\Delta t^* = \Delta t U_0/D = 3.5 \times 10^{-5}$ was also imposed, ensuring approximately 40 time steps per degree of turbine rotation. This temporal resolution is significantly higher than that recommended for the same turbine by McSherry *et al.* (2011) and Afgan *et al.* (2013). Spatial and temporal resolution of the AMI is particularly important during LES, where resolved turbulence should pass through the interface without experiencing significant numerical dissipation. This issue was experienced by Reese and Carolus (2008), and is analysed for the present study in Section 8.4.1.

Total simulation time was $T^* = TU_0/D = 9.2$, corresponding to one complete flow-through of the domain. Once the inlet flow had reached the rotor plane, data were sampled at $f_{sample} = n/300$ (100 times per BPF) for a total of 12 turbine rotations. Probes were used to monitor the characteristics of the inflow turbulence. The turbine thrust and power were recorded using the custom library *turboPerformance*, as well as far-field pressure using the FW-H equation. Receiver locations are denoted in Figure 8.4. The receiver distance was chosen to satisfy the far-field criteria $|\boldsymbol{r}| > D$ (Makarewicz, 2011), but still be in a range where noise impact of tidal turbines is expected to be important (Lloyd *et al.*, 2011*a*,*b*).

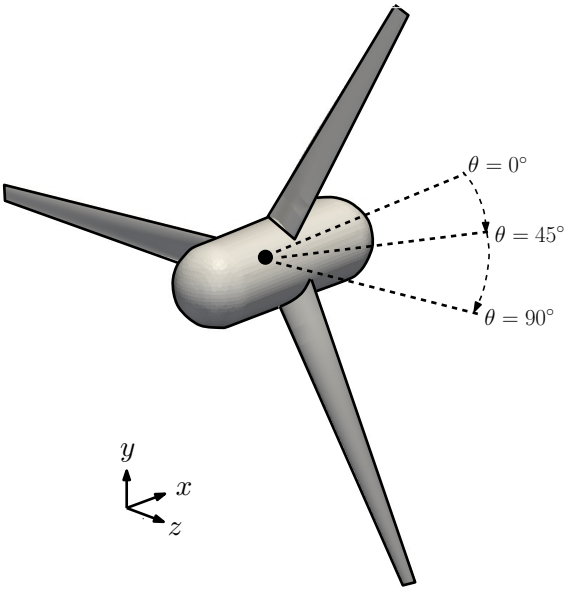

FIGURE 8.4: Coordinate system used in simulations. Acoustic predictions made at receiver angles $\theta = 0$, 45 and 90° and $|\boldsymbol{r}| = 2D$. Receiver angle of 0° corresponds to the rotor axis in the downstream direction; 90° is in the rotor plane. Note that the definition of θ is different from that given in Figure 3.3, which presented the nomenclature of the FW-H equation.

8.3.3 Analytical thrust loading noise model

As no experimental data is available for comparison, an analytical model for thrust loading noise has been used (Blake, 1984, chap. 10). It assumes one of two forms, depending on the ratio of the integral length scale to the rotor pitch. It is also a free-field model, *i.e.* the effects of solid boundaries on the flow and acoustic radiation are not taken into account. This model was chosen since it includes the effect of length scale anisotropy. This provides better validation for the simulated case, since typical models for wind turbine noise assume isotropic inflow (*e.g.* see Glegg *et al.*, 1987; Hubbard, 1991). The mean square thrust for a bandwidth Δf is approximated as

$$\overline{T^2}(f, \Delta f) =$$

$$\begin{cases} \dfrac{16\pi^3 \mathcal{L}_R^* \Delta f}{3R\, n} \left(\dfrac{qc}{J}\right)^2 \dfrac{\overline{u'^2}}{U_0^2} |\mathcal{S}\left(\dfrac{\omega^* c}{R}\right)|^2 \mathcal{F}\left(\omega^* \mathcal{L}_\theta^*\right) |\mathcal{A}\left(\omega^*\right)|^2, & \mathcal{L}_x > P \quad (8.4a) \\ \dfrac{16\pi^3 B \mathcal{L}_R^* \Delta f}{3R\, n} \left(\dfrac{qc}{J}\right)^2 \dfrac{\overline{u'^2}}{U_0^2} |\mathcal{S}\left(\dfrac{\omega^* c}{R}\right)|^2 \mathcal{F}\left(\omega^* \mathcal{L}_\theta^*\right), & \mathcal{L}_x << P/B \quad (8.4b) \end{cases}$$

where

$$\omega^* = \omega/\Omega, \qquad \mathcal{L}_R^* = \mathcal{L}_R/R \quad \text{and} \quad \mathcal{L}_\theta^* = \mathcal{L}_\theta/R \tag{8.5}$$

are the normalised angular frequency, and normalised radial and circumferential integral length scales; and

$$n = \Omega/2\pi \quad \text{and} \quad q = 1/2\rho_0 U_0^2 \tag{8.6}$$

are the rotational frequency and the dynamic pressure. The Sears and admittance functions are given by

$$|\mathcal{S}\left(\frac{\omega^* c}{R}\right)|^2 \approx \frac{1}{1 + \pi\omega c/U_R} \tag{8.7}$$

and

$$\mathcal{A}(\omega^*) = \frac{\sin(\pi\omega^*)\exp i(B-1)\left[\frac{\pi\omega^*}{B}\right]}{\sin(\frac{\pi\omega^*}{B})}. \tag{8.8}$$

The length scale function is

$$\mathcal{F}(\omega^*\mathcal{L}_\theta^*) = \frac{\mathcal{L}_\theta^*}{1+(\omega^*\mathcal{L}_\theta^*)^2}. \tag{8.9}$$

The integral length scales in Equations 8.4a and 8.4b are approximated as a circumferential average of the Cartesian length scales $\mathcal{L}_0$ used in the simulations, giving $\mathcal{L}_R = \mathcal{L}_\theta \approx 0.35\ m$.

The far field acoustic mean square pressure is derived from $\overline{T^2}$ using

$$\overline{p'^2}(\boldsymbol{r}, f, \Delta f) = \left(\frac{\kappa\cos\theta}{4\pi|\boldsymbol{r}|}\right)^2 \overline{T^2}(f, \Delta f). \tag{8.10}$$

Equation 8.10 assumes that the far-field pressure is radiated from a compact dipole, which requires $He << 1$. Assuming that $He = 0.5$ satisfies this condition sufficiently, and defining the source size L to be equal to the turbine diameter D, the compact assumption holds up to $f \approx 150\ Hz$ in water. This upper frequency limit is high enough to include the inflow turbulence noise spectrum or the present test case.

8.4 Turbine in open domain

8.4.1 Inflow turbulence

It is important to consider the effect of the rotating grid on the resolved turbulence. If eddies do not convect through the interface accurately, the rotor will not see the correct turbulence spectra. This issue is analysed in Figure 8.5, where views of the resolved velocity fluctuations are shown. Figure 8.5(a) shows that turbulence structures do convect through the AMI without experiencing a large amount of numerical dissipation. This is consistent with the formulation of the method and experience reported by Bensow (2013) (see Section 4.5). The largest interpolation error is seen at the corners of the AMI; since this is far away from the turbine, this is not expected to have a large effect on the fluctuations experienced by the rotor blades. Qualitative comparison of the streamwise slices shown in Figures 8.5(b) and 8.5(c) provides further evidence that small scale turbulence passes into the rotor region.

Figure 8.6 provides qualitative evidence that the range of resolved scales does not appear to be affected by the AMI. The grid cutoff of $2\overline{\Delta}$ has been realised, corresponding to a frequency of $\approx 47\ Hz$. An additional measure of the interpolation quality at the AMI

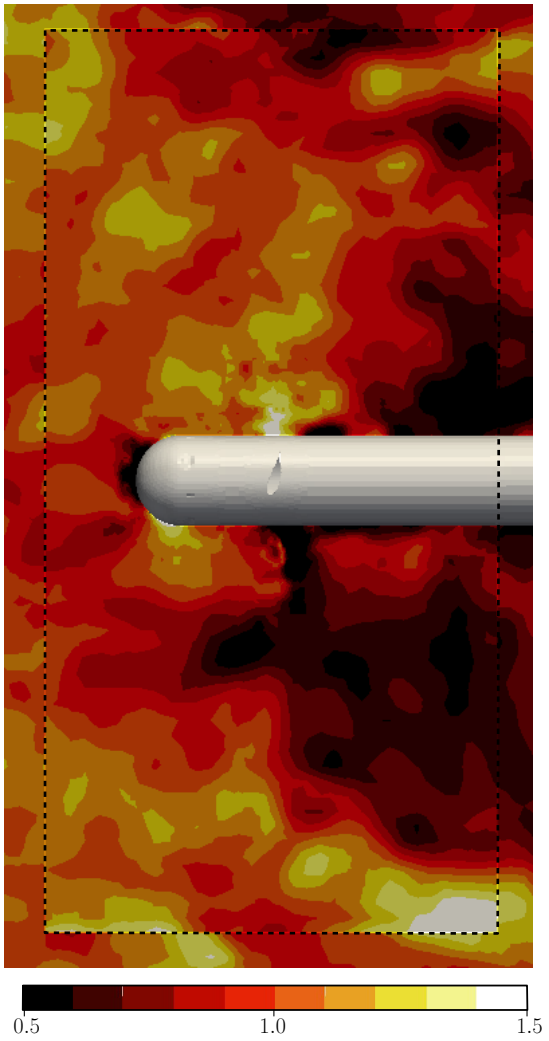

(a) Centreline constant z slice of axial velocity u^*. AMI outline visible as dashed line.

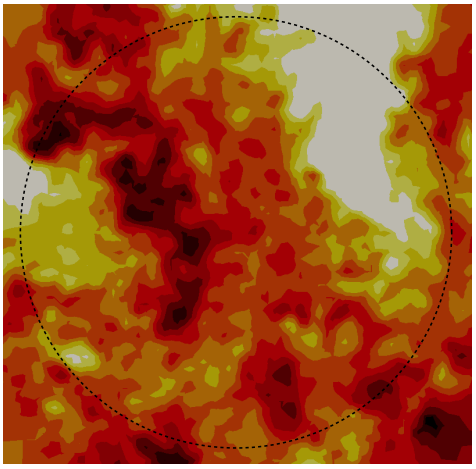

(b) Constant x slice of axial velocity u^* at $x/D = -0.375$. Colour scale as in Figure 8.5(a).

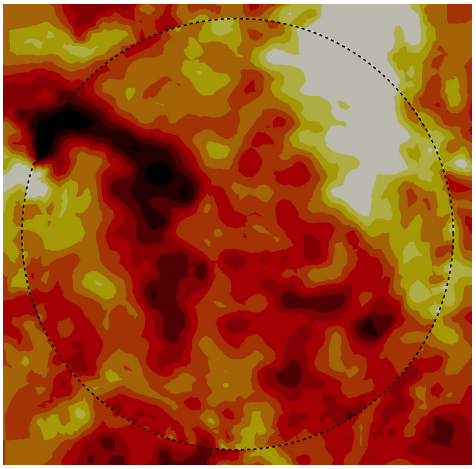

(c) Constant x slice of axial velocity u^* at $x/D = -0.25$. Colour scale as in Figure 8.5(a).

FIGURE 8.5: Effect of AMI on resolved turbulence: axial velocity upstream of turbine.

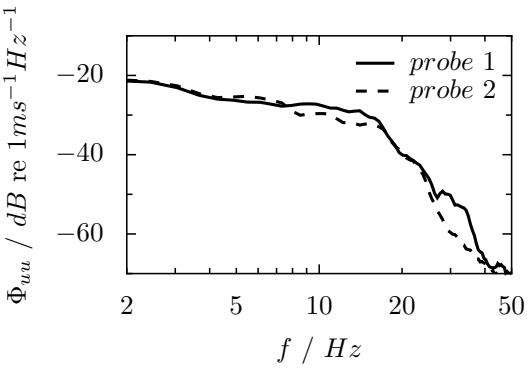

FIGURE 8.6: Streamwise velocity spectra at probe locations upstream and downstream of arbitrary mesh interface.

is a Courant number based on the turbine rotational velocity, *i.e.*

$$Co = \frac{\Omega R \Delta t}{\Delta x}, \tag{8.11}$$

where R is the radius of the AMI. Based on a cell size $\Delta x = 0.015\ m$, this results in $Co =$

0.0069. For comparison, Co has been estimated for simulations reported by McNaughton *et al.* (2013*a*). These authors addressed the laminar vortex shedding of a circular cylinder rotating perpendicular to the flow direction. The non-dimensional rotation rate based on the cylinder radius R is $\Omega R/U_0 = 0.5$, with the interface is placed at $4R$. This results in $Co \approx 0.064$, which is approximately an order of magnitude higher than that estimated for the present study. The cylinder case reported by McNaughton *et al.* (2013*a*) only concerns laminar flow solved using RANS, and hence a direct comparison is not strictly possible; a higher resolution is required for the tidal turbine case also reported by these authors (as also reported by Afgan *et al.* (2013)). The present study must provide a high resolution at the interface, due to the broadband nature of the turbulence passing through it. When simulating the same turbine using LES, Afgan *et al.* (2013) required that the grid rotation per time step should be less than half the interface cell size. They note however that the Courant number limit imposed by the cell sizes in the blade boundary layer results in a time step 10-30 times smaller than this requirement. For the present study, the time step is 35 times smaller than that recommended at the interface; thus the simulations are deemed well resolved in this respect.

Having deemed the AMI resolution to be sufficient, the turbulence statistics are now analysed in more detail. Since in the open domain case, the inflow turbulence will decay with streamwise distance, an increased turbulence intensity was input at the generator plane. Using the same method as described in Section 5.4, a value of $\mathcal{I} \approx 20\%$ was estimated. Table 8.3 summarises turbulence statistics sampled upstream of the turbine rotor plane.

TABLE 8.3: Summary of velocity probe data for tidal turbine in open domain. Probe locations shown to right of table, including rotor (solid lines) and AMI (dashed lines).

probe	1	2	3	4
x/D	-0.375	-0.25	-0.25	0.25
y/D	0.0	0.0	0.35	0.35
$\overline{u}$	1.20	0.97	1.11	0.81
$\mathcal{I}_x/\%$	13.8	15.7	19.3	24.0
$\mathcal{I}_y/\%$	12.7	15.2	17.0	21.0
$\mathcal{I}_z/\%$	15.0	20.2	19.7	21.6
$\mathcal{L}_x/m$	0.81	0.43	0.3	0.21

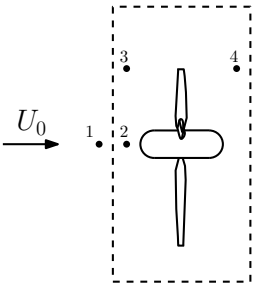

Turbulence intensity is higher than the desired value of 10% at both centreline probe locations. This is partially related to the increased value of $\mathcal{I}$ specified at the inflow plane in order to account for streamwise decay. However, the increase in $\mathcal{I}_x$ from probe locations 1 to 2 may be attributed to the blockage caused by the turbine rotor. This effect has also been observed for the stationary foil in Section 6.4. The over-prediction of $\mathcal{L}_x$ at probe location 1 is also a result of the inflow generator, which has been shown to give larger integral length scales than specified (see Section 5.4.3). A reduction in length scale is seen at probe location 2.

This is again related to the blockage of the rotor. Mean flow distortion of turbulence has indeed been shown to affect noise spectra (Amiet *et al.*, 1990; Simonich *et al.*, 1990). These authors addressed stretching of isotropic turbulence in relation to helicopter rotor noise. They concluded that stretching aligned with the rotor axis serves to reduce the upwash velocities on the the blades, and hence the noise. This scenario relates to a tidal turbine in terms of the principal axis of mean flow distortion. Since the turbine is a momentum extraction device however, the rotor acts to 'compress' the upstream flow, rather than stretch the streamwise length scales. This is accompanied by an increase in the integral time scale, in order to satisfy the continuity condition (a decrease in the integral time scale was predicted by Glegg *et al.* (2013) for a propeller).

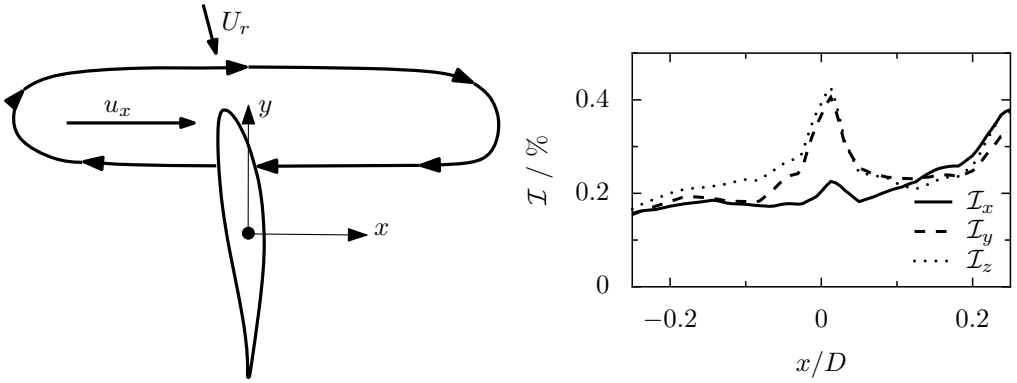

(a) Schematic showing turbine blade passing through an anisotropic eddy.

(b) Turbulence intensities sampled along a streamwise line at $r/R = 0.7$.

FIGURE 8.7: Effect of turbine rotor on local velocity fluctuations. For a typical blade section towards the blade tip, ϕ is small (typically $< 5°$ for optimum lift/drag ratio), meaning the upwash velocity is approximately equal to u_x.

This process is visualised in Figure 8.7(a), which depicts a schematic representation of a turbine blade encountering an anisotropic eddy. Since the optimum lift/drag ratio occurs between two and four degrees angle of attack (Molland *et al.*, 2004), and the section twist is small for the outer blade sections (1.5° at $r/R = 0.7$), the hydrodynamic pitch is also small ($< 5°$). This results in the local upwash velocity being effectively aligned with the streamwise direction. Figure 8.7(b) shows the turbulence intensity components along a streamwise line at $r/R = 0.7$. Based on the theory of Amiet *et al.* (1990), the compression described previously would lead to increased streamwise velocity fluctuations, with attenuation in the rotor plane (using the data presented by Batchelor and Proudman (1954), using rapid distortion theory). The increase in $\mathcal{I}_x$ observed in Figure 8.7(b) is small however, meaning it is hard to conclude whether or not this would have an effect on the radiated noise.

A visualisation of the flow is provided in Figure 8.8, which shows turbulence structures. The snapshot has been taken at $T^* = 1.3$, which corresponds to the transient phase of the simulation, in order to show the distinction between the inflow and wake turbulence. The fully developed turbine wake results from initialising the simulation from a solution

without inflow turbulence. On the left of the figure, the large streamwise length scale of the inflow turbulence may be observed; based on the specified parameters, scales as large as the rotor diameter should exist. Behind the rotor plane, tip vortices are seen to convect through the AMI. Vortices also form from the turbine hub. In the near wake region ($x/D < 5$) the wake structure appears fairly coherent, while further downstream, the increase in turbulence mixing leads to more fine scale structures.

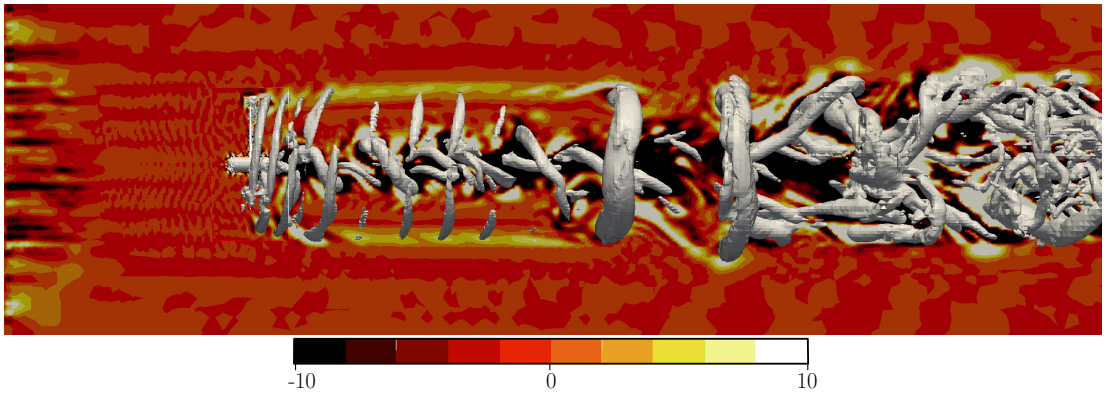

FIGURE 8.8: Flow visualisation of turbine in open domain at $T^* = 1.3$ (prior to inflow turbulence reacing turbine): isosurface of $Q = 10\ s^{-1}$ and x-y plane slice of ω_x^* at domain centreline. Inlet on left.

8.4.2 Unsteady loading

Performance assessment of the turbine can be made in terms of thrust and power. Figure 8.9(a) depicts time traces and corresponding spectra of the turbine thrust and power. The instantaneous thrust and power coefficients monitored during the simulation were calculated as

$$C_T(t) = \frac{2F_x(t)}{\rho_0 A U_0^2} \tag{8.12a}$$

and

$$C_P(t) = \frac{2\Omega Q(t)}{\rho_0 A U_0^3}, \tag{8.12b}$$

where F_x is the thrust (streamwise force), and Q is torque. The mean values for both numerical and experimental results are included in Figure 8.9(a), as well as in Table 8.4. An increase in thrust coefficient between the LES cases with and without inflow turbulence is seen. No corresponding increase in power is observed however. This agrees with similar studies from the literature (McNaughton *et al.*, 2013*b*). In comparison to the BEMT results, the LES value of $\overline{C}_T$ is closer to the experiment, while for $\overline{C}_P$ the BEMT shows better agreement. This is due to the use of wall functions in the LES, which (in OpenFOAM) have been shown to under-predict drag compared to a wall-resolved boundary layer (Banks, 2013). Since the BEMT includes empirical blade section lift and drag data, this effect is not as prominent when using this method. Afgan *et al.* (2013) found that a grid of 5×10^6 cells under-predicted thrust by $\approx 6\%$ compared

to a 21×10^6 cell grid. This may be a further reason for the discrepancy in the mean thrust prediction.

Root mean square performance coefficients from the present study are compared to those reported by Afgan *et al.* (2013). They reported results for $\mathcal{I} = 1$, 10 and 20%, at $\gamma = 20°$ and $\Lambda = 6$. Hence the cases are not exactly the same; the data presented in Table 8.4 are for $\mathcal{I} \approx 20\%$, since this is closest to the present study. The values of $\overline{C'}_{T,rms}$ and $\overline{C'}_{P,rms}$ for the present study are higher than those reported by Afgan *et al.* (2013); it is expected that increasing the total averaging time would improve these statistics, but without experimental comparison data this is hard to validate. The magnitudes of the *rms* values for the LES case with inflow turbulence are approximately 30 times higher than for the case without. Afgan *et al.* (2013) presented similarly small values for a case with $\mathcal{I} \approx 1\%$.

TABLE 8.4: Comparison of turbine performance coefficients: mean (top) and *rms* (bottom). Values from BEMT reported in Banks *et al.* (2013). Large eddy simulation cases with (†) and without (‡) inflow turbulence.

case	exp.	LES†	LES‡	BEMT
$\overline{C}_T$	1.00	0.98	0.90	0.86
$\overline{C}_P$	0.36	0.43	0.43	0.37

case	LES†	Afgan *et al.* (2013)	LES‡
$\overline{C'}_{T,rms}$	0.0535	0.0039	0.0015
$\overline{C'}_{P,rms}$	0.0510	0.0024	0.0017

Two main features are evident in Figure 8.9(a). The slowly varying part is associated with the passage of the largest length scales; these have a period of just over one second, corresponding to a length scale approximately twice the integral length. The higher frequency fluctuations may be attributed to the blades 'cutting' through long streamwise eddies. These effects may also be examined in Figure 8.9(b). The broadband spectra are characterised by haystacks close to the BPF and first harmonic[1] (at approximately 10 and 20 Hz). The decibel difference between the numerical spectra and representative smooth curve at these frequencies is indicated in the figure. A magnitude of $10\log_{10}(B)$ (or $\approx 4.8\ dB$) is also predicted by Blake (1984, chap. 10) using Equations 8.4a and 8.4b. This is due to the shape of the admittance function (Equation 8.8), which applies only when $\mathcal{L}_x >> P/B$.

An estimate of the turbine hydrodynamic pitch can be made using the local resultant flow velocity seen by a blade section. A radius $r = 0.7R$ was used, with streamwise and tangential inflow factors of $a = 0.32$ and $a' = 0.025$ estimated using blade element momentum theory Turnock *et al.* (2011). The pitch is given by $P/D = \pi \tan(\phi)$, where $\phi = \alpha + \gamma$ is the hydrodynamic pitch angle, defined in Figure 8.2(b) and α is the local angle of attack. This results in $\phi \approx 9.1°$ and $P/D \approx 0.5$, which implies $P/B \approx 0.134$.

[1]The blade passing frequency is taken to be the 0^{th} harmonic.

This confirms that the magnitude of the haystacks seen in Figure 8.9(b) is due to the streamwise integral length scale exceeding the rotor pitch. Jiang *et al.* (1994) used a similar analytical model to analyse propeller broadband forces. They emphasised the presence of only two prominent haystacks, whose peaks are skewed to slightly higher frequencies than the BPF and first harmonic. This effect can be seen in Figure 8.9(b), although the 1 Hz bandwidth of the spectra prevent the exact peak frequencies from being identified.

The haystacking observed in the thrust and power spectra can be further understood by comparing total rotor and single blade thrust. This is presented in Figure 8.10. The combined thrust from all three blades is also shown; this is equivalent to increasing the single blade thrust by $10\log_{10}(3)$. Note that the dashed line is comparable to the dashed line in Figure 8.9(b), which corresponds to a response spectrum where $\mathcal{L}_x < P$. Summing the blade thrust spectra removes phase information relating to blade-to-blade correlation, and hence the spectral humps are not captured.

Figure 8.11 presents distributions of mean and *rms* surface pressure on the turbine blades, for cases both with and without inflow turbulence. The data presented includes $\overline{C'}_{p,rms}$, the root mean square fluctuation, already used in Chapter 6. Additional pressure coefficients are defined using the local relative velocity, such that

$$\overline{C}_{pr} = \frac{2p}{\rho_0(U_0^2 + \Omega^2 r^2)}, \tag{8.13}$$

where p is either a mean or *rms* pressure. Whilst there is not a large difference between the cases with and without inflow turbulence in terms of $\overline{C}_p$, the *rms* pressure reveals the impact of the unsteady inflow on blade loading. This effect was noted, but not presented, by Afgan *et al.* (2013). Figure 8.11(a) shows higher values of $\overline{C'}_{p,rms}$ close to the blade leading edge for the case with inflow turbulence. This is comparable to the results presented in Chapter 6 for the stationary foil. As observed there, the pressure fluctuations are localised within $\approx 5\%$ of the leading edge. In the absence of inflow turbulence a different chordwise pressure distribution is observed. The effect is most clearly seen at $r/R = 0.3$, where $\overline{C'}_{p,rms}$ peaks in the front half of the suction side, and the back half of the pressure side. The suction side behaviour is explained by the acceleration of the fluid around the blade, which results in an unsteady surface pressure. Figure 8.11(c) confirms this. On the pressure side, the blade is partly separated, causing an increase in *rms* pressure. This is observed in Figure 8.11(e)).

Normalisation of *rms* pressure by local flow velocity is misleading in terms of examining acoustic pressure magnitude, hence the decision to present additional plots in Figure 8.11(a) using the freestream velocity for all radial sections. This clearly shows the increasing magnitude of the fluctuating pressure towards the blade tips.

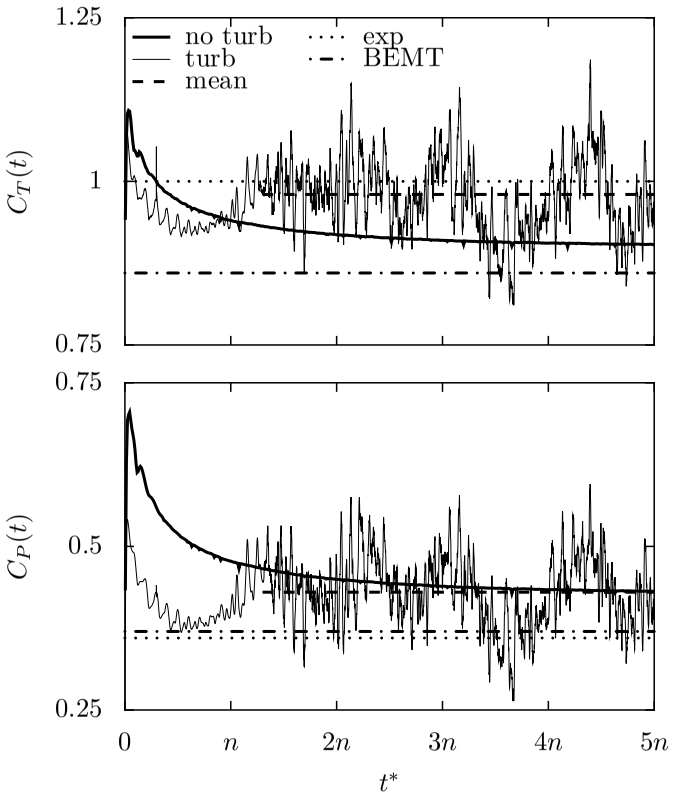

(a) Time trace of thrust and power coefficient for cases with and without inflow turbulence. Time non-dimensionalised by n. Dashed and dotted lines show numerical and experimental mean values, with averaging duration indicated by length of line.

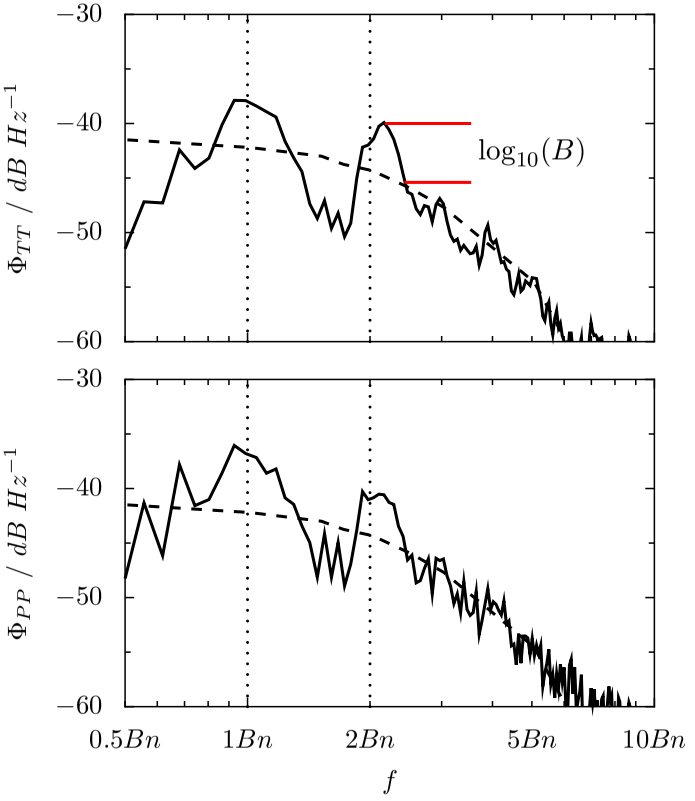

(b) Power spectral density of time traces. Dashed line indicates equivalent smooth spectrum ($\mathcal{L}_x << P$); dotted line denotes blade passing frequency and 1^{st} harmonic.

FIGURE 8.9: Turbine thrust and power, for turbine in open domain.

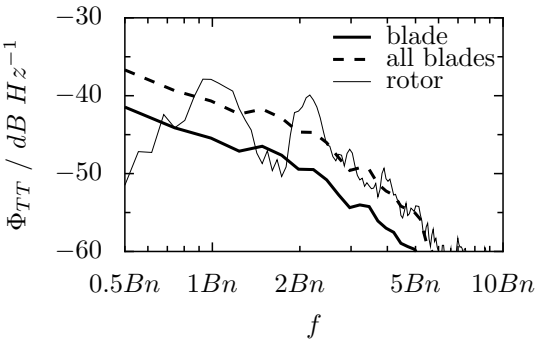

FIGURE 8.10: Comparison of thrust spectra for single blade, all blades and rotor. Spectral level for all blades is $10\log_{10}(3)$ higher than for single blade. Dashed line equivalent to dashed line in Figure 8.9(b).

8.4.3 Model scale acoustic predictions

The acoustic sources on the blades are viewed as SPL_w in Figure 8.12. The distribution of the acoustic sources is similar to that seen in Figures 8.11(b) and 8.11(c). A value range has been chosen to highlight the difference between the two cases; hence some of the detail of the source distribution in Figure 8.12(a) is not shown. The transitional flow in the case without inflow turbulence is again clear in Figure 8.12(b). Figure 8.12(a) shows a higher source level across most of the blade span, with the highest source amplitude located on the outer part of the blade. The exact spanwise and chordwise location of the highest SPL_w is unclear however, due to much of the source level exceeding the maximum value of 130 dB. This is addressed in Figure 8.13.

In order to locate the dominant acoustic source more accurately, the SPL_w has been re-scaled and displayed close to the tip ($r/R = 0.8 - 1.0$). Shown in Figure 8.13 this reveals that the acoustic source is centred in the outer region of the blade, but not at the tip ($r/R \approx 0.9$). This corresponds to the location of peak spanwise loading for a typical turbine blade (Turnock *et al.*, 2011), and is similar to that expected for trailing edge noise (Oerlemans *et al.*, 2007). In addition, the source is concentrated at the blade leading edge. This was expected based on the source distributions exhibited for stationary foils, both in the current work (Section 6.4) and for typical wind turbine aerofoils (Migliore and Oerlemans, 2004). Certain locations in Figure 8.13(a) do show a higher source level towards the trailing edge however. This is also revealed in Figure 8.14, and is explained by flow separation. A final point to note is the higher SPL_w on the suction side of the blade, which indicates that the far-field noise may be higher downstream of the device.

A further method for viewing acoustic sources is Powell's sound source term (Powell, 1964), first presented in Equation 2.22. It has previously been used to visualise turbomachinery noise, particularly in relation to noise reduction studies (*e.g.* see Corsini *et al.*, 2009; Fleig *et al.*, 2004). This measure is shown in Figure 8.14. Recalling that the fluctuating surface pressure (Figure 8.12) is a trace of the vorticity convecting over the blades (Powell, 1964), Powell's sound source shows a concentration at the blade leading edge, particularly on the suction side, as well as the blade tip.

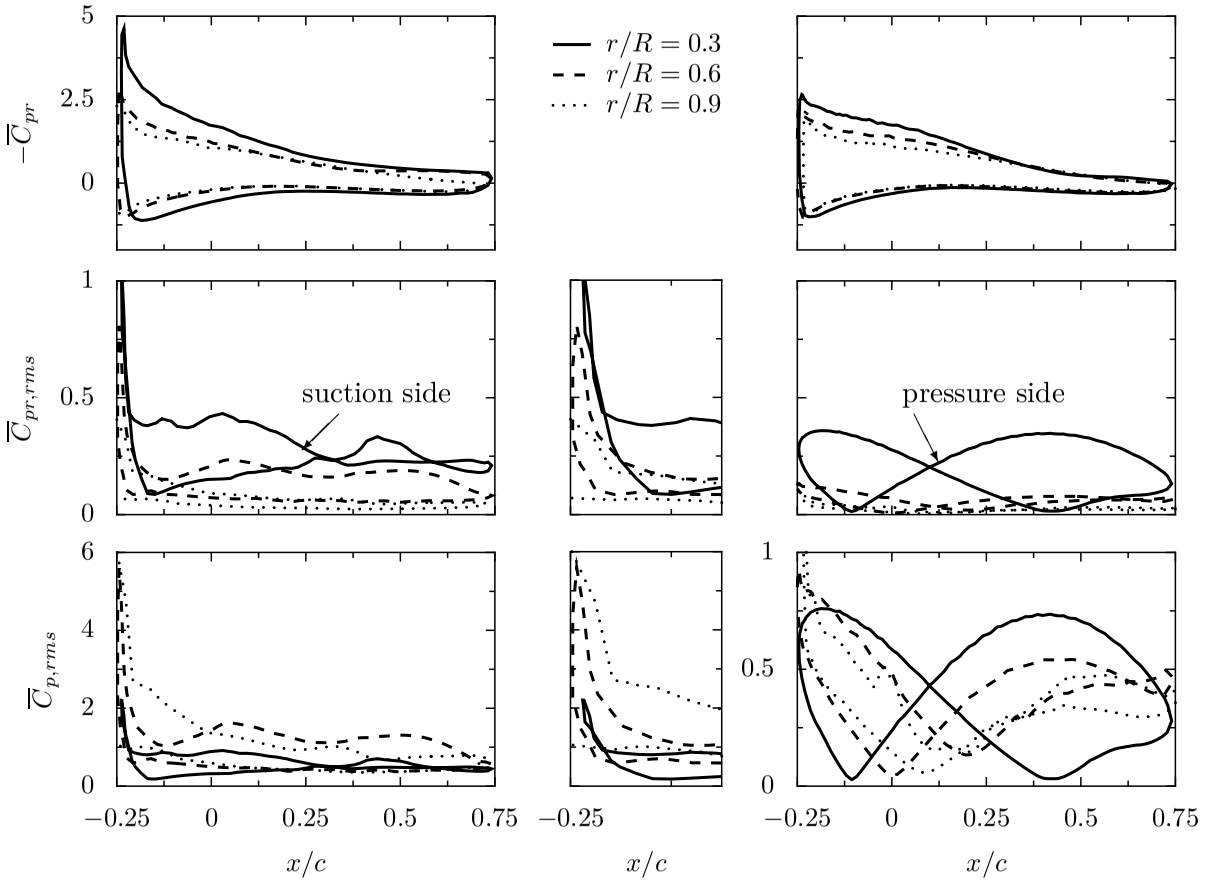

(a) Comparison of surface pressure coefficient distributions: mean (top); *rms* using local relative velocity (middle); *rms* using freestream velocity (bottom). Turbine cases with (left) and without (right) inflow turbulence, sampled at three radial locations blade span. Centre plots are $\overline{C}_{p,rms}$ showing only first 15% of chord. Note difference in scale for $\overline{C}_{p,rms}$ between cases with and without inflow turbulence.

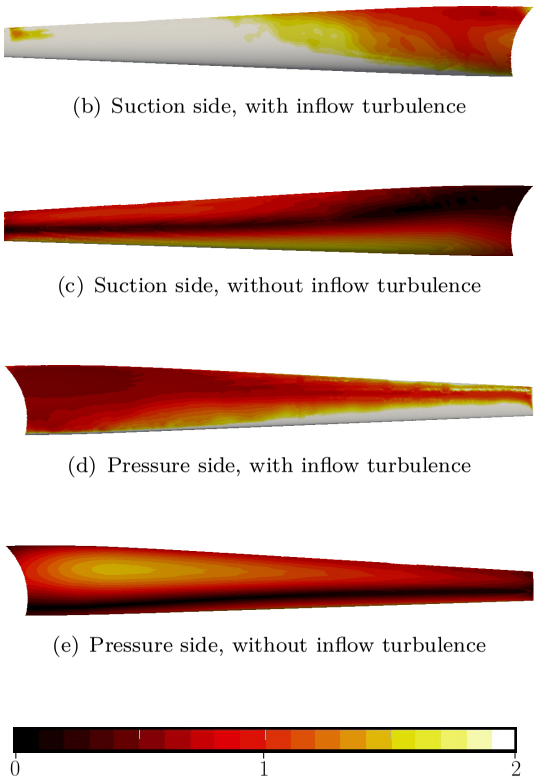

(b) Suction side, with inflow turbulence

(c) Suction side, without inflow turbulence

(d) Pressure side, with inflow turbulence

(e) Pressure side, without inflow turbulence

(f) colour scale

FIGURE 8.11: Comparison of surface pressure coefficient distributions with and without inflow turbulence: chordwise pressure distributions (a); blade surface $\overline{C}_{p,rms}$ (b)-(f).

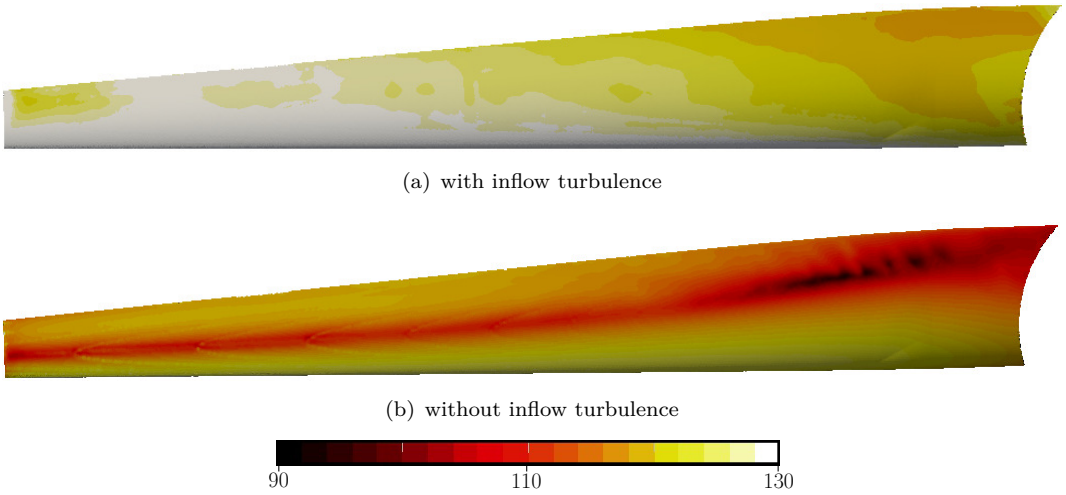

(a) with inflow turbulence

(b) without inflow turbulence

FIGURE 8.12: Acoustic source on suction (downstream) side of turbine blades for open domain, visualised as surface sound pressure level SPL_w ($p_0 = 1\mu Pa$). Colour scale in dB.

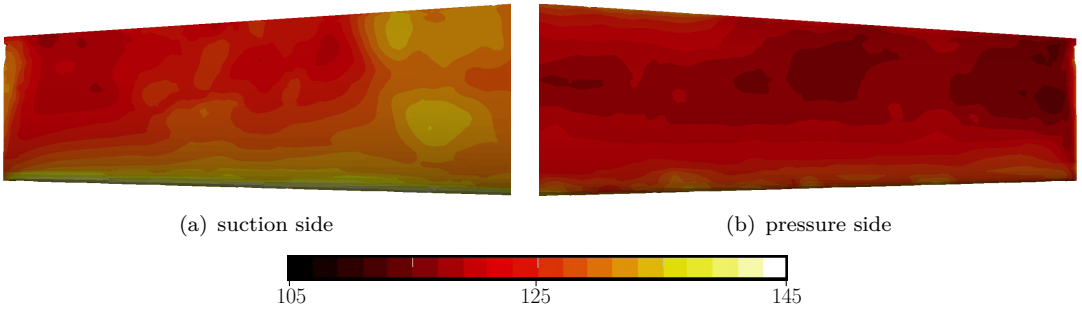

(a) suction side

(b) pressure side

FIGURE 8.13: Acoustic source on turbine blade tip, visualised as surface sound pressure level SPL_w ($p_0 = 1\mu Pa$). Colour scale in dB.

The difference between the source distributions is clear when comparing Figures 8.14(a) and 8.14(c). A localised region of the isosurface near to the blade trailing edge (see Figure 8.14(a) insert) is associated with flow separation. This constitutes an additional noise source which would not have been resolved if the blades had been modelled as slip walls. The separation is caused by a region of high velocity turbulence impinging onto blade 1, as shown in Figure 8.14(d). This shifts the local relative velocity, increasing the angle of attack, causing flow separation. In the absence of an increased inflow velocity, the size of this separated region is reduced, as shown in Figure 8.14(b).

Turbine noise was predicted using the free-field FW-H method (Equation 3.6) at the receiver angles given in Figure 8.4. It is known that the highest overall SPL for inflow turbulence noise occurs at $\theta = 0°$, based on the dipole assumption; this data is presented in Figure 8.15, with comparison to Blake's model. The numerical result compares favourably with the analytical model. The maximum discrepancy between numerical and analytical SPL is 5 dB, which occurs at the BPF. Differences between the two analytical scenarios presented are also clear, especially at low frequencies. Humps at the BPF and associated harmonics are well captured by the simulation. The intermediate

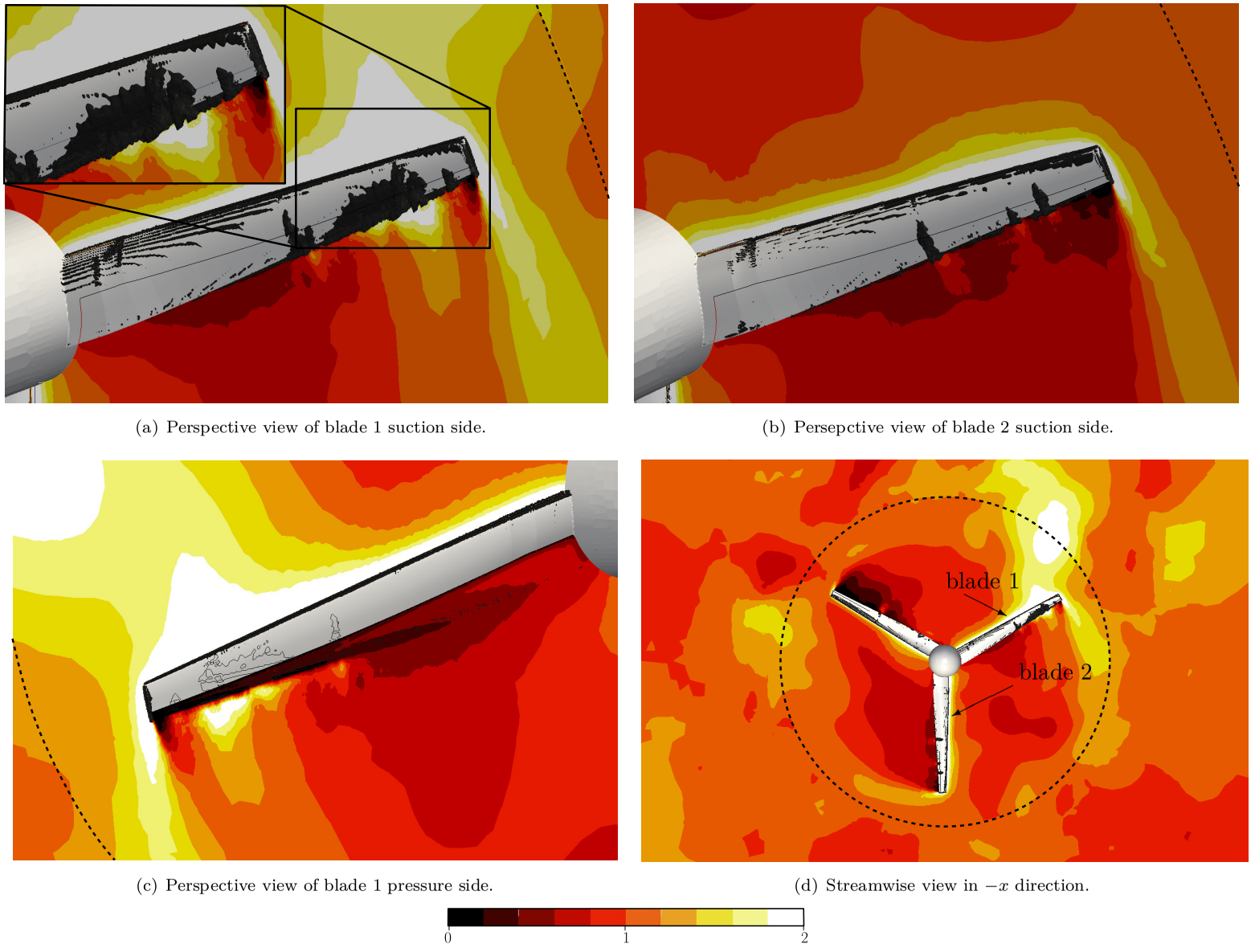

(a) Perspective view of blade 1 suction side.

(b) Persepctive view of blade 2 suction side.

(c) Perspective view of blade 1 pressure side.

(d) Streamwise view in $-x$ direction.

FIGURE 8.14: Distribution of Powell's sound source close to turbine blades: isosurfaces of $\mathcal{F} = \nabla \cdot (\boldsymbol{\omega} \times \boldsymbol{u}) = 5 \times 10^6$ (black) and rotor plane slices of normalised instantaneous axial velocity u^*.

humps are however not as clearly visible in the numerical spectrum as the analytical; this is partly related to the bandwidth of the *fft* and is most evident at low frequencies. This part of the spectrum would be more accurately predicted if the total simulation duration were increased.

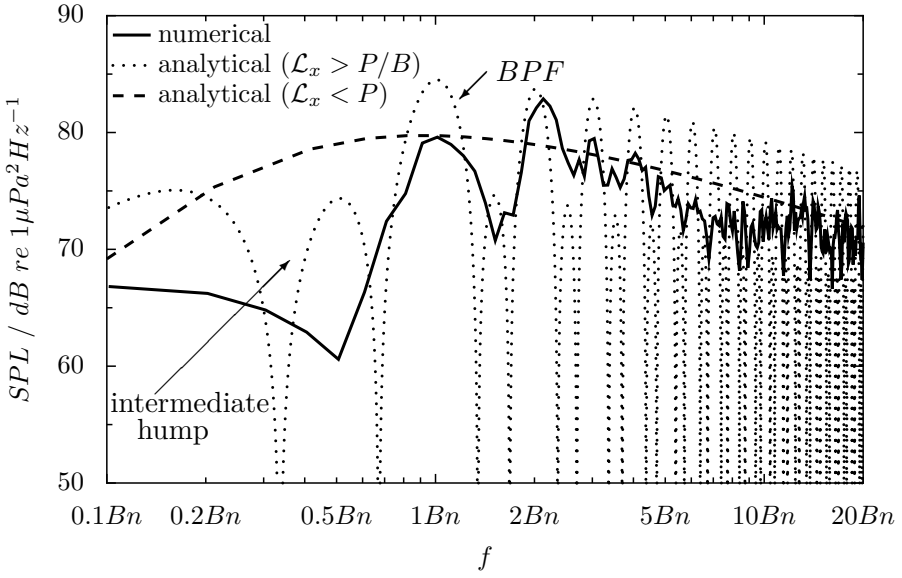

FIGURE 8.15: Sound pressure level for model scale turbine in open domain at $\theta = 0°$ and $|\boldsymbol{r}| = 2D$, predicted using FW-H equation and Blake's analytical model. $\Delta f = 1$ Hz. Dashed line indicates equivalent smooth analytical spectrum ($\mathcal{L}_x << P$); dotted line denotes analytical spectrum where $\mathcal{L}_x >> P/B$.

The effect of changing bandwidth on the SPL spectra is presented in Figure 8.16. The largest bandwidth of 6.75 Hz complies with the sampling criterion proposed by Michel *et al.* (2009) and discussed in Section 3.6.1. This requires that $T\Delta f = 25$; in this case the total averaging time of $T^* \approx 12$ results in a large bandwidth if the criterion is adhered to. This has a large effect on the spectral shape, since the turbine noise is dominant at low frequencies. It is also observed that small bandwidths of 0.1 and 0.01 Hz do not change the spectral amplitudes significantly, justifying the use of a 1 Hz bandwidth in Figure 8.15.

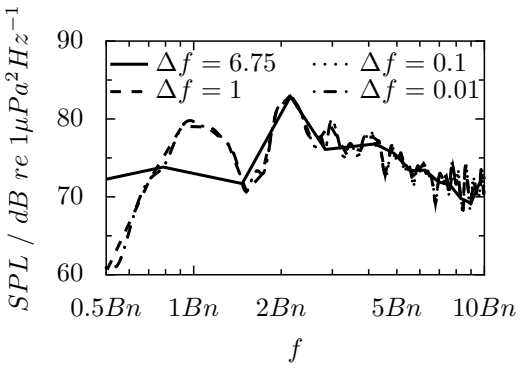

FIGURE 8.16: Effect of bandwidth on sound pressure level spectrum for model scale turbine in open domain at $\theta = 0°$ and $|\boldsymbol{r}| = 2D$. Bandwidths Δf in Hz.

Noise directivity is examined in Figure 8.17. Figure 8.17(a) compares the simulation result presented in Figure 8.15 to predictions made at $\theta = 45°$ and 90°. It is evident

that the expected behaviour of a pure acoustic dipole, assumed in the analytical model, is not fully realised in the simulation. At the BPF, a difference of approximately 20 dB is seen between receiver angles of 0° and 90°. This is also shown in terms of the overall sound pressure level, plotted in Figure 8.17(b). The overall sound pressure level (OASPL) is defined as

$$OASPL = 10 \log_{10} \left[\frac{\int_{f_1}^{f_2} \Phi_{pp} df}{p_0^2} \right], \tag{8.14}$$

which is the decibel level of the normalised acoustic energy across the frequency range $f_1 - f_2$. The reduction in $OASPL$ between 0° and 90° is ≈ 16 dB.

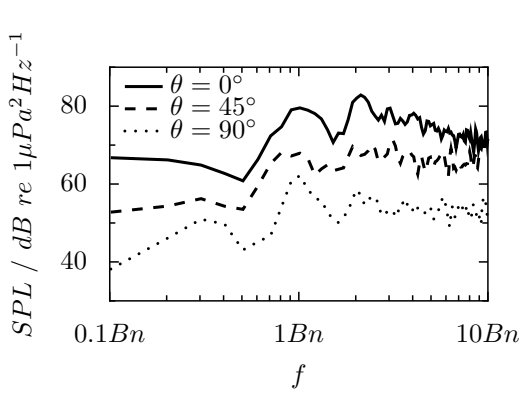

(a) Sound pressure level for model scale turbine in open domain for range of receiver angles, predicted using FW-H equation and Blake's analytical model. $\Delta f = 1$ Hz. Approximately 20 dB difference in SPL between $\theta = 0°$ and 90° at BPF.

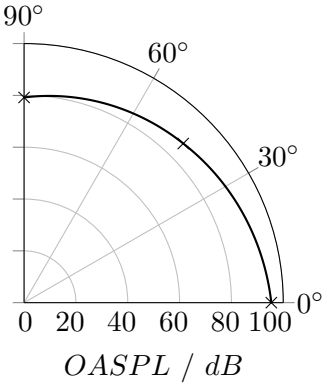

(b) Overall sound pressure level directivity for model scale turbine: $f_1 = 1$ Hz; $f_2 = 100$ Hz. Crosses denote values derived from data presented in Figure 8.17(a); solid line is a curve fit.

FIGURE 8.17: Noise directivity for model scale turbine: case with inflow turbulence, at $|\boldsymbol{r}| = 2D$.

Morton *et al.* (2012) observed a similar behaviour, with typically 10 dB difference between the same receiver angles. This monopole-like behaviour can be attributed to increased tip loading at low advance coefficients. The turbine advance coefficient ($J = \pi/\Lambda = 0.53$) is slightly lower than that used by Morton *et al.* (2012), where $J = 0.7$. The high tip loading for the present case (as was shown in Figure 8.13) explains this phenomenon. Hence there is potential for further investigation of the effect of turbine operating condition on noise directivity. Despite this, Figure 8.17(a) provides evidence of the improved predictive capabilities of the simulation compared to the analytical model used here.

The final comparison in this section is between cases with and without inflow turbulence. The noise directivity without inflow turbulence is shown in Figure 8.18, along with the data for the case with inflow turbulence at $\theta = 0°$ (already presented in Figure 8.15).

Since a 40 dB difference in SPL exists at all frequencies between the two data sets at $\theta = 0°$, it may be concluded that the loading noise in the turbine axis is negligible

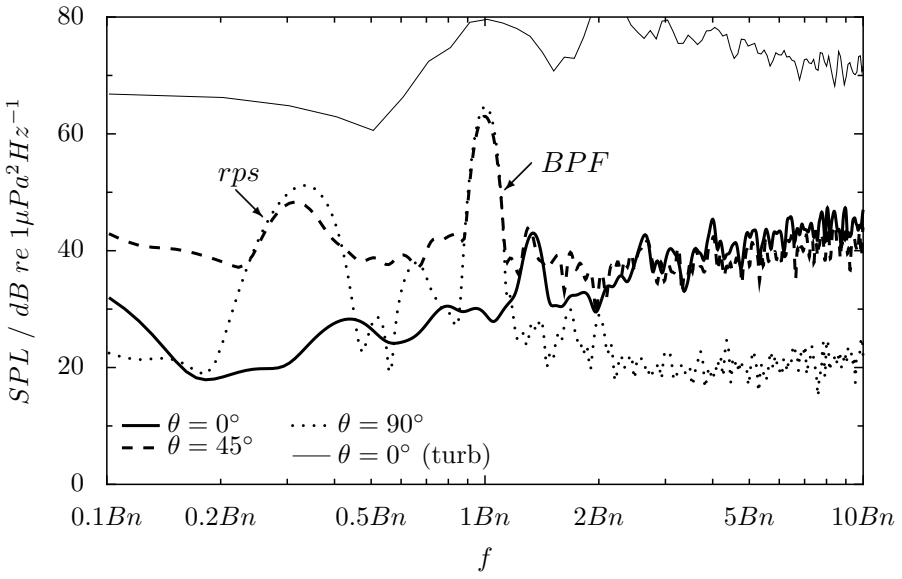

FIGURE 8.18: Noise directivity for model scale turbine: case without inflow turbulence, at $|\boldsymbol{r}| = 2D$. Steady loading (Gutin sound) indicated at rotation rate (rps) and blade passing frequency (BPF). Data for case with inflow turbulence at $\theta = 0°$ included for comparison ($turb$).

when the inflow is steady. This would be expected, since there are no incoming velocity fluctuations to generate unsteady thrust on the rotor. However, at $\theta = 45$ and 90°, there is clear evidence of a tonal noise component. This dominates at the BPF, but also appears to have some frequency content at $f = n$, and is known as *steady loading*, or *Gutin sound* (Gutin, 1948)[2]. This noise mechanism is also negligible on the rotor axis, and has a peak downstream of the rotor plane, as illustrated in Figure 8.19. Steady loading is negligible for subsonic rotors (Goldstein, 1976, chap. 3). This is shown by the $\approx 20\ dB$ difference between the maximum Gutin sound (at $\theta = 90°$) and the maximum unsteady loading (at $\theta = 0°$).

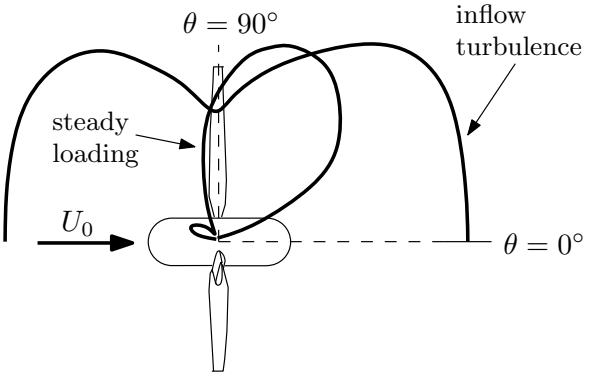

FIGURE 8.19: Schematic illustration of directivity for inflow turbulence and steady loading noise.

[2]The cited report is a translation of the original 1936 German publication Über das Schallfeld einer rotierenden Luftschraube, *Physikalische Zeitschrift der Sowjetunion*, **9**(1), pp. 57-71.

8.4.4 Full scale acoustic predictions

In order to carry out environmental impact studies, full scale turbine source levels are required. This data may be used to investigate animal response experimentally (Halvorsen *et al.*, 2011) or make noise impact predictions at the turbine design stage (Lloyd *et al.*, 2011*a*). Full scale turbine noise has been assessed using two approaches: scaling of the model scale simulation results from Section 8.4.3 (see Lloyd *et al.*, 2013*b*); and use of Blake's model for a full scale turbine (as reported in Lloyd *et al.*, 2011*b*).

Rudimentary scaling is based on the Strouhal number $St = fD/U_T$, where $U_T = \sqrt{R^2\Omega^2 + U_0^2}$ and the acoustic intensity I. It has also been assumed that the noise scales independently of the blade Reynolds number *i.e.* boundary layer tripping or turbulence does not affect inflow turbulence noise (Migliore and Oerlemans, 2004). Denoting model and full scale values by the subscripts 'M' and 'F', the frequency scales as

$$f_F = f_M \frac{n_F}{n_M}. \tag{8.15}$$

The acoustic intensity can be assumed to scale as

$$I \propto \frac{\rho_0 u^5 \mathcal{L}^2}{c_0^2 r^2}, \tag{8.16}$$

following Howe (1998*c*, chap. 3). This is a more general form of Equation 8.3. Hence, taking $u = U_T$,

$$\overline{p_F'^2} = \overline{p_M'^2} \left(\frac{U_F}{U_M}\right)^5 \left(\frac{\mathcal{L}_F}{\mathcal{L}_M}\right)^2 \left(\frac{r_M}{r_F}\right)^2. \tag{8.17}$$

It has been assumed that the speed of sound is constant between model and full scale.

The result of applying this scaling procedure to the model scale data is shown in Figure 8.20. Blake's model using full scale parameters is also included. The full scale turbine is assumed geometrically similar to the model scale device, with a scale factor of 27.5. This results in a rotor diameter of 22 m, which is reasonable for installed turbines (Betschart, 2012), and has been used for both analytical (Lloyd *et al.*, 2011*a*) and numerical (Lloyd *et al.*, 2013*b*) studies. The tidal velocity is taken to be 2.5 ms^{-1}, with the same turbulence characteristics as described in Section 8.3.1. Figure 8.20 is evidence that the scaling procedure is reasonably accurate for this simple case. The cutoff frequency, as a result of the scaling procedure, reduces to ≈ 14 Hz. In order to allow comparison between model and full scale data, and to published source levels, indicative full scale sound levels are provided in Table 8.5. This is necessary due to the use of a smaller bandwidth in the analytical model at full scale, as well as the need to compare to source levels quoted in the literature for 1 Hz and third-octave bandwidths.

The 1 Hz bandwidth SSL of 144 $1\mu Pa^2\ Hz^{-1}$ at 1 m is ≈ 6 dB lower than the peak value predicted from measurement data by Wang *et al.* (2007), using a similar scaling

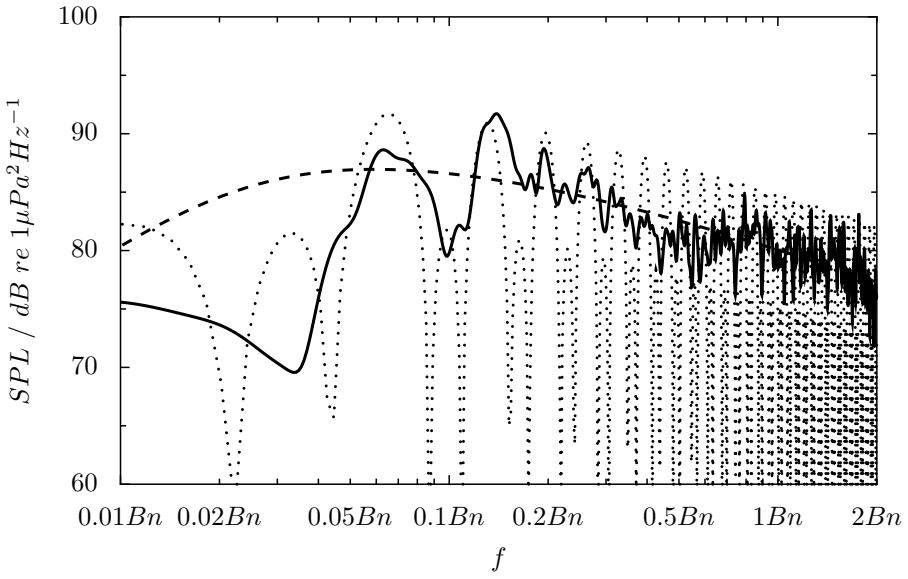

FIGURE 8.20: Sound pressure level for full scale turbine in open domain at $\theta = 0°$ and $|\boldsymbol{r}| = 2D$, predicted using scaling method and Blake's analytical model. $\Delta f = 0.01$ Hz. For SPL comparable to model scale data presented in Figure 8.15, see Table 8.5. Legend as in Figure 8.15.

TABLE 8.5: Full scale turbine noise levels at blade passing frequency, chosen to be representative of peak spectral level. Sound pressure level from scaled data.

acoustic quantity	Δf	correction	value	unit
SPL	0.01	-	88	dB re $1\mu Pa^2Hz^{-1}$
SPL	1	-	108	
SSL	0.01	$20\log_{10}(\lvert\boldsymbol{r}\rvert - 1)$	124	dB re $1\mu Pa^2Hz^{-1}$ at 1 m
SSL	1	$10\log_{10}(\Delta f)$	144	
third octave SSL	0.4	$10\log_{10}(\Delta f)$	140	

method. This discrepancy is likely due to cavitation noise, which was observed in the experiments, and has not been simulated. The cavitation number can be used to assess the likelihood of cavitation inception, and may be written as

$$\sigma = \frac{2(p_{atm} + \rho_0 g(H - h) - p_v)}{\rho_0(U_0^2 + \Omega^2 r^2)}, \tag{8.18}$$

where p_{atm} and p_v are the atmospheric and vapour pressures. Estimates for σ have been made for the full scale turbine operating in a 40 metre tidal channel resulting in $\sigma = 1.65$ (top dead centre); 2.55 (mid-depth) and 3.50 (bottom dead centre). Comparing these values to the section pressures presented in Figure 8.11(a), cavitation inception can be expected, based on the criterion $\sigma < -C_p$. Hence, cavitation is likely in the outer region of the blades which move closest to the free surface, and at higher velocity. Similar suction side leading edge cavitation was seen by Molland *et al.* (2004), who tested the NACA 63-815 section used to design the turbine blade simulated here.

A further noise source is expected to be mechanical noise, which results from the drive train components of the turbine. Account for this noise source can be made using a semi-empirical model (Lloyd *et al.*, 2011*a*). In this case, the resulting third-octave turbine source level is $\approx 160\ dB$ re $1\mu Pa^2\ Hz^{-1}$ at $1\ m$. In Lloyd *et al.* (2011*a*), the source level of the mechanical and hydrodynamic noise sources was estimated to be approximately equal. Assuming the two sources are incoherent, their sound pressure levels may be combined as

$$SPL_{AB} = 10\log_{10}\left(10^{\frac{SPL_A}{10}} + 10^{\frac{SPL_B}{10}}\right), \tag{8.19}$$

where 'A' and 'B' are two different incoherent sources. This results in a $\approx 3\ dB$ increase in combined source level.

8.5 Discussion

8.5.1 Environmental impact

It is noted that there is a difference in the frequency of the peak spectral amplitude between the numerical and experimental data of Wang *et al.* (2007). Whereas the tip vortex cavitation noise observed in the experiments was seen to dominate at 10-15 Hz, the equivalent frequency for inflow turbulence noise is $< 1\ Hz$. This is below the lowest frequency available from hearing threshold data for marine species (Richards *et al.*, 2007), and hence it is hard to assess its environmental impact. The cutoff frequency of the spectrum does however lie within the range of hearing threshold data. At $10\ Hz$, typical values for fish' hearing threshold and ocean background noise are $80\ dB$ re $1\mu Pa^2$ (Richards *et al.*, 2007) and $75\ dB$ re $1\mu Pa^2 Hz^{-1}$ (Urick, 1996, chap. 7) respectively. The latter value is typical of shipping noise. Although the simulation does not resolve spectra up to the highest frequency of interest in terms of environmental impact ($\approx 100\ Hz$), the maximum amplitude of the hydrodynamic noise is captured.

Based on the SPL of $108\ dB$ quoted in Table 8.5, no *hearing threshold shift* would be expected. This requires the SPL to exceed the species' hearing threshold by at least $75\ dB$ for 8 hours within a 24 hour period (Richards *et al.*, 2007). Hearing threshold shift has been predicted at a range of $|\boldsymbol{r}| = 2D$ however (Lloyd *et al.*, 2011*a*). Including an empirical model for mechanical noise, and accounting for an array of three turbines, a third-octave SPL of $140\ dB$ re $1\mu Pa^2 Hz^{-1}$ was estimated at $160\ Hz$. This agrees with full scale measurements of tidal turbine source levels used to carry out environmental impact assessments (Halvorsen *et al.*, 2011; Parvin *et al.*, 2005), and suggests that mechanical noise may be more important at higher frequencies than inflow turbulence noise.

As the unsteady inflow conditions experienced by installed turbines are difficult to avoid, noise reduction of devices could focus on reducing tip speed, due to the fifth power

dependency of acoustic pressure on velocity (see Equation 8.17). Since turbines typically have an optimum tip speed ratio of 5-6 (Bahaj *et al.*, 2007), the most effective way to lower tip speed is to reduce turbine diameter. Due to the fact that turbine power is proportional to D^2u^3, the energy generation of smaller turbines will reduce significantly. This may be counteracted however by the installation of multiple devices (Starzmann *et al.*, 2013). Although decisions regarding the pay-off between optimal turbine diameter and number of turbines are more frequently driven by economic considerations, a move towards utilising numerous smaller turbines would reduce overall noise radiation per unit of power generated. Assuming that all turbines have the same source level, the noise due to an array of turbines would increase by $10\log_{10}(N_D)$ compared to a single device, where N_D is number of devices.

8.5.2 Fluid structure interaction analyses

The low frequency of the full scale inflow turbulence noise suggests that noise may also radiate from the turbine support structure, via load transfer through the rotor shaft. The peak frequency of tidal site inflow turbulence (Milne *et al.*, 2010, 2011) and structural vibration (Carruthers and Marmo, 2011) has been shown to lie in the range 0.1-1 Hz. Inflow turbulence has been shown to increase maximum blade root bending moment and fatigue loads (Milne *et al.*, 2010). Hence modelling tidal turbines in realistic environments is important for blade structural and manufacturing design in addition to studying acoustic radiation. Using flexible blades it is possible to increase turbine power and reduce thrust by allowing blades to twist (Nicholls-Lee *et al.*, 2013). Flapwise bending (streamwise tip deflection) has also been shown to affect mean turbine power (Banks *et al.*, 2013; Jo *et al.*, 2013). Banks *et al.* (2013) used the present simulation methodology combined with a simplified blade structural model (Bercin *et al.*, 2013) to model quasi-steady fluid structure interaction (FSI).

Hence there is potential for the present simulations to be used to study turbine performance and loads in more detail. For example, stochastic blade root bending moment could be extracted from the results already obtained. This would provide information on peak dynamic structural loads, which inform blade design. If the simulations presented here were dynamically coupled with a structural model, the effect of FSI on turbine performance and loads could be modelled. Neither of these analyses have been presented however since they are not the main focus of the current work.

8.5.3 Turbine in tidal channel flow

The present study only includes some of the turbulence statistics of a 'realistic' tidal channel. The anisotropy of the length scales may be considered the most important property to include, since it generally contributes to the characteristic haystacks seen in

the loading and noise spectra. This was the case for an aero engine ingesting atmospheric turbulence (Majumdar and Peake, 1998). The authors assumed the inflow turbulence was initially isotropic (von Kármán spectrum) with rapid distortion theory applied to account for the streamwise stretching of the length scales. Although in the present study anisotropic length scales are included, using a numerical simulation means that some of the effects of turbulence-rotor interaction typically modelled using rapid distortion theory are accounted for implicitly. In the case of a turbine this results in compression of the streamwise length scales, thereby reducing the number of haystacks observed, and increasing the streamwise velocity fluctuations (as predicted by Amiet *et al.* (1990)).

The full effects of turbulence-rotor interaction in a realistic environment cannot be fully captured without including inhomogeneity however. This implies that the modification of the turbulence by the wall is accounted for. Glegg *et al.* (2013) showed that the presence of a wall reduces the time scales below the rotor, which the authors note is the region of highest turbulence intensity in a boundary layer. Inhomogeneity of the mean velocity *i.e.* a boundary layer profile of $\overline{u}$ would also contribute to this modification. In order to assess the effect of a tidal channel on turbine response, typical mean and fluctuating velocity profiles were developed based on the models presented by Stacey *et al.* (1999). These are shown in Figure 8.21, and are scaled to match the values used in the present study at the hub height. Variations in the inflow turbulence properties across the rotor height are:

- -9 to $+4\%$ for $\overline{u}$ (and therefore $\mathcal{L}_x$);
- -32 to $+30\%$ for $\mathcal{I}_x$;
- and $\pm 50\%$ for $\overline{u'v'}$.

The largest effect of inhomogeneous inflow is thus expected to result from the streamwise turbulence intensity varying over the rotor height. Coupled with the presence of the wall, this would modify the noise spectra. For example, Glegg *et al.* (2013) predicted that rapid distortion causes the peak-to-trough amplitude of the haystacks to increase. Including these effects would provide further evaluation of the ability of the present methodology to capture complex turbulence-rotor interactions, and allow more realistic predictions of tidal turbine noise. It is also noted that the 'recycling' approach of Churchfield *et al.* (2013) may be appropriate for simulating this case. This would reduce the streamwise development length of the inflow turbulence, which is important since the turbine is located only three diameters from the inlet in the present study.

8.5.4 Comments on simulation scalability

Having applied rudimentary scaling to the acoustic data, it is useful to understand if full scale simulations of the same problem are possible at the current time. Generally

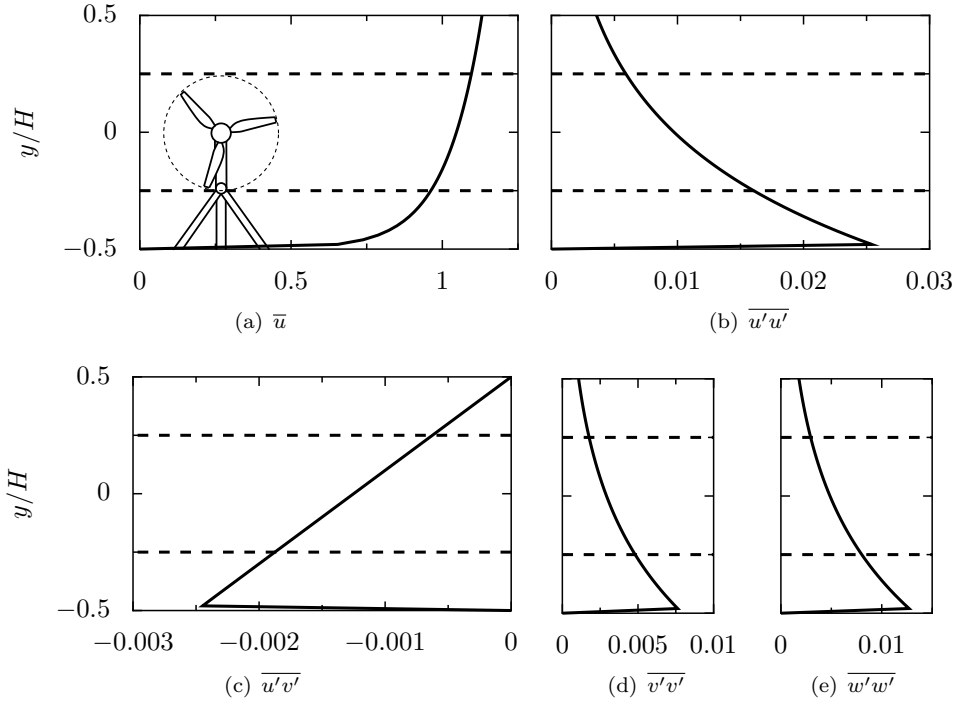

FIGURE 8.21: Modelled tidal channel inflow turbulence profiles. Non-dimensionalised by U_0.

speaking the scalability of CFD results is poor if the same grid is used, since the increase in Reynolds number leads to much finer resolution requirements. In the case of inflow turbulence noise however, the grid size upstream of the turbine is a key issue.

Figure 8.22 shows the normalised Kolmogorov spectra based on the vertical length scale $\mathcal{L}_y$ and $\mathcal{I} = 10\%$. A difference between model and full scale spectra is only observed for wavenumbers greater than $\kappa L \approx 10^3$. This increase is based on the Reynolds number dependency of the ratio of large and small scales outlined in Section 2.2. The grid cutoff corresponding to the model scale simulation is $\kappa L \approx 50$ however. This means that, assuming all inflow turbulence properties scale geometrically ($\mathcal{L}$) or remain the same ($\mathcal{I}$), the same grid could be used to simulate the full turbine.

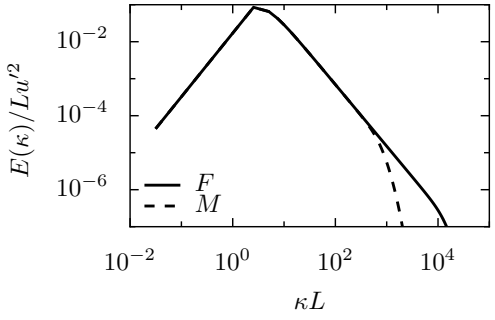

FIGURE 8.22: Scaled Kolmogorov spectra for tidal turbine inflow turbulence: model and full scale.

Any grid refinement at full scale would rather focus on the blade geometry and wake resolution. Without further near-wall refinement, the Δy_w^+ of 40 used here would increase to ≈ 150. This may in fact still be acceptable; full scale RANS computations of a similar

turbine used Δy_w^+ values of $11 - 500$ alongside scalable wall functions (McNaughton *et al.*, 2013*b*). Since this type of wall function is used in OpenFOAM, it is reasonable to assume that the grid would still be suitable at full scale. If further near-wall refinement was used to reduce Δy_w^+, this could be achieved by adding a single layer of cells using *snappyHexMesh*. In terms of temporal resolution, the only expected difference would be in the maximum allowable time step. Since a constant TSR is assumed between model and full scale, the tip speed of the full scale turbine will be higher by a factor U_F/U_M. Based on the assumed parameters, full scale simulations would take $\approx 80\%$ longer, maintaining a maximum Courant number of four. This represents the main drawback of performing full scale simulations in this case.

8.6 Summary

Estimates of both model and full scale tidal turbine acoustic sources and noise radiation due to inflow turbulence have been presented. The results in this chapter represent the first detailed numerical study of tidal turbine noise prediction. Haystacks, caused by blade-to-blade correlation, were captured by the simulation. The maximum peak-to-trough amplitude of the haystacks is 12 dB, which occurs at the blade passing frequency; this is also approximately 5 dB higher than the equivalent smooth spectrum. In the present study, including anisotropic length scales in the inflow turbulence statistics was therefore found to be important. One result not previously presented in the literature was the spanwise location of the acoustic source. It is found that this is centred in the outer region of the blade, in a similar manner to trailing edge noise.

A scaling method has been shown to successfully provide full scale predictions of tidal turbine hydrodynamic noise. This allowed environmental impact assessments to be made, reinforcing the findings of simplified modelling performed by the author (Lloyd *et al.*, 2011*a*,*b*). The maximum spectral source level, which was estimated at the blade passing frequency, is 144 dB re $1\mu Pa^2Hz^{-1}$ at 1 m. It has been concluded that this noise source is unlikely to have any physical impact on marine species (fish). The issue of structural vibration and induced noise radiation requires further investigation however.

As part of methodology verification, a quantitative investigation of the cell sizes on the arbitrary mesh interface was presented. This confirmed that the inflow turbulence convects through the interface without significant numerical diffusion. This is important for broadband turbulence-rotor interaction, and has previously been reported as a problem (Carolus *et al.*, 2007). In performing this analysis, a Courant number based on the rotational velocity of the grid was defined. It was found that the temporal resolution of the interface in the present study exceeds recommended requirements provided in the literature. The OpenFOAM interface algorithm is second-order and fully conservative, which is particularly important when performing large eddy simulations.

9

Summary and Conclusions

This monograph has presented a detailed study of numerical predictions of inflow turbulence noise. This noise source is important in many engineering scenarios, since the flow upstream of a rotor is typically turbulent. A review of background theory and literature has identified appropriate numerical methods (Chapters 2 and 3). Details of the numerical approach adopted were outlined in Chapter 4. The chosen approach allows some of the complexity of 'engineering' scenarios to be included by generating inhomogeneous, anisotropic turbulence. The filtered Navier-Stokes equations are solved, in order to resolve the majority of the unsteady loading (and noise source) in a time-dependent manner. Attention was paid to the selection of appropriate turbulence models and numerical methods, using test cases to justify the choices made.

Chapter 5 was dedicated to analysing the performance of two inflow turbulence generators (ITGs). Noise predictions initially focussed on a rigid aerofoil experiencing inflow turbulence (Chapter 6). Deficiencies in both methods were highlighted in terms of their applicability to the chosen test case. Having validated this methodology, examinations of different turbulence characteristics and foil geometries was made in Chapter 7. The final results chapter addressed anisotropic turbulence using the forward stepwise method of Kim *et al.* (2013). The noise of a tidal turbine, operating in both free-field and blocked flow conditions, was simulated, demonstrating the capabilities of the chosen approach to simulate 'full-rotor' turbomachinery noise.

9.1 Overall conclusions

The key outcomes of the work can be related to the numbered objectives laid out in Chapter 1 as follows:

1. The choice of appropriate methodology (specifically turbulence modelling approach) was dictated by the desire to simulate broadband noise. Large eddy simulation (LES) was selected since it allows a range of turbulence scales, and hence broadband noise sources, to be resolved. In addition, the use of the finite volume method allows complex geometries to be gridded relatively easily whilst maintaining second-order accurate solution. Acoustic predictions were made using the Ffowcs Williams-Hawkings acoustic analogy (a common approach for low Mach number flows) thereby removing the need to resolve acoustic waves on the computational grid. One of the advantages of using an open source CFD code was the ability to easily modify and extend the functionality available; this included implementing the acoustic analogy in to the flow solver.

2. Flow and force predictions were found to be sensitive to both turbulence modelling and numerical methods. The inter-dependency of grid quality, choice of turbulence model and discretisation scheme makes assessing the impact of each of these factors independently a difficult task. It is important however to gain some understanding of appropriate numerical models, since grids used in hydrodynamics will remain coarse for some time in terms of recommended resolution requirements. It is recommended that 'dynamic' models and schemes are adopted in this case, as this allows the modelled contribution to the turbulence dissipation to be varied both in space and time, improving solution accuracy.

3. Synthetic turbulence generators were investigated as a method for modelling appropriate inflow characteristics. This approach provides the ability to prescribe turbulence characteristics on complex grids based on heuristic estimates; hence such methods are more suited to engineering simulations than inflow recycling techniques. The synthetic vorton method (SVM; Kornev and Hassel, 2007; Kornev *et al.*, 2009) was found to be the best choice for simulating homogeneous isotropic inflow turbulence, based on predictions of Von Kármán type spectra and prescribed statistics. For inhomogeneous flows, the divergence-free forward stepwise method (FSM; Kim *et al.*, 2013; Xie and Castro, 2008) is preferred, since it shows the fastest streamwise development of Reynolds stress profiles, while avoiding spurious pressure fluctuations.

4. Both the cited methods have been used to predict the noise radiated from stationary foils experiencing inflow turbulence. One particular advantage of these simulations is the removal of any turbulent boundary layer resolution, since this is not important for simulating inflow turbulence noise. This means that simulations

require much less onerous spatial and temporal resolution close to the foil, making multiple evaluations more feasible within a limited computational resource. The advantage of the numerical approach is the explicit inclusion of foil geometry effects on the flow and noise prediction, which may not be accounted for in analytical models. Deficiencies in both methods were identified however.

5. Looking to examine noise generation in an engineering scenario, the methodology was applied to simulating tidal turbine hydrodynamic noise. This represents the first such simulation reported in the literature. The full rotor geometry was included in the simulation, thus all interactions between rotor and inflow turbulence are captured; this allowed haystacks (spectral humps caused by cutting of the long streamwise length scales) to be predicted. Full scale noise estimates were made based on scaling laws, which allow for environmental impact assessments to be made, and compare well to analytical predictions.

9.2 Turbulence modelling and numerical methods

Chapters 3 and 4 presented an assessment of five LES subgrid models and three convection schemes. The implicit LES technique was also investigated, whereby the numerical scheme acts as a subgrid model by providing appropriate levels of dissipation. The effect of the subgrid model was found to be substantial despite 80% of the turbulence kinetic energy being resolved on the grid. Although this condition cannot necessarily be satisfied *a priori*, the grids used have been designed to minimum LES quality guidelines.

The more complex models were found to be better at accounting for the interaction between the resolved and modelled scales, thereby improving Reynold stress distribution and dynamic force prediction. The 'dynamic mixed Smagorinsky' subgrid model used in this work allows the contribution of the subgrid viscosity to vary depending on the local grid size and flow gradients; this reduces unphysical dissipation and improves force prediction compared to the Smagorinsky model. For the test cases reported, implicit LES was not found to be superior to explicit subgrid modelling, and was generally too dissipative. While this approach may be attractive in some instances, when resolving dynamic forces and pressures the accuracy of the discretisation schemes becomes more important.

In this work, a hybrid convection scheme (*filteredLinear*) was used. This is designed to remove artificial wiggles in the velocity field which result from using fully central differencing for convection dominated flows on coarse grids. The scheme however avoids the excessive numerical dissipation typically observed for traditional blended schemes, by applying the upwinding dynamically, both in space and time. The preferred setup of this scheme was to let the limiter apply up to 100% upwinding if necessary, providing the best compromise between stability and accuracy; this setup gave the best prediction

of vortex shedding from a smooth circular cylinder. This is the first reported analysis of such a scheme, which is currently specific to OpenFOAM.

9.3 Assessment of inflow turbulence generators

A comparison of two ITGs revealed some significant differences between them. The SVM injects 'vortons' onto the domain inlet, and allows simple specification of turbulence parameters suitable for engineering scenarios. However, the inhomogeneity of the inflow turbulence statistics was found to affect the induced pressure fluctuations, which has implications for unsteady simulations of engineering problems, especially acoustics. The reported results represent one of the first studies to investigate this phenomenon. It was found that inhomogeneity of the Reynolds stresses caused a larger increase in *rms* pressure than length scales. In this case, the inlet pressure fluctuations are approximately three times larger than for the homogeneous case.

This issue has been overcome by the divergence-free FSM, which introduces velocity fluctuations onto a virtual grid within the inner loop of the PISO algorithm. This has been shown to remove pressure fluctuations by forcing the synthetic turbulence to satisfy the continuity equation prior to being added to the physical domain (Kim *et al.*, 2013). Thus, this approach represents a promising method when specifying fully inhomogeneous anisotropic inflow properties.

The FSM was however found to produce larger than expected streamwise vortices. When simulating homogeneous isotropic turbulence, this has an impact on the isotropy of the turbulence statistics, particularly the integral length scale. In addition, the pressure and foil lift spectra presented do not show the correct broadband shape. Discussions with the method's developer did not solve this problem, resulting in a combination of the FSM and SVM being used to investigate foil acoustic sources. When inhomogeneous and/or anisotropic inflow was required (Chapter 8), the FSM must be used, for two reasons: removal of artificial pressure fluctuations; and ability to specify anisotropic length scales. The simplicity of the SVM means that the integral length scale is specified as an isotropic scalar value.

9.4 Foil noise

This work includes one of the first studies to model inflow turbulence (leading edge) noise of a foil using a synthetic turbulence generator. Comparable studies of the same test case (Deniau *et al.*, 2011) produced poor acoustic predictions due to the LES resolving features of the laminar boundary layer and leading edge separation; since the boundary layer tripping used in the experiments could not be replicated numerically, the boundary

layer was not resolved at all in the present simulations. Using a slip condition on the foil surface negates the issue of spurious noise sources, in a similar way to the Euler equations solver used by Deniau *et al.* (2011) and Clair *et al.* (2012)[1]. This makes the spatial and temporal resolution requirements far less prohibitive, meaning simulation time may be reduced, or averaging times increased. For example, the simulations reported in Chapter 6 use a time step of 5×10^{-6} s to satisfy a Courant number limit of unity. This compares to 1×10^{-6} s used in Lloyd *et al.* (2013*a*), when the boundary layer was resolved. Comparison of the spatial and temporal resolution of the present study to those in the literature found it to be well resolved; the temporal resolution is particularly important when deriving the acoustic spectra.

Numerical noise predictions compare favourably with experimental and analytical data. The agreement between measured and predicted sound pressure level (SPL) is best at low to mid frequencies, where the discrepancies are within 4 dB. At higher frequencies, the numerical results over-predicted SPL by up to 15 dB. This was attributed to the induced pressure fluctuations of the SVM, which were not anticipated based on the claims of the method's developers (Kornev *et al.*, 2009). This could also be related to the use of the compact formulation of the FW-H equation; the compact formulation is appropriate for most hydroacoustics scenarios, but not strictly for the test case presented. This was not expected to be an issue due to the localised nature of the leading edge noise source. One key advantage of the numerical approach to inflow turbulence noise is that the effect of leading edge shape in terms of mean flow distortion is explicitly included; contrast this with Amiet's model, where modifications using rapid distortion theory must be added to approximate this effect (Moreau *et al.*, 2005), since the original model was formulated based on thin aerofoil theory.

The method has been shown to provide the ability to analyse differences in noise spectral amplitude caused by changes in foil shape. The thickness effect documented in the literature (Devenport *et al.*, 2010; Hutcheson *et al.*, 2012; Roger and Moreau, 2010) has been demonstrated by comparing the spectrum derived for a NACA 65 to that for a flat plate. The magnitude of the reduction in SPL due to increased thickness (*i.e.* NACA section) was shown to be in the range estimated from published data at low frequencies (*e.g.* see Paterson and Amiet, 1976), cited in Moreau *et al.* (2005). However, for higher frequencies the effect is less clear, due to the over-prediction of the SPL caused by the inlet pressure fluctuations. In addition, the effect of thickness distribution has been analysed, by simulating a C4 section, which is more relevant to marine propulsor design than the NACA 65. The differences in acoustic source location and magnitude between the two foil profiles are small; hence a recommendation regarding which has the lowest noise 'profile' cannot currently be made using the present methodology. However, a discussion of design considerations for hydrofoils highlighted 'competing' noise sources; reducing broadband noise may result in increased tonal or cavitation noise.

[1]It may also be avoided by using a foil section profile which does not exhibit leading edge separation at zero degrees angle of attack.

9.5 Tidal turbine noise

The final chapter presented noise predictions of a model scale tidal turbine, the first such analysis using LES. While the assumption of free field acoustic radiation is not true in reality, this simulation further validates and develops the methodology to model both anisotropic inflow turbulence and distributed acoustic sources. The effect of blade-to-blade correlation has been captured for this case, including the slight skewness of the peaks in the haystacks. This effect was noted by Jiang *et al.* (1994), but not included in the analytical model used here for validation purposes (Blake, 1984, chap. 10). One of the key limitations of analytical models for rotating blades, which are based on segmenting the span, is the need for the blade segment to be wider than the local correlation length (Roger and Moreau, 2010). If inhomogeneous inflow properties are specified, this condition may not easily be satisfied over an entire revolution. Hence the inclusion of such effects numerically may offer significant advantage.

The present study also elucidated the spanwise distribution of the inflow turbulence noise source, something that has not previously been presented in detail in the literature. It was found that the source is centred at approximately 90% of the turbine radius, which corresponds to the location of peak thrust loading. This was seen to cause a more monopole-like noise directivity, which is in agreement with the literature (*e.g.* see Morton *et al.*, 2012). Derived far-field sound spectra were used to provide full scale estimates of tidal turbine hydrodynamic noise, for use in environmental impact assessments. The full scale numerical spectra were shown to be in good agreement with analytical estimates. Spectral source level amplitude of 144 dB re $1\mu Pa^2\ Hz^{-1}$ at 1 m was not expected to cause physical impact on fish in this case for the low frequencies considered ($< 10\ Hz$). Additional semi-empirical modelling has shown that a higher broadband spectral source level, including mechanical noise and multiple turbines, of 160 dB re $1\mu Pa^2\ Hz^{-1}$ at 1 m could have this effect, but at higher frequency ($\approx 160\ Hz$; Lloyd *et al.* (2011*a*)).

One difficulty associated with the methodology was the inability to separate different broadband noise sources on the turbine blades. Flow separation on the blade suction side was identified; this additional noise source could not separated from the inflow turbulence noise, due to the way the FW-H equation was implemented. Comparisons to broadband noise models (Grosveld, 1985; Hubbard, 1991) may help in this investigation of this. In addition, including the turbine mast in the simulations is expected to provide an additional noise source, due to its interaction with the turbine wake. The mast will not only affect the upstream flow around the blades, but should become an acoustic source due to the highly turbulent flow impinging onto it from the turbine.

9.6 Recommendations for further work

There are a number of immediate areas for further work, which have not been carried due to time constraints. These include:

- Further evaluation of the inflow turbulence generators at higher Reynolds numbers, more akin to marine scenarios ($10^6 - 10^7$). In this case the development length of turbulence profiles is expected to be shorter than the channel case used here.
- Modifying the SVM to remove the issue of artificial pressure fluctuations. This could be achieved by following Kim *et al.* (2013) and adding the synthetic turbulence inside the PISO loop, or re-formulating the method in terms of vorticity (Poletto *et al.*, 2013).
- Implementing a non-compact form of the FW-H equation into OpenFOAM. This would be more appropriate for certain test cases (particularly those in air), or when multiple acoustic sources must be predicted (*e.g.* leading edge and vortex shedding noise). Note also the recent publication of the 'Farassat 2B' numerical implementation (Farassat and Casper, 2012), which has been designed for use with LES data.
- Improving the grid quality of the tidal turbine. More specifically, aim to use structured or hybrid gridding techniques to provide a better resolution of the complex blade geometry, which is not easily captured using *snappyHexMesh*. This could also focus on creating a boundary layer grid.

In the future, it may also be useful to:

- resolve viscous boundary layers, thereby allowing additional noise sources to be captured;
- include the turbine mast in simulations, in order to capture blade-mast interaction, and the associated noise generation prcoesses;
- apply the method to dedicated marine propulsor test cases, thereby providing further validation of the approach against a targeted set of measurements;
- evaluate far-field sound using a numerical method, such as the boundary element method. In this way, the effects of acoustic interactions with surrounding surfaces could be accounted for.

A

An Acoustic Analogy Implementation Using OpenFOAM

The equation implemented is a form of the loading term of the FWH equation (Equation 3.6) for a solid surface. This may be written as

$$p'(\boldsymbol{x},t) \approx \frac{1}{4\pi c_0}\frac{\partial}{\partial t}\oiint_S \left[\frac{x_i - y_i}{|\boldsymbol{r}|^2} n_j p_{ij}\left(\boldsymbol{y}, t - \frac{|\boldsymbol{r}|}{c_0}\right)\right] dS, \tag{A.1}$$

which more closely represents the implementation than Equation 3.6. A schematic representation of the acoustic analogy approach is depicted in Figure A.1. One of the key points is the simplicity with which the compact formulation of the acoustic analogy is implemented, using the existing code architecture of OpenFOAM. The main code modifications are shown in Figure A.2, and are based on utilising the existing OpenFOAM library '*forces*', which accesses the patch surface pressure. The code performs each of the following stages within each time step, for the designated patches '`patchi`':

1. Calculate the pressure time derivative '`dpdt`' within the solver (not shown);
2. Calculate the receiver location vector '`Rl`' for each patch face;
3. Obtain the surface pressure time derivative '`dpsdt`' from `dpdt`;
4. Read the speed of sound '`cRef`';
5. Calculate the far-field acoustic pressure '`pa`', and write to file.

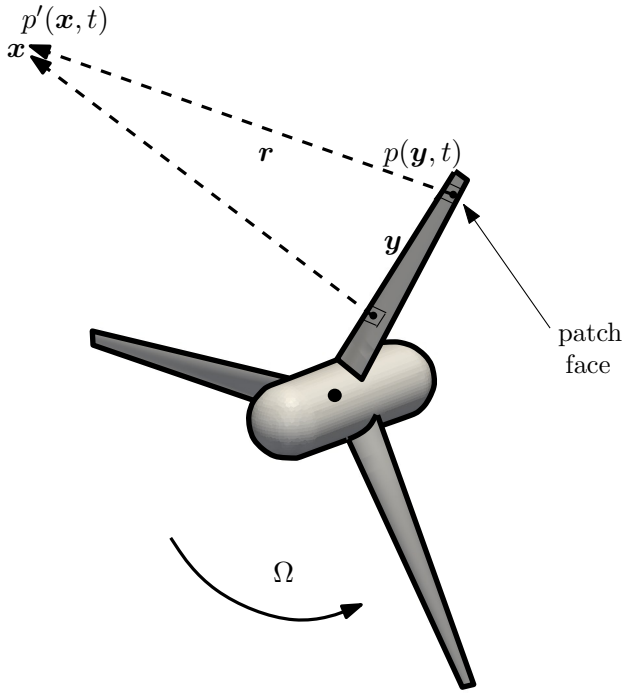

FIGURE A.1: Schematic of acoustic analogy approach for turbine noise simulation.

```
forAllConstIter(labelHashSet, patchSet_, iter)
    {
    label patchi = iter.key();
    vectorField Rl
            (
             recLoc_.origin() - mesh.C().boundaryField()[patchi]
            );
    vectorField dpsdt(Sfb[patchi]*(dpdt.boundaryField()[patchi]));
    scalar cRef=cRef_;
    pa += (rho(p)/(4 * mathematicalConstant::pi * cRef))*sum((Rl / magSqr(Rl)) & dpsdt);
    }
```

FIGURE A.2: Code used to calculate compact Ffowcs Williams-Hawkings equation.

B

Finite Volume Discretisation

B.1 Spatial discretisation of the Navier-Stokes equations

This section details the discretisation of each term of the Navier-Stokes equations, resulting in the semi-discretised form given in Equation 4.8. The derivations are presented here in terms of $\overline{u}$, the streamwise filtered velocity; the same principles apply to other transport equations and variables however.

The unsteady acceleration term, using second-order discretisation (Equation 4.6), may be written as

$$\begin{aligned}\int_{V_P} \overline{u}(\boldsymbol{y})dV &= \int_{V_P} [\overline{u}_P + (\boldsymbol{y} - \boldsymbol{y}_P) \cdot (\nabla \overline{u})_P]dV \\ &= \overline{u}_P \int_{V_P} dV + \left[\int_{V_P} (\boldsymbol{y} - \boldsymbol{y}_P)dV\right] \cdot (\nabla \overline{u})_P \\ &= \overline{u}_P V_P. \end{aligned} \tag{B.1}$$

Utilising Gauss' theorem (Equation 4.3.1), the convection term may be written as

$$\begin{aligned}\int_{V_P} \nabla \cdot (\overline{u}\ \overline{u}) dV = \oiint_S (\overline{u}\ \overline{u}) \cdot n dS &= \sum_f \int_f (\overline{u}\ \overline{u}) \cdot n dS \\ &= \sum_f \mathbf{A}_f \cdot (\overline{u}\ \overline{u})_f \\ &= \sum_f \mathbf{A}_f \cdot \overline{u}_f \overline{u}_f \\ &= \sum_f F \overline{u}_f \end{aligned} \tag{B.2}$$

where $F = \mathbf{A}_f \cdot \overline{u}_f$ is the face flux contribution from $\overline{u}$. Similarly the diffusion term becomes

$$\begin{aligned}\int_{V_P} \nabla \cdot (\nu_{eff} \nabla \overline{u}) dV = \oiint_S (\nu_{eff} \nabla \overline{u}) \cdot n dS &= \sum_f \int_f (\nu_{eff} \nabla \overline{u}) \cdot n dS \\ &= \sum_f \mathbf{A}_f \cdot (\nu_{eff} \nabla \overline{u})_f \\ &= \sum_f (\nu_{eff})_f \mathbf{A}_f \cdot (\nabla \overline{u})_f . \end{aligned} \tag{B.3}$$

The pressure gradient term is discretised as a source term. Linearising and following the same procedure as in Equation B.1 results in

$$\int_{V_P} -\frac{1}{\rho} (\nabla \overline{p}) dV = -\frac{1}{\rho} (\nabla \overline{p}) V_P . \tag{B.4}$$

B.2 Convection schemes in OpenFOAM

B.2.1 Properties of the central differencing scheme

Details of the behaviour of the central differencing (CD) scheme are included here since they motivate the use of a hybrid scheme in certain cases. A CD scheme offers better accuracy than an upwind scheme, and hence is commonly used in LES. Versteeg and Malalasekera (1995*d*, chap. 5) analyse the properties of a CD scheme. They address the following:

- *boundedness* - an increase in ϕ at $\boldsymbol{P}$ should result in an increase at $\boldsymbol{N}$.
- *transportiveness* - the direction of influencing (upwind direction) should be accounted for in the scheme.
- *accuracy* - the truncation error of the scheme, which also affects stability.

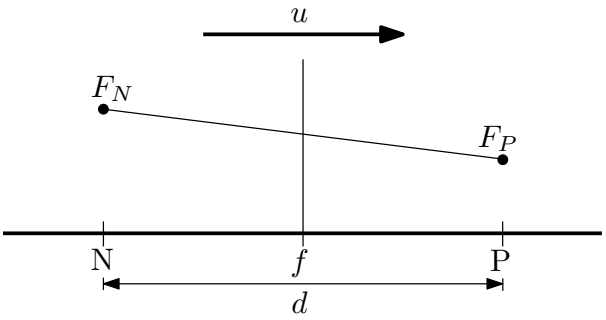

FIGURE B.1: Schematic representation of one dimensional convection.

In examining these properties, the ratio of convection to diffusion, known as the cell Péclet number is used. Referring to the definitions in Figure B.1, this may be defined as

$$Pe = \frac{\rho u}{\Gamma / d} \tag{B.5}$$

where Γ is the diffusion coefficient. A high value of Pe implies a convection dominated flow. Hence $\boldsymbol{P}$ should be increasingly influenced by an upstream $\boldsymbol{N}$. In this case, a CD scheme does not possess the transportiveness property, since it includes influencing from all neighbour cells. Additionally, it may be shown that the boundedness and accuracy (stability) properties are only satisfied when $Pe < 2$ (Versteeg and Malalasekera, 1995*d*, chap. 5).

It may be difficult to satisfy this criterion for high speed flows, or when coarse grids are used. In this case, the accuracy of the CD scheme diminishes. Unboundedness may lead to unphysical 'wiggles' in the flow solution, known as *staggering* or *over-/under-shoot*. This is caused by dispersion (phase) error, which results from the fact that the CD scheme is a second-order scheme *i.e.* the highest order term in the scheme is odd. These effects are reported in Section 4.3.2.

In order to satisfy the properties described above, a hybrid differencing scheme may be used. Blending a central differencing scheme with an upwind differencing (UD) scheme introduces inaccuracy in the flow solution since UD schemes are dissipative. This results from the first-order nature of an UD scheme, since the highest order term in the scheme is even. The difference in accuracy between CD and UD schemes can also be imagined in terms of the effect of grid refinement. Since the CD scheme has a truncation error $\propto \Delta y^2$, the accuracy of the flow solution will increase faster than for the UD scheme, which has a truncation error $\propto \Delta y$.

B.2.2 Total variation diminishing schemes

Information regarding total variation diminishing (TVD) schemes is provided as background for Section 4.3.2. Further description may also be found in Jasak (1996). Total variation diminishing schemes satisfy boundedness *i.e.* they are unconditionally stable;

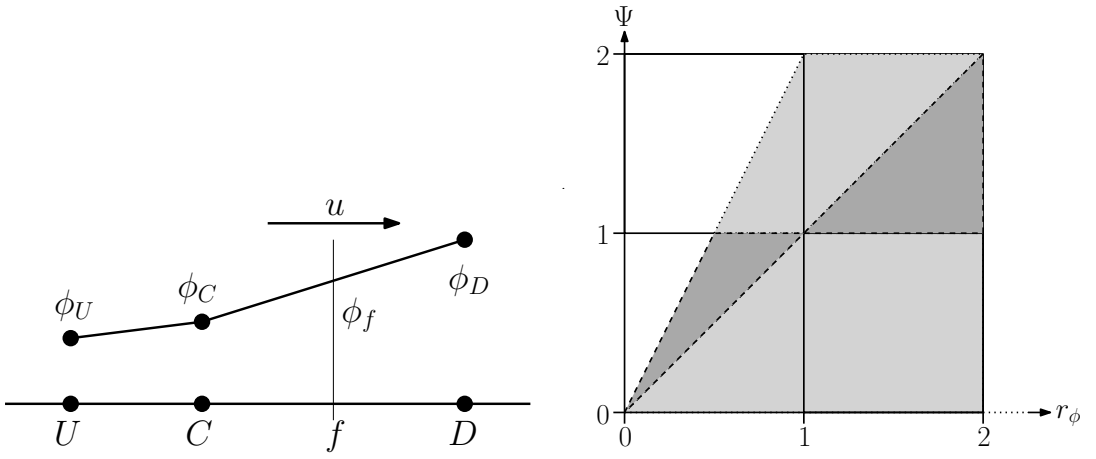

(a) Variation of a variable around a face.

(b) TVD diagram: light grey regions satisfy TVD condition; dark grey regions satisfy second-order accuracy.

FIGURE B.2: Definition of total variation diminishing scheme parameters (adapted from Jasak (1996)).

the TVD condition for a variable was given in Equation 4.13. Referring to Figure B.2(a), the ratio of consecutive gradients of a variable ϕ may be written as

$$r_\phi = \frac{\phi_C - \phi_U}{\phi_D - \phi_C} \tag{B.6}$$

where 'U', 'C' and 'D' refer to upwind, central and downwind cell centres. Based on this, Sweby (1984) showed that a condition on the limiter to satisfy boundedness is

$$0 \leq \left(\frac{\Psi(r_\phi)}{r_\phi}, \Psi(r_\phi) \right) \leq 2. \tag{B.7}$$

This condition is illustrated in Figure B.2(b), where the light grey shaded region satisfies Equation B.7. In addition the dark grey shaded region denotes values of r_ϕ and Ψ which result in second-order accuracy. Next, a description of the *filteredLinear* scheme is provided, which satisfies the TVD condition by locally and dynamically adjusting Ψ.

B.2.3 *filteredLinear* differencing scheme

An example of a hybrid differencing scheme used in this work is the OpenFOAM scheme *filteredLinear*. The description refers to the one dimensional case presented in Figure B.1. The scheme uses the difference in flux between the current cell P and its neighbours N,

$$\Delta F = F_N - F_P, \tag{B.8}$$

and the gradients of F_N and F_P along the direction vector between the two cell centres P and N as

$$(\nabla F)_P = d \cdot \nabla(F_P) \qquad (\nabla F)_N = d \cdot \nabla(F_N). \tag{B.9}$$

The Sweby limiter is defined as

$$\Psi = (1 + \Pi) - \Upsilon \left[\frac{min\left(|\Delta F - (\nabla F)_P|, |\Delta F - (\nabla F)_N|\right)}{max\left(|(\nabla F)_P|, |(\nabla F)_N|\right)} \right] \tag{B.10}$$

where Π and Υ are the overshoot and gradient scaling coefficients, which may each take a value between zero and one. In this work, $\Pi = 0$ and $\Upsilon = 1$. Using $\Upsilon = 1$ effectively increases the chance of upwinding being applied. Recalling that $\Psi = 0$ corresponds to a fully upwind scheme, upwinding will be added if the term in square brackets increases. This occurs if the difference in flux across the face ΔF is larger than the face-neighbour gradient ∇F. In this work, simulations use the *filteredLinear2V* scheme, which applies this procedure to each coordinate direction individually.

References

Abbott, I.H. and von Doenhoff, A.E. (1959), *Theory of wing sections*. 2nd edn., New York: Dover publications, pp. 111–123, ISBN 486-60586-8.

Afgan, I., McNaughton, J., Rolfo, S., Apsley, D., Stallard, T. and Stansby, P. (2013), Turbulent flow and loading on a tidal stream turbine by LES and RANS. *International Journal of Heat and Fluid Flow*, **in press**, doi:10.1016/j.ijheatfluidflow.2013.03.010.

Alexander, W.N., Devenport, W., Morton, M.A. and Glegg, S.A.L. (2013), Noise from a rotor ingesting a planar turbulent boundary layer. In: *Proceedings of the 19th AIAA/CEAS Aeroacoustics Conference*, 27th-29th May, Berlin, doi:10.2514/6.2013-2285.

Amiet, R. (1975), Acoustic radiation from an airfoil in a turbulent stream. *Journal of Sound and Vibration*, **41**(4): pp. 407–420, doi:10.1016/S0022-460X(75)80105-2.

— (1976), Noise due to turbulent flow past a trailing edge. *Journal of Sound and Vibration*, **47**(3): pp. 387–393, doi:10.1016/0022-460X(76)90948-2.

Amiet, R., Simonich, J. and Schlinker, R. (1990), Rotor noise due to atmospheric turbulence ingestion. Part II - Aeroacoustic results. *Journal of Aircraft*, **27**(1): pp. 15–22, doi:10.2514/3.45892.

Andersen, P., Kappel, J.J. and Spangenberg, E. (2009), Aspects of propeller developments for a submarine. In: *Proceedings of the 1st International Symposium on Marine Propulsors*, 22nd-24th June, Trondheim.

Argüelles Díaz, K.M., Fernández Oro, J.M., Blanco Marigorta, E. and Santolaria Morros, C. (2009), Numerical prediction of tonal noise generation in an inlet vaned low-speed axial fan using a hybrid aeroacoustic approach. *Proceedings of the Institution of Mechanical Engineers, Part C: Journal of Mechanical Engineering Science*, **223**(9): pp. 2081–2098, doi:10.1243/09544062JMES1426.

Ask, J. and Davidson, L. (2006), The sub-critical flow past a generic side mirror and its impact on sound generation and propagation. In: *Proceedings of the 12th AIAA/CEAS Aeroacoustics Conference*, 8th-10th May, Cambridge, doi:10.2514/6.2006-2558.

Baba-Ahmadi, M. and Tabor, G.R. (2009), Inlet conditions for LES using mapping and feedback control. *Computers & Fluids*, **38**(6): pp. 1299–1311, doi:10.1016/j.compfluid.2009.02.001.

Bahaj, A.S., Molland, A.F., Chaplin, J.R. and Batten, W. (2007), Power and thrust measurements of marine current turbines under various hydrodynamic flow conditions in a cavitation tunnel and a towing tank. *Renewable Energy*, **32**(3): pp. 407–426, doi:10.1016/j.renene.2006.01.012.

Bailly, C. and Juvé, D. (1999), A stochastic approach to compute subsonic noise using linearized Euler's equations. In: *5th AIAA/CEAS Aeroacoustic Conference and Exhibit*, 10th-12th May, Bellevue, pp. 496–506, doi:10.2514/6.1999-1872.

Banks, J. (2013), *Modelling the propelled resistance of a freestyle swimmer using Computational Fluid Dynamics*. Ph.D. thesis, University of Southampton.

Banks, J., Bercin, K., Lloyd, T.P. and Turnock, S.R. (2013), Fluid structure interaction analyses of tidal turbines. In: *Proceedings of the 16th Numerical Towing Tank Symposium*, 2nd-4th September, Mülheim.

Bardina, J., Ferziger, J.H. and Reynolds, W.C. (1980), Improved subgrid-scale models for large eddy simulation. In: *AIAA Fluid and Plasma Dynamics Conference*, 14th-16th July, Snowmass, doi:10.2514/6.1980-1357.

Batchelor, G. and Proudman, I. (1954), The effect of rapid distortion of a fluid in turbulent motion. *The Quarterly Journal of Mechanics and Applied Mathematics*, **7**(1): pp. 83–103, doi:10.1093/qjmam/7.1.83.

Bensow, R. and Liefvendahl, M. (2008), Implicit and explicit subgrid modeling in LES applied to a marine propeller. In: *Proceedings of the 38th AIAA Fluid Dynamics Conference and Exhibit*, 23rd-26th June, Seattle, doi:10.2514/6.2008-4144.

Bensow, R.E. (2013), Simulation of unsteady propeller loads using OpenFOAM. In: *Proceedings of the 16th Numerical Towing Tank Symposium*, 2nd-4th September, Mülheim.

Bensow, R.E. and Bark, G. (2010), Implicit LES predictions of the cavitating flow on a propeller. *Journal of Fluids Engineering*, **132**(4): pp. 041,302–1 – 041,302–10, doi:10.1115/1.4001342.

Bercin, K., Lloyd, T., Xie, Z.T. and Turnock, S.R. (2013), Efficient method for analysing fluid-structure interaction of horizontal axis tidal turbine blades. In: *Proceedings of the 10th European Wave and Tidal Energy Conference*, 2nd-5th September, Aalborg.

Betschart, M. (2012), Andritz Hydro Hammerfest. In: *Ocean Renewable Energy Group Annual Conference*, 13th-14th September, Halifax,

URL `http://www.marinerenewables.ca/wp-content/uploads/2012/09/Michael-Betschart-OREG-2012.pdf`.

Billson, M., Eriksson, L.E., Davidson, L. and Jordan, P. (2004), Modeling synthetic anisotropic turbulence and its sound emission. In: *Proceedings of the 10th AIAA/CEAS Aeroacoustics Conference*, 10th-12th May, Manchester, doi:10.2514/6.2004-2857.

Blackmore, T., Batten, W.M. and Bahaj, a.S. (2013), Inlet grid-generated turbulence for large-eddy simulations. *International Journal of Computational Fluid Dynamics*, **27**(6-7): pp. 307–315, doi:10.1080/10618562.2013.819972.

Blake, W. (1984), Aero-hydroacoustics for ships Volume II. *Tech. Rep. DTNSRDC-84/010*, David W. Taylor Naval Ship Research and Development Center, Bethesda.

Bogey, C. and Bailly, C. (2006), Large eddy simulations of round free jets using explicit filtering with/without dynamic Smagorinsky model. *International Journal of Heat and Fluid Flow*, **27**(4): pp. 603–610, doi:10.1016/j.ijheatfluidflow.2006.02.008.

Bogey, C., Bailly, C. and Juvé, D. (2002), Computation of flow noise using source terms in linearized Euler's equations. *AIAA Journal*, **40**(2): pp. 235–243, doi:10.2514/2.1665.

Boudet, J., Grosjean, N. and Jacob, M.C. (2005), Wake-airfoil interaction as broadband noise source: a large-eddy simulation study. *Aeroacoustics*, **4**(1&2): pp. 93 – 115, doi:10.1260/1475472053730093.

Boussinesq, J. (1877), *Essai sur la théorie des eaux courantes*, vol. 23. Paris: Imprimerie Nationale, p. 680.

Brentner, K.S. and Farassat, F. (1998), An analytical comparison of the acoustic analogy and Kirchoff formulation for moving surfaces. *AIAA Journal*, **36**(8): pp. 1–17, doi:10.2514/2.558.

— (2003), Modeling aerodynamically generated sound of helicopter rotors. *Progress in Aerospace Sciences*, **39**(2-3): pp. 83–120, doi:10.1016/S0376-0421(02)00068-4.

Brooks, T.F. and Marcolini, M.A. (1986), Airfoil tip vortex formation noise. *AIAA Journal*, **24**(2): pp. 246–252, doi:10.2514/3.9252.

Brooks, T.F., Marcolini, M.A. and Pope, D.S. (1986), Airfoil trailing-edge flow measurements. *AIAA Journal*, **24**(8): pp. 1245–1251, doi:10.2514/3.9426.

Brooks, T.F., Pope, D.S. and Marcolini, M.A. (1989), Airfoil self-noise and prediction. *Tech. Rep. NASA RP-1218*, NASA Langley Research Center, Hampton, VA.

Cabot, W. and Moin, P. (2000), Approximate wall boundary conditions in the large-eddy simulation of high Reynolds number flow. *Flow, Turbulence and Combustion*, **63**(1-4): pp. 269–291, doi:10.1023/A:1009958917113.

Carlton, J. (2007), *Marine propellers and propulsion*. 2nd edn., Oxford: Butterworth-Heinemann, pp. 247–260, ISBN 978-0750681506.

Carolus, T.H., Schneider, M. and Reese, H. (2007), Axial flow fan broad-band noise and prediction. *Journal of Sound and Vibration*, **300**(1-2): pp. 50–70, doi:10.1016/j.jsv.2006.07.025.

Carruthers, B. and Marmo, B.A. (2011), Device modelling, simulation & vibration analysis. In: *Proceedings of the 9th European Wave and Tidal Energy Conference*, 5th-9th September, Southampton.

Catlett, M.R., Anderson, J.M. and Stewart, D.O. (2012), Aeroacoustic response of propellers to sheared turbulent inflows. In: *Proceedings of the 18th AIAA/CEAS Aeroacoustics Conference*, 4th-6th June, Colorado Springs, doi:10.2514/6.2012-2137.

Çengel, Y.A. and Cimbala, J.M. (2006*a*), *Fluid mechanics. Fundamentals and applications*. New York: McGraw-Hill, pp. 515–606, ISBN 978-0073044651.

— (2006*b*), *ibid*. pp. 607–658.

Christophe, J. (2011), *Application of hybrid methods to high frequency aeroacoustics*. Ph.D. thesis, Université Libre de Bruxelles.

Christophe, J., Anthoine, J., Rambaud, P., Schram, C. and Moreau, S. (2007), Prediction of incoming turbulent noise using a combined numerical/semi-empirical method and experimental validation. In: *Proceedings of the West-East High Speed Flow Field Conference*, 19th-22nd, Moscow.

Churchfield, M.J., Li, Y. and Moriarty, P.J. (2013), A large-eddy simulation study of wake propagation and power production in an array of tidal-current turbines. *Philosophical transactions. Series A, Mathematical, physical, and engineering sciences*, **371**(20120421): pp. 1–15, doi:10.1098/rsta.2012.0421.

Clair, V., Polacsek, C., Garrec, T.L. and Reboul, G. (2012), CAA methodology to simulate turbulence-airfoil noise. In: *Proceedings of the 18th AIAA/CEAS Aeroacoustics Conference*, 4th-6th June, Colorado Springs, doi:10.2514/6.2012-2189.

Clair, V., Polacsek, C., Le Garrec, T., Reboul, G., Gruber, M. and Joseph, P. (2013), Experimental and numerical investigation of turbulence-airfoil noise reduction using wavy edges. *AIAA Journal*: pp. 1–19, doi:10.2514/1.J052394.

Colonius, T. and Lele, S.K. (2004), Computational aeroacoustics: progress on nonlinear problems of sound generation. *Progress in Aerospace Sciences*, **40**(6): pp. 345–416, doi:10.1016/j.paerosci.2004.09.001.

Comte-Bellot, G. and Corrsin, S. (1966), The use of a contraction to improve the isotropy of grid-generated turbulence. *Journal of Fluid Mechanics*, **25**(4): pp. 657–682, doi:10.1017/S0022112066000338.

Corsini, A., Rispoli, F. and Sheard, A.G. (2009), Aerodynamic performance of blade tip end-plates designed for low-noise operation in axial flow fans. *Journal of Fluids Engineering*, **131**(8): pp. 081,101–1 – 081,101–13, doi:10.1115/1.3026723.

Crighton, D.G. (1975), Basic principles of aerodynamic noise generation. *Progress in Aerospace Sciences*, **16**(1): pp. 31–96, doi:10.1016/0376-0421(75)90010-X.

Curle, N. (1955), The influence of solid boundaries upon aerodynamic sound. *Proceedings of the Royal Society A: Mathematical, Physical and Engineering Sciences*, **231**(1187): pp. 505–514, doi:10.1098/rspa.1955.0191.

Daniels, S.J., Castro, I.P. and Xie, Z.T. (2013), Peak loading and surface pressure fluctuations of a tall model building. *Journal of Wind Engineering and Industrial Aerodynamics*, **120**: pp. 19–28, doi:10.1016/j.jweia.2013.06.014.

de Laborderie, J., Moreau, S. and Berry, A. (2013), Compressor stage broadband noise prediction using a large-eddy simulation and comparisons with a cascade response model. In: *19th AIAA/CEAS Aeroacoustics Conference*, 27th-29th May, Berlin, doi:10.2514/6.2013-2042.

de Wilde, J.J. and Huijsmans, R.H.M. (2001), Experiments for high Reynolds numbers VIV on risers. In: *Proceedings of the 11th International Society of Ocean and Polar Engineering Conference*, Stavanger, pp. 400–405.

de Wilde, J.J., Huijsmans, R.H.M. and Tukker, J. (2006), Experimental investigation into the vortex formation in the wake of an oscillating cylinder using Particle Image Velocimetry. In: *Proceedings of the 16th International Society of Ocean and Polar Engineering Conference*, 28th May-2nd June, San Francisco, pp. 798–805.

Deniau, H., Dufour, G., Boussuge, J.F., Polacsek, C. and Moreau, S. (2011), Affordable compressible LES of airfoil-turbulence interaction in a free jet. In: *Proceedings of the 17th AIAA/CEAS Aeroacoustics Conference*, June, 5th-8th June, Portland, doi:10.2514/6.2011-2707.

Devenport, W.J., Staubs, J.K. and Glegg, S.A. (2010), Sound radiation from real airfoils in turbulence. *Journal of Sound and Vibration*, **329**(17): pp. 3470–3483, doi:10.1016/j.jsv.2010.02.022.

di Mare, L., Klein, M., Jones, W.P. and Janicka, J. (2006), Synthetic turbulence inflow conditions for large-eddy simulation. *Physics of Fluids*, **18**(2): pp. 1–11, doi:10.1063/1.2130744.

Dieste, M. (2011), *Random-vortex-particle methods applied to broadband fan interaction noise*. Ph.D. thesis, University of Southampton.

Dieste, M. and Gabard, G. (2010), Predicting broadband fan interaction noise using a random-vortex-particle method. In: *Proceedings of the 20th International Congress on Acoustics*, 23rd-27th August, Sydney.

Erbe, C. (2013), Underwater noise of small personal watercraft (jet skis). *The Journal of the Acoustical Society of America*, **133**(4): pp. EL326–30, doi:10.1121/1.4795220.

Erbe, C., McCauley, R., McPherson, C. and Gavrilov, A. (2013), Underwater noise from offshore oil production vessels. *The Journal of the Acoustical Society of America*, **133**(6): pp. EL465–470, doi:10.1121/1.4802183.

Ewert, R. (2008), Broadband slat noise prediction based on CAA and stochastic sound sources from a fast random particle-mesh (RPM) method. *Computers & Fluids*, **37**(4): pp. 369–387, doi:10.1016/j.compfluid.2007.02.003,.

Ewert, R. and Schröder, W. (2003), Acoustic perturbation equations based on flow decomposition via source filtering. *Journal of Computational Physics*, **188**(2): pp. 365–398.

Ewert, R., Dierke, J., Siebert, J., Neifeld, A., Appel, C., Siefert, M. and Kornow, O. (2011), CAA broadband noise prediction for aeroacoustic design. *Journal of Sound and Vibration*, **330**(17): pp. 4139–4160, doi:10.1016/j.jsv.2011.04.014.

Farassat, F. (1975), Theory of noise generation from moving bodies with an application to helicopter rotors. *Tech. Rep. TR R-451*, NASA, Washington, D.C.

Farassat, F. and Casper, J. (2012), Broadband noise prediction when turbulence simulation is available - Derivation of Formulation 2B and its statistical analysis. *Journal of Sound and Vibration*, **331**(10): pp. 2203–2208, doi:10.1016/j.jsv.2011.07.044.

Farrell, P. and Maddison, J. (2011), Conservative interpolation between volume meshes by local Galerkin projection. *Computer Methods in Applied Mechanics and Engineering*, **200**(1-4): pp. 89–100, doi:10.1016/j.cma.2010.07.015.

Feymark, A., Alin, N., Bensow, R. and Fureby, C. (2012), Numerical simulation of an oscillating cylinder using large eddy simulation and implicit large eddy simulation. *Journal of Fluids Engineering*, **134**(3): pp. 031,205–1 – 031,205–10, doi:10.1115/1.4005766.

Ffowcs Williams, J. and Hawkings, D. (1969), Sound generation by turbulence and surfaces in arbitrary motion. *Philosophical Transactions of the Royal Society A: Mathematical, Physical and Engineering Sciences*, **264**(1151): pp. 321–342, doi:10.1098/rsta.1969.0031.

Fleig, O., Iida, M. and Arakawa, C. (2004), Wind turbine blade tip flow and noise prediction by large-eddy simulation. *Journal of Solar Energy Engineering*, **126**(4): pp. 1017–1024, doi:10.1115/1.1800551.

Fureby, C. (2007), ILES and LES of complex engineering turbulent flows. *Journal of Fluids Engineering*, **129**(12): pp. 1514–1523, doi:10.1115/1.2801370.

Gant, S. and Stallard, T. (2008), Modelling a tidal turbine in unsteady flow. In: *Proceedings of the 18th International Ocean and Polar Engineering Conference*, Vancouver, pp. 473–479.

Georgiadis, N.J., Rizzetta, D.P. and Fureby, C. (2010), Large-eddy simulation: Current capabilities, recommended practices, and future research. *AIAA Journal*, **48**(8): pp. 1772–1784, doi:10.2514/1.J050232.

Germano, M., Piomelli, U., Moin, P. and Cabot, W. (1991), A dynamic subgrid-scale eddy viscosity model. *Physics of Fluids*, **3**(7): pp. 1760–1765, doi:10.1063/1.857955.

Gill, J., Zhang, X. and Joseph, P. (2013*a*), Symmetric airfoil geometry effects on leading edge noise. *The Journal of the Acoustical Society of America*, **134**(4): pp. 2669–80, doi:10.1121/1.4818769.

Gill, J., Zhang, X., Joseph, P. and Node-Langlois, T. (2013*b*), Effects of real airfoil geometry on leading edge gust interaction noise. In: *Proceedings of the 19th AIAA/CEAS Aeroacoustics Conference*, 27th-29th May, Berlin, pp. 1–15, doi:10.2514/6.2013-2203.

Giret, J.C., Sengissen, A., Moreau, S., Sanjosé, M. and Jouhaud, J.C. (2012), Prediction of the sound generated by a rod-airfoil configuration using a compressible unstructured LES solver and a FW-H analogy. In: *Proceedings of the 18th AIAA/CEAS Aeroacoustics Conference*, 4th-6th June, Colorado Springs, doi:10.2514/6.2012-2058.

Glegg, S., Baxter, S. and Glendinning, A. (1987), The prediction of broadband noise from wind turbines. *Journal of Sound and Vibration*, **118**(2): pp. 217–239, doi:10.1016/0022-460X(87)90522-0.

Glegg, S.A.L., Morton, M. and Devenport, W.J. (2012), Rotor inflow noise caused by a boundary layer : theory and examples. In: *Proceedings of the 18th AIAA/CEAS Aeroacoustics Conference*, June, 4th-6th June, Colorado Springs, doi:10.2514/6.2012-2263.

Glegg, S.A.L., Kawashima, E., Lachowski, F., Devenport, W.J. and Alexander, W.N. (2013), Inflow distortion noise in a non axisymmetric flow. In: *Proceedings of the 19th AIAA/CEAS Aeroacoustics Conference*, 27th-29th May, Berlin, doi:10.2514/6.2013-2286.

Goldstein, M.E. (1976), *Aeroacoustics*. New York: McGraw-Hill, pp. 113–188, ISBN 0-07-023685-2.

Greschner, B. and Thiele, F. (2012), Broadband noise analysis of a rotor-stator-cascade using wall modeled LES simulation. In: *Proceedings of the 18th AIAA/CEAS Aeroacoustics Conference*, 4th-6th June, Colorado Springs, doi:10.2514/6.2012-2308.

Greschner, B., Thiele, F., Jacob, M.C. and Casalino, D. (2008), Prediction of sound generated by a rod-airfoil configuration using EASM DES and the generalised Lighthill/FW-H analogy. *Computers & Fluids*, **37**(4): pp. 402–413, doi:10.1016/j.compfluid.2007.02.013.

Griffiths, G., Enoch, P. and Millard, N. (2001), On the radiated noise of the Autosub autonomous underwater vehicle. *ICES Journal of Marine Science*, **58**(6): pp. 1195–1200, doi:10.1006/jmsc.2001.1120.

Grinstein, F.F., Margolin, L.G. and Rider, W.J. (2007), *Implicit large eddy simulation: computing turbulent fluid dynamics*. Cambridge: Cambridge University Press, p. 546, ISBN 978-0-521-86982-9.

Grosveld, F.W. (1985), Prediction of broadband noise from horizontal axis wind turbines. *Journal of Propulsion and Power*, **1**(4): pp. 292–299, doi:10.2514/3.22796.

Gruber, M. (2012), *Airfoil noise reduction by edge treatments*. Ph.D. thesis, University of Southampton.

Gutin, L. (1948), On the sound field of a rotating propeller. *Tech. Rep. 1195*, National Advisory Committee for Aeronautics, Washington, D.C.

Halvorsen, M., Carlson, T. and Copping, A. (2011), Effects of tidal turbine noise on fish hearing and tissues. *Tech. Rep. PNNL-20786*, Pacific Northwest National Laboratory, Sequim.

Hinze, J.O. (1975), *Turbulence*. 2nd edn., New York: McGraw-Hill, pp. 1–72, ISBN 978-0070290372.

Hirsch, C. (2007*a*), *Numerical computation of internal and external flows*. 2nd edn., Oxford: Butterworth-Heinemann, pp. 27–64, ISBN 9780080550022.

— (2007*b*), *ibid.* p. 656.

— (2007*c*), *Numerical computation of internal and external flows*. 2nd edn., Oxford: Butterworth-Heinemann, pp. 105–140, ISBN 978-0750665940.

Howe, M.S. (1998*a*), *Acoustics of fluid-structure interactions*. Cambridge: Cambridge University Press, pp. 101–156, ISBN 0-521-63320-6.

— (1998*b*), *ibid.* pp. 1–100.

— (1998*c*), *ibid.* pp. 157–233.

Howell, A. (1945), Fluid dynamics of axial compressors. *Proceedings of the Institution of Mechanical Engineers*, **153**(1): pp. 441–452, doi:10.1243/PIME_PROC_1945_153_049_02.

Huang, S., Li, Q. and Wu, J. (2010), A general inflow turbulence generator for large eddy simulation. *Journal of Wind Engineering and Industrial Aerodynamics*, **98**(10-11): pp. 600–617, doi:10.1016/j.jweia.2010.06.002.

Hubbard, H.H. (1991), Aeroacoustics of large wind turbines. *The Journal of the Acoustical Society of America*, **89**(6): p. 2495, doi:10.1121/1.401021.

Hunt, J.C.R. (1973), A theory of turbulent flow round two-dimensional bluff bodies. *Journal of Fluid Mechanics*, **61**(04): pp. 625–706, doi:10.1017/S0022112073000893.

Hutcheson, F.V., Brooks, T.F. and Stead, D.J. (2012), Measurement of the noise resulting from the interaction of turbulence with a lifting surface. *International Journal of Aeroacoustics*, **11**(5): pp. 675–700, doi:10.1260/1475-472X.11.5-6.675.

Issa, R. (1986), Solution of the implicitly discretised fluid flow equations by operator-splitting. *Journal of Computational Physics*, **62**(1): pp. 40–65, doi:10.1016/0021-9991(86)90099-9.

ITTC (1987), Cavitation committee report. In: *18th International Towing Tank Conference*, 18th-24th October, Kobe.

James, M. and Lloyd, T. (2013), Large eddy simulations of circular cylinders at a range of Reynolds numbers. In: *Proceedings of ITTC Workshop of Wave Run-up and Vortex Shedding*, 17th-18th October, Nantes.

Jarrin, N., Benhamadouche, S., Laurence, D. and Prosser, R. (2006), A synthetic-eddy-method for generating inflow conditions for large-eddy simulations. *International Journal of Heat and Fluid Flow*, **27**(4): pp. 585–593, doi:http://dx.doi.org/10.1016/j.ijheatfluidflow.2006.02.006.

Jarrin, N., Prosser, R., Uribe, J.C., Benhamadouche, S. and Laurence, D. (2009), Reconstruction of turbulent fluctuations for hybrid RANS/LES simulations using a synthetic-eddy method. *International Journal of Heat and Fluid Flow*, **30**(3): pp. 435–442, doi:10.1016/j.ijheatfluidflow.2009.02.016.

Jasak, H. (1996), *Error analysis and estimation for the finite volume method with applications to fluid flows*. Ph.D. thesis, Imperial College London.

Jasak, H., Jemcov, A. and Tuković, v. (2007), OpenFOAM: A C++ library for complex physics simulations. In: *International Workshop on Coupled Methods in Numerical Dynamics*, 19th-21st September, Dubrovnik, pp. 47–66.

Jiang, C.W., Chang, M. and Liu, Y. (1994), The effect of turbulence ingestion on propeller broadband forces. In: *Proceedings of 19th Symposium on Naval Hydrodynamics*, 23rd-28th August, Seoul, pp. 751–769.

Jo, C.h., Lee, J.h., Kim, D.y. and Lee, K.h. (2013), Performance of horizontal axis tidal current turbine with blade deformation. In: *Proceedings of the 10th European Wave and Tidal Energy Conference*, 2nd-5th September, Aalborg.

Juvé, D. (2009), Aeroacoustics research in Europe: the CEAS-ASC report on 2008 highlights. *Journal of Sound and Vibration*, **328**(1-2): pp. 213–242, doi:10.1016/j.jsv.2009.07.022.

Kärrholm, F.P. (2008), *Numerical modelling of diesel spray injection , turbulence interaction and combustion*. Ph.D. thesis, Chalmers University of Technology.

Kato, C., Iida, A., Takano, Y., Fujita, H. and Ikegawa, M. (1993), Numerical prediction of aerodynamic noise radiated from low Mach number turbulent wake. In: *Proceedings of the 31st Aerospace Sciences Meeting and Exhibit*, 11th-14th January, Reno, NV, doi:10.2514/6.1993-145.

Kim, H.J., Lee, S. and Fujisawa, N. (2006), Computation of unsteady flow and aerodynamic noise of NACA0018 airfoil using large-eddy simulation. *International Journal of Heat and Fluid Flow*, **27**(2): pp. 229–242, doi:10.1016/j.ijheatfluidflow.2005.08.007.

Kim, Y., Castro, I.P. and Xie, Z.T. (2013), Divergence-free turbulence inflow conditions for large-eddy simulations with incompressible flow solvers. *Computers & Fluids*, **84**: pp. 56–68, doi:10.1016/j.compfluid.2013.06.001.

Klein, M., Sadiki, A. and Janicka, J. (2003), A digital filter based generation of inflow data for spatially developing direct numerical or large eddy simulations. *Journal of Computational Physics*, **186**(2): pp. 652–665, doi:10.1016/S0021-9991(03)00090-1.

Kolmogorov, A. (1991), The local structure of turbulence in incompressible viscous fluid for very large Reynolds numbers. *Proceedings of the Royal Society A: Mathematical, Physical and Engineering Sciences*, **434**(1890): pp. 9–13, doi:10.1098/rspa.1991.0075.

Kornev, N.V. and Hassel, E. (2007), Method of random spots for generation of synthetic inhomogeneous turbulent fields with prescribed autocorrelation functions. *Communications in Numerical Methods in Engineering*, **23**(1): pp. 35–43, doi:10.1002/cnm.880.

Kornev, N.V., Shchukin, E., Taranov, E., Kröger, H., Turnow, J. and Hassel, E. (2009), Development and implemention of inflow generator for LES and DNS applications in OpenFoam. In: *Proceedings of the Open Source CFD International Conference 2009*, 12th-13th November, Barcelona.

Kornev, N.V., Taranov, A., Shchukin, E. and Kleinsorge, L. (2011), Development of hybrid URANS-LES methods for flow simulation in the ship stern area. *Ocean Engineering*, **38**(16): pp. 1831–1838, doi:10.1016/j.oceaneng.2011.09.024.

Lamb, H. (1945), *Hydrodynamics*. 6th edn., Cambridge: Cambridge University Press, pp. 31–61, ISBN 978-0486602561.

Lau, A.S., Haeri, S. and Kim, J.W. (2013), The effect of wavy leading edges on aerofoil-gust interaction noise. *Journal of Sound and Vibration*, **332**(24): pp. 6234–6253, doi:10.1016/j.jsv.2013.06.031.

Leonard, A. (1974), Energy cacade in large-eddy simulations of turbulent fluid flows. *Advances in Geophysics*, **18**(Part A): pp. 237–248, doi:10.1016/S0065-2687(08)60464-1.

Li, Y. and Çalişal, S.M. (2010), Numerical analysis of the characteristics of vertical axis tidal current turbines. *Renewable Energy*, **35**(2): pp. 435–442, doi:10.1016/j.renene.2009.05.024.

Lighthill, M. (1952), On sound generated aerodynamically. I. General theory. *Proceedings of the Royal Society A: Mathematical, Physical and Engineering Sciences*, **211**(1107): pp. 564–587, doi:10.1098/rspa.1952.0060.

— (1954), On sound generated aerodynamically. II. Turbulence as a source of sound. *Proceedings of the Royal Society A: Mathematical, Physical and Engineering Sciences*, **222**(1148): pp. 1–32, doi:10.1098/rspa.1954.0049.

Lilly, D. (1992), A proposed modification of the Germano subgrid-scale closure method. *Physics of Fluids*, **4**(3): pp. 633–635, doi:10.1063/1.858280.

Lloyd, T., Humphrey, V. and Turnock, S. (2011*a*), Noise modelling of tidal turbine arrays for environmental impact assessment. In: *Proceedings of the 9th European Wave and Tidal Energy Conference*, 5th-9th September, Southampton, UK.

Lloyd, T., Turnock, S. and Humphrey, V. (2011*b*), Modelling techniques for underwater noise generated by tidal turbines in shallow waters. In: *Proceedings of the 30th International Conference on Ocean, Offshore and Arctic Engineering*, 19th-24th June, Rotterdam.

Lloyd, T., Gruber, M., Turnock, S.R. and Humphrey, V. (2012), Simulation of inflow turbulence noise. In: *Proceedings of the 15th Numerical Towing Tank Symposium*, 7th-9th October, Cortona.

— (2013*a*), Using an inflow turbulence generator for leading edge noise predictions. In: A. Talamelli, M. Oberlack and J. Peinke (eds.), *Proceedings of iTi Conference in Turbulence 2012*, vol. 149, Heidelberg: Springer-Verlag, ISBN 978-3-319-01860-7, pp. 211–216.

Lloyd, T.P., Turnock, S.R. and Humphrey, V.F. (2013*b*), Computation of inflow turbulence noise of a tidal turbine. In: *Proceedings of the 10th European Wave and Tidal Energy Conference*, 2nd-5th September, Aalborg.

Lorenzoni, V., Tuinstra, M. and Scarano, F. (2012), On the use of time-resolved particle image velocimetry for the investigation of rod-airfoil aeroacoustics. *Journal of Sound and Vibration*, **331**(23): pp. 5012–5027, doi:10.1016/j.jsv.2012.05.034.

Lund, T.S., Wu, X. and Squires, K.D. (1998), Generation of turbulent inflow data for spatially-developing boundary layer simulations. *Journal of Computational Physics*, **140**(2): pp. 233–258, doi:10.1006/jcph.1998.5882.

Majumdar, S.J. and Peake, N. (1998), Noise generation by the interaction between ingested turbulence and a rotating fan. *Journal of Fluid Mechanics*, **359**: pp. 181–216, doi:10.1017/S0022112097008318.

Makarewicz, R. (2011), Is a wind turbine a point source? *The Journal of the Acoustical Society of America*, **129**(2): pp. 579–81, doi:10.1121/1.3514426.

Maruta, Y. and Kotake, S. (1983), Separated flow noise of a flat plate at large attack angles. *Journal of Sound and Vibration*, **89**(3): pp. 335–357, doi:10.1016/0022-460X(83)90541-2.

McNaughton, J., Afgan, I., Apsley, D.D., Rolfo, S., Stallard, T. and Stansby, P.K. (2013*a*), A simple sliding-mesh interface procedure and its application to the CFD simulation of a tidal-stream turbine. *International Journal for Numerical Methods in Fluids*, doi:10.1002/fld.3849.

McNaughton, J., Rolfo, S., Apsley, D.D., Stallard, T. and Stansby, P.K. (2013*b*), CFD power and load prediction on a 1MW tidal stream turbine with typical velocity profiles from the EMEC test site. In: *Proceedings of the 10th European Wave and Tidal Energy Conference*, 2nd-5th September, Aalborg.

McSherry, R., Grimwade, J., Jones, I., Mathias, S., Wells, A. and Mateus, A. (2011), 3D CFD modelling of tidal turbine performance with validation against laboratory experiments. In: *Proceedings of the 9th European Wave and Tidal Energy Conference*, 5th-9th September, Southampton, UK.

Meneveau, C. and Katz, J. (2000), Scale-Invariance and Turbulence Models for Large-Eddy Simulation. *Annual Review of Fluid Mechanics*, **32**(1): pp. 1–32, doi:10.1146/annurev.fluid.32.1.1.

Meneveau, C., Lund, T.S. and Cabot, W.H. (1996), A Lagrangian dynamic subgrid-scale model of turbulence. *Journal of Fluid Mechanics*, **319**: pp. 353–385, doi:10.1017/S0022112096007379.

Menter, F.R. and Egorov, Y. (2010), The scale-adaptive simulation method for unsteady turbulent flow predictions. Part 1: Theory and model description. *Flow, Turbulence and Combustion*, **85**(1): pp. 113–138, doi:10.1007/s10494-010-9264-5.

MEPC (2007), Shipping noise and marine mammals. *Tech. Rep. MEPC 57/INF.4*, International Maritime Organisation.

Merz, S., Kinns, R. and Kessissoglou, N. (2009), Structural and acoustic responses of a submarine hull due to propeller forces. *Journal of Sound and Vibration*, **325**(1-2): pp. 266–286, doi:10.1016/j.jsv.2009.03.011.

Michel, U., Eschricht, D., Greschner, B., Knacke, T., Mockett, C. and Thiele, F. (2009), Advanced DES methods and their application to aeroacoustics. In: S.H. Peng, P. Doerffer and W. Haase (eds.), *Progress in Hybrid RANS-LES Modelling*, Heidelberg: Springer-Verlag, pp. 59–76, doi:10.1007/978-3-642-14168-3_5.

Migliore, P. and Oerlemans, S. (2004), Wind tunnel aeroacoustic tests of six airfoils for use on small wind turbines. *Journal of Solar Energy Engineering*, **126**(4): p. 974, doi:10.1115/1.1790535.

Milne, I.A., Sharma, R.N., Flay, R.G.J. and Bickerton, S. (2010), The role of onset turbulence on tidal turbine blade loads. In: *Proceedings of the 17th Australasian Fluid Mechanics Conference*, 5th-9th December, Auckland.

— (2011), Characteristics of the onset flow turbulence at a tidal-stream power site. In: *Proceedings of the 9th European Wave and Tidal Energy Conference*, 5th-9th September, Southampton.

Mish, P.F. and Devenport, W.J. (2006*a*), An experimental investigation of unsteady surface pressure on an airfoil in turbulence - Part 1: Effects of mean loading. *Journal of Sound and Vibration*, **296**(3): pp. 417–446, doi:10.1016/j.jsv.2005.08.008.

— (2006*b*), An experimental investigation of unsteady surface pressure on an airfoil in turbulence - Part 2: Sources and prediction of mean loading effects. *Journal of Sound and Vibration*, **296**(3): pp. 447–460, doi:10.1016/j.jsv.2005.08.009.

Moin, P. and Kim, J. (2006), Numerical investigation of turbulent channel flow. *Journal of Fluid Mechanics*, **118**: pp. 341–377, doi:10.1017/S0022112082001116.

Molland, A., Turnock, S.R. and Hudson, D.A. (2011), *Ship resistance and propulsion.* New York: Cambridge University Press, pp. 343–355, ISBN 978-0-521-76052-2.

Molland, A.F., Bahaj, A.S., Chaplin, J.R. and Batten, W.M.J. (2004), Measurements and predictions of forces, pressures and cavitation on 2-D sections suitable for marine current turbines. *Proceedings of the Institution of Mechanical Engineers, Part M: Journal of Engineering for the Maritime Environment*, **218**(2): pp. 127–138, doi:10.1243/1475090041651412.

Moreau, S., Roger, M. and Jurdic, V. (2005), Effect of angle of attack and airfoil shape on turbulence-interaction noise. In: *Proceedings of the 11th AIAA/CEAS Aeroacoustics Conference*, May, 23rd-25th May, Monterey, doi:10.2514/6.2005-2973.

Moriarty, P., Guidati, G. and Migliore, P. (2005), Prediction of turbulent inflow and trailing-edge noise for wind turbines. In: *11th AIAA/CEAS Aeroacoustics Conference*, 23rd-25th May, Monterey, doi:10.2514/6.2005-2881.

Morton, M., Devenport, W., Alexander, W.N., Glegg, S.A.L. and Borgoltz, A. (2012), Rotor inflow noise caused by a boundary layer: inflow measurements and noise predictions. In: *Proceedings of the 18th AIAA/CEAS Aeroacoustics Conference*, 4th-6th June, Colorado Springs, doi:10.2514/6.2012-2120.

Moser, R.D., Kim, J. and Mansour, N.N. (1999), Direct numerical simulation of turbulent channel flow up to Re_τ=590. *Physics of Fluids*, **11**(4): pp. 943–945, doi:10.1063/1.869966.

Nicholls-Lee, R., Turnock, S. and Boyd, S. (2013), Application of bend-twist coupled blades for horizontal axis tidal turbines. *Renewable Energy*, **50**: pp. 541–550, doi:10.1016/j.renene.2012.06.043.

Norberg, C. (2003), Fluctuating lift on a circular cylinder: review and new measurements. *Journal of Fluids and Structures*, **17**(1): pp. 57–96, doi:10.1016/S0889-9746(02)00099-3.

Oerlemans, S., Sijtsma, P. and Mendezlopez, B. (2007), Location and quantification of noise sources on a wind turbine. *Journal of Sound and Vibration*, **299**(4-5): pp. 869–883, doi:10.1016/j.jsv.2006.07.032.

Oerlemans, S., Fisher, M., Maeder, T. and Kögler, K. (2009), Reduction of wind turbine noise using optimized airfoils and trailing-edge serrations. *AIAA Journal*, **47**(6): pp. 1470–1481, doi:10.2514/1.38888.

Olausson, M. and Eriksson, L.E. (2009), Rotor wake/stator broadband noise calculations using hybrid RANS/LES and chorochronic buffer zones. In: *15th AIAA/CEAS Aeroacoustics Conference*, 11th-13th May, Miami, pp. 1–12, doi:10.2514/6.2009-3338.

Pamiés, M., Weiss, P.E., Garnier, E., Deck, S. and Sagaut, P. (2009), Generation of synthetic turbulent inflow data for large eddy simulation of spatially evolving wall-bounded flows. *Physics of Fluids*, **21**(4): pp. 045,103–1 – 045,103–15, doi:10.1063/1.3103881.

Pan, Y.C. and Zhang, H.X. (2010), Numerical hydro-acoustic prediction of marine propeller noise. *Journal of Shanghai Jiaotong University*, **15**(6): pp. 707–712, doi:10.1007/s12204-010-1073-4.

Parvin, S., Workman, R., Bourke, P. and Nedwell, J. (2005), Assessment of tidal current turbine noise at the Lynmouth site and predicted impact of underwater noise at Strangford Lough. *Tech. Rep. 628 R 0102*, Subacoustech Ltd.

Patankar, S. (1980), *Numerical heat transfer and fluid flow*. New York: McGraw-Hill, pp. 113–135, ISBN 0-07-048740-5.

Paterson, R. and Amiet, R. (1976), Measurement of the noise resulting from the interaction of turbulence with a lifting surface. *Tech. Rep. CR-2733*, United Technologies Research Center.

Perret, L., Delville, J., Manceau, R. and Bonnet, J.P. (2006), Generation of turbulent inflow conditions for large eddy simulation from stereoscopic PIV measurements. *International Journal of Heat and Fluid Flow*, **27**(4): pp. 576–584, doi:10.1016/j.ijheatfluidflow.2006.02.005.

— (2008), Turbulent inflow conditions for large-eddy simulation based on low-order empirical model. *Physics of Fluids*, **20**(7): pp. 075,107–1 – 075,107–17, doi:10.1063/1.2957019.

Peth, S., Seo, J., Moon, Y. and Jacob, M.C. (2006), Computation of aerodynamic noise from rod wake-airfoil interactions. In: *Proceedings of ECCOMAS CFD*, 5th-8th September, Delft, pp. 1–16.

Piomelli, U. and Balaras, E. (2002), Wall-layer models for large-eddy simulations. *Annual Review of Fluid Mechanics*, **34**: pp. 349–374, doi:10.1146/annurev.fluid.34.082901.144919.

Poletto, R., Revell, A., Craft, T. and Jarrin, N. (2013), Divergence free synthetic eddy method for embedded LES inflow boundary conditions. *Flow, Turbulence and Combustion*, **to appear**.

Pope, S.B. (2000*a*), *Turbulent flows*. Cambridge: Cambridge University Press, pp. 3–9, ISBN 978-0521598866.

— (2000*b*), *ibid.* pp. 182–263.

— (2000*c*), *ibid.* pp. 264–332.

— (2000*d*), *ibid.* pp. 34–82.

— (2000*e*), *ibid.* pp. 344–357.

— (2000*f*), *ibid.* pp. 558–640.

Powell, A. (1964), Theory of vortex sound. *The Journal of the Acoustical Society of America*, **36**(1): pp. 177–195, doi:10.1121/1.1918931.

Raichel, D.R. (2006), *The science and applications of acoustics*. 2nd edn., New York: Springer, pp. 31–71, ISBN 978-0387-26062-4.

Reboul, G., Polacsek, C., Lewy, S. and Heib, S. (2008), Aeroacoustic computation of ducted-fan broadband noise using LES data. In: *Acoustics'08 Paris*, 29th June-4th July, Paris, pp. 4077–4082, doi:10.1121/1.2934519.

Reese, H. and Carolus, T.H. (2008), Axial fan noise: towards sound prediction based on numerical unsteady flow data - a case study. *Acoustics'08 Paris*, **123**(5): pp. 4069–4074, doi:10.1121/1.2934518.

Reese, H., Kato, C. and Carolus, T.H. (2007), Large eddy simulation of acoustical sources in a low pressure axial-flow fan encountering highly turbulent inflow. *Journal of Fluids Engineering*, **129**(3): pp. 263–272, doi:10.1115/1.2427077.

Rhie, C. and Chow, W. (1983), Numerical study of the turbulent flow past an airfoil with trailing edge separation. *AIAA Journal*, **21**: pp. 1525–1532, doi:10.2514/3.8284.

Richards, S., Harland, E. and Jones, S. (2007), Underwater noise study supporting scottish executive strategic environmental assessment for marine renewables. *Tech. Rep. 06/02215/2*, QinetiQ Ltd.

Roger, M. and Moreau, S. (2010), Extensions and limitations of analytical airfoil broadband noise models. *International Journal of Aeroacoustics*, **9**(3): pp. 273–306, doi:10.1260/1475-472X.9.3.273.

Rosetti, G.F., Vaz, G. and Fujarra, A.L.C. (2012), URANS calculations for smooth circular cylinderflow in a wide range of Reynolds numbers: solution verification and validation. *Journal of Fluids Engineering*, **134**(12): pp. 121,103–1 – 121,103–18, doi:10.1115/1.4007571.

Saad, Y. (2003), *Iterative methods for sparse linear systems*. 2nd edn., Philadelphia: Society for Industrial and Applied Mathematics, p. 547.

Sagaut, P. (2006*a*), *Large eddy simulation for incompressible flows*. Berlin: Springer-Verlag, pp. 209–280, ISBN 978-3540263449.

— (2006*b*), *ibid.* pp. 15–44.

Salvatore, F. and Ianniello, S. (2003), Preliminary results on acoustic modelling of cavitating propellers. *Computational Mechanics*, **32**(4-6): pp. 291–300, doi:10.1007/s00466-003-0486-4.

Scharpf, D.F. and Mueller, T.J. (1995), An experimental investigation of the sources of propeller noise due to the ingestion of turbulence at low speeds. *Experiments in Fluids*, **18**(4): pp. 277–287, doi:10.1007/BF00195098.

Seo, J. and Moon, Y. (2007), Aerodynamic noise prediction for long-span bodies. *Journal of Sound and Vibration*, **306**(3-5): pp. 564–579, doi:10.1016/j.jsv.2007.05.042.

Seol, H., Pyo, S., Suh, J.C. and Lee, S. (2004), Numerical study of non-cavitating underwater propeller noise. *Noise & Vibration Worldwide*, **35**(6): pp. 11–26, doi:10.1260/0957456041648489.

Seol, H., Suh, J.C. and Lee, S. (2005), Development of hybrid method for the prediction of underwater propeller noise. *Journal of Sound and Vibration*, **288**(1-2): pp. 345–360, doi:10.1016/j.jsv.2005.01.015.

Sharland, I. (1964), Sources of noise in axial flow fans. *Journal of Sound and Vibration*, **1**(3): pp. 302–322, doi:10.1016/0022-460X(64)90068-9.

Siddon, T.E. (1973), Surface dipole strength by cross-correlation method. *The Journal of the Acoustical Society of America*, **53**(2): pp. 619–630, doi:10.1121/1.1913366.

Simonich, J.C., Amiet, R.K., Schlinker, R.H. and Greitzer, E.M. (1990), Rotor noise due to atmospheric turbulence ingestion-Part I: Fluid mechanics. *Journal of Aircraft*, **27**(1): pp. 7–14, doi:10.2514/3.45891.

Smagorinsky, J. (1963), General circulation experiments with the primitive equations. I. The basic experiment. *Monthly Weather Review*, **91**(3): pp. 99–165, doi:10.1175/1520-0493(1963)091<0099:GCEWTP>2.3.CO;2.

Smirnov, A., Shi, S. and Celik, I. (2001), Random flow generation technique for large eddy simulations and particle-dynamics modeling. *Journal of Fluids Engineering*, **123**(2): pp. 359–371, doi:10.1115/1.1369598.

SONIC (2013), Suppression Of underwater Noise Induced by Cavitation. URL `http://www.sonic-project.eu`.

Spalart, P.R. (2000), Strategies for turbulence modelling and simulations. *International Journal of Heat and Fluid Flow*, **21**: pp. 252–263, doi:10.1016/S0142-727X(00)00007-2.

Spalart, P.R., Jou, W., Strelets, M. and Allmaras, S. (1997), Comments on the feasibility of LES for wings, and on a hybrid RANS/LES approach. In: *Proceedings of the 1st AFOSR International Conference on DNS/LES*, 4th-8th August, Ruston.

Spalart, P.R., Shur, M.L., Strelets, M.K. and Travin, A.K. (2011), Initial noise predictions for rudimentary landing gear. *Journal of Sound and Vibration*, **330**(17): pp. 4180–4195, doi:10.1016/j.jsv.2011.03.012.

Spalding, D.B. (1961), A single formula for the "Law of the Wall". *Journal of Applied Mechanics*, **28**(3): pp. 455–458, doi:10.1115/1.3641728.

Spille-Kohoff, A. and Kaltenbacher, H. (2001), Generation of turbulent inflow data with a prescribed shear-stress profile. In: Liu, Sakell and Beutner (eds.), *DNS/LES Progress and Challenges*, Greyden Press, pp. 319–326.

Stacey, M.T., Monismith, S.G. and Burau, J.R. (1999), Measurements of Reynolds stress profiles in unstratified tidal flow. *Journal of Geophysical Research*, **104**(C5): pp. 10,933–10,949, doi:10.1029/1998JC900095.

Stansby, P. (2003), A mixing-length model for shallow turbulent wakes. *Journal of Fluid Mechanics*, **495**: pp. 369–384, doi:10.1017/S0022112003006384.

Starzmann, R., Baldus, M., Groh, E., Hirsch, N., Lange, N.A. and Scholl, S. (2013), Full-scale testing of a tidal energy converter using a tug boat. In: *Proceedings of the 10th European Wave and Tidal Energy Conference*, 2nd-5th September, Aalborg.

Svennberg, U. and Fureby, C. (2010), Vortex-shedding induced trailing-edge acoustics. In: *Proceedings of the 48th AIAA Aerospace Sciences Meeting*, 4th-7th January, Orlando, doi:10.2514/6.2010-12.

Sweby, P.K. (1984), High resolution schemes using flux limiters for hyperbolic conservation laws. *SIAM Journal on Numerical Analysis*, **21**(5): pp. 995–1011, doi:10.1137/0721062.

Tabor, G.R. and Baba-Ahmadi, M. (2010), Inlet conditions for large eddy simulation: a review. *Computers & Fluids*, **39**(4): pp. 553–567, doi:10.1016/j.compfluid.2009.10.007.

Tabor, G.R., Baba-Ahmadi, M., de Villiers, E. and Weller, H.G. (2004), Construction of inlet conditions for LES of a turbulent channel flow. In: *Proceedings of the European Conference on Computational Fluid Dynamics*, 24th-28th July, Jyväskylä, pp. 1–12.

Taylor, G. (1938), The spectrum of turbulence. *Proceedings of the Royal Society A: Mathematical, Physical and Engineering Sciences*, **164**(919): pp. 476–490, doi:0.1098/rspa.1938.0032.

Terracol, M., Manoha, E., Herrero, C., Labourasse, E., Redonnet, S. and Sagaut, P. (2005), Hybrid methods for airframe noise numerical prediction. *Theoretical and Computational Fluid Dynamics*, **19**(3): pp. 197–227, doi:10.1007/s00162-005-0165-5.

Testa, C., Ianniello, S., Salvatore, F. and Gennaretti, M. (2008), Numerical approaches for hydroacoustic analysis of marine propellers. *Journal of Ship Research*, **52**(1): pp. 57–70.

The OpenFOAM Foundation (2011), Programmer's guide, version 2.1.0. *Tech. rep.*

Turnock, S.R., Phillips, A.B., Banks, J. and Nicholls-Lee, R. (2011), Modelling tidal current turbine wakes using a coupled RANS-BEMT approach as a tool for analysing power capture of arrays of turbines. *Ocean Engineering*, **38**(11-12): pp. 1300–1307, doi:10.1016/j.oceaneng.2011.05.018.

Urick, R. (1996), *Principles of underwater sound for engineers*. 3rd edn., New York: McGraw-Hill, pp. 202–236, ISBN 978-0932146625.

van Driest, E.R. (1956), On turbulent flow near a wall. *Journal of the Aeronautical Sciences*, **23**(11): pp. 1007–1011, doi:10.2514/8.3713.

van Wijngaarden, E. (2005), Recent developments in predicting propeller-induced hull pressure pulses. In: *Proceedings of the 1st International Ship Noise and Vibration Conference*, 20th-21st June, London, pp. 1–8.

Veloudis, I., Yang, Z., McGuirk, J.J., Page, G.J. and Spencer, A. (2007), Novel implementation and assessment of a digital filter based approach for the generation of LES inlet conditions. *Flow, Turbulence and Combustion*, **79**(1): pp. 1–24, doi:10.1007/s10494-006-9058-y.

Versteeg, H.K. and Malalasekera, W. (1995*a*), *An introduction to fluid dynamics: The finite volume method*. Harlow: Longman Group, pp. 10–40, ISBN 0-582-21884-5.

— (1995*b*), *ibid.* p. 257.

— (1995*c*), *ibid.* pp. 192–209.

— (1995*d*), *ibid.* pp. 103–134.

Wagner, C., Hüttl, T. and Sagaut, P. (2007), *Large-eddy simulation for acoustics*. 2nd edn., Cambridge: Cambridge University Press, pp. 1–23, ISBN 978-0-511-29466-2.

Wan, B., Benra, F.K. and Dohmen, H.J. (2013), Application of a new numerical solver to turbomachinery flow problems. *Proceedings of the Institution of Mechanical Engineers, Part A: Journal of Power and Energy*, **227**(6): pp. 628–636, doi:10.1177/0957650913497359.

Wang, D., Atlar, M. and Sampson, R. (2007), An experimental investigation on cavitation, noise, and slipstream characteristics of ocean stream turbines. *Proceedings of the Institution of Mechanical Engineers, Part A: Journal of Power and Energy*, **221**(2): pp. 219–231, doi:10.1243/09576509JPE310.

Wang, M. (1999), LES with wall models for trailing-edge aeroacoustics. In: *Annual Research Briefs 1999*, Centre for Turbulence Research, Stanford University/NASA Ames, pp. 355–364.

Wang, M., Freund, J.B. and Lele, S.K. (2006), Computational prediction of flow-generated sound. *Annual Review of Fluid Mechanics*, **38**(1): pp. 483–512, doi:10.1146/annurev.fluid.38.050304.092036.

Wang, Q., Zhou, H. and Wan, D. (2012), Numerical simulation of wind turbine blade-tower interaction. *Journal of Marine Science and Application*, **11**(3): pp. 321–327, doi:10.1007/s11804-012-1139-9.

Weinmann, M., Sandberg, R.D. and Doolan, C. (2010), Flow and noise predictions for a tandem cylinder configuration using novel hybrid RANS/LES approaches. In: *16th AIAA/CEAS Aeroacoustics Conference*, 7th-9th June, Stockholm, doi:10.2514/6.2010-3787.

Welch, P. (1967), The use of fast Fourier transform for the estimation of power spectra. *IEEE Transactions on Audio Electroacoustics*, **15**(2): pp. 70–73, doi:10.1109/TAU.1967.1161901.

Weller, H.G., Tabor, G.R., Jasak, H. and Fureby, C. (1998), A tensorial approach to computational continuum mechanics using object-oriented techniques. *Computers in Physics*, **12**(6): pp. 620–631, doi:10.1063/1.168744.

Williamson, C.H.K. (1996), Vortex dynamics in the cylinder wake. *Annual Review of Fluid Mechanics*, **28**(1): pp. 477–539, doi:10.1146/annurev.fl.28.010196.002401.

Wojno, J.P., Blake, W.K. and Mueller, T.J. (2002*a*), Turbulence ingestion noise, part 1: Experimental characterization of grid-generated turbulence. *AIAA Journal*, **40**(1): pp. 16–25, doi:10.2514/2.1636.

— (2002*b*), Turbulence ingestion noise, part 2: Rotor aeroacoustic response to grid-generated turbulence. *AIAA Journal*, **40**(1): pp. 26–32, doi:10.2514/2.1637.

Xie, Z.T. and Castro, I.P. (2008), Efficient generation of inflow conditions for large eddy simulation of street-scale flows. *Flow, Turbulence and Combustion*, **81**(3): pp. 449–470, doi:10.1007/s10494-008-9151-5.

Zang, Y., Street, R. and Koseff, J. (1993), A dynamic mixed subgrid-scale model and its application to turbulent recirculating flows. *Physics of Fluids A: Fluid Dynamics*, **5**(12): pp. 3186–3196, doi:10.1063/1.858675.